

Salt-driven fibrinogen self-assembly into nanofibers and their biofunctionality

Dissertation

submitted for the degree of
Doctor of Natural Sciences
– Dr.-rer. nat –

Faculty 2 Biology/Chemistry
University of Bremen

by

Stephani Stamboroski

Bremen, August 2024

Dissertation

zur Erlangung der Doktorwürde

– Dr.-rer. nat –

Eingereicht im Fachbereich 2 (Biologie/Chemie) der Universität Bremen

von

Stephani Stamboroski

Bremen, August 2024

1. Referee

Prof. Dr. rer. nat. Dorothea Brüggemann

Hochschule Bremen, Fakultät 4, E-202, Neustadtswall 30, 28199 Bremen, Germany

2. Referee

Prof. Dr. Andreas Hartwig

Fraunhofer Institute for Manufacturing Technology and Advanced Materials IFAM,
Wiener Strasse 12, 28359 Bremen, Germany

Date of defense: 25.10.2024



Universität
Bremen

Universität Bremen | Fachbereich 02 |
Postfach 33 04 40, 28334 Bremen

Universität Bremen
Fachbereich 2
Prüfungsamt Chemie
z. Hd. Frau Frauke Ernst
Leobener Straße

28359 Bremen
Deutschland

Prüfungsamt
Chemie

Frauke Ernst
Geschäftsstelle
Fachbereich 02
Leobener Str. / NW2
D-28359 Bremen

Verwaltungspavillon 06
Tel. 0421 218-62802
Fax 0421 218-9862802
frauke.ernst@uni-bremen.de
www.fb2.uni-bremen.de

Versicherung an Eides Statt

| | |
|---------------|-----------------------|
| Name, Vorname | Stamboroski, Stephani |
| Straße | - |
| Ort, PLZ | - |

Ich, Stephani Stamboroski,

versichere an Eides Statt durch meine Unterschrift, dass ich die vorstehende Arbeit selbständig und ohne fremde Hilfe angefertigt und alle Stellen, die ich wörtlich dem Sinne nach aus Veröffentlichungen entnommen habe, als solche kenntlich gemacht habe, mich auch keiner anderen als der angegebenen Literatur oder sonstiger Hilfsmittel bedient habe.

Ich versichere an Eides Statt, dass ich die vorgenannten Angaben nach bestem Wissen und Gewissen gemacht habe und dass die Angaben der Wahrheit entsprechen und ich nichts verschwiegen habe.

Die Strafbarkeit einer falschen eidesstattlichen Versicherung ist mir bekannt, namentlich die Strafandrohung gemäß § 156 StGB bis zu drei Jahren Freiheitsstrafe oder Geldstrafe bei vorsätzlicher Begehung der Tat bzw. gemäß § 161 Abs. 1 StGB bis zu einem Jahr Freiheitsstrafe oder Geldstrafe bei fahrlässiger Begehung.

Ort, Datum / Unterschrift

Ort, Datum: _____

Erklärungen zur elektronischen Version und zur Überprüfung einer Dissertation

Hiermit betätige ich gemäß §7, Abs. 7, Punkt 4, dass die zu Prüfungszwecken beigelegte elektronische Version meiner Dissertation identisch ist mit der abgegebenen gedruckten Version.

Ich bin mit der Überprüfung meiner Dissertation gemäß §6 Abs. 2, Punkt 5 mit qualifizierter Software im Rahmen der Untersuchung von Plagiatsvorwürfen einverstanden.

Unterschrift

DECLARATION ON THE CONTRIBUTION OF THE CANDIDATE TO A MULTI-AUTHOR ARTICLE/MANUSCRIPT WHICH IS INCLUDED AS A CHAPTER IN THE SUBMITTED DOCTORAL THESIS

Chapter 2: Principles of fibrinogen fiber assembly *in vitro*

Contribution of the candidate in % of the total workload (up to 100% for each of the following categories):

| | |
|--|----------------|
| Experimental concept and design: | ca. 75 % |
| Experimental work and/or acquisition of (experimental) data: | Not applicable |
| Data analysis and interpretation: | ca. 75 % |
| Preparation of Figures and Tables: | ca. 60 % |
| Drafting of the manuscript: | ca. 60 % |

Chapter 3: Influence of divalent metal ions on the precipitation of the plasma protein fibrinogen

Contribution of the candidate in % of the total workload (up to 100% for each of the following categories):

| | |
|--|-----------|
| Experimental concept and design: | ca. 80 % |
| Experimental work and/or acquisition of (experimental) data: | ca. 75 % |
| Data analysis and interpretation: | ca. 75 % |
| Preparation of Figures and Tables: | ca. 100 % |
| Drafting of the manuscript: | ca. 90 % |

Chapter 4: Influence of highly saline aqueous solutions of monovalent alkali metal ions on fibrinogen self-assembly *in vitro*

Contribution of the candidate in % of the total workload (up to 100% for each of the following categories):

| | |
|--|----------|
| Experimental concept and design: | ca. 80 % |
| Experimental work and/or acquisition of (experimental) data: | ca. 80 % |
| Data analysis and interpretation: | ca. 80 % |

| | |
|------------------------------------|-----------|
| Preparation of Figures and Tables: | ca. 100 % |
| Drafting of the manuscript: | ca. 90 % |

Chapter 5: Effect of interface-active polymers on the salt crystal size in waterborne hybrid materials

Contribution of the candidate in % of the total workload (up to 100% for each of the following categories):

| | |
|--|-----------|
| Experimental concept and design: | ca. 70 % |
| Experimental work and/or acquisition of (experimental) data: | ca. 70 % |
| Data analysis and interpretation: | ca. 75 % |
| Preparation of Figures and Tables: | ca. 100 % |
| Drafting of the manuscript: | ca. 75 % |

Chapter 6: Nanofiber topographies enhance platelet-fibrinogen scaffold interactions

Contribution of the candidate in % of the total workload (up to 100% for each of the following categories):

| | |
|--|----------|
| Experimental concept and design: | ca. 60 % |
| Experimental work and/or acquisition of (experimental) data: | ca. 40 % |
| Data analysis and interpretation: | ca. 40 % |
| Preparation of Figures and Tables: | ca. 40 % |
| Drafting of the manuscript: | ca. 30 % |

“Ciência inteligente não é aquela que resolve detalhes e fecha portas, mas a que abre novas
questões e possibilidades”

“Intelligent science is not that which solves details and closes doors, but that which opens
new questions and possibilities”

Suzana Herculano-Houzel

I would like to dedicate this doctoral dissertation to my Parents
Thanks for teaching us to never stop dreaming

ABSTRACT

The significant role of fibrinogen in relevant biological processes within the blood coagulation and wound healing cascade has led to its widespread utilization as novel biological materials for tissue engineering and wound treatment. The conversion of fibrinogen to fibrin by thrombin serves as a fundamental step, initiating the creation of a 3D-nanofibrous matrix that acts as a provisional extracellular matrix for subsequent tissue repair.

Inspired by this process, the current work explores the fabrication of fibrinogen nanofibers *in vitro* in enzyme-free environments, without addition of thrombin. Although various techniques have been devised to generate fibrin-like networks of fibrinogen, the primary factors influencing *in vitro* fibrinogen fiber formation remain unclear. Salt-induced fibrinogen self-assembly has gained especial attention recently since fibrous fibrinogen can be generated with a good yield and without using any organic solvent that could affect fibrinogen conformation, however a comprehensive mechanism for this phenomenon is yet to be completely understood.

Therefore, the aim of this thesis is to understand the fibrinogen-salt interactions during fibrinogen self-assembly under *in vitro* conditions in order to fabricate nanofiber scaffolds with reproducible topography and composition for later applications in tissue engineering. To achieve this purpose, five studies have been conducted with four of them to investigate the principal influences on the self-assembly of fibrinogen *in vitro* and to propose a mechanism to help explaining the salt induced fibrinogen self-assembly. Additionally, a fifth study on the interaction with blood cells is presented that demonstrates the application of nanofibrous fibrinogen derived from highly saline solutions as a scaffold biomaterial.

The first study in this thesis provides an overview and identifies the primary factors influencing the formation of fibrinogen nanofibers *in vitro*. Numerous experimental conditions and parameters were identified to have an influence on fiber formation, which were categorized into three main groups: substrate interactions, denaturing, and non-denaturing buffer conditions. Results suggest that salts in the non-denaturing buffers category play an important role in fiber formation, since they are used to dissolve fibrinogen and are always present in many of the techniques used to prepare fibrinogen fibers. Therefore, the second and third study of this dissertation focused on investigating the influence of divalent and monovalent metal salts when drying fibrinogen in the presence of those varying salts.

Divalent and monovalent ions are involved in numerous essential biological reactions. Calcium ions as divalent ions, for instance, are fundamental to the initial stages of clot formation, leading to the hypothesis that calcium and other divalent ions would induce fibrinogen self-assembly *in vitro*. Still, none of the divalent salts tested, including those containing Ca^{2+} , Mg^{2+} , Zn^{2+} , or Cu^{2+} ions, resulted in the formation of fibrous fibrinogen layers. On the contrary, only smooth fibrinogen layers were obtained after drying fibrinogen in the presence of divalent chlorides, independently on their concentration. On the other hand, as shown previously in other studies, monovalent salts present in phosphate buffered saline (PBS) were able to trigger fibrinogen self-assembly *in vitro* after a drying step.

Hence, the third study in this PhD thesis explored the impact of various monovalent cations combined with different anions on fibrinogen fibrillogenesis. A range of monovalent salts underwent testing to assess their capability to form fibrous fibrinogen layers. Depending on the specific combination of cation and anion, diverse fibrinogen morphologies leading with varied topographies were observed. Furthermore, a direct correlation emerged between the surface composition of fibrinogen layers, post-washing to remove salt crystals, and the resulting morphologies. The varied fibrinogen layer morphologies obtained were explained by considering two dimensional Hofmeister effects and protein-salt interactions. The best cation-anion combination of salts to form fibrinogen nanofibers were the ones containing a kosmotropic cation (e.g. Na^+) with a kosmotropic anion (e.g. H_2PO_4^-).

During the course of this thesis, it was observed that salts exert an influence on fibrinogen precipitation and morphology just as much as fibrinogen impacts salts. Thus, the fourth study investigated how fibrinogen, and for comparison, other proteins, affect the precipitation and morphology of sodium chloride crystals. The examination of crystal shape variations based on the added protein highlighted the complexity and significance of this dual interaction between proteins and salts. A clear transition from cubic halite crystals to dendrites was noted when proteins as fibrinogen or collagen were added during the precipitation of sodium chloride crystals.

The fifth study of this thesis explored the biocompatibility of the fibrinogen nanofibers obtained from drying fibrinogen in the presence of highly saline solutions. Specifically, the response of blood platelets to different fibrinogen topographies was studied. The results revealed that increased topography, caused for instance by nanofibers, more prominently activated blood platelets compared to smooth fibrinogen layers.

The findings of this thesis are summarized in a final discussion chapter. In conclusion, the results obtained provide insights into the fundamental mechanism of fibrinogen precipitation in different topographies and nanofiber formation, suggesting a dependence on specific ion binding, enhancement of the hydrophobic effect during the drying process and the influence of ions on the hydration shell of the fibrinogen molecule. Moreover, through this research, the ability to modulate the structure of fibrinogen nanofibers using various salt solutions was demonstrated, laying the foundation for the development of more stable supramolecular nanofibers with potential applications in tissue engineering and wound healing in the future.

Keywords: Fibrinogen; Nanofibers; Biomaterials; Hofmeister series; Protein-salt interactions; Wound healing

ZUSAMMENFASSUNG

Die wichtige Rolle von Fibrinogen bei verschiedenen kritischen biologischen Prozessen innerhalb der Blutgerinnungskaskade und der Wundheilung hat dazu geführt, dass dieses Protein bei der Entwicklung neuer biologischer Materialien für das Tissue Engineering und die Wundbehandlung weit verbreitet ist. Die enzymatische Umwandlung von Fibrinogen zu Fibrin durch Thrombin ist ein grundlegender Schritt, der die Bildung einer 3D-Nanofasermatrix einleitet, die als provisorische extrazelluläre Matrix für die anschließende Gewebereparatur dient.

Inspiziert von diesem natürlichen Prozess wird in der aktuellen Arbeit die Herstellung von Fibrinogen-Nanofasern *in vitro* in einer enzymfreien Umgebung ohne Zugabe von Thrombin untersucht. Obwohl verschiedene Techniken entwickelt wurden, um solch fibrinähnliche Netzwerke aus Fibrinogen zu erzeugen, sind die wichtigsten Faktoren, die die Bildung von Fibrinogen fasern *in vitro* beeinflussen, noch unklar.

Die salzinduzierte Selbstorganisation von Fibrinogen hat in letzter Zeit besondere Aufmerksamkeit erregt, da so Nanofasengerüste aus Fibrinogen ohne die Verwendung von organischen Lösungsmitteln, die die Fibrinogenkonformation beeinträchtigen könnten, hergestellt werden können. Obwohl viele Parameter in diesem Prozess bereits reproduzierbar eingestellt werden können, ist der grundlegende Mechanismus für dieses Phänomen jedoch noch nicht vollständig geklärt.

Ziel der vorliegenden Arbeit ist es daher, zu untersuchen, welche Faktoren zur Bildung von Fibrinogen-Nanofasern *in vitro* beitragen und welche Protein-Salz-Wechselwirkungen diesen Prozess unterstützen. Zu diesem Zweck wurden vier Studien durchgeführt, um die wichtigsten Einflüsse auf die Selbstorganisation von Fibrinogen *in vitro* zu untersuchen und einen Mechanismus zur Erklärung der salzinduzierten Selbstassemblierung von Fibrinogen vorzuschlagen. Darauf aufbauend wurde eine fünfte Studie durchgeführt, die die Anwendung von Fibrinogen aus stark salzhaltigen Lösungen als Biomaterial für Scaffolds zeigt.

Die erste Studie gibt einen Überblick und identifiziert die wichtigsten Faktoren, die die Bildung von Fibrinogen-Nanofasern *in vitro* beeinflussen. Es wurden zahlreiche experimentelle Bedingungen und Parameter identifiziert, die einen Einfluss auf die Faserbildung haben und die in drei Hauptgruppen eingeteilt wurden: Substratinteraktionen, denaturierende und nicht denaturierende Pufferbedingungen. Die Ergebnisse deuten darauf hin, dass Salze in der Kategorie der nicht-denaturierenden Puffer eine wichtige Rolle bei der Faserbildung spielen, da sie zum Lösen von Fibrinogen verwendet werden und bei vielen der Techniken zur

Herstellung von Fibrinogenfasern immer vorhanden sind. Daher wurde in der zweiten und dritten Studie dieser Dissertation der Einfluss von zwei- und einwertigen Metallionen beim Trocknen von Fibrinogen in Gegenwart unterschiedlicher Salze untersucht.

Zweiwertige und einwertige Ionen sind an zahlreichen wichtigen biologischen Reaktionen beteiligt. Vor allem zweiwertige Ionen, wie z. B. Kalzium-Ionen, sind für die Anfangsphase der Blutgerinnung von grundlegender Bedeutung, was zu der Hypothese führte, dass Kalzium und andere zweiwertige Ionen die Selbstorganisation von Fibrinogen *in vitro* fördern könnten. Doch keines der untersuchten zweiwertigen Salze, einschließlich der Ca^{2+} -, Mg^{2+} -, Zn^{2+} - oder Cu^{2+} -Ionen, führte zur Bildung von faserigen Fibrinogenschichten. Im Gegensatz dazu wurden nach dem Trocknen von Fibrinogen in Gegenwart von zweiwertigen Chloriden unabhängig von deren Konzentration nur glatte Fibrinogenschichten gebildet. Andererseits konnten einwertige Salze in phosphatgepufferter Kochsalzlösung (PBS), wie bereits in anderen Studien gezeigt, die Fibrinogen-Selbstorganisation *in vitro* nach einem Trocknungsschritt auslösen.

In der dritten Studie dieser Doktorarbeit wurde daher die Wirkung verschiedener einwertiger Kationen in Kombination mit verschiedenen Anionen untersucht. Eine Reihe von einwertigen Salzen wurde getestet, um ihre Fähigkeit zur Bildung faseriger Fibrinogenschichten zu beurteilen. Je nach der spezifischen Kombination aus Kation und Anion wurden verschiedene Fibrinogenmorphologien beobachtet, die zu unterschiedlichen Topografien führten. Außerdem zeigte sich ein direkter Zusammenhang zwischen der Oberflächenzusammensetzung der Fibrinogenschichten nach dem Waschen zur Entfernung von Salzkristallen und den daraus resultierenden Morphologien. Die unterschiedliche Morphologie der Fibrinogenschichten wurden durch die Berücksichtigung von Hofmeister-Effekten und Protein-Salz-Wechselwirkungen erklärt. Die beste Kationen-Anionen-Kombination von Salzen zur Bildung von Fibrinogen-Nanofasern waren solche, die ein kosmotropes Kation (z. B. Na^+) mit einem kosmotropen Anion (z. B. H_2PO_4^-) enthalten.

Im Laufe dieser Arbeit wurde festgestellt, dass Salze die von Fibrinogen Ausfällung und die resultierende Morphologie genauso beeinflussen wie das Fibrinogen die vorhandenen Salze. Daher wurde in der vierten Studie untersucht, wie Fibrinogen und zum Vergleich auch andere Proteine die Ausfällung und Morphologie von Natriumchloridkristallen beeinflussen. Die Untersuchung der Veränderungen der Kristallform in Abhängigkeit vom zugegebenen Protein verdeutlichte die Komplexität und Bedeutung dieser doppelten Wechselwirkung zwischen Proteinen und Salzen. Es wurde ein deutlicher Übergang von kubischen Halitkristallen zu Dendriten festgestellt, wenn Proteine wie Fibrinogen oder Kollagen während der Ausfällung von Natriumchloridkristallen zugesetzt wurden.

Die fünfte Studie dieser Arbeit widmet sich der Untersuchung der Biokompatibilität von Fibrinogen-Nanofasern, die durch Trocknen von Fibrinogen in Gegenwart von stark salzhaltigen Lösungen hergestellt wurden. Insbesondere wurde die Reaktion von Blutplättchen auf verschiedene Fibrinogentopografien untersucht. Die Ergebnisse zeigen, dass eine erhöhte Topografie, z. B. durch Nanofasern, die Blutplättchen stärker aktiviert als glatte Fibrinogenschichten.

Die Forschungsergebnisse wurden in einem abschließenden Diskussionskapitel zusammengefasst. Insgesamt bieten die erzielten Ergebnisse Einblicke in den grundlegenden Mechanismus der Bildung von Fibrinogen-Nanofasern in verschiedenen Topografien durch die Anwesenheit von Salzen. Sie deuten auf eine Abhängigkeit von der Bindung spezifischer Ionen, die Verstärkung des hydrophoben Effekts während des Trocknungsprozesses und den Einfluss der Ionen auf die Hydrathülle des Fibrinogenmoleküls hin. Darüber hinaus konnten wir zeigen, dass sich die Struktur von Fibrinogen-Nanofasern mit Hilfe verschiedener Salzlösungen modulieren lässt. Dies ebnet den Weg für die Entwicklung stabilerer supramolekularer Nanofasern, die in Zukunft in der Gewebezüchtung und Wundheilung eingesetzt werden könnten.

Stichwörter: Fibrinogen; Nanofasern; Biomaterialien; Hofmeister-Reihe; Protein-Salz-Wechselwirkungen; Wundheilung

ACKNOWLEDGEMENTS

I would like to thank Prof. Dr. Dorothea Brüggemann for her continuous support and encouragement throughout this thesis, especially at the more challenging times during the pandemic. I am very thankful for her guidance, supervision, and the scientific discussions we had.

I would like to thank Prof. Dr. Andreas Hartwig for accepting the invitation to be part of this examination committee, and for his insightful comments and suggestions.

I would like to express my sincere gratitude to Prof. Dr. Bernd Mayer for his support throughout the course of this work, and for the opportunity of staying at the Fraunhofer IFAM after my Master thesis.

My special thanks to Dr. Stefan Dieckhoff, Dr. Peter Schiffels and Dr. Michael Noeske for all the support, patience, time spent on discussions and sharing of ideas. Without their support and encouragement this thesis would not have been possible.

I would like to thank the financial, scientific support and networking of the Fraunhofer TALENTA program, where I had the great opportunity to meet, connect and learn from many inspiring women.

I am very thankful to Thomas Kowalik, Katharina Richter, Thomas Lukasczyk, Annika Stalling, Ralph Wilken, Jonas Aniol, Andreas Volkmann, Kai Brune, Julian Heine, Andreas Krenz and Karsten Thiel for their training and access to different techniques at IFAM that made this thesis possible.

Many thanks to Dr. Welchy Leite Cavalcanti as a colleague and friend for all her support before and during this time. This period of PhD work was made easier due to the time shared with colleagues. In this regard, I would like to thank all the colleagues of the OE418, especially the ones from AG Applied Computational Chemistry. Also, a big thank you to my colleagues at the Brüggemann's lab, especially Eva Eilers, Deepanjalee Duta and Arundhati Joshi who made the daily work in the lab more fun.

Thank you to the students I had the opportunity to co-supervise, Jana Lierath, Kwasi Boateng and Antoine Kwame. The exchange we had was very rich and has produced many results.

I would like to thank God for blessing me with a great family and friends and giving me the purpose and encouragement needed to continue and finalize this work. In this regard, the biggest thanks go of course to my family and friends for their continuous support, patience,

encouragement and for all the time spent together that made life easier especially at the stressful times. Thank you, Mom and Dad for being my inspiration, for being always there when I needed and for encouraging me and doing your best to allowing us to study and pursuing our dreams. Especial thanks to my brothers and my second family Carrillos Bebers. Thank you for the friends in Germany who are like family here and make the life abroad much easier and happier. Thank you for the friends in Brazil who even far away always find some time to be present. Thank you also to my therapist Lucimara for her patience, mentoring and support during these years, especially at the most challenging times.

There are not enough words to thank my husband Vinicius. Without his endless support, patience, love, caring and encouragement this journey would not be possible. Thank you for sharing the life with me and make everything more colorful, interesting, and possible by having you by my side. Also thank you to our daughter, Marianne, who gave us a new purpose in life and allowed me to experience the greatest love in the world.

PUBLICATION LIST & SCIENTIFIC CONTRIBUTIONS

Publications as part of the cumulative dissertation:

The scientific publications listed below were produced as part of this dissertation. The context of these publications is presented in the following chapters of this thesis.

Published papers

- (a) Stamboroski, S., Joshi, A., Noeske, P. L. M., Köppen, S., & Brüggemann, D. (2021). Principles of fibrinogen fiber assembly *in vitro*. *Macromolecular Bioscience*, 21(5), 2000412.
- (b) Stamboroski, S., Boateng, K., Lierath, J., Kowalik, T., Thiel, K., Köppen, S., Noeske, P. L. M., & Brüggemann, D. (2021). Influence of divalent metal ions on the precipitation of the plasma protein fibrinogen. *Biomacromolecules*, 22(11), 4642-4658.
- (c) Stamboroski, S., Boateng, K., Leite Cavalcanti, W., Noeske, M., Beber, V. C., Thiel, K., Grundwald, I., Schiffels, P., & Brüggemann, D. (2021). Effect of interface-active proteins on the salt crystal size in waterborne hybrid materials. *Applied Adhesion Science*, 9(1), 1-22
- (d) Kenny, M., Stamboroski, S., Taher, R., Brüggemann, D., & Schoen, I. (2022). Nanofiber Topographies Enhance Platelet-Fibrinogen Scaffold Interactions. *Advanced Healthcare Materials*, 11(14), 2200249

To be submitted

- (a) Stamboroski, S., Boateng, K., Lierath, J., Aniol, J., Schiffels, P., Noeske, P. L. M., Brüggemann, D. Influence of highly saline aqueous solutions of monovalent alkali metal ions on fibrinogen self-assembly *in vitro*.

Further publications (not part of this thesis):

- (a) Dias, L. F.G, Rheinheimer, J. P., Gomes, O. P., Noeske, M., Stamboroski, S., Bronze-Uhle, E. S., & Lisboa-Filho, P. N. (2022). Bisphosphonates on Smooth TiO₂: Modeling and Characterization. *ChemistrySelect*, 7(19), e202200286.
- (b) Dias, L. F. G., Stamboroski, S., Noeske, M., Salz, D., Rischka, K., Pereira, R., & Lisboa-Filho, P. N. (2020). New details of assembling bioactive films from dispersions of amphiphilic molecules on titania surfaces. *RSC advances*, 10(65), 39854-39869.

Conference contributions:

- (a) S. Stamboroski, K. Stapelfeldt, M. Michaelis, D. Brüggemann, “Secondary structure changes of fibrinogen in the presence of salt”. *13th North German Biophysics Meeting*, 17 January 2020,| Borstel, Germany
- (b) S. Stamboroski, N. Suter, K. Stapelfeldt, T. Wunsch, M. Michaelis, D. Brüggemann, “Self-assembled fibrinogen nanofibers: a multiscale scaffold platform for wound healing”, *Material Science and Engineering Congress (MSE)*, 22-25 September 2020, Virtual
- (c) S. Stamboroski, I. Schoen, R. Taher, Y. Roger, A. Hoffmann, D. Brüggemann. “Interaction of blood platelets in mesenchymal stem cells with self-assembled fibrinogen nanofibers.” *6th European Symposium on Biomaterials and Related Areas (BioMAT)*, 05-06 May 2021, Virtual
- (d) S. Stamboroski, W. L. Cavalcanti, D. Brüggemann, “Salt-induced self-assembly of fibrinogen nanofibers: How the development of new biomaterials can benefit from a virtual materials marketplace”. *6th NanoTech France 2021 International Conference and Exhibition*, 23-25 June 2021, Virtual
- (e) S. Stamboroski, A. Joshi, D. Dutta and D. Brüggemann, "Fibrous biopolymer scaffolds as synthetic ECM mimetics for soft tissue engineering" *Brazilian Materials Research Society Meeting (SBPMat)*, 30 August – 03 September 2021, Virtual
- (f) S. Stamboroski, A. Joshi, M. Kenny, R. Taher, I. Schoen, D. Brüggemann, “How do cells involved in wound healing interact with self-assembled fibrinogen nanofibers?” *Annual Meeting of the German Society for Biomaterials (DGBM)*, 07-08 October 2021, Virtual
- (g) S. Stamboroski, K. Boateng, J. Lierath, T. Kowalik, K. Thiel, G. Lause, S. Köppen, M. Noeske & D. Brüggemann. “Variances in the precipitation behaviour of fibrinogen in the presence of mono- and divalent salts”. *26th Fibrinogen Workshop*, 12-16, 2022 June, Jongny sur Vevey, Switzerland
- (h) S. Stamboroski, A. Joshi, M. Kenny, R. Taher, I. Schoen & D. Brüggemann. “Interaction of cells involved in wound healing with self-assembled fibrinogen nanofibers”. *26th Fibrinogen Workshop*, 12-16 June, 2022, Jongny sur Vevey, Switzerland.

Bachelor and Master thesis co-supervision:

(a) Bachelor thesis: Jana Lierath, Universität Bremen, FB1: B. Sc. in Physics, 2021, Title: “Secondary structure of fibrinogen upon drying in the presence of divalent salts”;

(b) Master thesis: Kwasi Boateteg, Universität Bremen, FB5: M.Sc. Materials Chemistry and Mineralogy, 2021, Title: “Precipitation characteristics of varying salts in the presence of fibrinogen”;

(c) Master thesis: Antoine Eyram Kwame, FB5: M.Sc. Materials Chemistry and Mineralogy, 2022, Title: “Binding of extracellular matrix and plasma proteins to self-assembled fibrinogen scaffolds”;

TABLE OF CONTENTS

| | |
|--|-------|
| ABSTRACT | X |
| ZUSAMMENFASSUNG..... | XIII |
| ACKNOWLEDGEMENTS..... | XVI |
| PUBLICATION LIST & SCIENTIFIC CONTRIBUTIONS | XVIII |
| LIST OF FIGURES | XXIII |
| LIST OF TABLES | XXVI |
| 1. INTRODUCTION & RESEARCH AIM | 1 |
| 1.1. Background..... | 1 |
| 1.2. Tissues | 1 |
| 1.3. Extra-cellular matrix | 2 |
| 1.4. Wound healing..... | 5 |
| 1.5. Fibrinogen and the blood coagulation cascade..... | 6 |
| 1.6. Fibrinogen as a building block for biomaterials | 9 |
| 1.7. Fibrinogen-salt interactions <i>in vitro</i> | 14 |
| 1.8. Research aim..... | 18 |
| 2. PRINCIPLES OF FIBRINOGEN FIBER ASSEMBLY IN VITRO..... | 20 |
| 2.1. Motivation & Hypothesis | 20 |
| 3. INFLUENCE OF DIVALENT METAL IONS ON THE PRECIPITATION OF THE PLASMA PROTEIN FIBRINOGEN 38 | |
| 3.1. Motivation & Hypothesis | 38 |
| 4. INFLUENCE OF HIGHLY SALINE AQUEOUS SOLUTIONS OF MONOVALENT ALKALI METAL IONS ON FIBRINOGEN SELF-ASSEMBLY <i>IN VITRO</i> | 67 |
| 4.1. Motivation & Hypothesis | 67 |
| 5. EFFECT OF INTERFACE-ACTIVE POLYMERS ON THE SALT CRYSTAL SIZE IN WATERBORNE HYBRID MATERIALS | 110 |
| 5.1. Motivation & Hypothesis | 110 |
| 6. NANOFIBER TOPOGRAPHIES ENHANCE PLATELET-FIBRINOGEN SCAFFOLD INTERACTIONS..... | 133 |
| 6.1. Motivation & Hypothesis | 133 |
| 7. SUMMARIZING DISCUSSION & FUTURE PERSPECTIVES | 155 |
| 7.1. <i>IN VITRO</i> FIBRILLOGENESIS OF FIBRINOGEN | 157 |
| 7.1.1. Main factors contributing to fibrinogen fibrillogenesis <i>in vitro</i> | 157 |
| 7.1.2. Fibrinogen precipitates prepared from highly saline solutions | 160 |

| | | |
|--------|--|-----|
| 7.2. | THE COMPLEX MUTUAL INTERACTIONS BETWEEN FIBRINOGEN AND VARIOUS SALTS | 161 |
| 7.2.1. | Fibrinogen precipitates formed from divalent and monovalent salts | 162 |
| 7.2.2. | New insights into the mechanism of fibrinogen self-assembly in vitro | 168 |
| 7.2.3. | The co-influence of proteins and salt precipitation | 177 |
| 7.3. | BIOFUNCTIONALITY OF FIBRINOGEN SCAFFOLDS | 178 |
| 7.4. | FUTURE PERSPECTIVES | 181 |
| | REFERENCES | 185 |

LIST OF FIGURES

Figure 1-1: Example of a normal ECM function and structure with its basic components. BM stands for basement membrane (reproduced with permission from (Frantz et al., 2010). Copyright Journal of Cell Science 2010) 3

Figure 1-2: Schematic representation of the fibrinogen molecule with: three pairs of polypeptide chains, referred to as A α (blue), B β (red), and γ (green) chains. Fibrinogen structure features two globular domains, known as D-domains, at each end. The D-domains are connected in the middle by the helical coiled E-domain. Adapted from Köhler et al. (Köhler et al., 2015). 6

Figure 1-3: Schematic representation of the blood coagulation cascade that involves a series of enzymatic reactions based on different clotting factor. The cascade contains three pathways: intrinsic, extrinsic, and common. Thrombin (Factor IIa) acts on the common pathway leading to the formation fibrin from fibrinogen. 8

Figure 1-4: Fiber extrusion process of protein-based nanofibers. In this process, a biopolymer feed solution is pressed against a anodic aluminum oxide (AAO) membrane leading to the extrusion of protein-based nanofibers. Adapted from (Raoufi et al., 2015). 12

Figure 1-5: Hofmeister series: on the left side (blue) are located more kosmotropic ions, which are characterized by the salting-out (aggregation) of proteins; on the right side (yellow) are located more chaotropic ions, which induce the salting-in (solubilization) of proteins. The kosmotropic and chaotropic ions possess opposing characteristics in terms of water surface tension, protein solubility, protein denaturation, protein stability and protein hydrophobicity. | Adapted from Kang et al and Nihonyanagi et al. (Kang et al., 2020; Nihonyanagi et al., 2014). 16

Figure 7-1: Schematic representation of the main findings from this PhD thesis according to their Chapters 155

Figure 7-2: Sketch of the standard operating procedure for fibrinogen nanofiber assembly and scaffold post-treatment used in this thesis. Fibrinogen solutions were prepared in Tris buffer. Reference planar samples were prepared by drying fibrinogen solution in Tris. Fibrous samples were prepared by mixing the fibrinogen solution with different salts. After mixing both solutions, the samples were placed in a chamber where temperature and humidity were

- controlled and left overnight for drying. The precipitated fibrinogen layers were then cross-linked with formaldehyde vapor and subsequently washed. 161
- Figure 7-3: Comparison of monovalent and divalent salts in terms of fibrillogenesis and roughness obtained after drying fibrinogen solutions with different salts and varying ion combinations. Images of fibrinogen dried in presence of divalent salts were modified and reproduced with permission from (Stamboroski, Boateng, et al., 2021). Copyright © 2021, American Chemical Society. 163
- Figure 7-4: Hofmeister Series obtained for the formation of fibrinogen nanofibers based on the studies presented in Chapters 3 and 4. Left side (blue) of the image shows kosmotropic anions and cations, which have a higher tendency to salting out and form fibrinogen nanofibers. Right side (yellow) shows the more chaotropic cations and anions with the tendency of salting in and form smooth layers. 166
- Figure 7-5: The important entities and their interactions in aqueous supramolecular chemistry. Grey lines indicate non-covalent interactions between the three components water, salt, and solute, as well as the interactions between solutes, between ions, and between waters. Reproduced with permission ((Gibb, 2011) Copyright 2011 Wiley-VCH Verlag GmbH&Co. KGaA, Weinheim). 167
- Figure 7-6: Sketch of the proposed mechanism by Koo et al. of surface-induced fibrinogen self-assembly. (A) Adsorption of the initial layer directly onto the surface where the hydrophobic D and E regions are preferentially adsorbed, and the hydrophilic α C regions remain free to interact with other molecules. (B) Once the surface is coated with monomers (represented by the image of a trinodular structure), subsequent molecules can migrate and self-assemble into protofibrils. (C) Attractive forces between the α C domains on the exterior of the protofibrils induce further coalescence of the fibers into increasingly larger ones, which remain anchored onto the surface. Reproduced with permission (Jaseung Koo et al., 2012). Copyright © 2012 American Chemical Society. 169
- Figure 7-7: Summarizing sketch of the proposed mechanisms for fibrinogen precipitation by drying fibrinogen with highly saline solutions of different salts. The first scenario presents what happens during precipitation of fibrinogen in the presence of salts that contain a combination of chaotropic ions, e.g. the divalent salts studied in Chapter 3 (CaCl_2 , MgCl_2 and others) that resulted in smooth fibrinogen layers upon drying. The second scenario illustrates fibrinogen aggregation in the presence of salts that contain chaotropic and kosmotropic ions, e.g.

monovalent cations with chlorides or divalent cations with sulfates as presented in Chapter 4, that resulted in rough fibrinogen layers or partial nanofiber formation. The third scenario proposes a mechanism for fibrinogen nanofiber formation when fibrinogen is dried with salts composed of kosmotropic ions, such as monovalent cations with phosphate or sulfate anions, that were also presented in Chapter 4..... 176

LIST OF TABLES

Table 1-1: Nomenclature of the coagulation proteins/clotting factors. Adapted from Palta et al. (Palta et al., 2014) 7

1. INTRODUCTION & RESEARCH AIM

1.1. BACKGROUND

Fibrinogen is a protein naturally found in the body and intrinsically involved in blood coagulation giving support to the blood clot and stopping bleeding. During the wound healing, fibrin (originated from fibrinogen) and fibronectin-rich extracellular matrix, or provisional matrix, emerge creating binding sites and topographic cues for cell adhesion (Barker & Engler, 2017; Pereira et al., 2002).

With the development of tissue engineering techniques, fibrinogen and its ability to form fibers has found a growing application as a biomaterial, especially on scaffolding, as a mimicking device of the extra-cellular matrix. Despite many fabrication techniques for fibrinogen nanofibers being available, the majority of them either involve the use of solvents (e.g. electrospinning, which impact functionality) or have a low yield (e.g. freeze drying, which impact feasibility).

In recent years, the salt-induced self-assembly of fibrinogen has emerged as a method, which provides high yield, whilst keeping the conformation and functionality of the protein. Moreover, to ensure the use of fibrinogen as a biomaterial for scaffold applications, it is critical to understand how cells behave in contact with the nanofibrous structure of self-assembled fibrinogen. Nonetheless, the mechanisms behind the salt-fibrinogen interactions leading to the formation of fibrinogen nanofibers are not yet fully elucidated.

In the following sections the fundamentals of the concepts related to this topic will be discussed and detailed: tissues (Section 1.2), extracellular matrix (Section 1.3), wound healing (Section 1.4), fibrinogen and the blood coagulation cascade (Section 1.5), fibrinogen as a building block for biomaterials (Section 1.6), and fibrinogen-salt-interactions *in vitro* (Section 1.7). Finally, the research aim and respective objectives of this doctoral thesis are given in Section 1.8.

1.2. TISSUES

In biology, the structural formation of the body follows a hierarchical level of complexity across different length scales: from molecular via nano- and microscopic organization to macroscopic levels (as in whole organs) (Cowin, 2000). A tissue can be defined as a term used in biology to describe a group or collection of cells that work together to perform a specific function within an organism (Cowin, 2000). A tissue is composed of a group of similar cells and their intercellular material, the so-called extracellular matrix (ECM) (Theocharis et al., 2016). As a next organization level, the grouping of multiple tissues form organs. Organs are also

systematised into organ systems as, for example, the circulatory system, which consists of the heart and blood vessels. Finally, organ systems come together to create an entire organism. Animal tissues are commonly classified into four basic types (Verma et al., 2020):

- Epithelial tissue lines the surfaces of organs, cavities, and structures both internally and externally. It serves as protective barriers with specialized functions such as absorption, secretion, or sensory reception. Examples of epithelial tissue include the epithelial lining of the respiratory tract, skin, and digestive system.
- Connective tissue provides support, structure, and connection between different tissues and organs. It consists of cells embedded in an extracellular matrix composed of fibers and ground substance. Examples of connective tissue include bone, cartilage, blood, and adipose tissue.
- Muscle tissue is responsible for force transmission and enabling movement. The muscle tissue is further divided into three types, namely skeletal muscle, which is involved in voluntary movement; smooth muscle, found in the walls of organs and blood vessels; and cardiac muscle, which is specific to the heart.
- Nervous tissue comprises neurons and supporting cells called glial cells. It forms the basis of the nervous system, whilst being responsible for transmitting and processing information. It is involved in functions such as sensation, coordination, and control of body activities.

In this regard, the ECM is present in various tissues throughout the body, providing tissue connection, and influencing cell adhesion, proliferation, and differentiation. The ECM is intimately linked to the structure, function, and regulation of tissues (Theocharis et al., 2016). Its composition and properties vary across the different tissues, as further discussed in the next section.

1.3. EXTRA-CELLULAR MATRIX

The extracellular matrix is the non-cellular and vital component of all tissues and organs (Frantz et al., 2010). The ECM is a unique dynamic and tissue specific complex three-dimensional structure formed by water, proteins, glycoproteins, and proteoglycans (Badylak, 2002; Frantz et al., 2010). The cells that forms the tissues interact with the ECM and are embedded in this macromolecular network (Theocharis et al., 2016). The main functions of the ECM are to offer structural support, biomechanical and biochemical cues for its cells constituents. It is therefore

innately involved in numerous cellular processes as cellular migration, proliferation, differentiation, morphogenesis and homeostasis (Frantz et al., 2010; Theocharis et al., 2016).

Figure 1-1 shows an example of a normal ECM function and structure with its major cellular and non-cellular components. The ECM is composed of numerous components to hold the cells together. The composition of the ECM varies tremendously from tissue to tissue and with age (Frantz et al., 2010; Kular et al., 2014). Fibrous proteins as collagen, elastin, fibronectin and laminin are known to give not only physical support to the ECM, but also have an active role in many cells processes. Complementary, proteoglycans fill the ECM with a hydrogel that resists to compression and interact with a variety of ligands (Frantz et al., 2010; Varki et al., 1999).

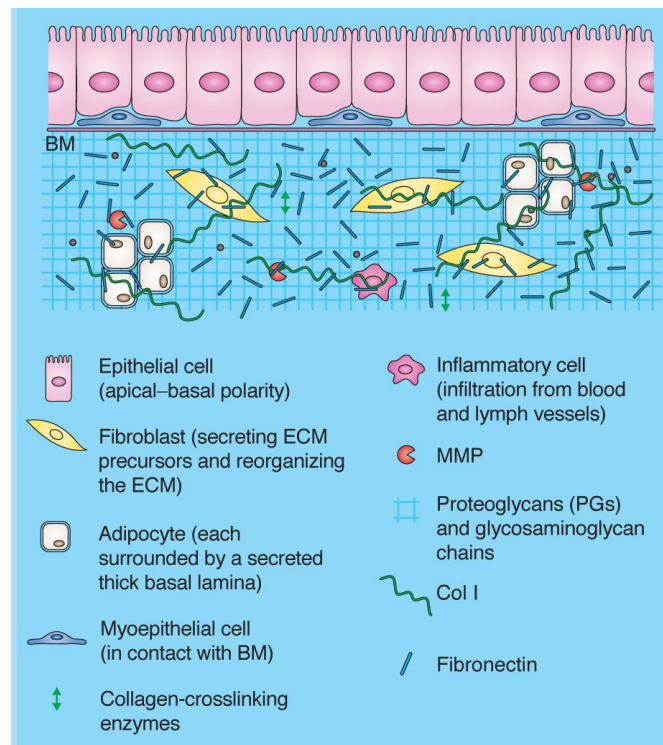


Figure 1-1: Example of a normal ECM function and structure with its basic components. BM stands for basement membrane (reproduced with permission from (Frantz et al., 2010). Copyright Journal of Cell Science 2010)

Collagen, which forms the main structural component of the ECM, is also the most abundant protein of the ECM. It is composed of a triple-stranded helix that can assemble into fibers and networks, depending on the type of collagen (Frantz et al., 2010). To date, more than 20 collagen types were identified and reported in literature. Collagen is present as fibrils in tissues that need to resist to mechanical stresses (shear, tension or pressure) as bones, cartilage, tendons and skin. Only collagen types I, II, III, V and XI can form fibers, while types IV, VIII and X can form networks (Badylak, 2002; Bosman & Stamenkovic, 2003). Each different collagen

contributes to distinct structural and regulatory functions of the ECM. Collagen type I, for instance, is the primary structural collagen and is universally present in the body, except in cartilage (Bosman & Stamenkovic, 2003; Kular et al., 2014). Type IV collagen is incorporated into the basal membrane of all vascular structures and is a substantial ligand for endothelial cells (Badylak, 2002; Frantz et al., 2010).

Elastin, is another important fibrous protein of the ECM and it is closely connected to collagens (Kular et al., 2014). This protein provides elasticity to tissues that undergo repeated stretch as connective tissues, blood vessels and skin. Elastin is formed from tropoelastin precursors, which assembles and crosslinks via its lysine residues by lysine oxidase (K. Wang et al., 2021). Due to its extensive cross-linked structures, elastin is a resilient protein that degrades slowly, with a half-life of 70 years (K. Wang et al., 2021).

One more important fibrous component of the ECM is fibronectin. It is a glycoprotein with a complex structure consisting of two almost identical subunits, that are each composed of three modules with distinct structures (Theocharis et al., 2016). The modules are arranged to form binding domains for a variety of proteins and carbohydrates (Badylak, 2002; Pankov & Yamada, 2002). Fibronectin has a dual function in ECM. The fibers formed by fibronectin help with the structural support to the cells and the complex and specific molecular structure gives unique modulating effects upon cell behavior (Badylak, 2002). Fibronectin is also related to the phenomenon of mechanosensing, which is the ability of cells and tissues to sense mechanical forces in their environment and convert these mechanical cues into biochemical signals that influence cellular responses (Scott et al., 2015; Vogel, 2018).

Fibronectin is fundamentally involved in cell adhesion, growth, migration, and differentiation. The principal region of fibronectin to bind to integrins of the cells is the RGD (tripeptide sequence of Arg-Gly-Asp) (Kular et al., 2014). The importance of fibronectin is not restricted to cell binding and support, but fibronectin plays a key role in wound healing and embryonic development as a direct binding partner of fibrinogen and fibrin (Kular et al., 2014; Makogonenko et al., 2002; Theocharis et al., 2016).

Proteoglycans (PGs) are complex molecules essential for the ECM function. They are formed from a protein core with one or more covalently attached glycosaminoglycan (GAG) chains. GAGs are long polysaccharides containing repeating disaccharide units (Frantz et al., 2010; Theocharis et al., 2016). PGs can be found in the ECM, but also inside or at the surface of the cells. Proteoglycans are, therefore, classified in three main families according to its protein,

localization and GAG composition: small leucine-rich proteoglycans (SLRPs), modular proteoglycans and cell-surface proteoglycans (Frantz et al., 2010; Theocharis et al., 2016).

As a consequence of their unique and varying structures, PGs have numerous functions in the ECM. Some proteoglycans are essential for hydration, as well as gel formation to resist compressive forces, while others can interact with many growth factors, cytokines, chemokines, cell surface receptors and ECM proteins, contributing to modulate cell adhesion, migration and proliferation, as well as wound repair (Bosman & Stamenkovic, 2003; Frantz et al., 2010; Theocharis et al., 2016).

With its extraordinary structure and functions, the ECM serves as the main inspiration of engineered-tissue scaffolds for tissue reconstruction. As noted above, the ECM is actively involved in wound healing and tissue reconstruction.

1.4. WOUND HEALING

When an injury occurs and tissue is ruptured, blood gets in contact with collagen, which rapidly activates blood platelets starting the blood coagulation cascade. As a first step to avoid excessive bleeding and to protect the underlying tissue, a fibrin blood clot is formed at the site of the injury (Broughton et al., 2006). Tissue repair is a series of overlapping events and it is usually divided in four phases: haemostasis, inflammation, proliferation and remodelling (S. Guo & Dipietro, 2010; Midwood et al., 2004).

Haemostasis is the first stage in wound healing and starts immediately after tissue damage. The activated platelets start to aggregate while fibrin polymerizes and form a network that helps to stabilize the blood clot and stop bleeding. The insoluble fibrin is formed by the enzymatic cleavage of the soluble fibrinogen by action of thrombin. The clot acts as a provisional matrix being a scaffold for the recruitment of tissue cells in the wounded area. The migration of inflammatory cells to this matrix, starts the next phase of wound healing (S. Guo & Dipietro, 2010; Laurens & deMaat, 2006). During the inflammation phase, neutrophils and macrophages migrate and infiltrate into the clot to remove cellular debris and pathogens of the wound. Moreover, macrophages release cytokines which stimulates fibroblasts and promote angiogenesis (Broughton et al., 2006).

The third stage of wound healing is the proliferation. This phase overlaps with the inflammation and is characterized by the proliferation of epithelial cells and fibroblasts in the wound site. The provisional matrix starts to be substituted with granulation tissue composed of collagen and fibronectin (Midwood et al., 2004). Following the proliferation phase and collagen deposition,

wound healing enters the remodelling phase. This final stage can take months to years and consists on the deposition of fibronectin and collagen in an organized network (Broughton et al., 2006) and ECM remodelling (S. Guo & Dipietro, 2010).

Clearly blood coagulation is a crucial step in wound healing and the provisional matrix serves as another inspiration for tissue engineering. Fibrinogen plays a key role at this early stage of wound healing. More details on this complex pathway to stop bleeding and how fibrinogen is involved in the blood coagulation cascade will be presented in the next section.

1.5. FIBRINOGEN AND THE BLOOD COAGULATION CASCADE

Fibrinogen (Fg), also known as Factor I, is a soluble glyco-protein found in blood plasma and is one of the key components involved in wound healing and blood clotting processes (Rajangam & An, 2013). The typical concentration of fibrinogen in the human blood plasma ranges between 150 and 400 mg/dl (Asselta et al., 2006). Structurally, as shown in Figure 1-2, fibrinogen is a 340 kDa large, complex molecule composed of three pairs of polypeptide chains, referred to as $A\alpha$, $B\beta$, and γ chains. The structure of fibrinogen consists of a length of approximately 45 nm, featuring two globular domains known as D-domains at each end. These D-domains are connected in the middle by helical coiled-coil rods (the E-domain). The fibrinogen molecule is composed of six chains, and these chains are held together by a total of 29 disulfide bonds, resulting in the formation of two half molecules. Within the structure, the αC region, which represents the C-terminal segment of the $A\alpha$ chain, as well as the N-terminal parts of both the $A\alpha$ and $B\beta$ chains, are primarily disordered (Medved & Weisel, 2009; Mosesson, 2005; Weisel & Litvinov, 2017).

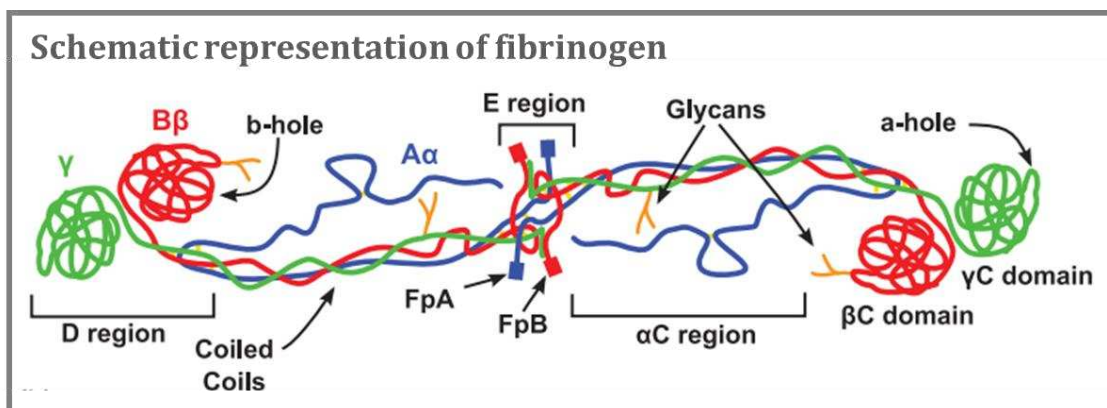


Figure 1-2: Schematic representation of the fibrinogen molecule with: three pairs of polypeptide chains, referred to as $A\alpha$ (blue), $B\beta$ (red), and γ (green) chains. Fibrinogen structure features two globular domains, known as D-domains, at each end. The D-domains are connected in the middle by the helical coiled E-domain. Adapted from Köhler et al. (Köhler et al., 2015).

In its normal state, fibrinogen remains soluble in the blood. However, in the case of a tissue injury, the blood coagulation is triggered and fibrinogen is cleaved by the enzyme thrombin (Kattula S et al., 2017). During the process of fibrin polymerization, thrombin acts to cleave the two pairs of fibrinopeptides (FbA and FbB) located at the central domain of fibrinogen. Subsequently, the exposed A- and B knobs on the fibrinogen molecules bind to the corresponding a- and b-holes present on adjacent fibrinogen molecules. This binding interaction initiates the transformation of fibrinogen from its soluble form into insoluble fibrin, resulting in the formation of a fibrin network. More details and an image depicting this mechanism of fibrinogen cleaved to fibrin and subsequently fibrin polymerization can be seen in Chapter 2, Figure 4.

The blood coagulation is a complex process dealing with several interactions, transformations and factors. The main factors involved in blood coagulation are listed in Table 1-1. The factors are identified by roman numerals with the activated form of the factor being represented with an “a”, e.g. XIIa. Fibrinogen and the other coagulation factors (except factors II, IV and VIII) are produced in the liver (Palta et al., 2014).

Table 1-1: Nomenclature of the coagulation proteins/clotting factors. Adapted from Palta et al. (Palta et al., 2014)

| Clotting Factor # | Clotting Factor Name | Function |
|-------------------|----------------------------------|---|
| I | Fibrinogen | Clot formation (soluble) |
| Ia | Fibrin | Clot formation (insoluble) |
| II | Prothrombin | Activation of I, V, VII, VIII, XI, XIII, platelets |
| IIa | Thrombin | Active form of prothrombin |
| III | TF | Co-factor of VIIa |
| IV | Calcium | Facilitates coagulation factor binding to phospholipids |
| V | Proaccelerin, labile factor | Co-factor of X-prothrombinase complex |
| VII | Stable factor, proconvertin | Activates factors IX, X |
| VIII | Antihæmophilic factor A | Co-factor of IX-tenase complex |
| IX | Antihæmophilic factor B | Activates X: Forms tenase complex with factor VIII |
| X | Stuart-Prower factor | Prothrombinase complex with factor V, activates factor II |
| XI | Plasma thromboplastin antecedent | Activates factor IX |
| XII | Hageman factor | Activates factor XI, VII and prekallikrein |
| XIII | Fibrin-stabilising factor | Crosslinks fibrin |

The blood coagulation cascade contains three pathways: the extrinsic, the intrinsic and the common (see Figure 1-3). The first two are relatively independent of each other, but converging into the common pathway, which in both cases ends with thrombin activation and fibrin

formation (Monroe et al., 2002). These pathways involve a series of enzymatic reactions and the activation of various clotting factors in a tightly regulated manner to achieve haemostasis, i.e. the process of maintaining blood flow and preventing excessive bleeding (Palta et al., 2014).

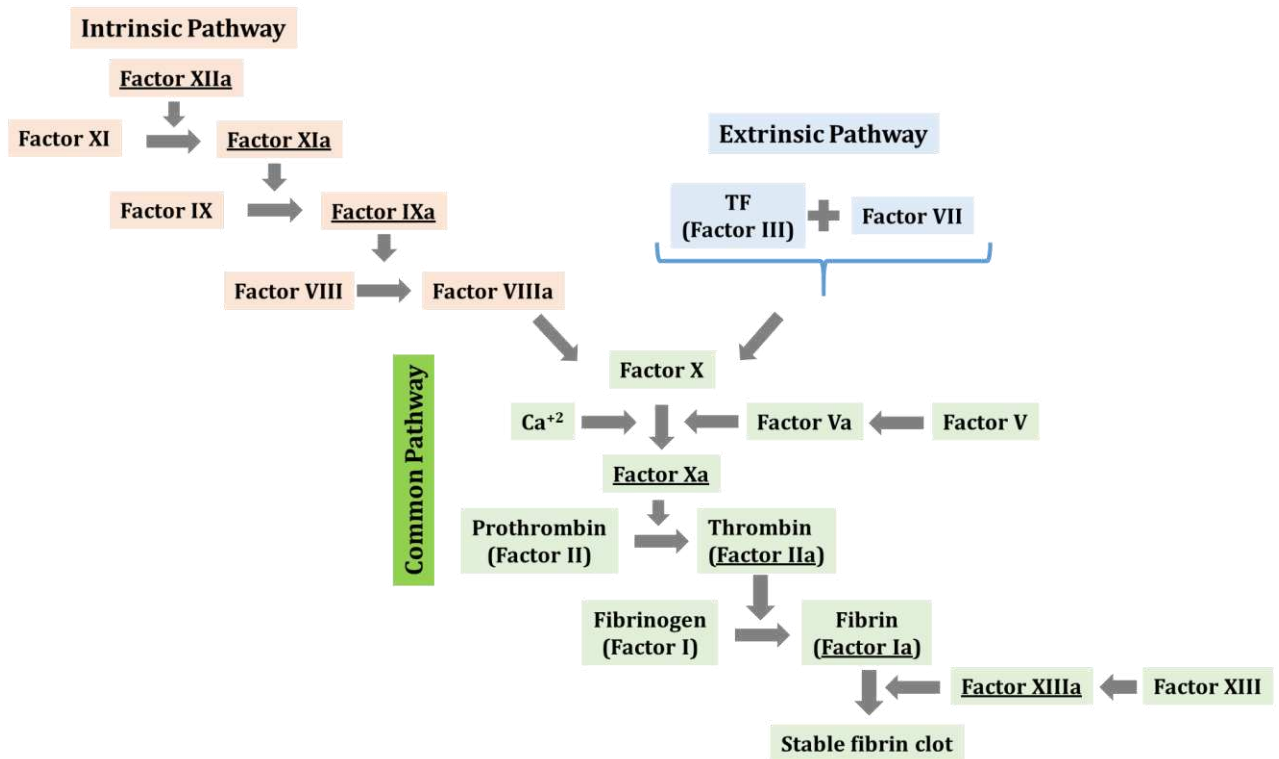


Figure 1-3: Schematic representation of the blood coagulation cascade that involves a series of enzymatic reactions based on different clotting factor. The cascade contains three pathways: intrinsic, extrinsic, and common. Thrombin (Factor IIa) acts on the common pathway leading to the formation fibrin from fibrinogen.

The extrinsic pathway is initiated by tissue damage. It starts with the release of tissue factor (TF), also known as factor III, from damaged cells or tissues. TF forms a complex with circulating factor VII (factor VIIa). This TF-VIIa complex activates factor X (respectively factor Xa). The extrinsic pathway provides a rapid response to tissue injury, and it plays a major role in initiating the clotting process.

The intrinsic pathway is triggered by factors present within the blood itself. It begins with the activation of factor XII (factor XIIa) by contact with exposed to proteins such as collagen, kininogen or negatively charged surfaces (Stavrou & Schmaier, 2010). Factor XIIa activates factor XI (factor XIa), which, in turn, activates factor IX (factor IXa). Factor IXa then combines with factor VIII (factor VIIIa) to form a complex that activates factor X (factor Xa). In this regard, the intrinsic pathway amplifies the clotting response and provides a means of coagulation in the absence of tissue damage. Regardless of intrinsic or extrinsic nature, both pathways converge to the common pathway by activating the factor X. Once activated, factor

Xa combines with factor V (factor Va), calcium ions (Ca^{+2}), and phospholipids on the surface of platelets to form a complex known as the prothrombinase complex (Tracy & Mann, 1983). The prothrombinase complex then converts prothrombin (factor II) into its active form, thrombin (factor IIa). Thrombin, in turn, converts soluble fibrinogen (factor I) into insoluble fibrin (factor Ia) strands, leading to the formation of a blood clot. The final stage of the blood coagulation is ended with the activation of the fibrin-stabilizing factor (factor XIIIa), which crosslinks fibrin forming a stable fibrin clot.

The extrinsic, intrinsic, and common pathways of blood coagulation work in ensemble to ensure proper clot formation while maintaining a fine equilibrium to prevent both haemorrhage and uncontrolled clotting. During the cascading process of blood coagulation (BENNETT, 2006), fibrinogen interacts with several proteins (e.g. thrombin, integrin, Von Willebrand factor), cells (e.g. platelets, leucocytes), as well as salts (e.g. K^+ , Na^+ , Mg^{+2} , Ca^{+2} , Cl^-) (Giavarina, 2017). Due to its versatility, fibrinogen is finding a growing application as a biomaterial in tissue engineering, which will be further discussed in the next section.

1.6. FIBRINOGEN AS A BUILDING BLOCK FOR BIOMATERIALS

Fibrinogen, as a natural protein, offers many advantages to be applied as a biomaterial. It has a pronounced adsorption tendency (Cieśła et al., 2013; Tsapikouni & Missirlis, 2007; Wasilewska & Adamczyk, 2011), can be assembled into fibrous or porous structures *via* different techniques (Joo et al., 2015; Rajangam & An, 2013) and therefore exhibits a high surface-to-volume ratio, so that its 3D fibrous structure with textured surface can induce ECM production. Moreover, fibrinogen has excellent properties with regards to tissue engineering, especially as a scaffold, such as (Mosesson, 2005; Nikolova & Chavali, 2019):

- **Biocompatibility:** as a naturally occurring protein in the body, it has a reduced risk of adverse reactions. In this regard, the possibility of the use from autologous scaffolds, i.e. tissue engineering constructs created using a person's own cells and tissues. The autologous approach for regenerative medicine can minimize the risk of immune rejection.
- **Biodegradability:** it can be gradually broken down and metabolized by the body over time, which is advantageous as it allows the scaffold to be replaced by newly formed tissue as the regeneration process progresses.
- **Cell attachment support:** based on integrin-mediated adhesion cells can adhere to fibrinogen-coated surfaces and begin to grow and divide, a crucial step in tissue formation.

- Cell signaling driver: it can be functionalized with various biochemical cues, such as growth factors or peptides, to provide signals that direct cell behavior and encourage specific cell differentiation into the desired tissue type.

In recent years, several studies have demonstrated the suitability of fibrinogen-based scaffolds for skin grafting (Solovieva et al., 2018), wound healing (Soleimanpour et al., 2022), bone regeneration (Vasconcelos et al., 2016), guiding endothelial cell behavior (Gugutkov et al., 2013) and support for differentiation of stem cells and cartilage production (Forget et al., 2016). As a versatile biomaterial, fibrinogen allows for the fabrication of scaffolds in various geometries, such as microspheres, micro-fibers, micro-tubes, nanoparticles, nanofibers, and hydrogels (Joo et al., 2015; Rajangam & An, 2013).

More recently, the use of biomaterials in the context of 3D-printing has widened the horizon of potential geometries for fibrinogen-based structures (de Melo et al., 2020), including porous, fibrous, microspheres, and solid free-form scaffolds (Mao et al., 2020). However, a main limitation of the 3D-printing approach is that fibrin (cross-linked form) is too viscous, which hinders proper ink extrusion, whilst fibrinogen, is not capable to maintain shape geometry (Nikolova & Chavali, 2019).

Despite being one of the most common applications of fibrinogen, scaffolding is not the only method to employ fibrinogen as a biomaterial. While fibrinogen-based scaffolds are widely used in tissue engineering, fibrinogen has several other important uses, such as an adhesive (Draf, 1986; Silberstein et al., 1988). In this latter case, fibrinogen-based adhesives are beneficial in surgeries where conventional methods of achieving hemostasis, such as sutures or staples, are not effective or practical.

Due to its characteristics of biocompatibility and biodegradability, another promising application of fibrinogen in regenerative medicine is a drug-delivery system (Sreerenganathan et al., 2014). In this regard, protein-based drug carriers exhibit reduced immunogenicity and are easily degraded and eliminated from the human body after serving as a drug vehicle (Joo et al., 2015). Due to its ability to form hydrogel-like structures, fibrinogen can construct a matrix that encapsulates drugs, leading to a gradual release over an extended period. This sustained release characteristic allows for less frequent drug administration, which helps maintain therapeutic levels for longer durations (Feng et al., 2022; Spicer & Mikos, 2010).

Regardless of its application, a main form of fibrinogen application is as a nanofibrous biomaterial (Gupta et al., 2014). Nanofibers offer a wide array of advantages due to their unique

properties and structures, which can mimic native blood clots and the ECM, making them highly relevant in tissue engineering applications. One significant advantage is their remarkably high surface area to volume ratio, which enhances surface for cell adhesion. Additionally, nanofibers exhibit high permeability and flexibility, which are highly desirable properties, for instance, for tissue engineering (Babitha et al., 2017). Another key benefit is their fine tunability, as properties like porosity, diameter, and surface chemistry can be controlled during fabrication, tailoring nanofibers to suit specific applications (Patel & Gundloori, 2023). In this regard, the selection of an appropriate fabrication technique of fibrinogen nanofibers depends on various factors, including costs, complexity, fiber yield and size, usage of hazardous materials, and the suitability of materials.

Electrospinning is a fabrication technique that involves using an electric field to produce protein-based nanofibers. In the electrospinning process, a syringe containing the fibrinogen solution is connected to a high-voltage power supply. When a high electric field is applied, the surface tension of the solution is overcome, and a thin jet of the solution is ejected from the syringe tip. As the jet travels towards a collector (usually a grounded plate), it undergoes rapid stretching and whipping due to the electric field, leading to the solidification of the fibrinogen fibers into nanofibers as the solvent evaporates (Huang et al., 2003).

This method allows for the fabrication of fibrinogen nanofibers with diameters of 3 nm up to 10 μ m, resembling the architecture of natural extracellular matrices in tissues (Wnek et al., 2003). The electrospun fibrinogen nanofibers can be further cross-linked or functionalized to enhance their mechanical properties, biocompatibility, and potential for various applications in tissue engineering, wound healing, drug delivery, and regenerative medicine (McManus et al., 2007; McManus et al., 2006).

Wnek et al. (Wnek et al., 2003) were among the first to electrospin 3D-fibrinogen nanofibrous structures with controlled pore sizes. Subsequently, researchers have successfully produced fibers ranging from approximately 80 to 700 nm and scaffold structures of up to 36 cm², depending on the fibrinogen concentration (S. Sell et al., 2008; S. A. Sell et al., 2010; Wnek et al., 2003). Furthermore, the biological activity of electrospun fibrinogen scaffolds has been investigated in various studies, showing the biocompatibility of the fibers with human bladder cells (Mcmanus et al., 2007), cardiac fibroblasts (McManus et al., 2007), endothelial cells (Gugutkov et al., 2013), and human mesenchymal stem cells (Forget et al., 2016).

Nonetheless, electrospinning still presents several disadvantages in the context of biomaterials, for instance, the reliance on high voltage and organic solvents (Mirzaei-Parsa et al., 2018), which might impact the biofunctionality of proteins (Kumbar et al., 2008; Raoufi et al., 2015), as well as, the high concentration of fibrinogen (100- 200 mg/mL) required for the fabrication of nanofibers (Carlisle et al., 2009; Wnek et al., 2003).

The process of freeze-drying, a thermal phase separation technique commonly used in scaffold fabrication, allows for the creation of various scaffold structures by manipulating separation conditions (Mottaghitlab et al., 2013; Samitsu et al., 2013). Despite its versatility, freeze-drying is characterized by time-consuming procedures, limited fiber yield, and constraints to a few polymeric materials. Furthermore, uniform fiber distribution and scalability remain challenging aspects (Rajangam & An, 2013; Raoufi et al., 2016).

The extrusion of protein-based nanofibers (as seen in Figure 1-4) is a fabrication technique that involves pushing a protein solution through a nanoporous alumina membrane to produce nanofibers of controlled dimensions (P. Guo et al., 2018). In this process, the protein solution is pressurized and extruded through a small opening, typically with the aid of a syringe or a specialized extrusion device. The extruded solution undergoes rapid stretching, resulting in the formation of nanofibers (P. Guo et al., 2018; Raoufi et al., 2016).

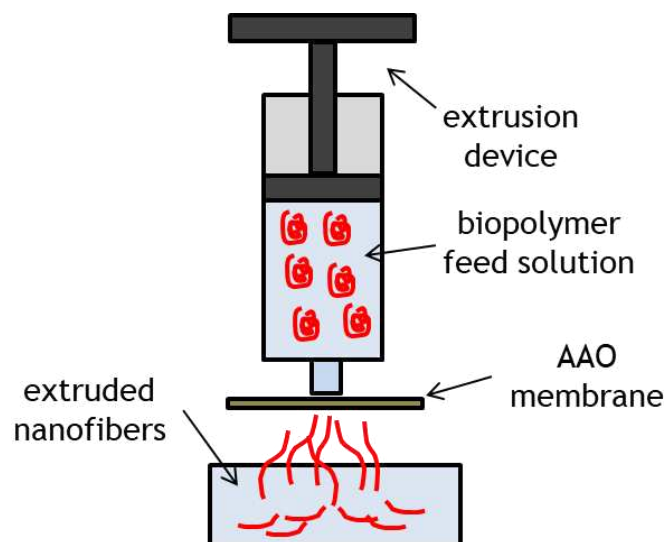


Figure 1-4: Fiber extrusion process of protein-based nanofibers. In this process, a biopolymer feed solution is pressed against a anodic aluminum oxide (AAO) membrane leading to the extrusion of protein-based nanofibers. Adapted from (Raoufi et al., 2015).

This technique is well-established for several protein-based biomaterials, such as fibronectin (Raoufi et al., 2015), fibrinogen, elastin, laminin and others (Raoufi et al., 2016). However, the

composition of the feed solution could potentially impact the fibrillogenesis of the proteins during nanofiber extrusion. Moreover, a limitation of this method is the inability to generate dense fibrinogen networks *via* extrusion, which hinders the large-scale production of fibrinogen scaffolds for tissue engineering applications (Stapelfeldt, Stamboroski, Mednikova, et al., 2019).

As naturally occurring in the human body, the process of fibrin polymerization is induced by thrombin (Weisel, 2005). However, due to its cost and potential adverse immune reactions (as well as thrombosis risk), the use of thrombin as raw material in large-scale can be inadequate (Strukova, 2006; Vasconcelos et al., 2016). This has prompted research into thrombin-free fabrication methods aiming to replicate the natural features of the ECM. The technique of self-assembly of protein nanofibers is based on the spontaneous formation of 3D nanostructures through non-covalent interactions, such as hydrogen bonds, van der Waals forces, hydrophobic interactions, and electrostatic interactions (Holzwarth & Ma, 2011; Palchesko et al., 2013).

The self-assembly technique, owing to its molecular nature and resemblance to the natural ECM formation, is capable of producing nanofibers with diameters as small as 5 to 8 nm, corresponding to the lowest scale of the ECM (Vasita & Katti, 2006). Practically, nanofiber fabrication through self-assembly relies on hydrophobic and ionic interactions (Liao et al., 2016). During self-assembly, nanofibers can be assembled on a surface or in solution (Palchesko et al., 2013), which offers two benefits (Vasita & Katti, 2006): (i) cells can readily adhere to the nanofiber during its formation, and (ii) the solution containing the nanofibers can be minimally invasively injected into the body.

In the context of fibrinogen, Chen et al. (G. Chen et al., 2011) demonstrated the possibility of thrombin-free fibrinogen self-assembly by controlling surface chemistry on a gold surface. Similarly, Koo et al. (Jaseung Koo et al., 2012) and Zhang et al. (L. Zhang et al., 2017) applied an analogous principle to reveal the self-assembly of fibrinogen on polymeric and metallic surfaces. Wei et al. (Wei, Reichert, & Jandt, 2008) were also able to produce fibrinogen nanofibrils in the absence of thrombin based on fibrinogen self-assembly in solution by denaturation of fibrinogen with ethanol (Wei, Reichert, & Jandt, 2008) or HCl (Wei, Reichert, Bossert, et al., 2008).

Hence, the self-assembly technique holds great potential for designing nanofibrous fibrinogen structures with improved mechanical properties, high biocompatibility and fiber sizes closely resembling the ECM (Holzwarth & Ma, 2011). Nevertheless, current self-assembly techniques, primarily surface-induced, have resulted in low fiber yield (G. Chen et al., 2011; J. Koo et al.,

2010; Jaseung Koo et al., 2012; Reichert et al., 2009; Wei, Reichert, & Jandt, 2008), which hinders the development of 3D structures to be used as scaffolds.

In order to address this issue, several authors have demonstrated the possibility of triggering fibrinogen self-assembly by salt-interactions (Hämisch et al., 2019; Hense et al., 2021; Hense & Strube, 2023b, 2023a; Reichert et al., 2009; Stapelfeldt, Stamboroski, Mednikova, et al., 2019; Stapelfeldt, Stamboroski, Walter, et al., 2019). However, very limited focus has been given to the understanding of the fundamental mechanisms leading to salt-induced fibrillogenesis. The knowledge about these mechanisms can provide a key understanding on the molecular interaction of fibrinogen with other molecules and ions involved during the blood coagulation cascade, as well as during tissue repair where fibrinogen interactions with ECM proteins and integrins are highly salt-dependent. Moreover, it can help to better understand other relevant physiological activities such as the interaction of fibrinogen with blood cells (Hu et al., 2016; Kenny et al., 2022), and fibrinogen amyloid formation (Chapman & Dogan, 2019; Cortes-Canteli et al., 2010; Jin et al., 2021; Page et al., 2019). Additionally, understanding the mechanism behind salt-induced fibrinogen fiber formation is needed for crafting tissue engineering scaffolds and biomaterial surfaces in personalized medicine that do not provoke pathogenic or thrombogenic reactions.

1.7. FIBRINOGEN-SALT INTERACTIONS *IN VITRO*

In its physiological state, fibrinogen exists in blood plasma as a soluble protein, which is under interaction with many salts available in the blood plasma, such as calcium chloride (CaCl_2), sodium chloride (NaCl), potassium chloride (KCl), as well magnesium chloride (MgCl_2), among others (Covington & Robinson, 1975; Nezafati et al., 2012; Weisel & Litvinov, 2017). For instance, the binding of calcium ions (Ca^{2+}) to fibrinogen plays a critical role in the coagulation cascade, as they act as a co-factor for the enzyme thrombin, which catalyses the conversion of fibrinogen into fibrin (Weisel & Litvinov, 2017).

The interaction of proteins (such as fibrinogen) with salts can be traced to the pioneering work of Hofmeister, which as early as 1888, discovered that the solubility of the protein from egg whites could be altered by the introduction of salts (Hofmeister, 1888).

The “Hofmeister series”, also commonly referred to as the lyotropic sequence, ranks ions based on their ability to affect protein solubility and stability. This behaviour is also discussed in the literature as “specific ion effect, SIE”, or lyotropic sequence. Several investigations have demonstrated the relevance of the Hofmeister series, which postulates an explanation for the

behaviour of many protein-related mechanisms such as enzyme activity, protein stability, protein–protein interactions, protein crystallization, and even bacterial growth (Y. Zhang & Cremer, 2006).

As shown in Figure 1-5, in historical perspective, the Hofmeister series classifies ions into two groups (Gregory et al., 2022; Kang et al., 2020):

- Chaotropic ions (“water structure breaker”): these ions have a disruptive effect on the structure and stability of fibrinogen and other proteins. They decrease water surface tension, whilst increasing protein solubility. They can promote protein denaturation, unfolding, and hydrophobicity.
- Kosmotropic ions (“water structure maker”): these ions have a stabilizing effect on the structure of fibrinogen and other proteins. They increase water surface tension, whilst decreasing protein solubility. They maintain protein folding and promote protein–protein interactions. The presence of kosmotropic ions can help to maintain the stability and functionality of fibrinogen.

As reported in the early works related to ion-protein interactions, the “ion-protein” behaviour can be correlated with the phenomena of salting-in and salting-out (Hyde et al., 2017). Salting-out occurs when the solubility of a protein in an aqueous environment decreases with increasing salt concentration. On the other hand, salting-in is defined as situation in which the solubility of a protein in an aqueous environment increases with increasing salt concentration. The salting (in or out) is a driven mechanism for the aggregation or solubilisation of proteins (such as fibrinogen).

Concerning the influence of cations or anions on a salt, it is recognized that anions have a stronger influence on the protein behavior (e.g. protein solubility) than cations (Schwartz et al., 2010). In recent years, several authors have postulated that specific ion effects are counterion-dependent, i.e. in the presence of salt, the cation-anion combination influences protein behavior in a solution.

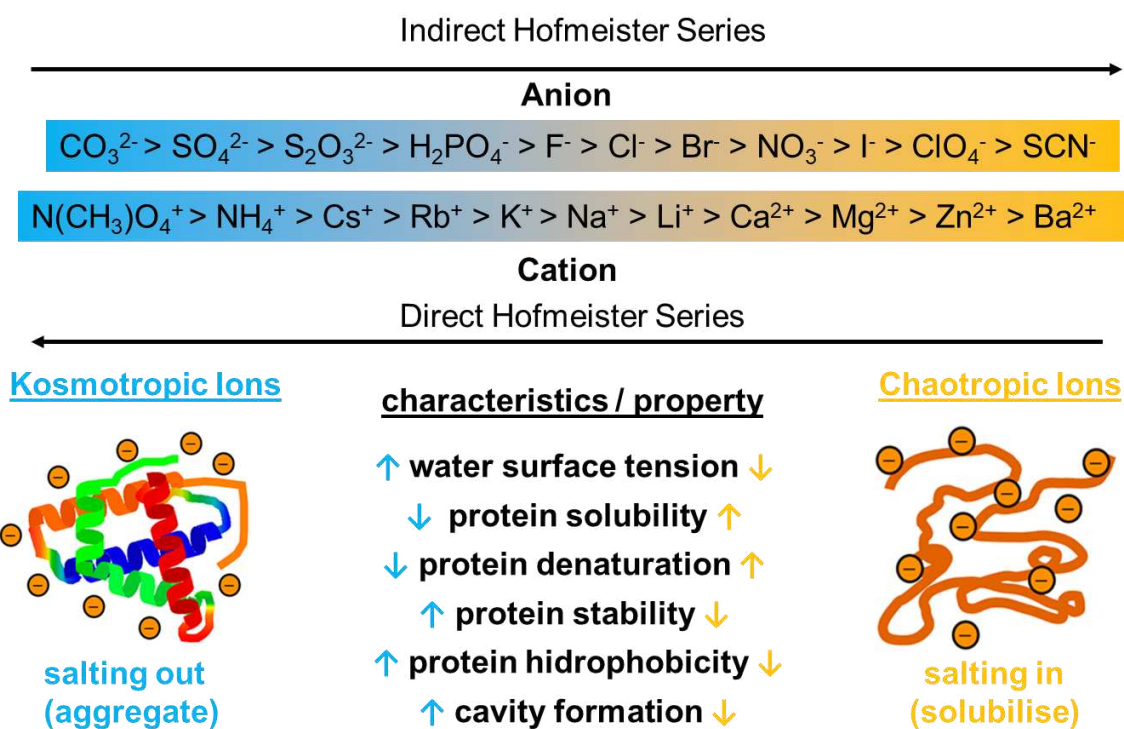


Figure 1-5: Hofmeister series: on the left side (blue) are located more kosmotropic ions, which are characterized by the salting-out (aggregation) of proteins; on the right side (yellow) are located more chaotropic ions, which induce the salting-in (solubilization) of proteins. The kosmotropic and chaotropic ions possess opposing characteristics in terms of water surface tension, protein solubility, protein denaturation, protein stability and protein hydrophobicity. [Adapted from Kang et al and Nihonyanagi et al. (Kang et al., 2020; Nihonyanagi et al., 2014).

Using bovine fibrinogen, Hense et al. (Hense et al., 2021) investigated the self-assembly of fibrinogen into hydro- and aerogels with fibrin-like structures. The authors postulate that the self-assembly is anion-induced in the presence of kosmotropic anions. The limitation of their approach is the requirement of relatively low temperatures (5-8 °C) for the formation of fibers. In the follow-up investigation (Hense & Strube, 2023a), the same group demonstrated a calcium (Ca^{+2})-induced fibrinogen hydrogel formation. However, to be able to form fibers at physiological temperatures, it was necessary the addition of a high concentration of fibrinogen (20-40 g/L), as well as NaCl (100 mM). More recently, Hense et al. (Hense & Strube, 2023b), based on the investigation of thrombin-free fibrillogenesis triggered by magnesium (Mg^{+2}), demonstrated that the fiber formation is only possible in the presence of kosmotropic anions.

For this reason, it has been suggested that separation of the Hofmeister effects into cationic and anionic contributions might be limiting, as the electroneutrality conditions requires the consideration of both (Okur et al., 2017). In this regard, specific counterions are known to be able of causing deviations in the Hofmeister series (Gregory et al., 2022; Murdoch et al., 2016; Okur et al., 2017; Y. Zhang et al., 2005).

The ion-protein (or salt-protein) relationship is very complex and specific, with a strong dependence on factors such as salt concentration, pH, protein conformation, surface, and temperature. Investigations have provided insights into the understanding of “specific ion effects” by correlating it to ion-macromolecules interactions intermediated by the solvation shell (or hydration shell when the solvent is water) (Andreev et al., 2017; Y. Zhang & Cremer, 2006). Moreover, it was suggested in the literature that the specific ion effect could also be understood in form of specific interactions between salt ions and the backbone and charged side chain groups at the protein surface (Okur et al., 2017).

Not only the chemical composition of salts, but also the secondary/tertiary structure of biomolecules, hydrophobic regions, as well as location of charged groups can impact the solvation shell leading to different functionality and structures (Laage et al., 2017). The hydration of ions such as Na^+ , K^+ , Mg^{2+} , Ca^{2+} and Cl^- in salt solutions can vary according to the cation-anions combination (monovalent or divalent), which in turn, can influence the ion-protein behavior (Houyang Chen & Ruckenstein, 2015).

Protein-salt interactions directly impact protein-protein interactions by, for instance, protein metal-directed self-assembly (Salgado et al., 2010; Zhao et al., 2016). The so-called “protein-protein-interactions” are involved in many biological phenomena, such as crystallization, gelation, and amorphous precipitation (J. Zhang, 2012). Moreover, recent studies have shown that neurodegenerative diseases, such as Alzheimer and Parkinson, can be driven by protein aggregation (Irvine et al., 2008; Kepchia et al., 2020).

Protein-protein interactions in salt solutions are quite complex due to the fact that proteins contain both positively and negatively charged regions, as well as, polar and apolar groups in their composition (Kastelic et al., 2015). The law of matching water affinities (LMWA) provides a template to explain the interaction strength between salt ions and proteins from a thermodynamic perspective. Here, protein-protein interactions are more favourable (and stable) when the water affinities of the interacting ion-protein are compatible (Collins, 1997). This is related to both the hydration level and size of both ions and protein structures on its surface.

Another interesting perspective is that not only proteins are affected by the presence of salt, but also salts are affected by the presence of proteins. Several authors have shown that salt crystallization takes place in different forms, when salts are crystalized from protein solutions (Goto et al., 2016). In this regard, proteins can act as nucleation sites, as crystal growth inhibitor/promoter, and also influence crystallisation kinetics (Dutta Choudhury et al., 2015).

However, most of the focus has been given to how salts can influence proteins, with limited research on the counterpart of this pairing, i.e. how proteins can affect salt behavior in solution.

1.8. RESEARCH AIM

Fibrinogen, as demonstrated in the previous sections, is a natural blood protein with outstanding properties (e.g. biocompatibility, biodegradability) to be employed as a building block for fibrous scaffolds in tissue engineering (Rajangam & An, 2013). Among the fabrication techniques for scaffold preparation, the self-assembly is very promising as it relies on molecular interactions resembling the natural ECM formation, which allows the formation of nanofibers (Vasita & Katti, 2006). In recent years, the salt-induced self-assembly of fibrinogen nanofiber has emerged as a simple and reproducible method for high yield, 3D-fabrication of fibrinogen scaffolds (Hense et al., 2021; Stapelfeldt, Stamboroski, Mednikova, et al., 2019; Stapelfeldt, Stamboroski, Walter, et al., 2019). However, fibrinogen-salt interactions are not fully understood as they depend on the cation-anion combination (monovalent, divalent or polyvalent ions), the properties of the protein solution (buffer, concentration, pH), as well as the structure of fibrinogen (conformation, charge, binding sites) (Gregory et al., 2022; Lendel & Solin, 2021).

The understanding of these phenomena is crucial for the fabrication of fibrinogen nanofibers through self-assembly in an enzyme-free environment, as protein-protein-interactions can be directly influenced (or tailored) to generate specific aggregation behaviour from fibrinogen. Moreover, for the implementation of fibrinogen in scaffolding applications, it is important to determine how cells interact with fibrinogen nanofibers. Nonetheless, the mechanisms behind fibrinogen self-assembly *in vitro* in the presence of salt leading to nanofiber formation, as well as the salt-fibrinogen interaction are not yet fully understood. Therefore, the aim of the present doctoral research work is the following:

“To understand the fibrinogen-salt interactions during fibrinogen self-assembly under *in vitro* conditions in order to fabricate nanofiber scaffolds with reproducible topography and composition for later applications in tissue engineering”

To achieve this aim, the following hypotheses are addressed in five consecutive studies that build the core of this work and are presented as already published work or work to be submitted in the following chapters.

- Presence of salt is one of the main factors for fibrinogen fibrillogenesis *in vitro* under non-denaturing conditions.

- Chapter 2: Review paper “Principles of fibrinogen fiber assembly *in vitro*”
- Divalent cations induce assembly of fibrinogen into nanofibers.
→ Chapter 3: Research paper “Influence of divalent metal ions on the precipitation of the plasma protein fibrinogen”
- Monovalent ions are a main driving force of fibrinogen fibrillogenesis in an enzyme-free environment.
→ Chapter 4: Research paper (to be submitted) “Influence of highly saline aqueous solutions of monovalent alkali metal ions on fibrinogen self-assembly *in vitro*”
- Presence of proteins influences the precipitation behavior of the monovalent salt NaCl.
→ Chapter 5: Research paper “Effect of interface-active polymers on the salt crystal size in waterborne hybrid materials”
- Self-assembled fibrinogen nanofibers influence blood platelet adhesion due to their special topography.
→ Chapter 6: Research paper “Nanofiber topographies enhance platelet-fibrinogen scaffold interactions”

In Chapter 7, the aforementioned studies and respective hypotheses are correlated within an overall discussion to present the main findings of the doctoral research work.

2. PRINCIPLES OF FIBRINOGEN FIBER ASSEMBLY *IN VITRO*

Status: this chapter was published at Macromolecular Bioscience (2021)

Stamboroski, S., Joshi, A., Noeske, P. L. M., Köppen, S., & Brüggemann, D. (2021). Principles of fibrinogen fiber assembly *in vitro*. Macromolecular Bioscience, 21(5), 2000412.

DOI: [10.1002/mabi.202000412](https://doi.org/10.1002/mabi.202000412)

2.1. MOTIVATION & HYPOTHESIS

Hypothesis addressed: Presence of salt is one of the main factors for fibrinogen fibrillogenesis *in vitro* under non-denaturing conditions.

The glycoprotein fibrinogen has been the focus of many studies that showed the potential of this molecule in forming nanofibers to be applied in wound healing and tissue engineering. As presented in Section 1.6, different methods are being used to produce fibrinogen nanofibers. Among those methods, one can highlight the self-assembly, due to its simple and fast way to produce nanofibers *in vitro*. Diverse strategies can be used to trigger fibrillogenesis of fibrinogen *in vitro*. However, it is not yet elucidated what are the main factors and experimental conditions leading to fibrinogen self-assembly *in vitro* without the addition of thrombin. Therefore, in this review Chapter, an overview of the present research status concerning fibrinogen fibrillogenesis and the main process-related driving forces for *in vitro* fibrinogen self-assembly are presented.

Hypothesis assessment: Confirmed.



Principles of Fibrinogen Fiber Assembly In Vitro

Stephani Stamboroski, Arundhati Joshi, Paul-Ludwig Michael Noeske, Susan Köppen, and Dorothea Brüggemann*

Fibrinogen nanofibers hold great potential for applications in wound healing and personalized regenerative medicine due to their ability to mimic the native blood clot architecture. Although versatile strategies exist to induce fibrillogenesis of fibrinogen in vitro, little is known about the underlying mechanisms and the associated length scales. Therefore, in this manuscript the current state of research on fibrinogen fibrillogenesis in vitro is reviewed. For the first time, the manifold factors leading to the assembly of fibrinogen molecules into fibers are categorized considering three main groups: substrate interactions, denaturing and non-denaturing buffer conditions. Based on the meta-analysis in the review it is concluded that the assembly of fibrinogen is driven by several mechanisms across different length scales. In these processes, certain buffer conditions, in particular the presence of salts, play a predominant role during fibrinogen self-assembly compared to the surface chemistry of the substrate material. Yet, to tailor fibrous fibrinogen scaffolds with defined structure–function-relationships for future tissue engineering applications, it still needs to be understood which particular role each of these factors plays during fiber assembly. Therefore, the future combination of experimental and simulation studies is proposed to understand the intermolecular interactions of fibrinogen, which induce the assembly of soluble fibrinogen into solid fibers.

to develop autologous scaffolds that promote wound healing and tissue repair.^[2,3] Nanofibrous fibrinogen scaffolds in particular offer very promising strategies for regenerative medicine as they mimic the nanoarchitecture of native blood clots and contain important binding sites to support cell adhesion.^[3,4] Hence, they can serve as a provisional extracellular matrix (ECM) during the initial wound healing phase and were even found to have immunomodulatory properties.^[5–8]

Interestingly, it is known that mutations or structural changes in fibrinogen can induce thrombosis.^[9] Fibrous fibrinogen aggregates were reported to support platelet binding, which may lead to thrombotic complications when hydrophobic polymer surfaces are used in the native tissue environment.^[10] Moreover, conformational changes in fibrinogen can lead to the formation of amyloid fibers, which are associated with diseases like hypertension or renal failure.^[11] Previous studies on the occurrence of Alzheimer's disease

have suggested that fibrinogen is infected by β -amyloids, which results in the oligomerization of fibrinogen.^[12,13] It is known today that a large number of neurodegenerative diseases are associated with the aggregation of proteins into amyloid fibers, which are therefore referred to as protein misfolding disorders.^[14–16] For many protein-based biomaterials it has been discussed that these amyloidogenic characteristics are related to

1. Introduction

Engineering the next generation of biomaterials with novel functionalities for personalized regenerative medicine requires a fundamental understanding of biological principles from the molecular to the cellular and tissue level.^[1] As a central player in the blood coagulation cascade, the adhesive glycoprotein fibrinogen has moved into the focus of tissue engineering

S. Stamboroski, Dr. P.-L. M. Noeske
Fraunhofer Institute for Manufacturing Technology and Advanced
Materials (IFAM)
Wiener Strasse 12, Bremen 28359, Germany
S. Stamboroski, Dr. A. Joshi, Prof. D. Brüggemann
Institute for Biophysics
University of Bremen
Otto-Hahn-Allee 1, Bremen 28359, Germany
E-mail: brueggemann@uni-bremen.de

The ORCID identification number(s) for the author(s) of this article can be found under <https://doi.org/10.1002/mabi.202000412>.

© 2021 The Authors. Macromolecular Bioscience published by Wiley-VCH GmbH. This is an open access article under the terms of the Creative Commons Attribution License, which permits use, distribution and reproduction in any medium, provided the original work is properly cited.

DOI: 10.1002/mabi.202000412

Dr. P.-L. M. Noeske
University of Applied Sciences Bremerhaven
An der Karlstadt 8, Bremerhaven 27568, Germany
Dr. S. Köppen
Hybrid Materials Interfaces Group
Faculty of Production Engineering and Bremen Center for Computational
Materials Science
University of Bremen
Am Fallturm 1, Bremen 28359, Germany
Dr. S. Köppen, Prof. D. Brüggemann
MAPEX Center for Materials and Processes
University of Bremen
Bremen 28359, Germany

conformational changes that occur during the manufacturing process.^[17] Based on this discussion, it becomes extremely important to understand the fundamental mechanisms responsible for fibrinogen fibrillogenesis, which will facilitate the development of non-pathogenic fiber scaffolds.

Under in vitro conditions, fibrinogen also assembles into nanofibers on various surfaces^[10,18,19] or in the presence of solvents and acidic pH values.^[20,21] In particular, when functional nanomaterials from fibrinogen were developed in the presence of organic solvents, the formation of amyloid fibrils was discussed.^[21,22] Such fiber assembly conditions resemble the denaturing effect of organic solvents and high electric fields, which evoke conformational changes during electrospinning that can affect the biofunctionality of protein fibers.^[23,24] Only recently, we reported that fibrinogen can self-assemble into dense nanofiber networks under physiological buffer conditions without introducing any amyloid transitions.^[25,26] Despite the high relevance of fibrinogen-based biomaterials, the underlying principles of fibrinogen fibrillogenesis under in vitro conditions are still not understood at all.

Although many experimental and atomistic studies have already shed light on fibrinogen conformations under different in vitro conditions it still remains unclear which of these parameters predominate fiber assembly. Therefore, our review categorizes different surface and buffer characteristics that favor the formation of fibrillar fibrinogen superstructures in a cell- and enzyme-free environment. Based on this categorization we discuss possible key factors that may contribute to the fundamental mechanism of in vitro assembly of fibrinogen fibers.

2. Structure, Properties, and In Vivo Assembly of Fibrinogen

To understand the fundamental principles of fibrinogen assembly into fibers under in vitro conditions, it is important to gain insight into the native structure of fibrinogen and its role during blood coagulation. Therefore, in this chapter we will introduce the molecular structure of fibrinogen in Section 2.1 and summarize details on the charge distribution in fibrinogen in Section 2.2, followed by a brief presentation of native fibrin fiber assembly upon enzymatic cleavage in Section 2.3.

2.1. Molecular Structure of Fibrinogen

Fibrinogen is a 340 kDa glycoprotein with a covalent dimeric structure that is mainly synthesized in hepatocytes.^[27] It is secreted into the blood plasma where it circulates at a concentration of 1.5–4 g L⁻¹.^[28,29] The fibrinogen molecule is organized into three regions of independently folded structural units: two distal globular D regions, which are connected to a central globular E region via α -helical triple coiled coils.^[27,29,30] The two identical subunits of the fibrinogen molecule are each composed of two sets of three non-identical A α -, B β -, and γ -polypeptide chains.^[29,31] In the central E region, the N-termini of all the six polypeptide chains are linked together via five disulfide bonds.^[27,32] At the N-termini of the A α - and B β -chains in the E region, the fibrinopeptides (Fp) A and B are

located. With only 16 amino acids these peptides constitute less than 2% of the overall mass of the fibrinogen molecule.^[27] They are polar and hydrophilic, which supports their cleavage by thrombin during blood coagulation.^[28]

From the E region, the A α -, B β -, and γ -chains symmetrically depart forming the two triple coiled-coils connectors, each held in register by two “disulfide rings” placed at their beginning and at their end.^[27,33,34] At the end of the connectors, the C-terminal parts of the B β - and γ -chains independently fold within the outer D regions,^[35] with only intrachain disulfide bridges being present.^[27,33] Instead, from the second disulfide ring the C-terminal regions of the A α -chains (α C regions) first reverse direction forming a fourth coiled helix,^[35] and then are thought to be mainly disordered, with only a small structured domain.^[36] It has also been proposed that two α C regions in a single fibrinogen molecule interact with each other and with the central E-region, forming a fourth nodule on top of it, and that they are “released” following Fp cleavage, actively contributing thereafter to the formation of fibrin (proto)fibrils.^[37,38] However, a recent study has cast doubts to the effective role of the α C regions in basic fibrin polymerization.^[39] In any case, these flexible and polar α C arms participate in crosslinking of fibrin during blood coagulation^[29] and could lead to different arrangements of the fibrinogen molecule.

From hydrodynamic studies, as a function of the pH value and the ionic strength of the surrounding buffer system, fibrinogen was hypothesized to exist in different shapes (see Figure 1). At neutral pH and physiological ionic strength, a compact shape with collapsed side chains compatible with that of the human fibrinogen crystal structure^[40] is predicted, where the molecules have been reported to have an “effective length” L_{ef} of 53–55 nm with the maximum extension length from crystallography being in the order of 47 nm. On the other hand, at more basic pH and low ionic strength individual fibrinogen molecules have been reported to adapt a more extended shape predicted from the L_{ef} of 63–68 nm.^[41,42]

Fibrinogen molecules dried under in vitro conditions were also characterized by electron microscopy, which revealed an approximate length of 45 nm and a diameter of 2–5 nm.^[37,43] Thus, dried fibrinogen also exhibited an elongated shape, which is known to be related to its particular biological function during blood coagulation.^[44] When the intermolecular interaction of fibrinogen in aqueous solution was studied with dynamic light scattering (DLS) the hydrodynamic radius R_H was found to change depending on the ionic strength and pH of the buffer system.^[41,42,44,45] Both, human and bovine fibrinogens, have R_H values of 10.5–10.7 nm in close to physiological solutions.^[42,46] In other solutions, for instance pure water or buffers with ionic strengths below 3×10^{-5} M, fibrinogen molecules are reportedly quite unstable forming large aggregates, which can reach dimensions up to 100 nm.^[47,48] However, aggregation of fibrinogen molecules can be reversed, for example by adding salts to increase the ionic strength to 0.15 M.^[47]

2.2. Charge Distribution within the Fibrinogen Molecule

The D and E regions of fibrinogen are considered less hydrophilic than the α C regions.^[49] Amino acid sequence analysis

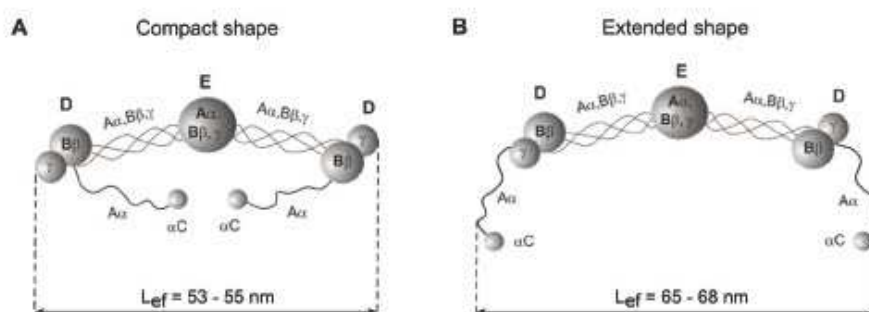


Figure 1. Possible molecular shapes of a fibrinogen molecule in electrolyte solutions derived from hydrodynamic measurements. A) Fibrinogen can assume a compact shape under physiological conditions having an ionic strength of 0.15 M and pH 7.4 or B) an extended shape in a solution with ionic strength of 0.01–0.1 M and pH > 9 or pH < 4. The effective length of the molecule (L_{ef}) under these conditions was calculated using experimentally determined intrinsic viscosity values. Adapted with permission.^[41] Copyright 2009, American Chemical Society.

revealed that the part of the $A\alpha$ chains emerging from the end of the coiled-coils is highly polar and hydrophilic,^[28,50] whereas the C-terminal residues of the αA chain, i.e., the αC regions, consist of unequally distributed polar and nonpolar amino acid residues.^[51] Therefore, the unstructured $A\alpha$ chain extending out from the main body (see Figure 1) contains both, hydrophobic and hydrophilic, regions, while the D, E, and αC regions have a greater hydrophobic content.^[52] However, the amino acid sequence analysis does not provide any information about surface properties on globular domains of the 3D molecule. At physiological pH, the distal D regions and the central E region of fibrinogen are negatively charged while the extending αC regions exhibit a positive charge.^[49] The fibrinopeptides A and B in the E region are short polar hydrophilic peptides.^[28] Theoretical predictions of molecular shapes of fibrinogen in electrolyte solutions (as shown in Figure 1) were used to determine the charge distribution within the fibrinogen molecule.^[42] Thus, an anisotropic charge distribution over the whole molecule was observed in the pH range of 5.8–9.5.^[42] Consequently, positive and negative charges within the fibrinogen molecule are separated by a considerable distance in this pH range.^[42]

Using the hydrodynamic radius R_H value of around 12 nm determined by DLS,^[53] the number of uncompensated, electrokinetic charges N_c on individual fibrinogen molecules was calculated from electrophoretic mobility data (see Figure 2).^[41,53,54] However, the absolute values reported from the calculations in ref. [41] should be considered with caution, since in the derivation of R_H from the diffusion coefficient, the dynamic viscosity η of the solution appears to have been substantially underestimated and seems to have a value close to that of water.^[46]

At low ionic strength of 10^{-4} M and an acidic pH 3.5, a positive charge of $N_c = +26$ ^[54] or $+31$ ^[53] has been reported. These results nearly exclude the possibility of aggregation of fibrinogen at these particular pH conditions, if the charges are uniformly distributed over the molecule. At an ionic strength of 10^{-2} M and a basic pH of 9.5 or 9.7, fibrinogen molecules were found to have a high negative charge of $N_c = -26$ ^[41] or -18 ,^[54] respectively. On the other hand, for an acidic pH of 3.5 with an ionic strength of 0.1 M a positive charge of $N_c = +22$ to $+26$ was reported.^[41,53,54] At the same time, when the ionic strength was increased to

0.15 M at an acidic pH of 3.5, the total N_c was reduced to $+13$.^[54] This reduced total charge indicates a screening effect due to the reduced electrostatic repulsion between individual molecules. When the pH was increased beyond the isoelectric point (IEP) of 5.8 to the physiological value of 7.4 at ionic strength of 0.15 M the overall net charge decreased to $N_c = -7$ as it was confirmed by electrophoretic mobility measurements.^[41,54] The reported N_c varies considerably likely as a result of the different techniques used and models applied to calculate the uncompensated charges on fibrinogen as well as the fibrinogen concentration adopted in the different studies.

Overall, a clear correlation between increasing ionic strength in the solution and a change in the number of uncompensated charges N_c per fibrinogen molecule toward an equilibrium value of zero charges can be observed as indicated by the dashed lines in Figure 2. This gradual change of N_c toward zero uncompensated charges can be associated with an increased charge shielding effect of fibrinogen molecules due to an increase in salt ion concentration in the dispersant^[55,56] that encompasses changes of the thickness and composition of the electrical double layer.^[57,58]

Sequence analysis revealed that at physiological ionic strength of 0.15 M fibrinogen is 41% polar, 26% charged, and 33% hydrophobic.^[59] When a coarse grain model of fibrinogen was used, which was based on its crystal structure,^[40] the far distal ends of the molecule were found to exhibit a more hydrophobic character than the rest of the protein and an overall net charge of -8 at pH 7.4 and a low ionic strength of 0.025 M was found.^[60] By including the αC regions in the same study a total negative charge of -12 at the same pH and low ionic strength was reported for the whole molecule.^[60] This implies an overall negative net charge of the αC region^[60] contrary to the work of Adamczyk et al., for which a positive net charge of $+3e$ is reported at pH 7.4^[42] for the αC -terminal domain.

For both, experimental and theoretical studies, the reported charge values vary significantly. Most of the theoretical studies^[59,61,62] are based on the 3ghg model only^[40] while Zuev et al. used an extended version of this structure.^[45] However, the different authors seem to assign their charges based on varying protocols. On the other hand, experimentally observed charge variations can be explained with varying buffer conditions and different fibrinogen sources or purity grades. To clarify the

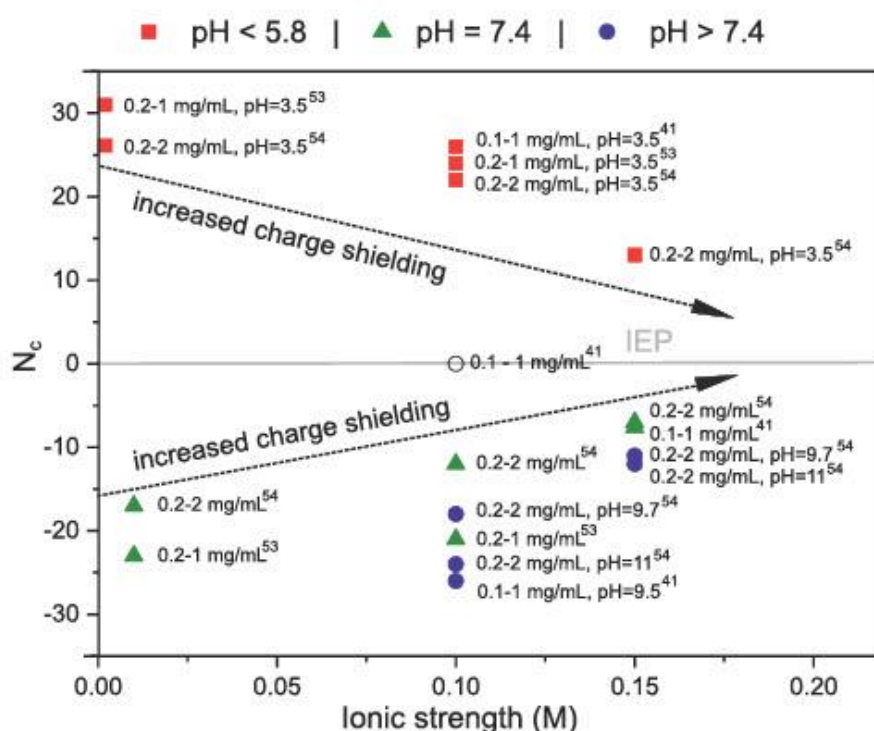


Figure 2. Number of uncompensated charges per fibrinogen molecule (N_c) as a function of the ionic strength - based on previous experimental studies.^{[4],53,54} Red squares represent the N_c at pH lower than 5.8; green triangles show N_c values at pH equal to 7.4 and blue balls depict N_c values at pH values above 7.4. The black hollow circle indicates zero charge for fibrinogen at its IEP. Fibrinogen molecules are positively charged at pH lower than its IEP and negatively charged for pH values above the IEP. With increasing ionic strength, the absolute N_c values decrease, which is due to the effect of charge shielding with higher salt concentrations (indicated by dashed lines to guide the eye).

question of the internal charge distribution within the fibrinogen molecule, a visualization of the isopotential surfaces can be helpful. With this visualization, the presence of asymmetrically distributed charged areas on the fibrinogen molecule at an ionic strength of 0.15 M was revealed^[61] as it is illustrated in Figure 3. Molecular dynamics (MD) studies confirmed the presence of a large negatively charged area per dimeric fibrinogen protomer, which was located on one side of the surface of the D region^[61] (see Figure 3).

Moreover, MD simulations showed that the concentration of fibrinogen in solution also affects the overall molecular conformation.^[45] Fibrinogen changes from a compact shape with ≈ 35 nm diameter in dilute solutions of 1×10^{-6} M fibrinogen to an extended shape with an approximate length of 70 nm in solutions with 100×10^{-6} M fibrinogen.^[45] Atomistic studies revealed that this change in molecular shape originated from a high internal molecular flexibility, which influences the overall hydrodynamic properties of the fibrinogen molecule.^[45,61] Due to this bending, owing to a molecular flexibility observed in MD trajectories, the effective length of full-length fibrinogen in solution was reported to be only about 35–37 nm for the intramolecular D–D domain distance,^[45] which is much smaller than the effective length reported in previous experimental studies.^[41,54] In addition, Zuev et al. found an approximate distance of 70 nm for the αC – αC domain distance, showing a much higher range,

since the αC domains are connected via highly flexible connection regions.^[45] Hence, this intrinsic flexibility is assumed to be responsible for the conformational variability of fibrinogen in solution/colloidal dispersion as well as upon adsorption to different inorganic surfaces.^[61]

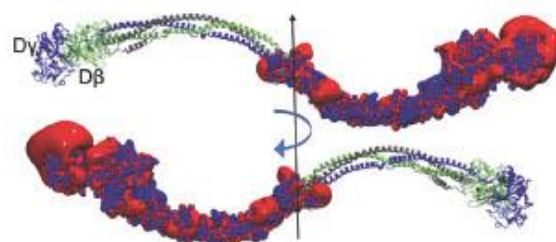


Figure 3. Typical bent conformation of the symmetric fibrinogen dimer. The molecular structure as published in the pdb entry 3ghg is displayed after 40 ns of MD simulations with α -, β -, and γ -chains colored in gray, green, and blue, respectively. For one symmetrical unit, the isopotential surfaces^[63,64] with values of $\pm 2 K_B T$ ^[65] show a non-uniform charge distribution along the molecule. Red indicates negative and blue displays positive potential values. Especially at the outer D_α domain, a higher negative charge density is visible as published in ref. [61]. Via rotation around 180° , the backside of the molecule is visible in the lower image of the fibrinogen molecule.

2.3. Fibrin Fiber Assembly during Blood Coagulation

Blood coagulation in vivo induces the formation of nanofibrous fibrin clots upon enzymatic cleavage of fibrinogen during the wound healing process.^[32] The formation of an insoluble fibrin network, the final step in blood coagulation, is achieved by a cascade of reactions and changes in the molecular shape of fibrinogen (see Figure 4).^[27,28,38,51] Initially, the enzyme thrombin cleaves off Fp A from the N-terminal portion of the A α chain in the E region of fibrinogen, generating the so-called "desAA fibrin monomer,"^[28] where the A α chains have acquired new N-terminal sequences termed as "knobs" "A".^[28,66] These knobs interact with "holes" "a", which are pockets that are constitutively open in the γ subunit of the D region of other fibrin(ogen) monomers.^[28,35,67] The binding of knobs "A" and holes "a" is termed as "A-a" interaction (see Figure 4).^[28] In the next, much slower step, the enzyme thrombin cleaves off Fp B from the N-terminal part of the B β chain of the fibrin oligomers.^[27,32] Thereby, the β chain of fibrinogen also acquires new N-terminal sequences called "B" knobs.^[28,66] These knobs bind to holes "b" in the β subunit of the D region of already engaged fibrin units, thus leading to "B-b" interactions.^[28,35] In the classic scheme of fibrin formation, two desAA-fibrin monomers are held together by knob-hole interactions to form a half-staggered dimer.^[28,68] These monomers continue to aggregate longitudinally to form fibrin oligomers, which assemble into two-stranded protofibrils.^[69] Finally, lateral aggregation of fibrin protofibrils into a 3D, multistranded network of insoluble fibrin fibrils takes place,

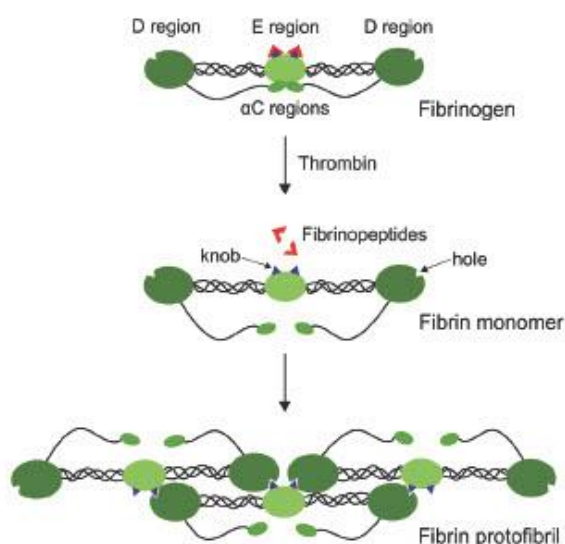


Figure 4. Formation of fibrin protofibrils from fibrinogen. A fibrin monomer is formed after the enzymatic cleavage of fibrinopeptides A and B (red) from a fibrinogen molecule by the enzyme thrombin. "Knobs" (blue) in the E region of fibrinogen are thus exposed allowing for interactions with "holes" present in the distal D regions of fibrinogen. This allows intermolecular "knob-hole" interactions between fibrin monomers, which cause the fibrin monomers to polymerize via non-covalent and dynamic association to form fibrin protofibrils.

aided by the cleavage of Fp B and the subsequent "B-b" interactions.^[28,32] A somewhat alternative mechanism involving delayed double-strand formation and early branching taking place at the protofibril formation step has also been proposed recently.^[70]

Interestingly, the formation of knobs "A" and the existence of holes "a," in particular the amino acid residues therein, are necessary and already sufficient to initiate fibrin polymerization.^[28,39] However, there has been evidence of both, an increase in the binding affinity between "a" holes and "A" knobs and a domain rearrangement in the D regions of fibrinogen, that favor the aggregation of protofibrils due to the "B-b" interactions.^[71,72] MD simulations have provided evidence of the allosteric regulation of "a" and "b" holes in the D-region of fibrinogen, which ultimately help to create lateral non-covalent connections between neighboring fibrin molecules via dynamic association.^[61,73]

Overall, the enzymatic conversion of fibrinogen to fibrin is accompanied by changes in the quaternary structure.^[32] Although the secondary structure of fibrinogen remains largely unchanged during thrombin-mediated conversion to fibrin,^[74] minor conformational changes from α -helices to β -sheets have previously been observed under in vitro conditions.^[75] The cleavage of Fp A and Fp B causes small conformational changes, which coupled to the Fp loss could weaken the intramolecular interactions between the α C arms and the central E region within individual fibrin molecules. Consequently, these regions could become available for intermolecular interactions between neighboring fibrin monomers,^[37,51] which are important in determining the structure and mechanical properties of the resulting fibrin network.^[76] Nevertheless, a direct evidence of this mechanism in solution is still lacking.

Fibrin aggregation into a nanofibrous network reinforces the initial plug formed by thrombocyte aggregation, leading to hemostasis and wound closure.^[77,78] The 3D plug consisting of the insoluble fibrin network and platelets is called a blood clot.^[78] As a consequence of blood coagulation in response to vascular damage, this fibrin-rich nanofiber network emerges immediately following an injury and enables tissue repair in vivo.^[79] This nanofibrous network, supported by platelets, serves as a provisional ECM, which ultimately undergoes a fibroblast-mediated remodeling to facilitate wound healing.^[79] Since fibrinogen and fibrin both have a high affinity for vascular endothelial growth factor and fibroblast growth factor, they play a critical role in the adhesion of endothelial cells and fibroblasts.^[80,81] Integrins facilitate the adhesion of cells to both, fibrinogen and fibrin, via Arg-Gly-Asp (RGD) binding sites present on the α -chains so that different cell types can migrate into a blood clot to promote tissue repair and regeneration.^[32,77,78]

3. Fiber Assembly of Fibrinogen In Vitro

Due to its variability of molecular conformations, fibrinogen is also able to assemble into fibers in vitro, without the enzymatic cleavage by thrombin so that no crosslinking mechanism is involved in the formation of fibrinogen fibers.

Although fiber formation of fibrinogen is very important to avoid thrombogenic reactions to fibrinogen-based biomaterials, the available literature on in vitro fiber assembly that we review here is very scattered. Nevertheless, various conditions were already found to induce intermolecular interactions of individual fibrinogen molecules in an enzyme- and cell-free in vitro environment, thus favoring the assembly into nanofibers. Different surface properties were associated with substrate-driven fiber formation of fibrinogen, which will be presented in Section 3.1. On the other hand, varying buffer conditions were reported to induce fiber assembly, which are summarized in Section 3.2.

3.1. Substrate-Driven Fibrillogenesis

Varying surface characteristics were found to favor fiber formation of fibrinogen in vitro. In Table 1 we have categorized these properties into the main groups of “hydrophobic surfaces” and “hydrophilic surfaces” to compare the manifold

environmental conditions, during which fiber assembly was reported. When comparing different environmental conditions, it needs to be taken into account that fibrinogen concentrations reported in Table 1 refer to the starting concentrations used in the respective studies. While some samples were completely dried prior to analysis (named “in air”), others were analyzed in aqueous environment (named “in liquid”). Based on these different treatments it needs to be assumed that the protein concentration as well as the ionic strength will have increased over the total incubation time, which makes it difficult to compare particular concentrations among different studies. With all surface characteristics summarized in Table 1 different hierarchical levels of fibrous superstructures were obtained, which ranged from small protofibrils, single nanofibers and nanofiber bundles to dense nanofiber networks. These different categories are based on the fiber dimensions and morphologies reported in the respective studies. Exemplary images of these different hierarchical fiber arrangements observed by substrate-driven fibrillogenesis are shown in Figure 5.

Table 1. Substrate-driven assembly of fibrinogen (Fg) into fibers. Properties of pristine substrate surfaces and associated buffer conditions, which were found to drive the assembly of fibrinogen into fibrous arrangements at different hierarchical levels.

| | Surface | Surface properties | Buffer | Metal ions | Ionic strength (molar) | pH | Fg concentration [$\mu\text{g mL}^{-1}$] | Temperature | In air/in liquid | Fiber morphology | Ref. |
|---------------------------|---|--------------------|------------------------------|---|------------------------|-----|--|---------------------|-------------------|--|------|
| Hydrophobic | HOPG with nanosteps | Hydrophobic | PBS | Na^+ , K^+ | 0.15 | 7.4 | 3–200 | 37 °C | In air | Single nanofibers, nanofiber bundles, and nanofiber networks | [18] |
| | | | Carbonate | Na^+ | 0.35 | 8.4 | | | | | |
| | Nanostructured polyethylene single crystal surfaces | Hydrophobic | PBS | Na^+ , K^+ | 0.15 | 7.4 | 0.5–5 | 37 °C | In air | Single nanofibers and nanofiber networks | [83] |
| | TOMA clay | Hydrophobic | TBS-EDTA | Na^+ | 0.15 | 7.4 | 4×10^3 | RT | In air | Nanofiber bundles | [84] |
| | TOMA clay | Hydrophobic | PBS | Na^+ , K^+ | 0.15 | 7.2 | 4×10^3 | 21 °C | In air/liquid | Nanofiber bundles and nanofiber networks | [19] |
| | Polystyrene | Hydrophobic | | | | | | In air | | | |
| | Poly(methyl methacrylate) | Hydrophobic | | | | | | | | | |
| | Polybutadiene | Hydrophobic | | | | | | | | | |
| | Polystyrene-Poly(4-vinylpyridine) as reference | Hydrophilic | | | | | | | | | |
| | Polystyrene | Hydrophobic | TBS-EDTA | Na^+ | 0.15 | 7.4 | 4×10^3 | RT | In air | Nanofiber networks | [10] |
| Poly(lactic acid) | Hydrophobic | | | | | | | | Nanofiber bundles | | |
| Poly(methyl methacrylate) | Hydrophobic | | | | | | | | | | |
| Hydrophilic | GM-HOPG | Hydrophilic | Phosphate | Na^+ | 0.02 | 7.2 | 2.3–23 | RT, 65 °C and 90 °C | In air | Protofibrils | [82] |
| | GM-HOPG | Hydrophilic | Phosphate | Na^+ | 0.02 | 7.2 | 2 | RT | In air | Protofibrils | [85] |
| | | | PBS | Na^+ , K^+ | 0.11 | 7.2 | | | | | |
| | | | PBS | Na^+ , K^+ , Ca^{2+} | 0.007 | 7.4 | 50–250 | | In liquid | | |
| | Au (111) | Hydrophilic | Tris-HCl | Na^+ , Mg^{2+} | 0.33 | 7.6 | 4 | RT | In liquid | Single nanofibers | [86] |
| Aluminum oxide membrane | Hydrophilic | PBS | Na^+ , K^+ | 0.15 | 7.4 | 10 | RT | In air | Nanofiber bundles | [87] | |

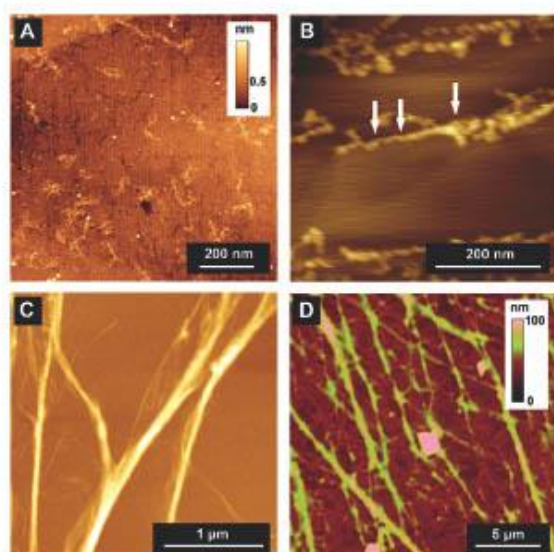


Figure 5. Representative images of different fibrillar assemblies induced by substrate-driven fibrillogenesis. A) AFM image of protofibrils on oligoglycine-hydrocarbon graphite-modified HOPG (reproduced with permission.^[82] Copyright 2018, Elsevier), B) AFM image of single nanofibers on HOPG with nanosteps (reproduced with permission.^[19] Copyright 2009, Wiley-VCH), C) optical microscope image of nanofiber bundles on poly(methylmethacrylate) surfaces (reproduced with permission.^[10] Copyright 2017, Elsevier), and D) AFM image of nanofiber networks on TOMA clay (reproduced with permission.^[19] Copyright 2012, American Chemical Society).

3.1.1. Fiber Formation on Hydrophobic Surfaces

Globular proteins are well known to unfold on hydrophobic surfaces.^[88] Interestingly, the fibrillar protein fibrinogen, which contains three globular regions, also experiences unfolding on hydrophobic surfaces,^[89] such as graphite.^[59,90] Therefore, it is likely that hydrophobic surfaces induce conformational changes in the fibrinogen molecule that lead to fiber assembly.

The influence of the chemical surface composition on fibrinogen conformation and fiber assembly was systematically studied by Koo and co-workers using a variety of hydrophobic surfaces.^[19,84] In a first study, synthetic fluoromica clay with a quaternary ammonium cation, triocylmethylammonium (TOMA) clay with a water contact angle (WCA) of 69° was used as a model hydrophobic surface to study the role of the α C region during fiber formation.^[19] Short nanofiber bundles with a height of 3.2 ± 1.2 nm were observed when 4 mg mL^{-1} fibrinogen in Tris-buffered saline (TBS) solution were incubated with TOMA surfaces for 8 min. When the adsorption time was increased to 20 min networks with long overlapping fibers were found, which exhibited a mean height of 19.2 ± 6.9 nm.^[19] After 18 h incubation the fiber dimensions increased even further, and networks with straight fibers and an average height of 30.7 ± 18.0 nm were observed (see Figure 5D).^[19] However, at concentrations below 1 mg mL^{-1} no fibers formed on TOMA. To study the particular role of the extending α C region in fiber formation on hydrophobic substrates a fibrinogen construct

lacking the intact α C region was prepared by plasmin digestion. When these des- α C fibrinogen molecules were incubated with TOMA surfaces in either TBS with Ethylenediaminetetraacetic acid (EDTA) or phosphate-buffered saline (PBS) for up to 24 h no fiber assembly was reported.^[19,84]

Following up on these results, the influence of different polymer surfaces on fibrinogen fibrillogenesis was studied using hydrophobic TOMA clay with a WCA of 69°.^[19] Moreover, hydrophilic mica was used as a reference substrate,^[19] which is known to have a WCA of 2.7°.^[91] On hydrophobic polymer surfaces such as polystyrene (PS), polybutadiene (PB), and poly(methyl methacrylate) with WCAs between 60° and 90° fibrinogen was found to assemble into fibers when the surfaces were incubated with 4 mg mL^{-1} fibrinogen solution in either TBS or PBS (see Figure 5C).^[10,19] On hydrophobic TOMA clay fibrinogen formed extended trinodular structures while hydrophilic references from polar mica clay (WCA = 46°) only yielded globular fibrinogen aggregates, but no fibers were formed.^[19] Likewise, no fibers were formed on poly(4-vinyl pyridine) (PVP), which only exhibited contact angles of 37°^[91] and 55°.^[10] When 2.5% of hydrophilic PVP were added to hydrophobic PS to achieve a WCA of 71°, fibrinogen still assembled into fibers. A higher content of PVP in PS, which reduced the WCA below 60°, however, prevented fiber formation.

Interestingly, when hydrophobic PS with a WCA of 82° was functionalized with increasing amounts of hydroxyl groups, fiber formation was suppressed completely despite the relatively high WCA. This finding indicates that changes in the surface chemistry can also alter the interaction with fibrinogen in addition to the WCA, and it was suggested that hydroxyl groups might interact with the α C regions, which are rich in carboxyl and amine groups.^[19,92] This interaction could possibly lead to a similar molecular conformation as otherwise postulated for fibrinogen on hydrophilic surfaces (see Section 3.1.2).^[52,93,94] Later on, hydrophobic PS surfaces were also exposed to UV-ozone to reduce the contact angle to 62° by increasing the surface charges. This treatment completely suppressed fiber formation,^[10] yet without changing the surface chemistry as it was previously achieved with the introduction of hydroxyl groups.^[19]

In summary, for hydrophobic surfaces with WCAs above 60° fiber formation was observed when 4 mg mL^{-1} fibrinogen were used, and with increasing incubation time the resulting fiber dimensions increased. It is known that fibrinogen strongly adsorbs to hydrophobic surfaces via the relatively more hydrophobic E and D regions.^[10] This adsorption to hydrophobic surfaces distorts the molecule into an extended shape and releases the outer α C regions, which are less hydrophobic (see Figure 6A).^[10] Such an extended fibrinogen conformation with lateral spreading has previously been reported for a wide range of hydrophobic surfaces including graphite, TOMA clay, and modified gold.^[19,93,95–97] Consequently, the molecule is extended and the α C regions are available to bind to adjacent fibrinogen molecules to induce fiber assembly.^[10,19,52,93,95,98]

Interestingly, no fiber assembly was observed when des- α C fibrinogen interacted with hydrophobic surfaces, or when low fibrinogen concentrations of 1 mg mL^{-1} were used. Hence, an involvement of accessible α C regions in fiber formation seems plausible.^[19,84,99] On the other hand, the plasmin digestion of fibrinogen that was used to prepare des- α C fibrinogen

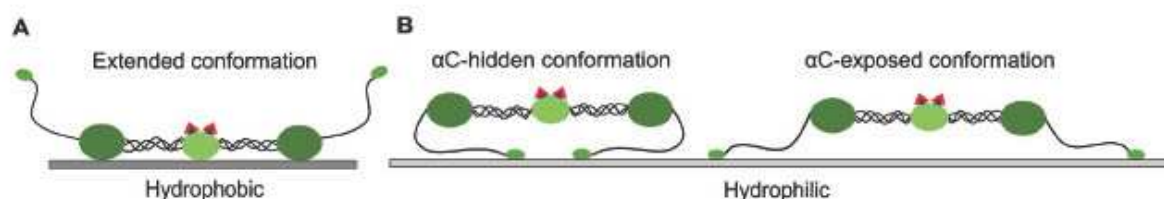


Figure 6. Schematic representation of proposed models of fibrinogen adsorption to surfaces. A) Fibrinogen molecules have been suggested to adsorb to hydrophobic surfaces via their D regions in an extended conformation, B) whereas adsorption of fibrinogen molecules to hydrophilic surfaces has been suggested to occur via its α C regions, either in a α C-hidden or α C-exposed conformation. Such schematic representations of these different conformations have been reported in many previous studies.^[19,52,93–95,98]

may have attacked the N-terminal ends of the β -chains.^[100] Based on this assumption it may also be possible that potentially missing portions of the β -chains play a role in fiber assembly when fibrinogen adsorbs to hydrophobic surfaces. In the future, studies with recombinant fibrinogens having intact N-terminals and constitutively deleted α C regions could also shed more light on this issue.

At the same time, conformational changes in the D region were found to occur upon fibrinogen adsorption on relatively hydrophobic but not on hydrophilic surfaces,^[101] which may mimic the effect of thrombin-induced fiber assembly.^[19] Moreover, fibrinogen molecules were reported to stay immobilized on some hydrophobic polymer surfaces to form fibers that were insoluble in aqueous solutions.^[19] This finding suggests that fibrinogen molecules may even have been irreversibly unfolded during adsorption onto hydrophobic polymer surfaces.

A particular example of hydrophobic surfaces leading to fiber assembly of fibrinogen are the nanostructured surfaces previously introduced by Jandt and co-workers.^[18,83] When fibrinogen in PBS or carbonate buffer (CB) was exposed to highly oriented pyrolytic graphite (HOPG) surfaces with 8 nm high steps, single nanofibers were formed after incubation at 37 °C for 30 min (see Figure 5B).^[18] After drying with nitrogen (N_2), fibrinogen preferentially adsorbed at the hydrophobic HOPG nanosteps and formed single parallel nanofibers with widths around 15 nm for low fibrinogen concentrations of 3–5 $\mu\text{g mL}^{-1}$, while 5–10 $\mu\text{g mL}^{-1}$ resulted in nanofiber bundles with diameters around 40 nm. With much higher concentrations of 200 $\mu\text{g mL}^{-1}$, dense porous fibrinogen layers or here called “nanofiber networks” were observed. However, when the adsorption of fibrinogen solutions to HOPG nanosteps was monitored directly in buffer using atomic force microscopy (AFM) fibrinogen did not assemble into fibers.

In a similar study, the assembly of fibrous fibrinogen structures on nanostructured, hydrophobic polyethylene single crystals (PE-SC) was reported.^[83] Hydrophobic PE-SC nanocrystals were fully covered with fibrinogen solution and stored at 37 °C for 2 h prior to rinsing with PBS or CB and drying with compressed air. Single nanofibers as well as networks of fibril-like structures were found on the hydrophobic PE-SC crystals.^[83] Interestingly, the fibrous networks resembled the fibrinogen structures previously observed on HOPG nanosteps^[18] although much lower protein concentrations were used. Overall, increasing protein concentrations yielded fibers with larger dimensions and a higher network density: 0.5 $\mu\text{g mL}^{-1}$ of fibrinogen yielded single nanofibers with an average width

of 30 ± 5 nm and 2 $\mu\text{g mL}^{-1}$ resulted in a nanofiber network with nanofiber widths of 45 ± 10 nm.^[83] With a concentration of 5 $\mu\text{g mL}^{-1}$ fibrinogen sponge-like structures with interconnected fibers were observed.^[83]

In conclusion, fiber formation on hydrophobic PE-SC nanocrystals and HOPG nanosteps was observed with much lower fibrinogen concentrations than on smooth hydrophobic polymer or TOMA surfaces. For these hydrophobic nanostructures, fiber assembly was explained by the preferential orientation of fibrinogen molecules along the crystallographic PE-SC directions or the parallel nanosteps, which favor intermolecular interactions and fiber assembly at the surface-buffer interface.^[18,83] This molecular orientation may originate from the intrinsic flexibility of fibrinogen,^[64] which encourages surface mobility on nanostructured surfaces.^[102] For the non-polar, hydrophobic PE-SC nanocrystals it was also assumed that fibrinogen adsorbs via its nonpolar D regions and the central E region, like it was suggested for varying smooth hydrophobic surfaces. Consequently, the polar α C-regions may also be involved in fiber assembly on PE-SC surfaces^[83] and it may be concluded that the particular nanotopographies were responsible for the fiber formation rather than the hydrophobic polymer itself. More experiments with similar nanotopographies from other materials will be required to fully understand their involvement in fibrinogen fibrillogenesis.

When comparing all studies of fibrinogen fibrillogenesis on the hydrophobic substrates in Table 1, it becomes clear that one important aspect also needs to be considered: the drying of fibrinogen samples. Jandt and co-workers even explicitly mentioned the influence of sample drying in their work on HOPG nanosteps where they did not observe any fiber formation during AFM monitoring in liquid.^[18] When fibrinogen solutions are dried during incubation, an increase in protein concentration and ionic strength takes place, which may actually be a major cause for fiber formation. However, this aspect has not been explicitly addressed among the studies available to date. Likewise, information on incubation times of fibrinogen with different surfaces have not been reported throughout all studies, either. Therefore, it is not yet possible to conclude whether fibrinogen fibers have already formed in solution or only after drying.

3.1.2. Fiber Formation on Hydrophilic Surfaces

In contrast to hydrophobic surfaces, for hydrophilic materials it has been suggested that fibrinogen adsorption can be caused by

electrostatic attraction, hydrogen bonding, coordinative interaction, or hydrophilic interactions.^[10] Yet, many of the studies focusing on hydrophobic substrates did not observe fibrillogenesis of fibrinogen on hydrophilic reference surfaces although fibrinogen was found to adsorb to them.^[10,19,84] In contrast to these studies fibrinogen was later found to assemble into fibers on a variety of hydrophilic materials ranging from modified graphite,^[82,85] gold,^[25,26,86] mica,^[20] and aluminum oxide^[87] to hydrophilic and silanized glass.^[25,26]

Klinov and co-workers reported the formation of fibrillar fibrinogen structures on HOPG surfaces with oligoglycine-hydrocarbon graphite modifier (GM-HOPG, WCA = 59°).^[82,85] Fibrinogen was exposed to the GM-HOPG surfaces for 1 s at low concentrations of 2–23 $\mu\text{g mL}^{-1}$, before the surfaces were incubated in water or PBS and subsequently dried with N_2 .^[82,85] AFM analysis revealed that fibrinogen on GM-HOPG underwent a transition from tri-nodular, native-like molecules into fibrillar structures (i.e., protofibrils, see Figure 5A).^[82,85] This transition was promoted when the incubation time was increased to 35 min.^[85] Moreover, by increasing the incubation temperature from room temperature (RT) to 65 or 90 °C, pre-denatured fibrinogen molecules were more likely to assemble into protofibrils.^[82] For AFM analysis in wet environment GM-HOPG was placed in PBS with additional CaCl_2 at RT before fibrinogen solutions between 50 and 250 $\mu\text{g mL}^{-1}$ were added. These *in situ* studies also revealed the formation of protofibrils on GM-HOPG in aqueous environment, which is in contrast to previous studies in aqueous environment.^[19] For fibrinogen on GM-HOPG it was concluded that protofibril formation was driven by the protein-surface interaction under both, dry and wet, conditions although no control experiment was performed where fibrinogen was dried in the presence of CaCl_2 -containing PBS.^[85]

Hydrophilic gold surfaces in (111) orientation were found to induce fibrinogen assembly into protofibrils in wet environment when 4 $\mu\text{g mL}^{-1}$ fibrinogen in Tris buffer were incubated on Au (111) for 50 min at pH 7.6.^[86] It has been postulated that the interaction of gold with sulfur atoms in the cysteines of the fibrinogen molecules leads to stable Au–S bonds that break the intramolecular disulfide bonds in the E domain, releasing the outer αC regions to interact with other fibrinogen molecules to assemble into nanofibers.^[86]

In contact with hydrophilic aluminum oxide nanopores, which are known to have a WCA of 25 to 30°,^[103] we recently observed fibrinogen to assemble into bundles of aligned nanofibers when a solution of 10 $\mu\text{g mL}^{-1}$ of fibrinogen in PBS was extruded through the pores.^[87] Scanning electron microscopy (SEM) analysis of extruded and dried bundles, which had formed in the shear flow of the protein solution through the nanopores, revealed that individual nanofibers exhibited diameters around 34 ± 3 nm.^[87] When the same process was applied to other proteins it was observed that the fiber dimensions depended on the protein concentration and the nanopore diameter.^[87] For extruded fibronectin nanofibers conformational changes were observed, which also correlated with pore size and protein concentration.^[104] Hence, it can be assumed that extrusion of fibrinogen nanofibers was actually driven by shear forces in the confined alumina nanopores rather than the surface properties.

Overall, when fibrinogen assembled into fibers on hydrophilic surfaces^[82,85–87] much lower fibrinogen concentrations were present than on smooth hydrophobic surfaces,^[10,19,84] and the protein concentrations were more in the range of previous studies on fibrinogen fiber assembly on hydrophobic nanostructures.^[18,83] In general, the adsorption energy of hydrophobic surfaces is higher (more negative) than for hydrophilic surfaces, which facilitates irreversible adsorption of fibrinogen to hydrophobic surfaces as compared to hydrophilic surfaces.^[44] However, on hydrophilic surfaces the αC regions have a higher affinity to directly adsorb to the surface than on hydrophobic surfaces (see Figure 6B).^[19] Hence, on hydrophilic surfaces the αC regions are less likely able to recruit other fibrinogen molecules, thus inhibiting the assembly of individual molecules into fibers.^[10,19]

Nevertheless, many studies reported fibrillogenesis of fibrinogen on hydrophilic surfaces as we have summarized in Table 1. In these works, it is very unlikely that the adsorption of more hydrophobic fibrinogen regions has occurred on the hydrophilic surfaces. Experimental studies on hydrophilic surfaces mainly reported two different conformations of fibrinogen molecules upon adsorption. A globular shape has been identified together with a more compact, bent conformation, where the αC regions are located between the D and E regions and the respective surface.^[10,19,52,93,94] This conformation is referred to as the “ αC -hidden” conformation (see Figure 6B). Under these conditions, no intermolecular αC -interactions between neighboring fibrinogen molecules are possible and an absence of molecular aggregation^[93] or fiber formation^[10,19] has been reported. On the other hand, fibrinogen molecules have been described to adapt a “flat-on” conformation on hydrophilic surfaces with visible αC regions, which is known as “ αC -exposed” conformation (see Figure 6B).^[52,105]

Regardless of the αC -hidden or the αC -exposed conformation of fibrinogen, its binding to hydrophilic surfaces has been reported to occur mainly through electrostatic interactions between negatively charged surfaces and positively charged αC regions at a lower pH range of 3.5–7.4.^[52,93,106] Under these low pH conditions, fibrinogen molecules can adsorb irreversibly to negatively charged surfaces because of a large (negative) binding energy.^[44] The αC -hidden conformation of fibrinogen on hydrophilic surfaces seems to prevail at physiological pH of 7.4, however this quickly changes to the “ αC -exposed” conformation on hydrophilic surfaces when the pH is changed to 3.5 and back to 7.4.^[95] A similar molecular reorientation has been observed on hydrophilic polyurethane, where fibrinogen first adsorbed loosely via its αC regions, followed by more favorable interactions via the D regions, which successively left the αC regions accessible for intermolecular interactions with surrounding fibrinogen molecules.^[98]

Although many studies have mentioned αC - αC interactions as a possible factor for fibrillogenesis of fibrinogen on hydrophilic surfaces, it is still not clear whether this is the major cause for *in vitro* fiber formation. In particular the role of the αC extensions was recently questioned in fibrin formation.^[39] Although Litvinov and co-workers recently provided direct evidence for specific interactions of αC regions with the central E region and other αC regions, these interactions were reported to be rather weak.^[107] Since the conformation of the αC regions within individual fibrinogen molecules is critically

dependent on pH, the properties of the buffer system will also be extremely important in understanding whether fibrinogen assembles into fibers on hydrophilic surfaces.

3.2. Buffer-Induced Fibrillogenesis

MD simulations of fibrinogen have previously underlined the interdependence of the surface properties and the molecular orientation and conformation of adsorbed fibrinogen molecules,^[59,61,108] which consequently influences whether molecular aggregation into fibrillar structures under in vitro conditions will take place or is prevented.^[10,19,86] Besides surface properties, buffer conditions like pH and ionic strength are known to influence the molecular orientation and conformation of fibrinogen. Although hydrophobic surfaces have previously been mentioned as the main driving force for fibrillogenesis of fibrinogen, a lot of studies also reported fiber assembly on hydrophilic surfaces.^[20–22,25,26,86] In these works the influence of different buffer conditions, such as pH, ionic strength, protein concentration, and the presence of metal ions, on the conformation and orientation of adsorbed fibrinogen molecules was studied, although these parameters were not considered as the main driving force for fibrillogenesis.^[54,94,95,109]

Only few studies have explicitly considered varying buffer conditions as being responsible for the formation of fibrinogen fibers when no enzymes or cells are present. Like for substrate-driven fibrillogenesis, they reported the assembly of fibrous superstructures with different hierarchical levels that ranged from protofibrils to single nanofibers and nanofiber bundles as well as to dense nanofiber networks that even resemble the morphology of native fibrin clots.^[20,21,25,26,48,110] Exemplary images of the different hierarchical fiber assemblies observed by buffer-induced fibrillogenesis are shown in Figure 7. In Table 2 we have categorized the different buffer conditions leading to fiber assembly into the groups of denaturing and non-denaturing buffer conditions. Again, the protein concentrations and ionic strengths refer to initial values used in the respective studies, which often lack detailed information on the incubation time. Nevertheless, an increase in fibrinogen and salt concentration over time needs to be assumed for all studies on buffer-induced fiber assembly upon drying.

3.2.1. Denaturing Buffer Conditions

Organic Solvents: Wei and co-workers observed the formation of nanofibers on hydrophilic mica surfaces when fibrinogen was mixed with ethanol (EtOH) at varying ratios and incubated at 37 °C for 1 h.^[21] AFM analysis in the dried state revealed thin, straight nanofibers with 4–5 μm length at 5 $\mu\text{g mL}^{-1}$ fibrinogen concentration. Interestingly, shorter fibers of $\approx 2 \mu\text{m}$ length were obtained with higher concentrations of 20 $\mu\text{g mL}^{-1}$ fibrinogen.^[21] At 50 $\mu\text{g mL}^{-1}$ branched nanofiber bundles were described whereas no fibers were formed with 200 $\mu\text{g mL}^{-1}$. At this concentration only spherical aggregates were observed on the mica surfaces.^[21] Variation of the ethanol content in a 20 $\mu\text{g mL}^{-1}$ fibrinogen solution revealed that thin protofibrils formed with a minimum of 33% of ethanol.^[21] The assembled

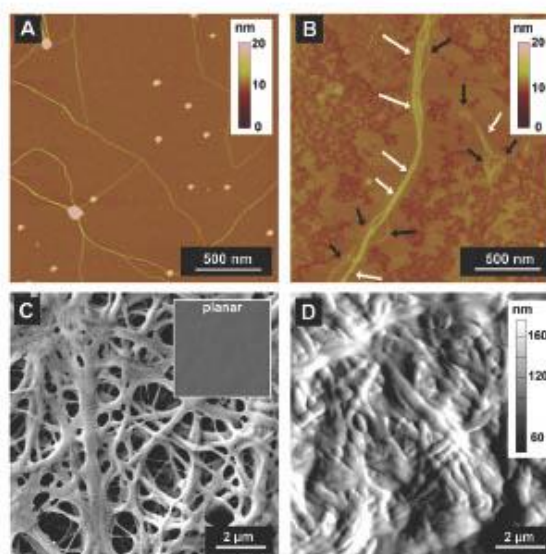


Figure 7. Representative images of buffer-induced fibrillogenesis of fibrinogen into different fibrillar superstructures. AFM images of A) single nanofibers in PBS buffer at acidic pH and B) nanofiber bundles in water at acidic pH (modified and reproduced with permission.^[20] Copyright 2008, American Chemical Society). C) SEM image of dry nanofiber networks prepared by salt-induced self-assembly, inset shows the contrasting smooth morphology of planar fibrinogen films prepared in NH_4HCO_3 (unpublished data), and D) AFM analysis of fixated, rehydrated fibrinogen nanofibers that were assembled on a gold surface in PBS buffer at pH 9 (modified and reproduced with permission.^[25] Copyright 2019, American Chemical Society).

fibers increased in thickness and length and became more branched when the ethanol content was increased to 80%.^[21] The same denaturing condition was later used to assemble fibrinogen nanofibers on silanized silicon wafers.^[22] In this study branched fibrinogen fibers were found to promote the nucleation and growth of hydroxyapatite crystals^[22] while they were previously used to aggregate gold nanoparticles along the fibers.^[21] Both studies claimed the preparation of amyloid-like fibers by ethanol denaturation since the fibers were found to be insoluble. Nevertheless, no detection of amyloid-specific characteristics by thioflavin T (ThT) staining^[112] or structural analysis by X-ray diffraction^[113] was presented to support these findings.

Organic solvents like dimethylformamide are also a major component of the well-established technique of electrospinning, which is commonly used to fabricate nanofibers from a variety of different (bio-)polymers.^[114–116] In 2003 electrospinning has been introduced for the first time to prepare nanofibrous mats from fibrinogen dissolved in a 9:1 mixture of 1,1,1,3,3,3-hexafluoro-2-propanol (HFP) and minimum essential medium (MEM).^[117] However, HFP was found to increase the α -helical content of fibrinogen by $\approx 25\%$ as compared to fibrinogen in physiological PBS solution.^[118] Since such conformational changes are often associated with protein denaturation and can lead to toxic reactions, a mixture of formic and acetic acid was recently introduced as an alternative solvent for electrospinning of fibrinogen.^[119] Even though organic solvents in combination with the high electric fields can induce denaturation during

Table 2. Buffer-driven assembly of fibrinogen (Fg) into fibers. Surface properties and associated buffer conditions, which were found to drive the assembly of fibrinogen into fibrous arrangements at different hierarchical levels.

| | Surface | Surface properties | Buffer | Metal ions | Ionic strength (molar) | pH | Fg concentration [$\mu\text{g mL}^{-1}$] | Temperature | In air/in liquid | Fiber morphology | Ref. |
|------------------------------|------------------------|--------------------|---------------------------------|---------------------------------------|------------------------|-----|--|-------------|------------------|--|-------|
| Denaturing buffer conditions | Mica | Hydrophilic | 32–76% EtOH | – | – | – | 5–50 | 37 °C | In air | Single nanofibers, nanofiber bundles, and nanofiber networks | [21] |
| | APTES-Graphene oxide | Hydrophilic | 76% EtOH | – | – | – | 20 | 37 °C | In air | Nanofiber bundles | [22] |
| | Mica | Hydrophilic | H ₂ O/HCl PBS/HCl | – Na ⁺ , K ⁺ | – 0.17 | 2 | 1–200 | 37 °C | In air | Single nanofibers, nanofiber bundles, and nanofiber networks | [20] |
| | Carbon coated TEM grid | Hydrophobic | H ₂ O/HCl | – | – | 3.6 | 4 | 37 °C | In air | Protofibrils | [110] |
| | HOPG | Hydrophobic | H ₂ O/NaCl | –/Na ⁺ | 0–0.17 | 5.5 | 1–150 | 21 °C | In air | Nanofiber networks | [111] |
| | GM-HOPG | Hydrophilic | | | | | | | In liquid | Protofibrils | |
| Non-denaturing buffers | Glass | Hydrophilic | PBS | Na ⁺ , K ⁺ | 0.07–0.75 | 7–9 | 2–5 × 10 ³ | RT | In air | Nanofiber networks | [26] |
| | | | Sodium phosphate | Na ⁺ | 0.01–0.15 | | | | | | |
| | | | NaCl | Na ⁺ | 0.38 | 7.4 | 5 × 10 ³ | | | | |
| | | | KCl | K ⁺ | 0.38 | | | | | | |
| | | | Potassium phosphate | K ⁺ | 0.05 | | | | | | |
| | APTES-coated glass | Hydrophilic | PBS | Na ⁺ , K ⁺ | 0.41 | 7.4 | 5 × 10 ³ | RT | In air | Nanofiber networks | [26] |
| | Gold | | | | | | | | | | |
| | Polystyrene | Hydrophobic | | | | | | | | | |
| | Quartz glass | Hydrophilic | PBS | Na ⁺ , K ⁺ | 0.37–0.42 | 7–9 | 2–5 × 10 ³ | RT | In air | Nanofiber networks | [25] |
| | Gold | | | | | | | | | | |

electrospinning,^[114] many studies demonstrated that electrospun fibrinogen nanofibers have great potential for tissue engineering.^[3,120] Good biocompatibility of electrospun fibrinogen fibers was found with neonatal rat cardiac fibroblasts,^[121] human bladder smooth muscle cells,^[122] endothelial cells,^[123] and human adipose derived mesenchymal stem cells.^[124] However, a major disadvantage of electrospinning is the high protein concentration of more than 100 mg mL⁻¹ required to produce nanofibrous fibrinogen scaffolds with reproducible diameters and porosity.^[3,117,125]

Acidic pH Conditions, Heating, and Protein Binding: Wei and co-workers also observed fiber assembly of fibrinogen on hydrophilic mica under acidic pH conditions.^[20] At neutral pH of 7.0 and a temperature of 37 °C varying fibrinogen concentrations were incubated with mica for 1 h, followed by air drying for 24 h. At low concentrations of 1 and 5 $\mu\text{g mL}^{-1}$ molecular fibrinogen was found to adsorb to the mica surfaces while aggregates were formed when the concentration was increased to 50 and 200 $\mu\text{g mL}^{-1}$, respectively.^[20] As soon as the pH was lowered to 2.0 the 1 and 5 $\mu\text{g mL}^{-1}$ fibrinogen solutions yielded single nanofibers and nanofiber bundles with several micrometers in length (see Figure 7A,B). Higher concentrations of 50 and 200 $\mu\text{g mL}^{-1}$ resulted in the formation of uniform nanofiber

networks.^[20] Interestingly, when the ionic strength in the acidic solution was increased to 0.17 M by adding 10×10^{-3} M phosphate and 150×10^{-3} M NaCl the assembled fibers differed in morphology. With 1 and 5 $\mu\text{g mL}^{-1}$ fibrinogen, long thin nanofibers and branched bundles were observed, which did not aggregate into thicker bundles as it was previously observed without the presence of metal ions.^[20] At high ionic strength with fibrinogen concentrations of 50 and 200 $\mu\text{g mL}^{-1}$ fibrillar networks were formed, which were less compact than without metal ions.^[20]

Recently, an acidic pH of 3.6 in combination with incubation at 37 °C for 1 h was found to induce gelation of highly concentrated fibrinogen solutions of 40 mg mL⁻¹.^[110] Analysis by transmission electron microscopy (TEM) revealed very thin, protofibril-like structures on the surface of acidic fibrinogen gels. The gels were found to be stable upon neutralization or increase in ionic strength and temperature.^[110] Likewise, Barinov and co-workers reported thermal denaturation of fibrinogen on GM-HOPG substrates upon heating to 65 or 90 °C, which resulted in the formation of fibrillar or globular aggregates.^[82] Only recently, the same group observed unfolding of fibrinogen molecules and aggregation into protofibrils on GM-HOPG substrates in the presence of the enzyme myeloperoxidase

in deionized water with a pH of 5.5.^[11] On the other hand, SEM analysis of dried fibrinogen-myeloperoxidase samples on HOPG revealed dense nanofiber networks, which resembled the dimensions and architecture of fibrinogen nanofibers prepared by our process of salt-induced self-assembly^[25,26] (see Section 3.2.2) although concentrations below 150 $\mu\text{g mL}^{-1}$ were used in this study.^[11] Barinov et al. suggested that the denaturation upon protein binding is driven by electrostatic interactions since myeloperoxidase is highly positively charged while fibrinogen is neutral at pH 5.5. Interestingly, when 171×10^{-3} M NaCl were added to the aqueous solution, absorbance spectrophotometry revealed a decline in fibrinogen aggregation. This reduced aggregation was interpreted by an increased Debye screening of charges in the electrolyte, which successively reduced the electrostatic attraction between fibrinogen and myeloperoxidase.^[11]

Overall, denaturing buffer conditions mainly induced fibrillogenesis for fibrinogen concentrations in the lower $\mu\text{g mL}^{-1}$ range whereas higher concentrations did not yield any fibers.^[20] When comparing the different buffers used during substrate- and buffer-driven fiber assembly in Tables 1 and 2 it can be seen that acidic pH values of 2 and 3.6 triggered fibrillogenesis of fibrinogen on both, hydrophobic and hydrophilic, surfaces.^[20,100] In the acidic pH regime, the fibrinogen molecule has a positive N_c (see Figure 2), which results in an extended conformation^[41] and thus promotes molecular aggregation. Although it was postulated that fibrinogen fibers, which assembled at pH 2, exhibit amyloid-like properties, no further analysis, for instance with a ThT staining, was presented to support this hypothesis.^[20] Nevertheless, it can be assumed that fiber formation at these low pH values is accompanied by fibrinogen denaturation, as it is known to occur for many other proteins.^[126–128]

With organic solvents, high temperatures or the presence of other enzymes than thrombin as alternative denaturing buffer conditions, fibrinogen fibers were also observed on hydrophilic substrates such as mica,^[21] (3-Aminopropyl)triethoxysilane (APTES)-coated graphene oxide,^[22] or GM-HOPG.^[82,111] Like acidic pH values, these buffer conditions have a tendency to completely unfold the fibrinogen molecule, thus inducing irreversible conformational changes.^[129,130] From other proteins it is already known that such denaturing factors lead to the formation of insoluble fibers.^[126,131,132] Since insoluble fibers are often associated with amyloid fibers^[133] it is very likely that denaturing buffer conditions can lead to pathogenic amyloid transitions, as postulated by Wei and co-workers.^[20]

3.2.2. Non-denaturing Buffer Conditions

In contrast to the works, which reported denaturing acidic pH to induce nanofiber assembly, we recently showed that fibrillogenesis of fibrinogen is also induced at neutral and basic pH conditions in the absence of thrombin.^[25,26] For hydrophilic substrates such as glass, quartz glass, gold, and glass with APTES modification as well as for hydrophobic PS we observed the formation of dense nanofiber networks in a pH range of 7–9 when metal ions were present during drying. SEM analysis revealed nanofibers with diameters between 100 and 300 nm, which were assembled into dense, porous networks

and thus resembled the nanoarchitecture of native fibrin clots (see Figure 7C).^[26] However, planar fibrinogen films with a very smooth surface topography were formed in the same pH range when NH_4HCO_3 buffer without any metal ions was used to dry fibrinogen at RT (see Figure 7C inset).^[26] Moreover, no fibers were observed on glass or gold at slightly acidic pH values of 5 or 6. We found that a minimum fibrinogen concentration of 2 mg mL^{-1} was required to induce fibrillogenesis and fiber networks became more dense when the concentration was raised to 5 mg mL^{-1} .^[26]

Apart from PBS other salt solutions containing bare sodium or potassium phosphate as well as NaCl and KCl also induced fiber formation upon salt-induced self-assembly.^[26] Interestingly, the ionic strength, which was associated with fiber formation, differed widely for the respective salts. With 5 mg mL^{-1} fibrinogen and pH 7.4, a minimum ionic strength of 0.07 M in PBS buffer induced fibrillogenesis, whereas a minimum ionic strength of 0.01 and 0.05 M, respectively, was required in bare sodium and potassium phosphate buffer to form fibers.^[26] However, in NaCl and KCl buffer, with 5 mg mL^{-1} fibrinogen at pH 7.4, a minimum ionic strength of 0.38 M was required to induce fiber assembly upon drying. Moreover, increasing ionic strength was found to yield higher fiber densities and coverage on hydrophilic glass substrates while the diameter of individual fibers remained unchanged.^[26]

To elucidate the role of secondary structure changes in the presence of salt buffers during drying we combined Fourier transform infrared and circular dichroism spectroscopy with morphological SEM analysis.^[25] These studies revealed that salt-induced self-assembly of fibrinogen nanofibers was accompanied by partial transitions from α -helices to β -sheets in the protein conformation. We could correlate these conformational trends with a morphological transition from planar to nanofibrous fibrinogen scaffolds, which were both found to depend on protein concentration and pH. Nevertheless, towards future applications in tissue engineering we could show with a ThT staining that the observed conformational changes were not accompanied by any pathogenic amyloid formation, which was supported by the observation that self-assembled nanofiber networks dissolved again in aqueous environment.^[25,26] Hence, a crosslinking step in formaldehyde vapor was introduced to stabilize the fibrinogen nanofibers in aqueous buffers (see Figure 7D), which did not affect the resulting secondary structure.^[25]

Interestingly, most studies that observed surface-driven fibrillogenesis of fibrinogen on hydrophobic and hydrophilic surfaces also used neutral to slightly basic pH without explicitly discussing the contribution of this parameter to fibrillogenesis (see Table 1). In this pH range fibrinogen has an overall negative N_c (see Figure 2) and is present in a compact shape,^[41] which in itself does not favor the aggregation into fibers. Accordingly, we showed that fibrinogen did not assemble into fibers at neutral to basic pH when no metal ions were present in the buffer.^[25,26] However, we reported fiber formation when the initial ionic strength in buffers of neutral pH was increased to a range of 0.01 to 0.85 M followed by a drying step.^[26] Moreover, our studies required a drying step to assemble fibrinogen nanofibers, which yielded a further increase in protein concentration and ionic strength. This observation underlines the

importance of increasing fibrinogen concentration and ionic strength for fiber assembly, as previously suggested by Jandt and co-workers.^[128] In another study, which focused on acidic buffer conditions, the Jandt group hypothesized that the presence of positively charged metal ions, such as K^+ and Na^+ , can mediate the self-assembly of fibrinogen molecules into fibers.^[20]

The particular influence of the ionic strength on fibrinogen aggregation in solution has been studied in more detail by Hämisch et al., who found fibrinogen to be very stable at physiological ionic strength while aggregation increased at lower ionic strength.^[48] They correlated the reduced aggregation probability of fibrinogen at high ionic strength with an increase in electrostatic screening that is mediated by the metal ions.^[48] This effect is also clearly visible in Figure 2 as a reduction of the total number of uncompensated charges N_c (indicated by dashed lines). Interestingly, on hydrophilic surfaces fibrinogen assembled into protofibrils at 0.007 M ionic strength^[85] or into single nanofibers at 0.33 M ionic strength^[86] when Ca^{2+} or Mg^{2+} ions were present in solution and no drying was involved. When Ca^{2+} and Zn^{2+} ions were

present during fibrinogen adsorption to hydrophilic glass surfaces these divalent ions favored the formation of nodular rod-like fibrinogen assemblies while monovalent K^+ or Na^+ ions yielded branched aggregates.^[134] Although we could already show that our novel self-assembly method to prepare fibrinogen fibers provides good control of several relevant parameters governing the fibrinogen assembly,^[25,26] more fundamental insight into parameters like ion charge and size, pH or fibrinogen concentration is required to understand the in vitro mechanisms that lead to fiber formation of fibrinogen.

4. Conclusion and Future Perspectives

Based on our findings in Tables 1 and 2 we have categorized the manifold factors leading to fibrillogenesis of fibrinogen in vitro into different groups and summarized them graphically in Figure 8. The categorization we introduced in our review shows that there are many experimental conditions and parameters that trigger the self-assembly of fibrinogen, which can either

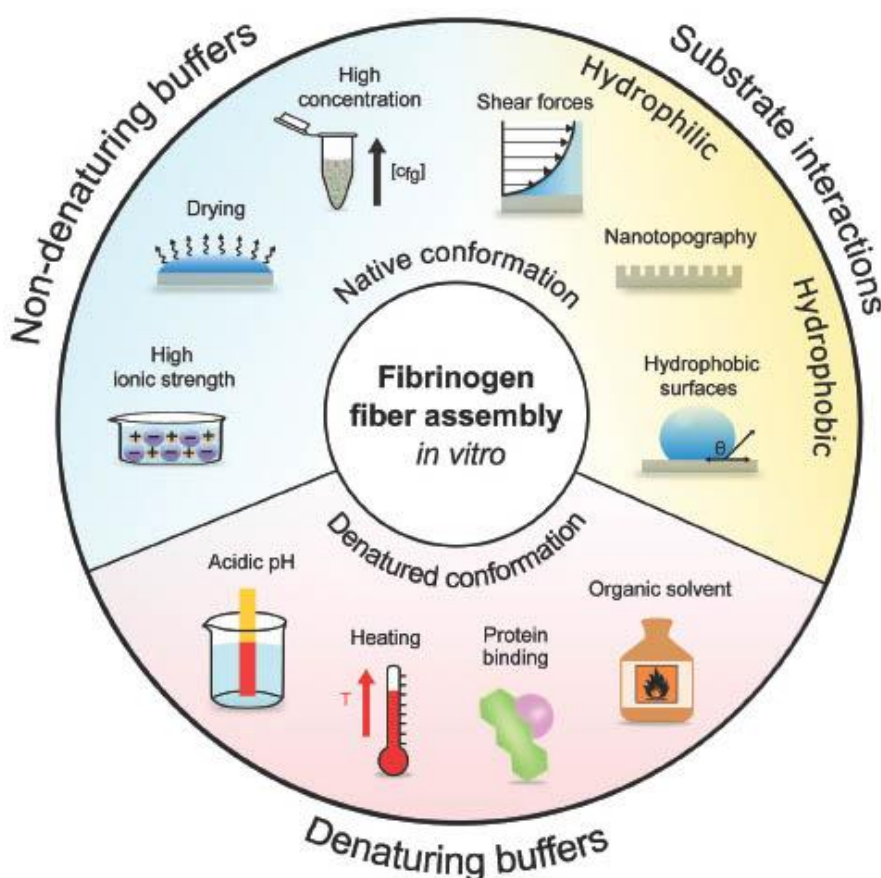


Figure 8. Schematic representation of in vitro conditions that favor fiber assembly of fibrinogen. Denaturing buffer conditions (red field) induce irreversible structural changes in the fibrinogen molecule leading to complete unfolding and denaturation, often including the central coiled-coil structures, which favors the assembly of insoluble fibrinogen fibers. Substrate interactions (yellow field) together with non-denaturing buffers (blue field) are mostly associated with a reversible extension of the fibrinogen molecule and mainly lead to the formation of soluble fibrinogen fibers.

maintain the native conformation of fibrinogen or denature the molecule. Accordingly, we have divided the main process-related driving forces for in vitro fibrillogenesis of fibrinogen into three major categories:

- denaturing buffers, leading to complete unfolding and irreversible changes in the conformation of fibrinogen molecules, which often result in the formation of insoluble fibrinogen fibers,
- substrate interactions comprising hydrophobic and hydrophilic surfaces, both interacting with fibrinogen molecules to induce fiber formation while maintaining a more native conformation,
- non-denaturing buffers, which favor the self-assembly of fibrinogen molecules into soluble fibrinogen fibers without inducing irreversible conformational changes.

Nevertheless, since all studies we discussed in this review were conducted involving different surfaces, it cannot be concluded unambiguously whether the mentioned buffer conditions are the sole driving force of fibrinogen fiber assembly. A detailed comparison of Tables 1 and 2 and in particular of our recent studies^[25,26] strengthens the hypothesis that monovalent metal ions play a major role when fibrinogen fibers assemble upon drying. Nevertheless, it will be important to also investigate the particular role of divalent ions during drying of fibrinogen solutions at varying pH values in comparison to the influence of monovalent ions. These studies will provide fundamental insight into the respective role of ion charge and size to understand possible steric constraints during the assembly of fibrinogen fibers. For future studies on fibrinogen fibrillogenesis, it will therefore be important to understand whether the presence of metal ions plays a predominant role compared to different surface properties, which will also require more extensive control experiments.

Based on our meta-analysis of the multiple factors that induce fibrillogenesis of fibrinogen under in vitro conditions, it becomes evident that a more thorough understanding of the underlying mechanisms is needed to develop fibrous, fibrinogen-based biomaterials with tailored morphology, biological activity, and defined degradation profiles. These characteristics will be important to use fibrinogen nanofibers, for instance, as novel wound dressing materials, co-culture systems, for blood vessel replacement or to support stem cell differentiation. Although the available literature on fibrinogen fiber assembly is very scattered, we could identify increased fibrinogen concentration and ionic strength as key parameters to favor fiber assembly. On the other hand, it remains elusive whether specific surface characteristics play a major role in fiber assembly since fibers were formed on both, hydrophilic and hydrophobic surfaces. Hence, in future studies, it will be important to understand whether individual parameters trigger the assembly of soluble fibrinogen into solid fibers or whether several conditions might actually be interrelated and jointly responsible for the fibrillogenesis of fibrinogen in vitro.

To understand the respective influence of individual in vitro conditions on fibrillogenesis in detail, further experimental studies on the intermolecular interaction of fibrinogen are required. These studies would benefit from recombinant

constructs that lack specific regions of the fibrinogen molecule to study their particular involvement in fibrillogenesis. Moreover, MD simulations will offer a powerful addition to these experimental studies to unravel the atomistic principles of fibrinogen assembly into fibers. Understanding the fundamental principles of these multiscale mechanisms during fibrinogen fibrillogenesis will be crucial to design functional tissue engineering scaffolds and biomaterial surfaces for personalized medicine that do not evoke any pathogenic or thrombotic reactions.

Acknowledgements

St.S. gratefully acknowledges funding of the internal program Fraunhofer TALENTA start and A.J. and D.B. were supported by the Emmy Noether program of the German Research Council (DFG) under grant number BR 5043/1-1.

Open access funding enabled and organized by Projekt DEAL.

Conflict of Interest

The authors declare no conflict of interest.

Keywords

blood coagulation, nanofibers, protein aggregation, self-assembly, tissue engineering scaffolds, wound healing

Received: December 4, 2020

Revised: January 15, 2021

Published online:

- [1] L. Rodríguez-Arco, A. Poma, L. Ruiz-Pérez, E. Scarpa, K. Ngamkham, G. Battaglia, *Biomaterials* **2019**, *192*, 26.
- [2] T.A. E. Ahmed, E. V. Dare, M. Hincke, *Tissue Eng., Part B* **2008**, *14*, 199.
- [3] T. Rajangam, S. S. A. An, *Int. J. Nanomed.* **2013**, *8*, 3641.
- [4] J. Y. Joo, Md. L. Amin, T. Rajangam, S. S. A. An, *Mol. Cell. Toxicol.* **2015**, *11*, 1.
- [5] K. A. Rieger, N. P. Birch, J. D. Schiffman, *J. Mater. Chem. B* **2013**, *1*, 4531.
- [6] S. Chen, B. Liu, M. A. Carlson, A. F. Gombart, D. A. Reilly, J. Xie, *Nanomedicine* **2017**, *12*, 1335.
- [7] D. M. Vasconcelos, R. M. Gonçalves, C. R. Almeida, I. O. Pereira, M. I. Oliveira, N. Neves, A. M. Silva, A. C. Ribeiro, C. Cunha, A. R. Almeida, C. C. Ribeiro, A. M. Gil, E. Seebach, K. L. Kynast, W. Richter, M. Lamghari, S. G. Santos, M. A. Barbosa, *Biomaterials* **2016**, *111*, 163.
- [8] E. V. Solovieva, A. Y. Fedotov, V. E. Mamonov, V. S. Komlev, A. A. Panteleyev, *Biomed. Mater.* **2018**, *13*, 025007.
- [9] R. A. S. Ariens, *J. Thromb. Haemostasis* **2013**, *11*, 294.
- [10] L. Zhang, B. Casey, D. K. Galanakis, C. Marmorat, S. Skoog, K. Vorvolakos, M. Simon, M. H. Rafailovich, *Acta Biomater.* **2017**, *54*, 164.
- [11] L. C. Serpell, M. Benson, J. J. Liepnieks, P. E. Fraser, *Amyloid* **2007**, *14*, 199.
- [12] M. Cortes-Canteli, J. Paul, E. H. Norris, R. Bronstein, H. J. Ahn, D. Zamolodchikov, S. Bhuvanendran, K. M. Fenz, S. Strickland, *Neuron* **2010**, *66*, 695.

- [13] H. J. Ahn, D. Zamolodchikov, M. Cortes-Canteli, E. H. Norris, J. F. Glickman, S. Strickland, *Proc. Natl. Acad. Sci. U. S. A.* **2010**, *107*, 21812.
- [14] F. Chiti, C. M. Dobson, *Annu. Rev. Biochem.* **2017**, *86*, 27.
- [15] G. Wei, Z. Su, N. P. Reynolds, P. Arosio, I. W. Hamley, E. Gazit, R. Mezzenga, *Chem. Soc. Rev.* **2017**, *46*, 4661.
- [16] D. Pinotsi, A. K. Buell, C. Galvagnion, C. M. Dobson, G. S. Kaminski Schierle, C. F. Kaminski, *Nano Lett.* **2014**, *14*, 339.
- [17] L. O. Tjernberg, A. Rising, J. Johansson, K. Jaudszems, P. Westermark, *J. Intern. Med.* **2016**, *280*, 153.
- [18] J. Reichert, G. Wei, K. D. Jandt, *Adv. Eng. Mater.* **2009**, *11*, 8177.
- [19] J. Koo, D. Galanakis, Y. Liu, A. Ramek, A. Fields, X. Ba, M. Simon, M. H. Rafailovich, *Biomacromolecules* **2012**, *13*, 1259.
- [20] G. Wei, J. Reichert, J. Bossert, K. D. Jandt, *Biomacromolecules* **2008**, *9*, 3258.
- [21] G. Wei, J. Reichert, K. D. Jandt, *Chem. Commun.* **2008**, 3903.
- [22] J. Wang, H. Wang, Y. Wang, J. Li, Z. Su, G. Wei, *J. Mater. Chem. B* **2014**, *2*, 7360.
- [23] R. N. Palchesko, Y. Sun, L. Zhang, J. M. Szymanski, Q. Jallerat, A. W. Feinberg, *Springer Handbook of Nanomaterials*, Springer, Berlin Heidelberg **2013**, p. 977.
- [24] C. P. Barnes, S. A. Sell, E. D. Boland, D. G. Simpson, G. L. Bowlin, *Adv. Drug Delivery Rev.* **2007**, *59*, 1413.
- [25] K. Stapelfeldt, S. Stamboroski, I. Walter, N. Suter, T. Kowalik, M. Michaelis, D. Brüggemann, *Nano Lett.* **2019**, *49*, 6554.
- [26] K. Stapelfeldt, S. Stamboroski, P. Mednikova, D. Brüggemann, *Biofabrication* **2019**, *11*, 025010.
- [27] J. W. Weisel, *Adv. Protein Chem.* **2005**, *70*, 247.
- [28] R. F. Doolittle, *Sci. Am.* **1981**, *245*, 126.
- [29] J. W. Weisel, R. I. Litvinov, *Subcell. Biochem.* **2017**, *82*, 405.
- [30] L. Medved, J. W. Weisel, *J. Thromb. Haemostasis* **2009**, *7*, 355.
- [31] M. W. Mosesson, K. R. Siebenlist, D. A. Meh, *Ann. N. Y. Acad. Sci.* **2001**, *936*, 11.
- [32] M. W. Mosesson, *J. Thromb. Haemostasis* **2005**, *3*, 1894.
- [33] R. F. Doolittle, *Annu. Rev. Biochem.* **1984**, *53*, 195.
- [34] R. F. Doolittle, D. M. Goldbaum, L. R. Doolittle, *J. Mol. Biol.* **1978**, *120*, 311.
- [35] G. Spraggon, S. J. Everse, R. F. Doolittle, *Nature* **1997**, *390*, 315.
- [36] R. A. Burton, G. Tsurupa, L. Medved, N. Tjandra, *Biochemistry* **2006**, *46*, 6674.
- [37] Y. I. Veklich, O. V. Gorkun, L. V. Medved, W. Nieuwenhuizen, J. W. Weisel, *J. Biol. Chem.* **1993**, *268*, 13577.
- [38] O. V. Gorkun, Y. I. Veklich, L. V. Medved, A. H. Henschen, J. W. Weisel, *Biochemistry* **1994**, *33*, 6986.
- [39] C. Duval, A. Profumo, A. Aprile, A. Salis, E. Millo, G. Damonte, J. S. Gauer, R. A. S. Ariens, M. Rocco, *J. Thromb. Haemostasis* **2020**, *18*, 802.
- [40] J. M. Kollman, L. Pandi, M. R. Sawaya, M. Riley, R. F. Doolittle, *Biochemistry* **2009**, *48*, 3877.
- [41] M. Wasilewska, Z. Adamczyk, B. Jachimska, *Langmuir* **2009**, *25*, 3698.
- [42] Z. Adamczyk, B. Cichocki, M. L. Ekiel-Jezewska, A. Słowicka, E. Wajnryb, M. Wasilewska, *J. Colloid Interface Sci.* **2012**, *385*, 244.
- [43] C. E. Hall, H. S. Slayter, *J. Biophys. Biochem. Cytol.* **1959**, *5*, 11.
- [44] M. Cieśla, Z. Adamczyk, J. Barbasz, M. Wasilewska, *Langmuir* **2013**, *29*, 7005.
- [45] Y. F. Zuev, R. I. Litvinov, A. E. Sitnitsky, B. Z. Idiyatullin, D. R. Bakirova, D. K. Galanakis, A. Zhmurov, V. Barsegov, J. W. Weisel, *J. Phys. Chem. B* **2017**, *121*, 7833.
- [46] B. Raynal, B. Cardinali, J. Grimbergen, A. Profumo, S. T. Lord, P. England, M. Rocco, *Thromb. Res.* **2013**, *132*, e48.
- [47] S. H. Kim, L. Haimovich-Caspi, L. Omer, C.-M. Yu, Y. Talmon, N.-H. L. Wang, E. I. Frances, *Langmuir* **2007**, *23*, 5657.
- [48] B. Hämsch, A. Büngeler, C. Kieler, A. Keller, O. Strube, K. Huber, *Langmuir* **2019**, *35*, 12113.
- [49] I. Van De Keere, R. Willaert, A. Hubin, J. Vereecken, *Langmuir* **2008**, *24*, 1844.
- [50] R. F. Doolittle, K. W. K. Watt, B. A. Cottrell, D. D. Strong, M. Riley, *Nature* **1979**, *280*, 464.
- [51] J. W. Weisel, L. Medved, *Ann. N. Y. Acad. Sci.* **2001**, *936*, 312.
- [52] T. C. Ta, M. T. Sykes, M. T. McDermott, *Langmuir* **1998**, *14*, 2435.
- [53] M. Wasilewska, Z. Adamczyk, *Langmuir* **2011**, *27*, 686.
- [54] Z. Adamczyk, A. Bratek-Skicki, P. Dąbrowska, M. Nattich-Rak, *Langmuir* **2012**, *28*, 474.
- [55] E. Seyrek, P. L. Dubin, C. Tribet, E. A. Gamble, *Biomacromolecules* **2003**, *4*, 273.
- [56] A. Dukhin, S. Dukhin, P. Goetz, *Langmuir* **2005**, *21*, 9990.
- [57] T. J. Lewis, *J. Phys. D: Appl. Phys.* **2005**, *38*, 202.
- [58] T. Abe, E. Sheppard, I. S. Wright, *J. Phys. Chem.* **1955**, *59*, 266.
- [59] S. Köhler, F. Schmid, G. Settanni, *Langmuir* **2015**, *31*, 13180.
- [60] K. Hyltegren, M. Hulander, M. Andersson, M. Skepö, *Biomolecules* **2020**, *10*, 413.
- [61] S. Köhler, F. Schmid, G. Settanni, *PLoS Comput. Biol.* **2015**, *11*, e1004346.
- [62] Ž. Sovová, J. Štikarová, J. Kaufmanová, P. Májek, J. Suttnar, P. Šácha, M. Malý, J. E. Dyr, *PLoS One* **2020**, *15*, e0227543.
- [63] T. J. Dolinsky, J. E. Nielsen, J. A. McCammon, N. A. Baker, *Nucleic Acids Res.* **2004**, *32*, W665.
- [64] N. A. Baker, D. Sept, S. Joseph, M. J. Holst, J. A. McCammon, *Proc. Natl. Acad. Sci. U. S. A.* **2001**, *98*, 10037.
- [65] W. Humphrey, A. Dalke, K. Schulten, *J. Mol. Graphics* **1996**, *14*, 33.
- [66] A. P. Laudano, R. F. Doolittle, *Biochemistry* **1980**, *19*, 1013.
- [67] V. C. Yee, K. P. Pratt, H. C. Côté, I. L. Trong, D. W. Chung, E. W. Davie, R. E. Stenkamp, D. C. Teller, *Structure* **1997**, *5*, 125.
- [68] J. D. Ferry, *Proc. Natl. Acad. Sci. U. S. A.* **1952**, *38*, 566.
- [69] H. P. Erickson, W. E. Fowler, *Ann. N. Y. Acad. Sci.* **1983**, *408*, 146.
- [70] M. Rocco, M. Molteni, M. Ponassi, G. Giachi, M. Frediani, A. Koutsoubas, A. Profumo, D. Trevarin, B. Cardinali, P. Vachette, F. Ferri, J. Pérez, *J. Am. Chem. Soc.* **2014**, *136*, 5376.
- [71] Z. Yang, I. Mochalkin, R. F. Doolittle, *Proc. Natl. Acad. Sci. U. S. A.* **2000**, *97*, 14156.
- [72] C. B. Geer, A. Tripathy, M. H. Schoenfisch, S. T. Lord, O. V. Gorkun, *J. Thromb. Haemostasis* **2007**, *5*, 2344.
- [73] S. E. Stabenfeldt, J. J. Gossett, T. H. Barker, *Blood* **2010**, *116*, 1352.
- [74] B. Dutta, B. E. Vos, Y. L. A. Rezus, G. H. Koenderink, H. J. Bakker, *J. Phys. Chem. B* **2018**, *122*, 5870.
- [75] R. I. Litvinov, D. A. Faizullin, Y. F. Zuev, J. W. Weisel, *Biophys. J.* **2012**, *103*, 1020.
- [76] J.-P. Collet, J. L. Moen, Y. I. Veklich, O. V. Gorkun, S. T. Lord, G. Montalescot, J. W. Weisel, *Blood* **2005**, *106*, 3824.
- [77] J. M. Reinke, H. Sorg, *Eur. Surg. Res.* **2012**, *49*, 35.
- [78] N. Laurens, P. Koolwijk, M. P. M. De Maat, *J. Thromb. Haemostasis* **2006**, *4*, 932.
- [79] T. H. Barker, A. J. Engler, *Matrix Biol.* **2017**, *60–61*, 1.
- [80] A. Sahni, T. Odrjic, C. W. Francis, *J. Biol. Chem.* **1998**, *273*, 7554.
- [81] I. K. Piechocka, N. A. Kurniawan, J. Grimbergen, J. Koopman, G. H. Koenderink, *J. Thromb. Haemostasis* **2017**, *15*, 938.
- [82] N. A. Barinov, A. D. Protopopova, E. V. Dubrovin, D. V. Klinov, *Colloids Surf., B* **2018**, *167*, 370.
- [83] C. Helbing, R. Stoeßel, D. A. Hering, M. M. L. Arras, J. Bossert, K. D. Jandt, *Langmuir* **2016**, *32*, 11868.
- [84] J. Koo, M. H. Rafailovich, L. Medved, G. Tsurupa, B. J. Kudryk, Y. Liu, D. K. Galanakis, *J. Thromb. Haemostasis* **2010**, *8*, 2727.
- [85] E. V. Dubrovin, N. A. Barinov, T. E. Schäffer, D. V. Klinov, *Langmuir* **2019**, *35*, 9732.
- [86] G. Chen, N. Ni, B. Wang, B. Xu, *ChemPhysChem* **2011**, *11*, 565.
- [87] M. Raoufi, N. Aslankoobi, C. Mollenhauer, H. Boehm, J. P. Spatz, D. Brüggemann, *Integr. Biol.* **2016**, *8*, 1059.
- [88] D. Coglitore, J.-M. Janot, S. Balme, *Adv. Colloid Interface Sci.* **2019**, *270*, 278.

- [89] P. Roach, D. Farrar, C. C. Perry, *J. Am. Chem. Soc.* **2005**, *127*, 8168.
- [90] N. A. Barinov, V. V. Prokhorov, E. V. Dubrovin, D. V. Klinov, *Colloids Surf., B* **2016**, *146*, 777.
- [91] L. Xu, A. Lio, J. Hu, D. F. Ogletree, M. Salmeron, *J. Phys. Chem. B* **1998**, *102*, 540.
- [92] R. F. Doolittle, K. W. K. Watt, B. A. Cottrell, D. D. Strong, M. Riley, *Nature* **1979**, *280*, (5722), 464.
- [93] K. L. Marchin, C. L. Berrie, *Langmuir* **2003**, *19*, 9883.
- [94] T. S. Tsapikouni, Y. F. Missirlis, *Colloids Surf., B* **2007**, *57*, 89.
- [95] Y. Hu, J. Jin, H. Liang, X. Ji, J. Yin, W. Jiang, *Langmuir* **2016**, *32*, 4086.
- [96] A. Agnihotri, C. A. Siedlecki, *Langmuir* **2004**, *20*, 8846.
- [97] P. S. Sit, R. Marchant, *Thromb. Haemostasis* **1999**, *82*, 1053.
- [98] M. L. Clarke, J. Wang, Z. Chen, *J. Phys. Chem. B* **2005**, *109*, 22027.
- [99] M. L. Rudee, T. M. Price, *J. Biomed. Mater. Res.* **1985**, *19*, 57.
- [100] A. Hurllet-Jensen, J. A. Koehn, H. L. Nossel, *Thromb. Res.* **1983**, *29*, 609.
- [101] N. Dragneva, O. Rubel, W. B. Floriano, *J. Chem. Inf. Mod.* **2016**, *56*, 706.
- [102] X. Zhang, I. Firkowska-Boden, M. M. L. Arras, M. J. Kastantin, C. Helbing, A. Özogul, E. Gnecco, D. K. Schwartz, K. D. Jandt, *Langmuir* **2018**, *34*, 14309.
- [103] T. Guo, K. Han, L. Heng, M. Cao, L. Jiang, *RSC Adv.* **2015**, *5*, 88471.
- [104] M. Raoufi, T. Das, I. Schoen, V. Vogel, D. Brüggemann, J. P. Spatz, *Nano Lett.* **2015**, *15*, 6357.
- [105] Z. Bai, M. J. Filiaggi, J. R. Dahn, *Surf. Sci.* **2009**, *603*, 839.
- [106] M. Nattich-Rak, Z. Adamczyk, M. Wasilewska, M. Sadowska, *Langmuir* **2013**, *29*, 11991.
- [107] R. I. Litvinov, S. Yakovlev, G. Tsurupa, O. V. Gorkun, L. Medved, J. W. Weisel, *Biochemistry* **2007**, *46*, 9133.
- [108] M. Agashe, V. Raut, S. J. Stuart, R. A. Latour, *Langmuir* **2005**, *21*, 1103.
- [109] K. Kubiak, Z. Adamczyk, M. Wasilewska, *J. Colloid Interface Sci.* **2015**, *457*, 378.
- [110] C. Rieu, *et al.*, **2020**, *1*, <https://doi.org/10.1101/2020.05.12.091793>.
- [111] N. A. Barinov, E. R. Pavlova, A. P. Tolstova, E. V. Dubrovin, D. V. Klinov, *bioRxiv* **2021**, <https://doi.org/10.1101/2021.01.06.425586>.
- [112] M. Biancalana, S. Koide, *Biochim. Biophys. Acta, Proteins Proteomics* **2010**, *1804*, 1405.
- [113] K. L. Morris, L. C. Serpell, *Methods Mol. Biol.* **2012**, *849*, 121.
- [114] R. N. Palchesko, Y. Sun, L. Zhang, J. M. Szymanski, Q. Jallerat, A. W. Feinberg, *Springer Handbook Nanomaterials*, (Eds:R. Vajtai) Springer, Berlin, Heidelberg **2013**, Nanofiber Biomaterials 977.
- [115] J. Xie, X. Li, Y. Xia, *Macromol. Rapid Commun.* **2008**, *29*, 1775.
- [116] A. Haider, S. Haider, I.-K. Kang, *Arab J. Chem.* **2018**, *11*, 1165.
- [117] G. E. Wnek, M. E. Carr, D. G. Simpson, G. L. Bowlin, *Nano Lett.* **2003**, *3*, 213.
- [118] C. R. Carlisle, C. Coulais, M. Namboothiry, D. L. Carroll, R. R. Hantgan, M. Guthold, *Biomaterials* **2009**, *30*, 1205.
- [119] M. J. Mirzaei-Parsa, A. Ghanizadeh, M. T. K. Ebadi, R. Faridi-Majidi, *Biomed. Mater. Eng.* **2018**, *29*, 279.
- [120] SellS. A. , Francis M. P. , GargK. , McClureM. J. , SimpsonD. G. , BowlinG. L. , *Biomedical Materials* **2008**, *3*, (4), 045001.
- [121] M. Li, M. J. Mondrinos, X. Chen, M. R. Gandhi, F. K. Ko, P. I. Lelkes, *J. Biomed. Mater. Res., Part A* **2006**, *79A*, 963.
- [122] M. Mcmanus, E. Boland, S. Sell, W. Bowen, H. Koo, D. Simpson, G. Bowlin, *Biomed. Mater.* **2007**, *2*, 257.
- [123] D. Gugutkov, J. Gustavsson, M. P. Ginebra, G. Altankov, *Biomater. Sci.* **2013**, *1*, 1065.
- [124] J. Forget, F. Awaja, D. Gugutkov, J. Gustavsson, G. Gallego Ferrer, T. Coelho-Sampaio, C. Hochman-Mendez, M. Salmeron-Sánchez, G. Altankov, *Macromol. Biosci.* **2016**, *16*, 1348.
- [125] M. C. Mcmanus, E. D. Boland, H. P. Koo, C. P. Barnes, K. J. Pawlowski, G. E. Wnek, D. G. Simpson, G. L. Bowlin, *Acta Biomater.* **2006**, *2*, 19.
- [126] M. Mališauskas, V. Zamotin, J. Jass, W. Noppe, C. M. Dobson, L. A. Morozova-Roche, *J. Mol. Biol.* **2003**, *330*, 879.
- [127] A.-S. Yang, B. Honig, *J. Mol. Biol.* **1993**, *231*, 459.
- [128] C. Tanford, R. Roxby, *Biochemistry* **1972**, *11*, 2192.
- [129] R. W. Hartley, D. F. Waugh, *J. Am. Chem. Soc.* **1960**, *82*, 978.
- [130] G. Marx, X. Mou, A. Hotovely-Salomon, L. Levdansky, E. Gaberman, D. Belenky, R. Gorodetsky, *J. Biomed. Mater. Res., Part B* **2008**, *84B*, 49.
- [131] C. M. Bryant, D. J. McClements, *Trends Food Sci. Technol.* **1998**, *9*, 143.
- [132] C. Lara, S. Gourdin-Bertin, J. Adamcik, S. Bolisetty, R. Mezzenga, *Biomacromolecules* **2012**, *13*, 4213.
- [133] B. H. Toyama, J. S. Weissman, *Annu. Rev. Biochem.* **2011**, *80*, 557.
- [134] K. Sankaranarayanan, A. Dhathathreyan, R. Miller, *J. Phys. Chem. B* **2010**, *114*, 8067.



Stephani Stamboroski is a Ph.D. student in the Fraunhofer Institute for Manufacturing Technology and Advanced Materials IFAM and in the group for nanoBiomaterials in the Institute for Biophysics at the University of Bremen, Germany. She studied Chemistry at the Federal University of Santa Catarina, Brazil and acquired an M.Sc. degree in Materials Chemistry and Mineralogy in the University of Bremen in 2019. Her current research focuses on investigating the potential of nanofibrous fibrinogen as biomimetic scaffold material to promote tailored interactions with other molecular key players involved in wound healing.



Arundhati Joshi received her Bachelor's degree in Microbiology from University of Pune, India. After obtaining her Master's degree in Biochemistry and Molecular Biology from the University of Bremen, Germany, she went on to pursue her Ph.D. at the Neurobiochemistry research group at the University of Bremen, Germany. After completing her Ph.D. in 2019, she joined the nanoBio-materials research group as a postdoc at the Institute for Biophysics at the University of Bremen, Germany. Her research focuses on understanding the interactions between cells and multifunctional protein scaffolds for future wound healing applications.



Paul-Ludwig Michael Noeske studied Chemistry at Ulm University, Germany and performed his Ph.D. thesis in the department surface chemistry and catalysis. In 2001 he joined the Fraunhofer Institute for Manufacturing Technology and Advanced Materials IFAM, Bremen, Germany, and holds a position as a research associate in the department Adhesion and Interface Research. In 2003, he passed a vocational training as DVS/EWF (Deutscher Verband für Schweißen und verwandte Verfahren e.V. / European Federation for Welding, Joining and Cutting) - European Adhesive Engineer. Since 2004, he frequently realizes lectureships at the University of Applied Sciences Bremerhaven, Germany, in Adhesive Bonding Technology, Surface Technology or Medical Engineering. His scale-comprehensive research ranges from interfacants to formation and long-term behavior of polymer/oxide interphases.



Susan Köppen studied Biochemistry at the University of Greifswald, Germany. After her Ph.D. in Physical Chemistry, she joined the Hybrid Materials Interfaces Group at the University of Bremen, Germany with a DFG young researchers award for "Grenzflächen und grenzflächen-dominierenden Prozesse." In this department, she established herself as a group leader with a strong focus on biomolecular modeling and modeling at solid liquid interfaces.



Dorothea Brüggemann studied Physics at the University of Bonn and RWTH Aachen University, Germany. After her Ph.D. in Biophysics at the Forschungszentrum Jülich, Germany, she was a postdoc at Trinity College Dublin, Ireland and a project leader at the Max Planck Institute for Intelligent Systems in Stuttgart, Germany. In 2016 she was awarded a DFG Emmy Noether grant to establish her independent research group for nanoBiomaterials in the Institute for Biophysics at the University of Bremen, Germany. Her interdisciplinary research focuses on the development of new biomaterials and processes to prepare multifunctional scaffolds for controlling cell interactions.

3. INFLUENCE OF DIVALENT CATIONS ON THE PRECIPITATION OF THE PLASMA PROTEIN FIBRINOGEN

Status: Paper published at *Biomacromolecules* (2021).

"Reprinted with permission from *Biomacromolecules* 2021, 22, 11, 4642–4658. Copyright 2021 American Chemical Society."

Stamboroski, S., Boateng, K., Lierath, J., Kowalik, T., Thiel, K., Köppen, S., Noeske, P. L. M, & Brüggemann, D. (2021). Influence of divalent metal ions on the precipitation of the plasma protein fibrinogen. *Biomacromolecules*, 22(11), 4642-4658.

DOI: [10.1021/acs.biomac.1c00930](https://doi.org/10.1021/acs.biomac.1c00930)

3.1. MOTIVATION & HYPOTHESIS

Hypothesis addressed: Divalent cations induce assembly of fibrinogen into nanofibers.

The many factors leading to fibrinogen self-assembly *in vitro* were presented in Chapter 2. Ionic strength, pH and fibrinogen concentration were identified as key parameters in fiber formation. In many previous studies the presence of metal ions showed to be an indispensable factor in fibrinogen fiber self-assembly. For instance, in the works from Stapelfeldt et al. well defined and densely formed nanofibers were observed when fibrinogen was precipitated in the presence of high ionic strength solutions of monovalent ions. However, other metal ions with double charge have not been tested on their capacity to form the same type of fibrinogen fibers. It is known that divalent metal ions as Ca^{2+} , Mg^{2+} , Cu^{2+} , and Zn^{2+} present in the human body are involved in blood coagulation and wound healing, which are also key functions of fibrinogen. Chapter 3 presents the study of the influence of selected divalent metal ions on the self-assembly and precipitation of fibrinogen in *in vitro* conditions without the addition of the enzyme thrombin.

Hypothesis assessment: Refuted. Findings support the conclusion that under experimental conditions of Chapter 2 divalent cations do not induce assembly of fibrinogen into nanofibers.



pubs.acs.org/Biomac

Article

Influence of Divalent Metal Ions on the Precipitation of the Plasma Protein Fibrinogen

Stephani Stamboroski, Kwasi Boateng, Jana Lierath, Thomas Kowalik, Karsten Thiel, Susan Köppen, Paul-Ludwig Michael Noeske, and Dorothea Brüggemann*

Cite This: *Biomacromolecules* 2021, 22, 4642–4658

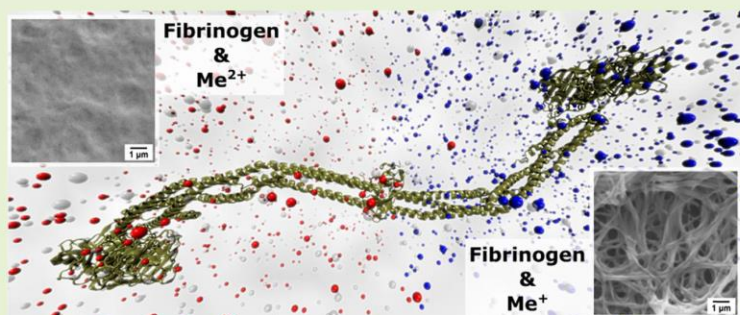
Read Online

ACCESS |

Metrics & More

Article Recommendations

Supporting Information



ABSTRACT: Fibrinogen nanofibers are very attractive biomaterials to mimic the native blood clot architecture. Previously, we reported the self-assembly of fibrinogen nanofibers in the presence of monovalent salts and have now studied how divalent salts influence fibrinogen precipitation. Although the secondary fibrinogen structure was significantly altered with divalent metal ions, morphological analysis revealed exclusively smooth fibrinogen precipitates. *In situ* monitoring of the surface roughness facilitated predicting the tendency of various salts to form fibrinogen fibers or smooth films. Analysis of the chemical composition revealed that divalent salts were removed from smooth fibrinogen films upon rinsing while monovalent Na^+ species were still present in fibrinogen fibers. Therefore, we assume that the decisive factor controlling the morphology of fibrinogen precipitates is direct ion–protein contact, which requires disruption of the ion-surrounding hydration shells. We conclude that in fibrinogen aggregates, this mechanism is effective only for monovalent ions, whereas divalent ions are limited to indirect fibrinogen adsorption.

1. INTRODUCTION

Many key functions of the dimeric plasma protein fibrinogen in contributing to blood coagulation and wound healing are controlled by divalent metal ions.¹ The thrombin-induced conversion of fibrinogen to a nanofibrous fibrin clot is initiated by the presence of Ca^{2+} ions.¹ This blood clot provides a provisional extracellular matrix (ECM), into which endothelial cells and fibroblasts migrate to assemble a new ECM by depositing fibronectin and collagen.² Therefore, fibrous fibrinogen scaffolds have become particularly attractive materials to support cell growth in regenerative medicine.^{3,4} A prerequisite for cell proliferation is the integrin-mediated adhesion to the Arg-Gly-Asp (RGD) binding site of fibrinogen, which is activated by divalent ions including Ca^{2+} , Mg^{2+} , and Mn^{2+} cations.⁵ Besides cell signaling, molecular binding of fibrinogen is driven by divalent ions, for instance, the Zn^{2+} -dependent interaction of fibrinogen with decorin⁶ or the involvement of Cu^{2+} ions in the formation of heparin-fibrinogen complexes.⁷ Moreover, Cu^{2+} ions are involved in wound healing where they stabilize fibrinogen and collagen by activating

proangiogenic growth factors, such as vascular endothelial growth factor (VEGF) and fibroblast growth factor (FGF) 1 and 2.^{8,9} The concentration of divalent ions in blood plasma typically varies from 2.2 to 2.7 mM for Ca^{2+} ,¹⁰ from 0.75 to 1 mM for Mg^{2+} ,¹¹ from 16 to 24 μM for Cu^{2+} ,¹² and from only 10 to 11.5 μM for Zn^{2+} .¹³

Under *in vitro* conditions, divalent metal ions were also found to influence fibrinogen aggregation in aqueous solutions.^{14,15} While Ca^{2+} , Mg^{2+} , and Mn^{2+} ions were not effective up to 10 mM¹⁵ or did not induce any aggregation at all,¹⁴ Cu^{2+} and Zn^{2+} ions already caused fibrinogen aggregation at salt concentrations below 10 mM.¹⁴ This aggregation behavior was also found to depend on fibrinogen concentration, ionic strength, and pH.¹⁵

Received: July 20, 2021

Revised: September 30, 2021

Published: October 20, 2021



ACS Publications

© 2021 The Authors. Published by American Chemical Society

4642

<https://doi.org/10.1021/acs.biomac.1c00930>
Biomacromolecules 2021, 22, 4642–4658

The difference in critical aggregation concentration of fibrinogen in the presence of different divalent cations might be explained by salting out or salting in effects, which are closely related to the Hofmeister series.¹⁶ In protein biochemistry, this classification describes the general tendency of proteins to aggregate in the presence of ions with varying charges and concentrations.¹⁶ Protein aggregates formed in salt solutions can be additionally stabilized or destabilized by salt bridges.¹⁷ At high salt concentrations exceeding 1 M, polar electron pair acceptor/donor (*i.e.*, Lewis acid/base) interactions also become important and may override electrostatic contributions during protein aggregation.^{18–20} In particular, for fibrinogen assembly and fibrillogenesis to occur at ionic saturation, pairwise interactions between Lewis acids and bases may dominate the dynamics of protein–protein interactions.

Austin et al. have recently reported that among other effects faced when approaching ionic saturation, the steric hindrance between ions, ion–ion pair correlations, the solvation shell around an ion, the ordering of water molecules in the interfacial layer, and notably the possibility of a zero charge due to the ion-specific penetration of a structured water layer at a particle surface need to be taken into consideration.²¹ However, experimental findings achieved for the influence of ions on protein aggregation, conformation, or altered morphology in aqueous media are discussed with a focus on differences in effects of the relative ion concentrations and often are limited to the Hofmeister series.²² Comprehensive considerations on concepts governing Hofmeister series^{23–25} or overarching principles for surfactants, polymers, colloids, and interface science based on Hofmeister series^{16,26,27} are discussed, including hydration, specific interactions of salt ions with the backbone, and charged side-chain groups at the protein surface in solution.^{23,28} In contrast, there are a large number of combined high-level spectroscopy, crystallography, and theoretical works that discuss the formation of the first and second hydrate shells in terms of (I) coordination number (CN),^{29–34} (II) direct ion–water molecule distances,^{31,32} and (III) the effect of the hydrogen-bonding water network.^{35–37} However, these works lack the bridge back to experimental observations with a coarser granularity for protein aggregation, like *in situ* studies or investigations of the mesoscopic or continuum material behavior, which are important to understand multiscale mechanisms like fiber assembly of fibrinogen in the presence of varying metal ions.³⁸ Relevant considerations with respect to the three latter aspects are summarized as follows:

(I) Concerning cation-specific effects, for the divalent alkaline earth metal cations, a coordination number (CN) of 6 is usually found with an octahedral arrangement of the water molecules around the ion.^{29,32} For the divalent transition-metal ions, the situation is not quite so clear. Here, CN values <6 tend to be found for divalent Cu²⁺ and Zn²⁺ ions.³⁴ A square-pyramidal geometry with five water molecules is proposed,^{30,33} which in the case of Cu²⁺ ions is energetically very close to the sixfold coordinated hydrate shell.³⁰ Thus, a mixed form of five- and six-coordinated ions is assumed, which would trigger a higher disorder in the surrounding water structure. For singly charged Zn(I) ions, in contrast to the classical monovalent ions, even smaller CN values down to 3 are documented³³ and explained with the asymmetric electron configuration in the 4s level.

(II) Next to CN, trends in the distances for first and second hydration shells around cations are reported in the literature. In general, the higher the charge density of the ion, the smaller the bond distance from ion to the oxygen atom of the first water

layer as well as the distance between first and second shells.^{31,32} Anyway, the distance values vary in recent studies depending on the way the ion–hydration shell distance is defined, which makes it difficult to compare values from different sources. Therefore, we have listed all values of the ionic properties we will use for our discussion of the ionic influence on fibrinogen precipitation in Table S1 in the Supporting Information.

(III) Ion-specific effects on the ion-surrounding water network are also discussed in recent works^{35,36} addressing electronic and polarization effects on the first and second water shells. It was found that cations with a low charge density weaken the hydrogen (H-) bonds of hydrating water molecules, whereas cations with a high charge density cause the formation of strong H-bonds,³⁶ which is the same for the reported ion–water molecule distances listed in Table S1. In general, induction effects perturb the hydrogen-bonding structure of water and its dynamics in the hydration shells. These effects are common for all ion species but are found more profound for stronger kosmotropic ions of higher charge density³⁵ and smaller sizes³⁶ following directly the Hofmeister series.

Since fibrinogen aggregation is a prerequisite for *in vitro* fiber formation, it is important to understand its precursor role in various fiber assembly processes that involve different ion types.³⁸ To date, several approaches exist to fabricate fibrinogen nanofibers *in vitro*, ranging from electrospinning^{39,40} and template-assisted extrusion⁴¹ to different self-assembly routines.³⁸ While electrospinning requires organic solvents and high electric fields, many self-assembly routines are based on hydrophobic surface interactions,³⁸ acidic pH values,^{42–44} or the addition of ethanol.^{45,46} Many of these conditions lead to conformational changes in the fibrinogen structure, can induce denaturation, or were even discussed to be associated with the formation of amyloid fibers.³⁸

Based on these drawbacks, we have recently introduced the physiological routine of salt-induced self-assembly to prepare dense networks of fibrinogen nanofibers on either hydrophilic or hydrophobic surfaces using a controlled drying process.⁴⁷ By combining Fourier transform infrared (FTIR) and circular dichroism (CD) spectroscopies, we could show that fiber assembly was accompanied by partial transitions from α -helices to β -strands.⁴⁸ Despite these conformational changes, no pathogenic amyloid formation was observed, and we could show that a cross-linking treatment with formaldehyde vapor did not affect the secondary structure of self-assembled fibrinogen fibers.⁴⁸ So far, we have exclusively used monovalent metal ions to induce fiber assembly of fibrinogen.^{47–49} Jandt and co-workers previously also postulated that positively charged metal ions like K⁺ and Na⁺ are responsible for fibrinogen fiber formation.⁴² Nevertheless, two other studies reported fiber assembly of fibrinogen in buffers containing either 2 mM Ca²⁺⁵⁰ or 5 mM Mg²⁺ ions.⁵¹ Interestingly, in both studies, only very thin protofibrils or single fibrinogen nanofibers are formed,^{50,51} which strongly differed from the dense fiber networks we obtained by salt-induced self-assembly with monovalent ions.^{47,48} Since both studies using divalent metal ions observed fiber assembly already in solution although very low ion concentrations were present,^{50,51} it is not yet known what effect divalent metal ions have on fibrinogen assembly when a drying step is introduced,³⁸ in particular when high ionic concentrations are present. Hence, for the first time, our present study focuses on the fundamental question whether different concentrations of divalent metal ions also induce fiber assembly of fibrinogen upon drying.

2. EXPERIMENTAL SECTION

2.1. Sample Preparation. Fibrinogen samples were prepared on either glass slides coated with (3-aminopropyl)triethoxysilane (APTES) for microscopic analysis or gold-coated glass slides for FTIR and light scattering analysis following our previous routines.^{47,48} In brief, round glass coverslips with a diameter of 12 mm (VWR, Darmstadt, Germany) were cleaned by immersion into freshly prepared piranha solution for 5 min. For the piranha solution, three parts of 95% sulfuric acid (VWR) were mixed with one part of 30% hydrogen peroxide solution (VWR). Then, the glass slides were washed five times with deionized water from a TKA water purification system (Thermo Fisher Scientific, Schwerte, Germany). Parts of the activated glass coverslips were dried with N₂ and modified with APTES by immersion in an ethanol solution (Honeywell, VWR) containing 5% APTES (Sigma-Aldrich, Steinheim, Germany) overnight at room temperature. The modified glasses were washed with ethanol and dried with N₂ for subsequent modification with fibrinogen. For FTIR studies, glasses were coated with an adhesion layer of 5 nm of chromium, followed by 25 nm of gold using an EM ACE600 high-vacuum sputter coater (Leica Microsystems, Wetzlar, Germany). Specifically for energy-dispersive X-ray spectroscopy (EDX), two samples were prepared on Si wafers. Buffer solutions of Tris (Tris(hydroxymethyl)-aminomethane (C₄H₁₁NO₃), Carl Roth GmbH, Karlsruhe, Germany) were prepared with a concentration of 10 mM using deionized water and adjusting the pH to 7.4 with concentrated HCl. Fibrinogen from human plasma (Merck KGaA, Darmstadt, Germany) was dissolved in 10 mM Tris (or 10 mM NH₄HCO₃) to prepare stock solutions of 10 mg/mL concentration. Subsequently, dialysis was carried out overnight to remove low-molecular-weight compounds with 14 kDa cutoff cellulose membrane dialysis tubing (Sigma-Aldrich). Individual salt solutions were prepared by dissolving the respective salt in 10 mM Tris buffer. The respective salts used to study fibrinogen precipitation were CaCl₂·2H₂O (calcium chloride dihydrate, Sigma-Aldrich), MgCl₂·6H₂O (magnesium chloride hexahydrate, Sigma-Aldrich), CuCl₂ (copper(II) chloride, Sigma-Aldrich), and ZnCl₂ (zinc chloride, Sigma-Aldrich) in concentrations of 20, 375, and 750 mM for all four salts. Moreover, the final pH of each salt solution was measured with a pH meter pH50+ DHS (XS Sensor, Italy), which resulted in a pH value of 7 for CaCl₂, 7.2 for MgCl₂, 7.6 for CuCl₂, and 5.4 for ZnCl₂. Additionally, to prepare fibrous reference samples, phosphate-buffered saline (PBS) was used in a concentration of 5X and pH of 7.4. Denatured fibrinogen samples were used as controls and prepared using 8 M guanidine hydrochloride (GdnHCl, Sigma-Aldrich) and 8 M urea (CH₄N₂O, AppliChem GmbH, Darmstadt, Germany) solutions.

2.2. Fibrinogen Precipitation. For microscopic and FTIR analyses, 60 μL of the fibrinogen stock solution and 60 μL of the respective divalent salt solution were successively pipetted onto APTES- or gold-coated glass slides. All samples were directly transferred to a home-built humidity chamber to be dried at 24 °C and 5% relative humidity overnight. Additionally, in accordance with our previous studies, reference samples on APTES, Si wafer, and gold were prepared by pipetting 60 μL of fibrinogen solution and 60 μL of deionized water, respectively, that were also dried at 24 °C but 30% relative humidity overnight.^{47,48} Denatured fibrinogen samples were prepared by applying 60 μL of the fibrinogen solution followed by 60 μL of either 8 M urea or 8 M GdnHCl and subsequent drying as stated above. All fibrinogen samples had a final concentration of 5 mg/mL fibrinogen, 5 mM Tris, and concentrations of the respective salts that varied from 10 mM to 187 mM (used for microscopic characterization) and 375 mM (used for light scattering, FTIR, surface composition, and microscopy analyses). The final concentration of the denatured agents was 4 M. After drying, all samples were transferred to an airtight container with a rubber cover to maintain the low humidity for a subsequent cross-linking step with formaldehyde vapor (CH₂O (FA), AppliChem GmbH). One microliter of 37% FA solution per cm³ was inserted into the container through the rubber cover with a syringe needle. The samples were incubated in this FA atmosphere for 2 h. Afterward, all samples were aired in a fume hood for 30 min. After cross-linking, the samples were washed with deionized water for 45 min

exchanging the water every 15 min. After the washing step, all fibrinogen samples were dried at room temperature for further analysis.

2.3. Microscopy Analysis of Dried Fibrinogen Precipitates.

The macroscopic coverage of dried fibrinogen samples was imaged with a Toolcraft digital microscope (Conrad Electronic SE, Hirschau, Germany). On the nanoscale, the morphology of precipitated fibrinogen was analyzed with scanning electron microscopy (SEM) after all samples were sputter-coated with a thin layer of gold using a 108 auto system (Tescan GmbH, Dortmund, Germany) for 25 s. Subsequently, SEM analysis was carried out with a Zeiss Supra 40 device (Carl Zeiss, Oberkochen, Germany) at an acceleration voltage of 3 kV using the secondary electron detector.

To obtain information on the chemical composition of fibrinogen precipitates prepared with different salts, we also performed energy-dispersive X-ray (EDX) measurements using a field emission scanning electron microscope (FESEM) of type FEI Helios 600 (DualBeam). EDX measurements were performed with an Oxford X-Max80 Silicon Drift Detector (SDD) with ATW2-window and an energy resolution down to 129 eV.

2.4. Light Scattering of Fibrinogen during and after Precipitation.

To follow the drying process of selected fibrinogen samples *in situ*, a light scattering sensor device OS 500 from Optosurf (Ettlingen, Germany) coupled with a Sartorius TE 3102 mass balance (Göttingen, Germany) were used. This setup was placed in a home-built chamber that was sealed with plastic and aluminum foil. To maintain a constant humidity value during *in situ* measurements, dry air was purged into the chamber continuously. The light scattering sensor was aligned at a measuring distance of 5 mm from the substrate surface and used a light-emitting diode (wavelength of 676 ± 1 nm) providing a spot with a width of 0.3 mm that was positioned in the center of the substrate. From light scattering analysis, we obtained information on the total intensity and the variance of the angle distribution (called Aq) of the detected light for the respective fibrinogen surfaces. The Aq parameter is described by Feidenhansl et al.,⁵² and in VDA 2009:2010-07,⁵³ it is proportional to the second statistical moment of the scattered light density⁵⁴ and it represents the optically measured roughness. Baseline signals were obtained by characterizing gold samples without any liquid on top. Subsequently, aqueous fibrinogen and salt solutions were applied to the gold surfaces as described above. We recorded the time-dependent intensity and Aq of the fibrinogen precipitates until the samples were completely dry. Next, the samples were cross-linked with FA vapor and washed (see Section 2.2). Subsequently, roughness maps of cross-linked and washed fibrinogen samples were obtained within an array of measuring spots with a lateral distance of 0.4 mm between neighboring measurement regions and a total map width of 20 mm.

2.5. Fourier Transform Infrared Reflection Spectroscopy.

For secondary structure analysis, dried fibrinogen precipitates on gold were analyzed with a Bruker Vertex 70 with IR Scope II (Bruker, Ettlingen, Germany) previously described.^{47,48} Briefly, FTIR spectra were recorded in 10 to 15 different positions with 4 cm⁻¹ resolution and 64 scans per measurement. At least three samples of each fibrinogen–salt combination were measured. The reference spectrum was measured against air and subtracted from the obtained spectra. All spectra were processed by the Bruker software package OPUS. After subtraction of water vapor absorbencies, the resulting spectra were smoothed using 7-17 point Savitzky–Golay function and baseline-corrected by rubber band baseline correction. Amide band positions were determined by peak integration using Origin 2020 (OriginLab Northampton). The secondary structure was calculated by deconvolution of amide I applying the same procedure as in our previous study (see also Section S2 in the Supporting Information).⁴⁸

2.6. XPS Analysis. The surface of dried and cross-linked fibrinogen precipitates was characterized by X-ray photoelectron spectroscopy (XPS) after rinsing with water. For analysis, a Kratos AXIS Ultra system with a monochromatized Al Kα X-ray source providing a photon energy of 1486.6 eV was used (Kratos Analytical Ltd., Manchester, U.K.). The base pressure of the analysis chamber was approximately 6 × 10⁻⁸ Pa. Spectra were acquired in the constant analyzer energy mode using pass energies of 80 eV for survey spectra, 20 eV for C 1s, N 1s, and O 1s detail

scans, and 40 eV for detailed scans in the Cl 2p, S 2p spectral region as well as for detecting metal-related signals. Spectrum fitting was performed using CasaXPS (Version 2.3.19PR1.0, Casa Software Ltd.). The binding energy scale of the spectra was aligned by centering the C 1s signal of the hydrocarbonaceous species at 285.0 eV. Signal areas were obtained following a linear background subtraction. Peak components were adjusted using a Gaussian–Lorentzian line shape GL(30) for fitting.

3. RESULTS AND DISCUSSION

Previously, we reported that various monovalent salt types, *i.e.*, different ion pairs, required different threshold concentrations to induce fibrillogenesis of fibrinogen.⁴⁷ To investigate whether divalent metal ions are also effective to induce fiber assembly from solution upon drying, we analyzed the morphology, secondary structure, and chemical composition of fibrinogen layers that were precipitated at varying concentrations of divalent metal ions.

3.1. Morphology and Drying of Fibrinogen Precipitates. Based on our previous study where fibrillogenesis of fibrinogen was induced in the presence of different monovalent salts with concentrations as low as 5 mM, we hypothesized that divalent metal ions may also be able to initiate fiber assembly at such low concentrations upon drying.^{38,47} Therefore, we studied the effect of different concentrations of divalent metal ions on the precipitation of fibrinogen using a protein concentration of 5 mg/mL throughout all experiments, which previously yielded fiber assembly with manifold monovalent salt types and concentrations.⁴⁷ Initially, fibrinogen was dried on APTES-coated glass substrates using 5 mM Tris buffer containing 10 mM CaCl₂, MgCl₂, CuCl₂, or ZnCl₂, which was close to physiological conditions.^{10–13} SEM analysis showed that the precipitates did not exhibit any fibrous surface topography (see Figure 1A–D). Instead, fibrinogen precipitates dried in the presence of 10 mM MgCl₂ or ZnCl₂ appeared very smooth (see Figure 1B,D) and resembled the morphology that we previously observed when fibrinogen was dried with 5 mM NH₄HCO₃.^{47,48} While drying with 10 mM CaCl₂ or CuCl₂ yielded evenly distributed holes in the fibrinogen surface (see Figure 1A,C). Those holes could be formed during solvent evaporation, as already reported by Jiang *et al.*⁵⁵ and Pervin *et al.*⁵⁶ for polymer films or during degassing of the residual water before performing the SEM measurement. Cross-sectional SEM analysis subsequently revealed that no fibers had formed in lower regions of the protein films either (see Supporting Information Figure S2A–D). Instead, very compact fibrinogen layers were found on the APTES-coated glasses. Comparatively, Dubrovin *et al.*⁵⁰ and Chen *et al.*⁵¹ observed fibrinogen fibril formation in the presence of 2 mM CaCl₂ and 5 mM MgCl₂, respectively. However, in both studies, the divalent cations were not present alone, but accompanied by other salts like sodium chloride⁵¹ or PBS, which primarily contained monovalent ions.⁵⁰

Interestingly, in our previous study, only 5 mM sodium phosphate could induce fibrillogenesis while a minimum of 25 mM potassium phosphate was required to achieve fiber assembly; on the other hand, 10 mM KCl did not induce any nanofiber formation.⁴⁷ Since different metal ions vary in size based on their hydration shell,⁵⁷ we wanted to find out whether following the law of mass action divalent ions may need to be present with higher concentrations during fibrinogen precipitation to induce fibrillogenesis. To test this hypothesis, we subsequently increased the concentration in our precipitation experiments to 187 mM for all divalent salts. This value

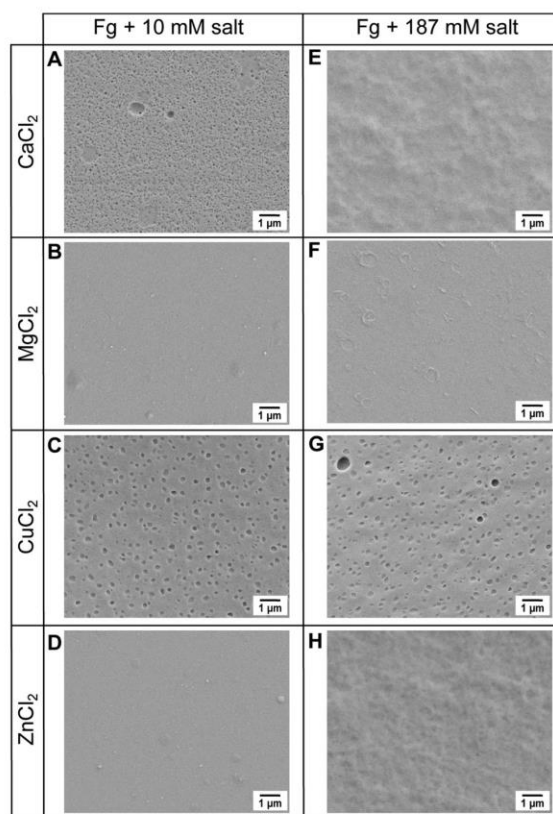


Figure 1. SEM images of fibrinogen precipitates on APTES-modified glasses prepared in the presence of different divalent metal ions: 5 mg/mL fibrinogen (Fg) in 5 mM Tris was dried with either 10 mM or 187 mM (A, E) CaCl₂, (B, F) MgCl₂, (C, G) CuCl₂, and (D, H) ZnCl₂. SEM images reveal the formation of smooth films for most fibrinogen layers. For fibrinogen precipitates with CuCl₂, evenly distributed holes are visible at the surface. With higher salt concentrations of CaCl₂ and ZnCl₂, the resulting fibrinogen surface appears rougher than with the other divalent salts.

corresponds to half the concentration of 2.5× phosphate-buffered saline (PBS), which contains various monovalent ions that were previously found to provide optimum conditions for fiber assembly of fibrinogen.⁴⁷ Although 187 mM concentration of divalent metal ions is far above the physiologically relevant concentration^{10–13} in comparison to monovalent ions, where NaCl is present with physiological concentrations of 0.15 M, we wanted to study whether such increased salt levels are suitable trigger factors to also induce fiber assembly with divalent ions. Moreover, 187 mM was used as the salt concentration to test the hypothesis whether divalent ions, because of their double charge compared with monovalent ions, need to be present at only half the optimum PBS concentration during fibrinogen precipitation to induce fibrillogenesis.

Morphological SEM analysis revealed that despite the increased salt concentration, no fibrinogen fiber formation was observed for any of the divalent salts (see Figure 1E–H). Fibrinogen precipitates prepared with 187 mM MgCl₂ and CuCl₂ exhibited the same morphology we observed with 10 mM, *i.e.*, a very smooth layer for MgCl₂ and evenly distributed holes for CuCl₂. For 187 mM CaCl₂ or ZnCl₂, however,

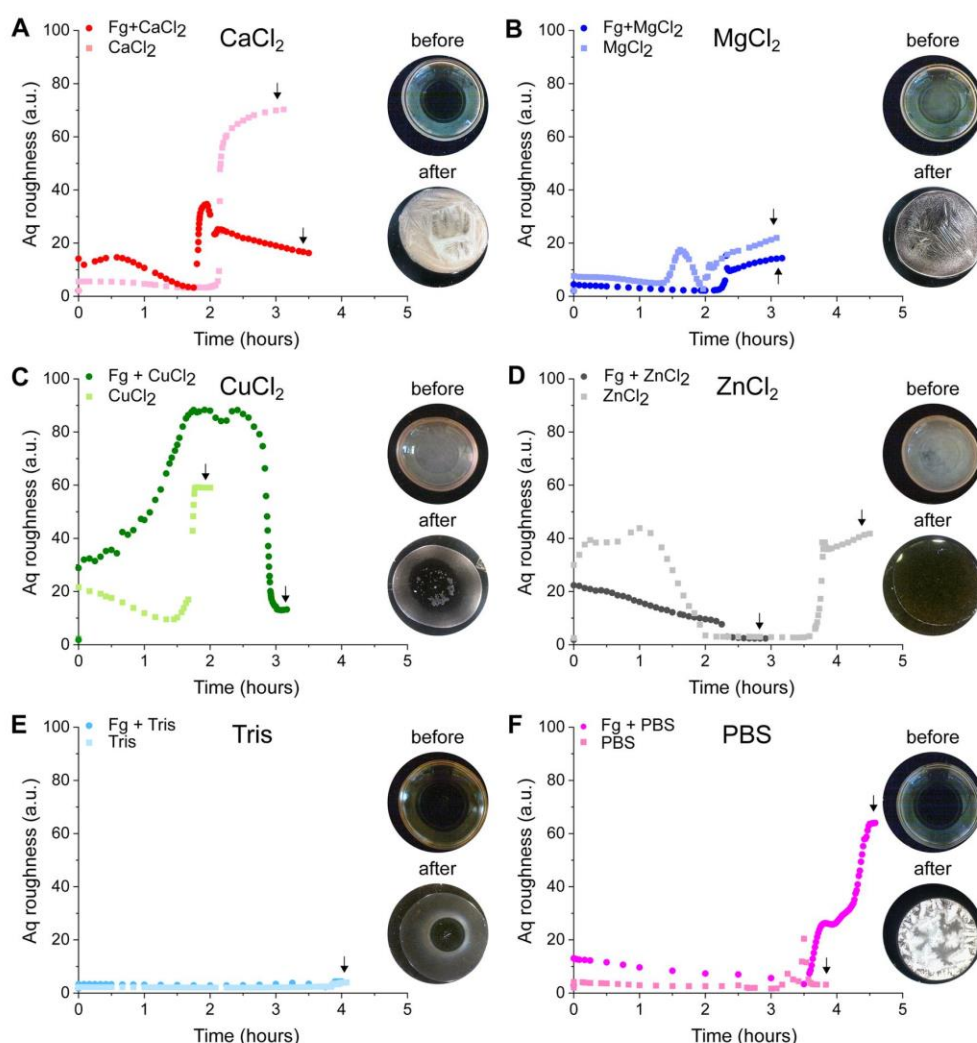


Figure 2. Aq profiles from light scattering analysis of fibrinogen precipitation on gold. In each plot, the dark colors represent the change in Aq surface roughness during the drying of droplets containing 5 mg/mL fibrinogen in 5 mM Tris and 375 mM (A) CaCl_2 , (B) MgCl_2 , (C) CuCl_2 , and (D) ZnCl_2 , and (E) only 5 mM Tris or (F) 2.5× PBS. The lighter colors show the Aq for the drying of droplets containing only the respective salt. The initial Aq values at 0 h represent the roughness of the underlying gold substrate before the respective fibrinogen solutions were added. Arrows point to the time at which the samples are completely dried. Insets show microscopic images of the different fibrinogen–salt droplets before and after drying. The diameter of all gold substrates in the insets is 12 mm.

fibrinogen precipitates showed a rougher topography than in the presence of 10 mM of the respective salts. Also for 187 mM, cross-sectional analysis revealed that fibrinogen precipitated into compact protein films for all salts (see Supporting Information Figure S2E–H). Based on these morphological findings, none of our above hypotheses could be confirmed for any of the divalent salts when a concentration of 187 mM was used.

When 5 mg/mL fibrinogen was previously dried with 375 mM KCl, we had observed the assembly of very sparsely distributed fibers while no fibers formed with lower KCl concentrations.⁴⁷ Since fibrinogen fibers exhibited different morphologies based on the particular type of monovalent salt used to assemble them,⁴⁷ we finally studied whether divalent ions may require even higher concentrations of 375 mM to induce fibrinogen formation. When 375 mM CaCl_2 or MgCl_2 was added to

fibrinogen solutions, they were rather transparent (see insets “before drying” in Figure 2A,B), while fibrinogen in 375 mM ZnCl_2 or CuCl_2 immediately turned turbid (see insets “before drying” in Figure 2C,D). Interestingly, after all fibrinogen films were dried completely, the initial turbidity of fibrinogen in ZnCl_2 or CuCl_2 had disappeared, and the precipitates appeared mostly transparent while dried fibrinogen with CaCl_2 or MgCl_2 had turned completely opaque (see insets “after drying” in Figure 2A–D). As shown in the insets of Figure 2A–D, regarding the thickness of the deposits, the macroscopic spatial deposition profiles of all fibrinogen–salt precipitates revealed centered drying patterns following the categorization provided by Devlin et al.⁵⁸ Pinning of the droplet contact line was observed throughout the drying process with all divalent ions, as both the initially applied droplet and the dried precipitates extended over

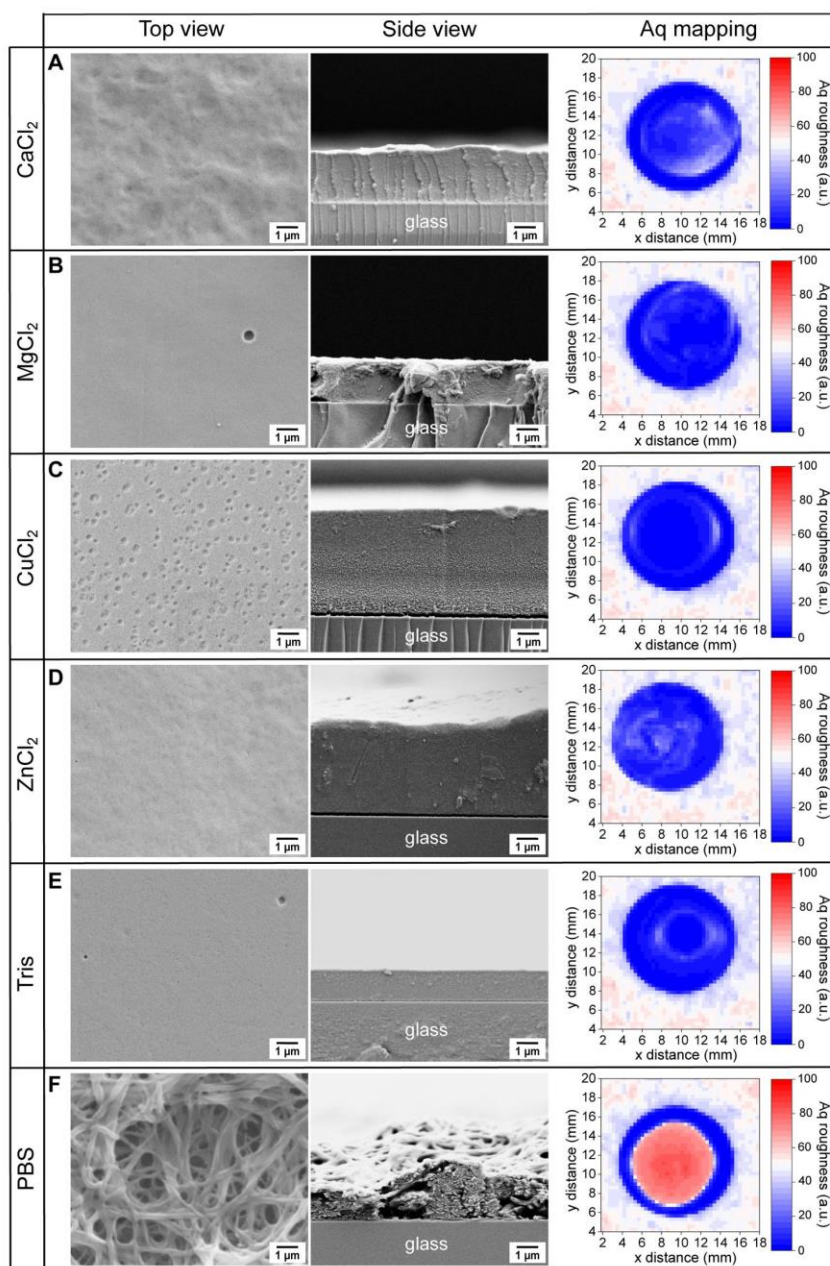


Figure 3. SEM images and Aq mappings of samples prepared after drying 5 mg/mL fibrinogen in the presence of different salts: (A) 375 mM CaCl_2 , (B) 375 mM MgCl_2 , (C) 375 mM CuCl_2 , (D) 375 mM ZnCl_2 , (E) 5 mM Tris alone, or (F) 2.5X PBS. For SEM analysis, all precipitates were prepared on APTES-modified glass, while for Aq mapping, fibrinogen films were prepared on gold. Top and side views of the resulting morphology do not show any fiber formation in the presence of divalent salts (A–D). Likewise, the measured final roughness is much lower for divalent salts compared with fibrinogen precipitates prepared with PBS (D) while fibrinogen in Tris is completely smooth (E).

approximately 90% of the substrate width. Only after the evaporation of more than 80 wt % water from the droplets, the reflectivity of the thinned and highly concentrated aqueous films finally decreased before they got completely dried on the surface of earlier fibrinogen–salt precipitates.

As reference samples, we also dried fibrinogen in 5 mM Tris background buffer alone (see Figure 2E) and in the presence of

2.5X PBS in Tris (see Figure 2F) to specifically induce fiber assembly *via* the presence of monovalent ions. Microscopic analysis of these references revealed that essentially the entire area of the originally applied fibrinogen–salt droplet was covered by the precipitates after drying. While Tris alone did not induce significant turbidity in 75% of the area overlaid by fibrinogen precipitates, fibrinogen dried in 2.5X PBS changed

from an almost transparent solution before drying to a consistently area-wide highly opaque deposit after drying. Upon closer microscopic inspection, precipitates from fibrinogen–PBS solutions displayed dendritically grown arrays of salt crystals with extensions up to 2 mm. These growth patterns of PBS in the presence of fibrinogen agree well with the study of Tarafdar and co-workers, who observed the formation of dendritic NaCl crystals with millimeter dimensions in the presence of gelatin.⁵⁹

Turbidity changes as we observed them in our divalent fibrinogen precipitates may indicate protein aggregation,⁶⁰ which can subsequently induce fiber formation.³⁸ Since we previously reported turbidity changes to be correlated with fiber formation when fibrinogen was dried in monovalent salts,⁴⁷ we now conducted angle-resolved light scattering measurements to follow fibrinogen precipitation *in situ*. During fibrinogen precipitation in the presence of divalent salts, we monitored the Aq roughness as a dynamic measure of the surface topography until the water was evaporated completely, which resulted in varying drying times between 3 and 4.5 h (see Figure 2). Figure 2A–D shows the time-dependent Aq changes of fibrinogen being dried with 375 mM of different divalent salts (indicated by symbols in strong colors) in comparison to the respective salt solutions being dried alone (represented by symbols in light colors). In these graphs, low Aq values indicate a very smooth surface, as, for instance, visible in the initial time point at 0 h (see Figure 2), which depicts the roughness for the underlying gold substrate before any fibrinogen solution was added. For all fibrinogen precipitates with divalent salts, the dynamic Aq roughness varied notably from the curve where the respective salts were dried alone. At the end of the drying process, the Aq curves for fibrinogen with CaCl₂, MgCl₂, and CuCl₂ all showed Aq values between 10 and 20 (see Figure 2A–C). This indicates a higher surface roughness than that for fibrinogen with ZnCl₂ (see Figure 2D), where the Aq value almost approached zero until the end of the drying process.

Interestingly, when divalent salts were dried alone, much higher Aq values were obtained at the end of the drying process. This observation indicates a clear contribution of fibrinogen to the drying of the respective salts, which can be interpreted as a “smoothing contribution” of the protein on salt precipitation.^{59,61} Furthermore, in general, fibrinogen seems to delay salt precipitation. Interestingly, when fibrinogen was dried in Tris alone, the Aq roughness was close to zero throughout the whole drying process, and the same trend was observed when Tris was dried without any fibrinogen (see Figure 2E). These Aq curves show that the surface roughness of fibrinogen in Tris is very close to the roughness of bare gold substrates. Overall, in the sample center, the highest Aq roughness around 60 was found after fibrinogen was dried with monovalent PBS while the drying of PBS alone mainly yielded Aq roughness values between 0 and 10 (see Figure 2F). Thus, fibrinogen was also found to influence the drying behavior of monovalent salts and vice versa. In summary, the trends in Aq roughness we observed for fibrinogen in different salt solutions correlated well with the results from our microscopic analysis, *i.e.*, for very low Aq values, we found almost transparent fibrinogen films while higher Aq values were correlated with highly turbid fibrinogen precipitates. These results show that *in situ* analysis of the Aq roughness is very well suited to follow the drying process of proteins in varying buffer systems. Moreover, when pinning of the contact line effects a preferentially vertical droplet drying, the time-dependent intermediate changes of Aq may indicate subsequent growth

regimes and reflect the vertical homogeneity of the deposited film.^{52,62}

To further investigate whether *in situ* monitoring of dynamic Aq changes can provide a tool to predict the surface topography of fibrinogen precipitates after drying, we subsequently cross-linked all dried fibrinogen precipitates with FA vapor and washed them to be analyzed by SEM (see Figure 3). For 375 mM concentration of the respective divalent salts, it can be seen that fibrinogen films precipitated with CaCl₂ or ZnCl₂ were rougher (see Figure 3A,D) than the corresponding films formed with MgCl₂ or CuCl₂ (see Figure 3B,C). Characteristic holes were again observed for CuCl₂. MgCl₂ induced the formation of very smooth fibrinogen films (see Figure 3D), which resembled the topography of fibrinogen precipitates prepared in Tris without any salts (see Figure 3E). Interestingly, the topography of fibrinogen films in Tris strongly resembled the planar fibrinogen scaffolds we had previously observed to assemble in NH₄HCO₃ buffer.^{47,48} As expected from our prior studies in NH₄HCO₃ buffer, in the presence of 2.5× PBS with monovalent ions, fibrinogen also assembled into dense nanofibers, when Tris was used as a background buffer (see Figure 3F).

Once again, no fibers were found in the lower fibrinogen regions with 375 mM divalent salts, either; all fibrinogen precipitates exhibited a compact structure (see Figure 3A–D, side view), which agrees with our findings from lower salt concentrations (see Figure S2). Remarkably, even in deeper regions of these water-rinsed films, neither salt crystallites nor voids that might have been left in a cross-linked fibrinogen matrix after dissolving potential inorganic solid inclusions were observed. This is in agreement with the optically transparent appearance of the not yet water-rinsed films that essentially indicates the absence of microscale phase boundaries with abrupt changes of refractive indices facilitating the scattering of visible light. Very smooth precipitates were also observed for fibrinogen in Tris, which confirmed the particularly compact character of these fibrinogen films (see Figure 3E). In contrast, fibers assembled with monovalent PBS showed a highly porous architecture that continued throughout the entire cross section (see Figure 3F). Previously, Helbing and co-workers tested different buffer systems to adsorb fibrinogen on polyethylene single crystals and observed fibril formation when PBS (pH 7.4) was used instead of calcium carbonate (CaCO₃, pH 9.2).⁶³ They assumed that the difference in pH of the buffers was solely responsible for fibrinogen fiber assembly in the case of PBS or agglomerate formation in the case of CaCO₃.⁶³ We showed recently, however, that higher pH values between 7 and 9 favor fibrinogen nanofiber assembly when PBS is present.^{47,48} Nevertheless, none of the divalent salts, which mainly exhibited a pH around 7, induced fiber formation of fibrinogen. In particular, all divalent salt buffers used in this study contained Cl[−] anions. Since we had previously observed fiber assembly of fibrinogen with NaCl, *i.e.*, with the same counter anion,⁴⁷ we are now able to conclude that fiber formation is exclusively or even essentially driven by the presence of metal cations in the fibrinogen aggregates. This conclusion agrees very well with a previous study by Jandt and co-workers who had hypothesized earlier on that positively charged metal ions like K⁺ and Na⁺ are responsible for fibrinogen fiber formation.⁴²

In addition to our morphological analysis by SEM, we conducted Aq roughness mapping of fibrinogen precipitates by angle-resolved light scattering (see Figure 3, last column). This method allowed us to complement the highly localized roughness information obtained from *in situ* light scattering

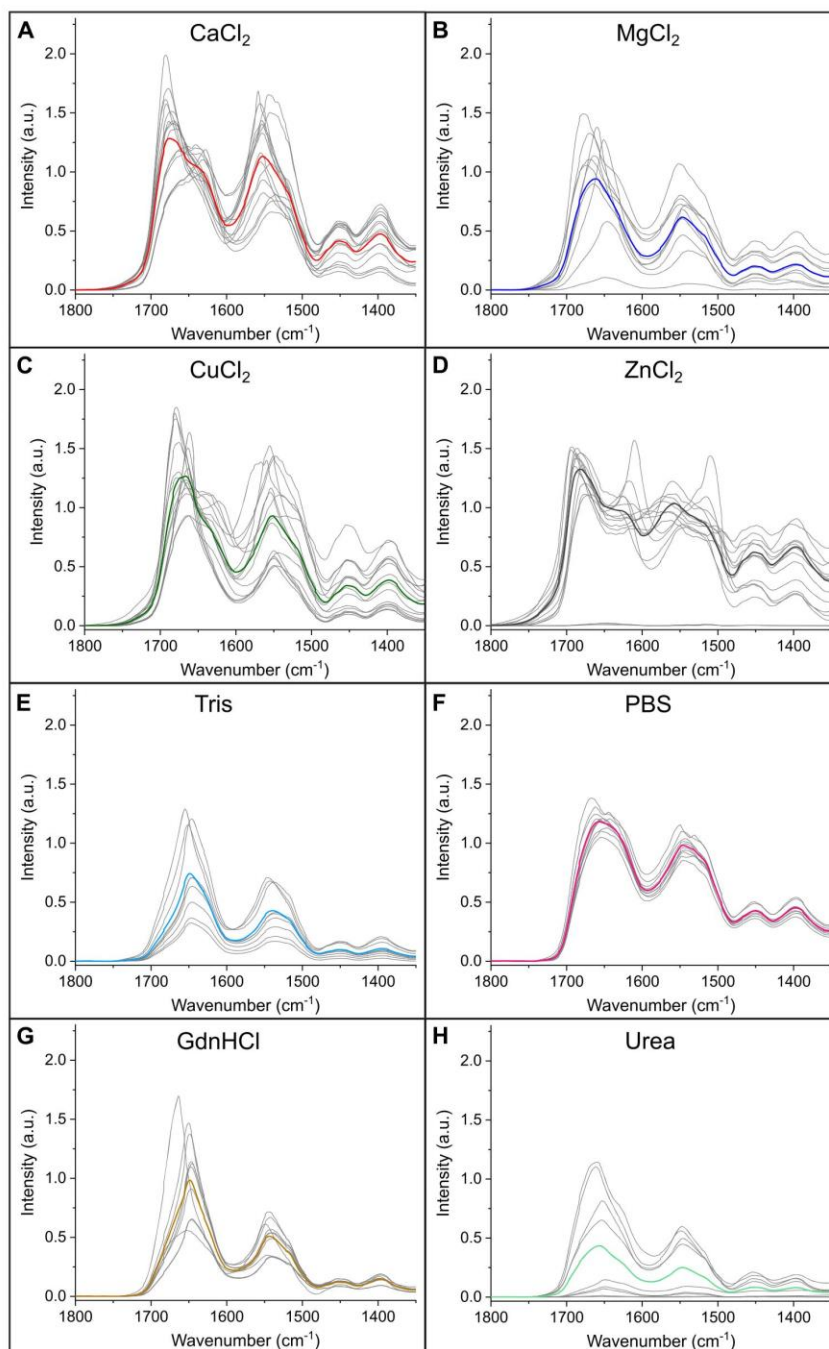


Figure 4. FTIR spectra in the region of the amide I and amide II bands for samples prepared after drying 5 mg/mL of fibrinogen in: (A) 375 mM CaCl_2 , (B) 375 mM MgCl_2 , (C) 375 mM CuCl_2 , (D) 375 mM ZnCl_2 , (E) 5 mM Tris, (F) 2.5 \times PBS, (G) 4 M GdnHCl, and (H) 4 M urea. Individual spectra obtained from different sample positions are depicted in gray, while the colored bold spectra show the respective average spectra obtained from these individual measurements.

with a spatially resolved roughness analysis over the entire sample surface. For all fibrinogen precipitates that were assembled with 375 mM of divalent salts, we obtained very low Aq values below 20 or even close to 0 (see Figure 3A–D),

which resembled the Aq map of fibrinogen dried in Tris alone (see Figure 3E). Aq values above 60 were observed exclusively for fibrinogen fibers assembled with 2.5 \times PBS, *i.e.*, when monovalent metal ions were present (see Figure 3F). The

laterally homogeneous Aq maps are in agreement with the SEM images taken in distinct samples regions showing random fiber arrangement without evident fiber alignment. These results confirm that—independent of the respective type of divalent metal ions present during fibrinogen precipitation—all fibrinogen films were comparably smooth in contrast to fibers assembled with 2.5× PBS. Moreover, these findings agree well with our preceding Aq *in situ* analysis where salt residues were still present in the samples while they had been removed before SEM analysis and Aq mapping by cross-linking and washing. As the mapping displayed in Figure 2C strikingly revealed the formation of a transiently very rough deposit during drying of droplets containing 5 mg/mL fibrinogen in 5 mM Tris and 375 mM of CuCl₂, we exemplarily performed further structural characterizations of precipitates that prevail before completing droplet drying and after laterally displacing the highly saline liquid by applying an airflow. Figure S4 in the Supporting Information shows the Aq roughness mapping and SEM images for the thus obtained clearly nonfibrous precipitates and the smoothening of the fibrinogen layer when washing the deposits after performing the fibrinogen cross-linking. From these findings, we infer that the morphologies shown in the side-view SEM images in Figure 3 after droplet drying in the presence of divalent salts are representative for the internal film structure even during precipitation. We recapitulate that even transitory fibrillogenesis is improbable in the presence of divalent salts.

Since APTES-coated glass slides were used for SEM analysis, gold-coated coverslips were used to monitor the Aq roughness *in situ*, and after drying as well as for subsequent FTIR analysis (see Section 3.2), we also analyzed corresponding fibrinogen precipitates on gold to study whether the underlying surface may affect the layer morphology (see Figure S3). These SEM images show that fibrinogen precipitates prepared on gold with a 375 mM concentration of the respective divalent salt exhibited the same morphology as on APTES-modified glass. Therefore, we conclude that fibrinogen precipitation from solutions of divalent salts was not influenced by the underlying surface chemistry. Similarly, in our previous study on fiber assembly with monovalent salt ions, we had observed that fibrinogen topography did not depend on the substrate material.⁴⁷ Thus, we conclude that divalent ions are also exclusively responsible for the topography that is formed during fibrinogen precipitation.

3.2. Influence of Divalent Ions on the Secondary Structure of Fibrinogen Precipitates. Previously, we reported conformational changes of fibrinogen from α -helical structures to β -strands when monovalent ions induced fiber assembly.⁴⁸ To understand whether divalent ions induce changes in the fibrinogen conformation despite the lack of fiber formation, we analyzed dried fibrinogen precipitates with FTIR spectroscopy. Since the most pronounced topographical features in dried fibrinogen films were found with 375 mM ion concentration, we used these samples for our FTIR analysis (see Figure 4A–D). The resulting spectra show strong variations, which were found to depend on the respective surface area in which the spectra were recorded. To account for these local variations, we averaged individual spectra obtained from different positions (thin gray lines) and displayed them together with the resulting average for each salt (colored bold lines). Again, planar fibrinogen films prepared in Tris alone were used as reference samples (see Figure 4E) together with fibrinogen fibers assembled in 2.5× PBS with Tris (see Figure 4F).

Since many of the FTIR spectra obtained with divalent ions showed strong variations in the amide I band shape and position, we also analyzed fibrinogen precipitates after exposure to denaturing agents using 4 M GdnHCl and 4 M urea, respectively (see Figure 4G,H). These denatured fibrinogen precipitates were additionally studied by SEM and Aq mapping (see Supporting Information Figure S5). It can be seen that none of the denatured fibrinogen films exhibited a smooth surface topography. Both denatured fibrinogen samples exhibited a clumpy surface topography. However, for urea, this effect was not visible in the cross section, which appeared very compact, while fibrinogen in GdnHCl also showed clumpy aggregates in lower sample regions. These morphological differences are also represented by the corresponding Aq maps where roughness values below 20 were found for dried fibrinogen in urea. GdnHCl, on the other hand, induced the formation of more elevated regions in dried fibrinogen precipitates, thus leading to localized roughness values around 60 while the remaining surface showed a roughness around 20.

In Figure 4A–D, it can be seen that variations among individual FTIR spectra were most pronounced for fibrinogen precipitates with divalent salts. This trend was accompanied by very strong variations in band intensity among the different spectra, which occurred due to local height variations in the fibrinogen layer. Additionally, variations in band shape were observed in different positions of the samples, suggesting a conformational diversity within each sample. In contrast, fibrinogen nanofibers assembled in monovalent 2.5× PBS yielded the narrowest distribution of FTIR spectra, which did not vary strongly in band intensity (see Figure 4F). For planar fibrinogen in Tris alone, we obtained very coherent FTIR spectra, whose band shape did not vary strongly while only variations in band intensity were visible (see Figure 4E). In addition, the bands of planar fibrinogen in Tris are much narrower than the bands of fibrinogen dried with PBS or with divalent salts. Interestingly, for both denatured fibrinogen samples (see Figure 4G,H), we also obtained rather coherent FTIR spectra, whose band shape did not vary as strongly as for the divalent fibrinogen precipitates. Overall, the band shapes for fibrinogen fibers in 2.5× PBS and for fibrinogen in Tris alone are in good agreement with our previous studies where NH₄HCO₃ was used as a background buffer.^{47,48}

When analyzing the position of the amide I bands (see Supporting Information Table S2), we found very pronounced variations for fibrinogen that precipitated in the presence of divalent salts (see Figure 4A–D): bands between 1630 and 1680 cm⁻¹ were found for CaCl₂, MgCl₂ yielded bands between 1647 and 1671 cm⁻¹, while bands for CuCl₂ ranged from 1630 cm⁻¹ to 1680 cm⁻¹, and ZnCl₂ yielded band positions between 1645 and 1686 cm⁻¹. For fibrinogen in Tris, amide I band positions were detected between the wavenumbers 1649 and 1670 cm⁻¹ (see Figure 4E), while for fibrinogen fibers prepared in 2.5× PBS, all amide I bands were located between 1648 and 1667 cm⁻¹ (see Figure 4F). For fibrinogen that was precipitated with 4 M GdnHCl, amide I band positions were rather stable (1647 and 1648 cm⁻¹) while the band position of fibrinogen denatured in 4 M urea ranged from 1647 cm⁻¹ to 1665 cm⁻¹. In direct comparison, the band position range of fibrinogen in divalent salts was much wider (24 to 50 cm⁻¹) than for fibrinogen in Tris alone (21 cm⁻¹) or in 2.5× PBS (19 cm⁻¹), which indicates that the fibrinogen conformation was strongly altered in the presence of divalent ions during drying.

To understand which secondary structure was associated with fibrinogen films that were precipitated in different divalent salts, we subsequently performed deconvolution analysis of the respective FTIR spectra using our previous routine (see also Supporting Information Section S2).⁴⁸ The resulting histogram in Figure 5 shows that the presence of divalent salts during

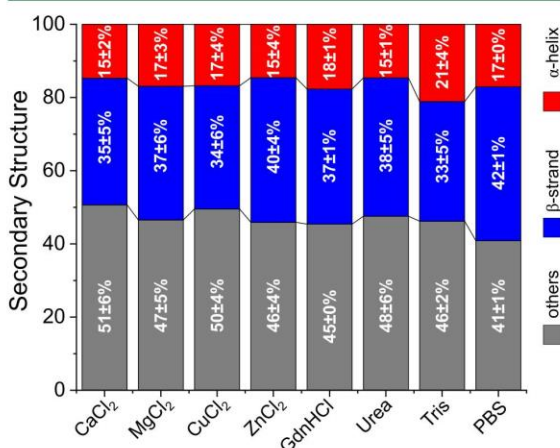


Figure 5. Comparison of secondary structure features of fibrinogen precipitates prepared in the presence of different salts and denaturing agents with 5 mM Tris background buffer. The histogram summarizes the results obtained by deconvolution analysis that was applied to the amide I bands of the FTIR spectra shown in Figure 4. Fibrinogen in the presence of divalent salts exhibited a secondary structure similar to that of fibrinogen with denaturing agents. All salts and denaturants induced a decrease in α -helices that was accompanied by an increase of β -strands and/or others compared to fibrinogen in Tris. Fibrinogen in PBS showed the highest β -strand percentage of all samples, while fibrinogen with Tris yielded the lowest β -strand content.

fibrinogen precipitation resulted in an average α -helix content of 15–17% for all salts. This α -helical content falls in the range of 15–18% we obtained when fibrinogen was precipitated in the denaturing agents GdnHCl and urea. Interestingly, when fibrinogen fibers were assembled in 2.5× PBS, the α -helix content was also around 17% while fibrinogen in Tris alone showed the highest α -helix content of all precipitates with 21 ± 4%. The lowest β -strand content was found for fibrinogen in Tris with 33 ± 5%, while the β -strand content of fibrinogen precipitates with divalent ions was slightly higher varying from 35 to 40%, and denatured fibrinogen films exhibited β -strand ratios in the same range with 37–38%. The highest β -strand ratio of 42 ± 1% was found when fibrinogen was assembled into fibers with 2.5× PBS. Interestingly, the average content of other secondary structures varied between 46 and 51% for fibrinogen in divalent salts, in denaturing agents, and in Tris alone, while the lowest content of other structures of 41 ± 1% was found for fibrinogen in 2.5× PBS.

Similarly to our previous study, there was an increase in β -strand structures that was accompanied by a decrease in the α -helical content in comparison to the reference planar sample prepared in Tris, even for fibrinogen with denaturing agents. Analogous trends in varying fibrinogen secondary structure were also found in other works that analyzed fibrinogen adsorption on various hydrophilic or hydrophobic surfaces.^{64,65} Other studies have investigated the mechanism and denaturation potential of GdnHCl and urea for various proteins.^{66–71} Thereby, the

relative effectiveness of the denaturing agents depends on the particular protein. Huerta-Viga and Woutersen, for instance, observed that β -sheet-rich proteins were more affected by GdnHCl than α -rich ones.⁶⁷ On the other hand, similarly to our trend, Emadi and Behzadi observed a transition from α -helices to β -sheet aggregates when adding GdnHCl to lysozyme.⁷¹ During denaturation of lysozyme with urea, however, the protein structure remained α -helical.⁷¹ Although structurally similar, GdnHCl and urea induce protein denaturation by different mechanisms, which might explain why we observed different secondary structures of fibrinogen dried in the presence of these two denaturants.⁶⁸

Protein folding and unfolding can be induced by direct binding of a ligand to a protein, ion effects, or by changing the structure of the solvent.^{16,72} The potential of different ions to stabilize a protein in solution and precipitate in a folded structure (*i.e.*, to salt out) has been described in the Hofmeister series.⁷³ The so-called chaotropic ions have the disorder-promoting tendency to “salt in” a protein by disrupting hydrogen bonds, which leads to protein unfolding.⁷⁴ On the other side are the kosmotropic ions with the order-making tendency of stabilizing hydrogen bridges, which ultimately leads to protein precipitation.⁷⁴ Urea, for example, has exclusively chaotropic effects, while GdnHCl, as a monovalent salt, has both ionic and chaotropic effects.⁷⁵ Therefore, it is highly interesting that the divalent cations used to precipitate fibrinogen in our present study induced similar secondary structure changes compared with the two denaturants. Small anions with high charge density, or with a moderate charge density like chlorides, have the tendency to stabilize and to salt out proteins, while hard and polyvalent cations like Mg²⁺ and Cu²⁺ tend to salt in and dissolve or even unfold a protein.¹⁶ When we compare the monovalent Na⁺ ions we previously found to induce fiber assembly^{47,48} with divalent cations in the Hofmeister series, it becomes obvious that Na⁺ has a higher tendency for salting out effects at an elevated ionic strength, while Ca²⁺, Mg²⁺, and Zn²⁺ are more prone to salting in at a moderate ionic strength.²⁷ Thus, it can be deduced from our results that divalent cations may interfere with fibrinogen monomers in drying salt solutions in a way that conformational changes occur, even before the solubility of the solution with salt is reached and precipitation of salt sets in. We assume that during protein solidification, fibrinogen growth units thus modified by divalent ions do not induce preferential growth directions. On the other hand, we have already established that monovalent ions tend to support conformations and intermolecular fibrinogen interactions that favor fiber formation and thus anisotropic fibrinogen–fibrinogen aggregation from saturated salt solutions.^{47,48} From a higher-level perspective, we therefore propose that salt-driven self-organization during droplet drying is governed by the comparatively poorly explored interactions among and between the co-solutes involved in an environment that evolves from a continuous and dynamic water solvent phase of a saturated solution to immobilized hydration shells that eventually collapse.

When comparing the secondary structure content of fibrinogen fibers assembled with 2.5× PBS in Tris with our previous study where NH₄HCO₃ was used as a background buffer, it can be seen that the respective conformational features agree well and were thus independent of the background buffer.⁴⁸ When fibrinogen was dried in NH₄HCO₃ alone to obtain planar films, however, we had previously obtained 28% α -helices, 25% β -strands, and 47% other structures, which was very

close to the structural features of native fibrinogen in different aqueous buffers that we obtained by CD spectroscopy (26% α -helices, 27% β -strands, and 47% other structures)⁴⁸ However, in the present study, fibrinogen in Tris yielded 21% α -helices, 33% β -strands, and 46% other structures, which was not as close to the native conformation in solution as fibrinogen in NH_4HCO_3 . Thus, the conformational fingerprint of dried fibrinogen precipitates in Tris buffer mainly differed from planar fibrinogen in NH_4HCO_3 via its α -helix and β -strand content, although the planar morphology we observed by SEM did not show any obvious differences.

Various buffer systems were previously found to influence the conformational stability of proteins,^{76,77} and it is well known that the presence of specific ligands or ions increases protein stability in solution.^{23,74,76} Ammonium and carbonate ions, for instance, have a tendency to stabilize and salt out proteins.²⁷ Since we previously used NH_4HCO_3 buffer while the present study was conducted in Tris, we hypothesize that the different ions in both buffers as well as the differences in pH (7.4 for Tris and 8.8 for NH_4HCO_3) may be responsible for the observed variations in fibrinogen conformation. Moreover, with NH_4HCO_3 being a highly volatile buffer that evaporates quickly in contrast to Tris, it is likely that more buffer residues are left in fibrinogen precipitates when Tris was used, which might also influence the resulting secondary structure.

In conclusion, the structural features of planar fibrinogen in Tris were closest to a more native fibrinogen conformation, yet further away than fibrinogen in NH_4HCO_3 ,⁴⁸ whereas all fibrinogen precipitates in divalent salts have a higher degree of disorder and strongly resembled the structural fingerprint of denatured fibrinogen films. In contrast, monovalent ions have a higher tendency to unfold fibrinogen from α -helices to β -strands structures than the divalent ions. As to be expected from the morphological SEM analysis, fibrinogen in divalent salts did not show any conformational changes that resembled the structure content we obtained for fibrinogen fibers in PBS. Despite the very pronounced conformational changes of fibrinogen in divalent salts, it is quite surprising that these precipitates exhibited a rather smooth surface topography, which resembled the morphology of fibrinogen dried in Tris. On the other hand, fibrinogen in denaturing agents precipitated with a more clumped morphology while exhibiting conformational changes that resembled those of smooth fibrinogen layers formed with divalent salts.

We speculate that the various fractions of denatured fibrinogen contribute to the observed changes of the opacity and a complex multiphase behavior during droplet drying and, moreover, cause the formed protein deposits to be composed of fibrinogen moieties with various molecular conformations as observed by our FTIR analysis. We hypothesize that during drying, these denatured species do not only show impaired intramolecular interactions but also weaker intermolecular interactions than required for fibrillogenesis. Dér et al. assessed salt-induced Hofmeister phenomena relating protein solidification with salt-induced changes of the hydrophobic/hydrophilic properties of protein–water interfaces.⁷⁸ And recently, Kainer et al.⁷⁹ highlighted that in high-salt regimes, especially the strength of hydrophobic and nonionic interactions is weakened by salts later in the Hofmeister series compared to salts earlier in the series, as may be exemplified by chlorides of divalent cations like Ca^{2+} , on the one hand, and alkali ions like Na^+ or K^+ , on the other hand. Accordingly, we suggest that salt-driven exposure of hydrophobic protein domains at the solvent-

accessible surface and enabling strong hydrophobic intermolecular interactions is a requisite of fibrillogenesis of fibrinogen because we only observed nanofibers in the presence of highly concentrated alkali-metal cations like K^+ or Na^+ , *i.e.*, the cationic counterpart of “Hofmeister-neutral” NaCl ,¹⁸ but not in alkaline earth or transition-metal dichloride solutions. Based on this rationale, we will assess in more detail the composition of solidified and dried fibrinogen materials with different textures in the subsequent section.

In our previous study, we had reported a clear correlation between the morphology of dried fibrinogen and its secondary structure in dependence of monovalent ions, *i.e.*, for fibrous and planar fibrinogen.^{47,48} Also recently, Barinov and co-workers reported myeloperoxidase-induced fibrinogen fiber formation associated with an increase in β -strand content.⁴⁴ However, in our present study with divalent ions, no correlation between morphology and secondary structure was found since fibrinogen precipitates with and without divalent salts showed very similar, rather smooth surface topographies while their structural fingerprints varied strongly. In particular, the secondary structure of fibrinogen dried in the presence of divalent ions was altered more significantly than with monovalent ions, which indicates a denatured conformation despite the smooth surface topography observed by SEM. Despite the high β -strand content we found for fibrinogen in the presence of divalent cations and denaturants, which is often observed when amyloid aggregates form fibrils under harsh conditions,⁸⁰ no fiber formation was observed for any of these fibrinogen precipitates. Similar observations were reported for lysozyme by Emadi and Behzadi who did not detect any fiber formation by AFM analysis when urea was used as a denaturing agent; instead, the protein partially maintained its α -helical structure.⁷¹ However, when lysozyme was completely converted to a β -strand conformation with GdnHCl and guanidine, thiocyanate protein aggregation and fibril formation were observed.⁷¹

Although the morphology of fibrinogen fibers that assembled with monovalent ions may be perceived as a highly unordered state of dried fibrinogen molecules in comparison to rather smooth precipitates that formed in the presence of either NH_4HCO_3 ^{47,48} or with divalent ions, our secondary structure analysis revealed that these morphological differences are associated with completely different degrees of molecular order: The highest degree of disorder was observed with divalent ions despite the smooth fibrinogen topography observed by SEM that was similar to our planar fibrinogen films previously assembled with NH_4HCO_3 .^{47,48} However, fibrinogen films formed in NH_4HCO_3 were associated with only minor shifts from α -helix to β -strand features compared with fibrinogen in solution.⁴⁸ Based on these findings, we conclude that the presence of divalent ions during fibrinogen precipitation may be based on mechanisms that are similar to fibrinogen aggregation in the presence of denaturing agents that strongly differ from those effects we previously observed for monovalent ions. Interestingly, other studies already suggested that fibrinogen can only assemble into fibers when its tertiary structure changes to release the αC regions.^{42,81,82} Therefore, it is possible that, similar to fibrin,⁸³ tertiary conformational changes play a more significant role in the fiber assembly of fibrinogen than secondary structure changes, as observed in the present and our previous studies.^{47,48} Hence, we conclude that only when specific interactions of certain ions with fibrinogen occur fibers can be assembled. Moreover, in contrast to previous studies where divalent ions in combination with monovalent

Table 1. Results for the Atomic Surface Concentration Given in Atomic % (atom %) Obtained from XPS Analysis When Investigating the Composition of Fibrinogen–Salt Precipitates on Glass Slides after Cross-Linking Fibrinogen (Fg) with FA Vapor and Rinsing with Pure Water for Distinct Rinsing Times^{a,b}

| sample | metal ion in starting solution | rinsing time (min) | [N] | [metal]/[N] | [Cl]/[N] | [S]/[N] | [P]/[N] |
|---------------------------------|----------------------------------|--------------------|------|-------------|----------|---------|---------|
| Fg and 2.5× PBS | Na ⁺ , K ⁺ | Metal = Na | | | | | |
| | | 0.5 min | 11.2 | 0.54 | 0.37 | 0.025 | 0.042 |
| | | 1 min | 13.7 | 0.18 | 0.057 | 0.026 | 0.013 |
| | | 30 min | 14.7 | 0.049 | 0.009 | 0.025 | - |
| | | 60 min | 16.2 | 0.034 | - | 0.028 | - |
| Fg and 375 mM MgCl ₂ | Mg ²⁺ | Metal = Mg | | | | | |
| | | 5 min | 15.9 | - | 0.014 | 0.021 | - |
| | | 30 min | 15.5 | - | - | 0.023 | - |
| Fg and 375 mM CaCl ₂ | Ca ²⁺ | Metal = Ca | | | | | |
| | | 5 min | 14.6 | 0.015 | 0.019 | 0.022 | - |
| | | 30 min | 16.4 | - | - | 0.022 | - |
| Fg and 375 mM CuCl ₂ | Cu ²⁺ | Metal = Cu | | | | | |
| | | 5 min | 14.5 | - | - | 0.018 | - |
| | | 30 min | 13.2 | - | - | 0.021 | - |
| Fg and 375 mM ZnCl ₂ | Zn ²⁺ | Metal = Zn | | | | | |
| | | 5 min | 14.2 | - | 0.007 | 0.017 | - |

^aFor all samples, either 375 mM concentration of the respective divalent salt or 2.5× PBS was used to precipitate 5 mg/mL fibrinogen upon drying.

^bHyphens (-) indicate that the concentrations were below the detection limit (DL).

Table 2. Atomic Concentration in Atomic % (atom %) Obtained from EDX Measurements at 10 kV When Investigating the Composition of Fibrinogen–Salt Precipitates on Glass Slides after Cross-Linking Fibrinogen (Fg) with FA Vapor and Rinsing for 5 min with Pure Water^{a,b}

| sample | metal ion in starting solution | rinsing time (min) | [metal]/[N] | [Cl]/[N] | [S]/[N] | [P]/[N] |
|---------------------------------|----------------------------------|--------------------|-------------|----------|---------|---------|
| Fg and 2.5× PBS | Na ⁺ , K ⁺ | Metal = Na | | | | |
| | | 1 min | 0.09 | 0.05 | 0.02 | 0.01 |
| | | 30 min | 0.01 | - | 0.02 | - |
| Fg and 375 mM MgCl ₂ | Mg ²⁺ | Metal = Mg | | | | |
| | | 5 min | - | 0.01 | 0.02 | - |
| Fg and 375 mM CaCl ₂ | Ca ²⁺ | Metal = Ca | | | | |
| | | 5 min | <0.01 | 0.02 | 0.02 | - |
| Fg and 375 mM CuCl ₂ | Cu ²⁺ | Metal = Cu | | | | |
| | | 5 min | - | - | 0.02 | - |
| Fg and 375 mM ZnCl ₂ | Zn ²⁺ | Metal = Zn | | | | |
| | | 5 min | 0.03 | 0.01 | 0.03 | - |

^aFor all samples, either a 375 mM concentration of the respective divalent salt or 2.5× PBS was used to precipitate 5 mg/mL fibrinogen upon drying. ^bHyphens (-) indicate that the concentrations were below the detection limit DL.

ions were found to induce fibril formation of fibrinogen in aqueous solutions,^{50,51} we did not observe any fiber formation upon drying.

So far, it is not clear, why the change from monovalent to divalent ions has such a drastic influence on the occurrence of fiber formation. We can only assume that the more compact hydration shells of divalent metal ions reported in Table S1 prevent the interaction of these ions with fibrinogen molecules in a way that excludes any tertiary changes as they might be possible with monovalent ions that exhibit larger hydration shells. Therefore, detailed studies on the effect of ions with different charges and sizes on the fibrinogen–ion interaction, their influence on fibrillogenesis, and dependence on aqueous and dry environments will be required as a next step. To unravel the fundamental mechanisms of fibrinogen fiber assembly across different length scales, these future studies will benefit from CD spectroscopy in solution and in the dried state⁴⁸ as well as from complementary molecular dynamics simulations.³⁸

3.3. Chemical Composition of Fibrinogen Precipitates with Divalent Ions. A first step into that direction is to clarify

whether specific interactions between fibrinogen and the salt or the corresponding cations and anions might affect the dissolution or desorption of metal or chloride ions. In this course, we show an analytical investigation on the elemental composition and in particular any metal-related signals at the protein surface of fibrinogen precipitates dried in the presence of a 375 mM concentration of divalent salts or with 2.5× PBS. All fibrinogen–salt precipitates were rinsed with water after cross-linking and analyzed by XPS. The resulting atomic surface concentrations are presented in Table 1, and detailed spectra are shown in Figure S6 in the Supporting Information.

Only for fibrinogen solidified from an aqueous solution containing 375 mM CaCl₂, a 5 min water rinsing after cross-linking the protein precipitate was observed not to be sufficient for achieving a complete removal of salt-related species from the film. However, the [Ca]/[N] ratio of 0.015 and the [Cl]/[N] ratio of 0.019 found after 5 min washing was no longer present when the washing time was extended to 30 min. In the presence of all other divalent salts, neither metal-related nor Cl-based moieties were detected, neither after 5 min nor after 30 min

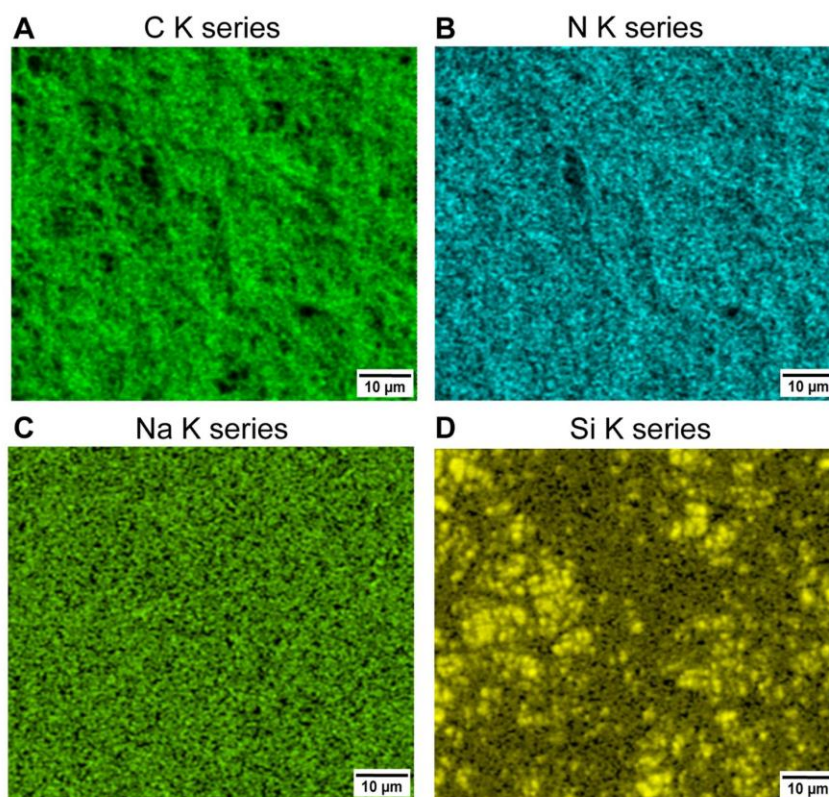


Figure 6. EDX mapping of fibrinogen precipitates prepared after dyeing 5 mg/mL fibrinogen with 2.5× PBS on Si wafer. EDX analysis (5 kV) was performed after cross-linking and washing the scaffold for 30 min. The elemental composition shows the distribution of (A) carbon, (B) nitrogen, (C) sodium, and (D) silicon on the prepared sample.

rinsing. From this finding, we infer that the precipitated salts contained in the fibrinogen films or deposited on top of the films rapidly got dissolved in water and were removed from the film surface when displacing the water droplet applied for rinsing. According to the EDX findings displayed in Table 2, this rationale is further supported when embracing essentially the complete film thickness within the information volume of EDX analysis because only minor concentrations of metal or chloride species contained in the starting solutions were found. Hence, we attribute these species to trace remainders.

When fibrinogen had been precipitated from an aqueous solution containing 2.5× PBS to form fibers, the detected atomic surface concentration of [N] increased from 11.2 to 16.2 between 0.5 min and 60 min washing. Accordingly, the [Na]/[N] content decreased from 0.54 to 0.049, and the [Cl]/[N] signal decreased from 0.37 to 0.009 when the washing time was extended from 0.5 to 30 min. Similarly, decreasing trends were found for the [S]/[N] and [P]/[N] ratios of fibrinogen–PBS precipitates. From these trends, we conclude once again that the precipitated salts contained in the fibrinogen films or deposited on top of the films rapidly got dissolved in water and were removed from the fiber surface when displacing the water droplet applied for rinsing. Remarkably, potassium species were not detected even though the PBS formulation contained KCl and KH_2PO_4 . However, even after a complete removal of phosphate and chloride as a consequence of 60 min washing, still a [Na]/[N] ratio of 0.034 was detected. As these Na^+ species do

not jointly occur with anionic constituents of the starting solution, we infer that these cations were attached to anionic sites in fibrinogen. We hypothesize that such incorporated Na^+ species are not causally related to our water-based rinsing of the precipitated salt–fibrinogen films but rather were absorbed so strongly in the fibrinogen already during protein solidification that they did not get released upon contact with water. We suggest anionic side-chain groups in fibrinogen to be potentially favored binding sites for Na^+ ions, and based on the observed [Na]/[N] concentration ratio and the amino acid composition of human fibrinogen,⁸⁴ we estimate that one-third of the possible carboxylate moieties are neutralized by alkali cations. According to the EDX findings displayed in Table 2, this rationale is further supported when embracing essentially the complete film thickness within the information volume of EDX analysis because 0.21 at% sodium concentrations and minor concentrations of chloride were found after 30 min of rinsing with water. Figure 6 shows the results of the EDX mapping obtained with an electron acceleration voltage of 5 kV for a fibrous fibrinogen film prepared using 2.5x PBS on a silicon wafer. As expected, carbon and nitrogen are evenly distributed showing the composition of the protein. The detected sodium is also detected on the whole selected surface area, sustaining the hypothesis that sodium cations were attached to anionic sites in fibrinogen. Moreover, Figure 6D still shows Si from the silicon wafer substrate, showing that despite the high protein

concentration (5 mg/mL), the surface is not completely covered by the porous film of fibrinogen nanofibers.

In summary, for all fibrinogen precipitates with dichloride, we observed that the metal cations and chloride anions had been removed completely after a rinsing period not exceeding 30 min, while fibrinogen precipitates prepared from monovalent PBS solutions contained significant concentrations of Na⁺ ions even after thorough removal of chloride or phosphate ions. From this finding, we infer that upon exposure to water, Na⁺ ions show a stronger interaction with cross-linked fibrinogen deposits than any of the divalent ions Mg²⁺, Ca²⁺, Cu²⁺, or Zn²⁺. This is rather an unexpected finding in view of the behavior observed for distinct protein-containing molecules, as may be exemplified by protein folds in B domains of adhesions that reveal calcium-tunable force response and owe their stability to the coordination of Ca²⁺ ions.⁸⁵ Therefore, our XPS and EDX results provide an excellent base for further studies on the assembly of fibrinogen in the presence of ions with different charges and sizes where we aim to elucidate their tendency to be absorbed into dried fibrinogen films or fibers. We expect to gain more insight by applying our methodology to quantitatively investigate the correlations between fiber formation on the one hand and concentration ratios of anionic side-chain groups in dispersed or solidified fibrinogen and monovalent metal or hydronium cations on the other hand.

If we now discuss our findings on salt-driven fibrillogenesis with the help of the ionic properties from Table S1, we can conclude that an increase in the charge density for cations leads to closer coordinative binding of the surrounding water molecules^{31,32} and results in the suppression of direct protein–ion contact with ligands originating from fibrinogen and especially side chains contributing to the cation complexation. We interpret our result to mean that fully hydrated divalent ions have indirectly weaker interactions with the protein than monovalent ions and that divalent ions can therefore be completely washed out of the protein aggregates. Until now, it has always been assumed that the resulting greater disorder in the nearby hydrogen-bond network^{35,36} leads to macroscopic salting in and out effects that directly influence the impact on (de)naturation of proteins along the Hofmeister series.^{31,74} However, the experiments rather indicate that potentially partly dehydrated sodium ions can bind directly to fibrinogen molecules because the surrounding hydrate shell is less strongly bound to these alkali-metal ions. This is also indicated by calculations of the potential mean force (PMF) in a recent work by Kiyohara and Kawai,³² who found significantly higher binding forces for divalent than monovalent ions to water. Any fully hydrated ion that is not incorporated in a weakly soluble salt can, in principle, be washed away as we confirmed in our XPS experiments with fibrinogen precipitates. In contrast, ions capable of breaking their hydration shell in favor of a direct protein–ion contact can be incorporated into the protein molecule and induce morphological changes (possibly even before protein solidification)—as we observed them by different tendencies in inducing the assembly of fibrinogen fibers.

4. CONCLUSIONS

In this study, we showed that divalent metal ions, irrespective of their concentration, did not induce any fiber assembly during fibrinogen precipitation, as we had previously observed with various monovalent ions. Although divalent ions induced strong changes in the protein conformation, these structural features were not correlated with any morphologically shaping

transitions. To monitor the interaction of fibrinogen with different salts already during drying, we used angle-resolved light scattering, which enabled us for the first time to follow the deposits resulting from fibrinogen precipitation in real time. In future studies, this technique will become a valuable *in situ* tool for predicting the tendency of various salts to induce fiber assembly of fibrinogen or other proteins. Moreover, with Aq mapping, XPS, and EDX analysis, we were able to distinguish between fibrous and nonfibrous fibrinogen precipitates based on the observed difference in surface roughness and metal-related signals. In particular, we observed that divalent salts were removed from cross-linked fibrinogen precipitates after washing with water while monovalent Na⁺ species could be detected in self-assembled fibers, which indicates that monovalent species might be coordinated in the fibrinogen films.

The clear difference between monovalent and divalent ions in their effect on salt-driven fibrinogen fibrillogenesis is the dissolubility of all nonmonovalent ions when washing cross-linked fibrinogen with water. This, together with the exclusion of any fiber-forming influences of nonmonovalent ions, allows us to conclude that the self-assembly of fibrinogen into nanofibers can only be induced by monovalent cations (and not multivalent cations or anions) in direct contact with the protein. The decisive factor seems to be that the hydration shell of monovalent cations is softer and can thus be broken and partly detached in contact with fibrinogen domains. However, to fully understand the formation of salt-induced fibrinogen nanofibers, further experimental and theoretical studies addressing individual protein regions and their conformation and complexation behavior in a highly saline environment are necessary.

■ ASSOCIATED CONTENT

SI Supporting Information

The Supporting Information is available free of charge at <https://pubs.acs.org/doi/10.1021/acs.biomac.1c00930>.

Overview of ionic properties, secondary structure analysis description and results showing cross-sectional SEM images, substrate influence on fibrinogen morphology, details on the influence of denaturing agents on fibrinogen morphology, and fitted XPS spectra (PDF)

■ AUTHOR INFORMATION

Corresponding Author

Dorothea Brüggemann – Institute for Biophysics, University of Bremen, 28359 Bremen, Germany; MAPEX Center for Materials and Processes, University of Bremen, 28359 Bremen, Germany; orcid.org/0000-0002-7140-3275; Email: brueggemann@uni-bremen.de

Authors

Stephani Stamboroski – Fraunhofer Institute for Manufacturing Technology and Advanced Materials IFAM, 28359 Bremen, Germany; Institute for Biophysics, University of Bremen, 28359 Bremen, Germany; orcid.org/0000-0002-8400-7909

Kwasi Boateng – Fraunhofer Institute for Manufacturing Technology and Advanced Materials IFAM, 28359 Bremen, Germany; Institute for Biophysics, University of Bremen, 28359 Bremen, Germany

Jana Lierath – Fraunhofer Institute for Manufacturing Technology and Advanced Materials IFAM, 28359 Bremen,

Germany; Institute for Biophysics, University of Bremen, 28359 Bremen, Germany

Thomas Kowalik – Fraunhofer Institute for Manufacturing Technology and Advanced Materials IFAM, 28359 Bremen, Germany

Karsten Thiel – Fraunhofer Institute for Manufacturing Technology and Advanced Materials IFAM, 28359 Bremen, Germany

Susan Köppen – Hybrid Materials Interfaces Group, Faculty of Production Engineering and Bremen Center for Computational Materials Science, University of Bremen, 28359 Bremen, Germany; MAPEX Center for Materials and Processes, University of Bremen, 28359 Bremen, Germany; orcid.org/0000-0001-7626-9936

Paul-Ludwig Michael Noeske – Fraunhofer Institute for Manufacturing Technology and Advanced Materials IFAM, 28359 Bremen, Germany

Complete contact information is available at:

<https://pubs.acs.org/10.1021/acs.biomac.1c00930>

Author Contributions

St.S. planned and performed experiments, analyzed data, and was involved in writing the manuscript. K.B. and J.L. performed experiments and analyzed data. T.K. planned experiments, discussed data, and was involved in writing the manuscript. K.T. planned and performed experiments and analyzed data. S.K. analyzed and discussed data and was involved in writing the manuscript. M.N. planned and performed experiments and was involved in writing the manuscript, D.B. conceived the idea, planned experiments, analyzed data, and was involved in writing the manuscript. All authors have given approval to the final version of the manuscript.

Notes

The authors declare no competing financial interest.

ACKNOWLEDGMENTS

The authors gratefully acknowledge funding by the Emmy Noether program of the German Research Council (DFG) via grant number 267326782. S.S. was financially supported by the internal program Fraunhofer TALENTA start. The authors thank Julian Heine for access to the light scattering device, Petra Witte for her support with scanning electron microscopy, and R. Brodmann and B. Brodmann (OptoSurf GmbH) for instrumental discussions with respect to surface investigations based on the light scattering technique.

REFERENCES

- Weisel, J. W.; Litvinov, R. I. Fibrin Formation, Structure and Properties. In *Sub-Cellular Biochemistry*; Springer, 2017; Vol. 82, pp 405–456.
- Barker, T. H.; Engler, A. J. The Provisional Matrix: Setting the Stage for Tissue Repair Outcomes. *Matrix Biol.* **2017**, *60–61*, 1–4.
- Joo, J. Y.; Amin, M. L.; Rajangam, T.; An, S. S. A. Fibrinogen as a Promising Material for Various Biomedical Applications. *Mol. Cell. Toxicol.* **2015**, *11*, 1–9.
- Rajangam, T.; An, S. S. A. Fibrinogen and Fibrin Based Micro and Nano Scaffolds Incorporated with Drugs, Proteins, Cells and Genes for Therapeutic Biomedical Applications. *Int. J. Nanomed.* **2013**, *8*, 3641–3662.
- Zhang, K.; Chen, J. F. The Regulation of Integrin Function by Divalent Cations. *Cell Adhes. Migr.* **2012**, *6*, 20–29.
- Dugan, T. A.; Yang, V. W. C.; McQuillan, D. J.; Höök, M. Decorin Binds Fibrinogen in a Zn²⁺-Dependent Interaction. *J. Biol. Chem.* **2003**, *278*, 13655–13662.

(7) Lages, B.; Stivala, S. S. Copper Ion Binding and Heparin Interactions of Human Fibrinogen. *Biopolymers* **1973**, *12*, 961–974.

(8) Borkow, G.; Gabbay, J.; Dardik, R.; Eidelman, A. I.; Lavie, Y.; Grunfeld, Y.; Ikher, S.; Huszar, M.; Zatzoff, R. C.; Marikovsky, M. Molecular Mechanisms of Enhanced Wound Healing by Copper Oxide-Impregnated Dressings. *Wound Repair Regen.* **2010**, *18*, 266–275.

(9) Stelling, M. P.; Motta, J. M.; Mashid, M.; Johnson, W. E.; Pavão, M. S.; Farrell, N. P. Metal Ions and the Extracellular Matrix in Tumor Migration. *FEBS J.* **2019**, *286*, 2950–2964.

(10) Goldstein, D. A. *Clinical Methods: The History, Physical, and Laboratory Examinations Chapter 143: Serum Calcium*; Butterworths, 1990; Vol. 130.

(11) Gillham, M.; Sidebotham, D. Water and Electrolyte Disturbances. In *Cardiothoracic Critical Care*; Elsevier Inc., 2007; pp 470–480.

(12) Ellingsen, D. G.; Møller, L. B.; Aaseth, J. Copper. In *Handbook on the Toxicology of Metals*, 4th ed.; Elsevier Inc., 2015; Vol. 1, pp 765–786.

(13) Sandstead, H. H. Zinc. In *Handbook on the Toxicology of Metals*, 4th ed.; Elsevier Inc., 2015; Vol. 1, pp 1369–1385.

(14) Steven, F. S.; Griffin, M. M.; Brown, B. S.; Hulley, T. P. Aggregation of Fibrinogen Molecules by Metal Ions. *Int. J. Biol. Macromol.* **1982**, *4*, 367–369.

(15) Maeda, H.; Kishi, T.; Ikeda, S.; Sasaki, S.; Kito, K. Interaction of Human Fibrinogen with Divalent Metal Chlorides. *Int. J. Biol. Macromol.* **1983**, *5*, 159–162.

(16) Hyde, A. M.; Zultanski, S. L.; Waldman, J. H.; Zhong, Y. L.; Shevlin, M.; Peng, F. General Principles and Strategies for Salting-Out Informed by the Hofmeister Series. *Org. Process Res. Dev.* **2017**, *21*, 1355–1370.

(17) Pylaeva, S.; Brehm, M.; Sebastiani, D. Salt Bridge in Aqueous Solution: Strong Structural Motifs but Weak Enthalpic Effect. *Sci. Rep.* **2018**, *8*, No. 13626.

(18) Neagu, A.; Neagu, M.; Dér, A. Fluctuations and the Hofmeister Effect. *Biophys. J.* **2001**, *81*, 1285–1294.

(19) Bosshard, H. R.; Marti, D. N.; Jelesarov, I. Protein Stabilization by Salt Bridges: Concepts, Experimental Approaches and Clarification of Some Misunderstandings. *J. Mol. Recognit.* **2004**, *17*, 1–16.

(20) van Oss, C. J. Acid–Base Interfacial Interactions in Aqueous Media. *Colloids Surf., A* **1993**, *78*, 1–49.

(21) Austin, J.; Fernandes, D.; Ruzsala, M. J. A.; Hill, N.; Corbett, J. Routine, Ensemble Characterisation of Electrophoretic Mobility in High and Saturated Ionic Dispersions. *Sci. Rep.* **2020**, *10*, No. 4628.

(22) Cacace, M. G.; Landau, E. M.; Ramsden, J. J. The Hofmeister Series: Salt and Solvent Effects on Interfacial Phenomena. *Q. Rev. Biophys.* **1997**, *30*, 241–277.

(23) Okur, H. I.; Hladilková, J.; Rembert, K. B.; Cho, Y.; Heyda, J.; Dzubella, J.; Cremer, P. S.; Jungwirth, P. Beyond the Hofmeister Series: Ion-Specific Effects on Proteins and Their Biological Functions. *J. Phys. Chem. B* **2017**, *121*, 1997–2014.

(24) Salis, A.; Ninham, B. W. Models and Mechanisms of Hofmeister Effects in Electrolyte Solutions, and Colloid and Protein Systems Revisited. *Chem. Soc. Rev.* **2014**, *43*, 7358.

(25) Xie, W.; Liu, C.; Yang, L.; Gao, Y. On the Molecular Mechanism of Ion Specific Hofmeister Series. *Sci. China Chem.* **2014**, *57*, 36–47.

(26) Cassou, C. A.; Williams, E. R. Anions in Electrothermal Supercharging of Proteins with Electrospray Ionization Follow a Reverse Hofmeister Series. *Anal. Chem.* **2014**, *86*, 1640–1647.

(27) Kang, B.; Tang, H.; Zhao, Z.; Song, S. Hofmeister Series: Insights of Ion Specificity from Amphiphilic Assembly and Interface Property. *ACS Omega* **2020**, *5*, 6229–6239.

(28) Moghaddam, S. Z.; Thormann, E. The Hofmeister Series: Specific Ion Effects in Aqueous Polymer Solutions. *J. Colloid Interface Sci.* **2019**, *555*, 615–635.

(29) Chizhik, V. I.; Egorov, A. V.; Pavlova, M. S.; Egorova, M. I.; Donets, A. V. Structure of Hydration Shell of Calcium Cation by NMR Relaxation, Car-Parrinello Molecular Dynamics and Quantum-Chemical Calculations. *J. Mol. Liq.* **2016**, *224*, 730–736.

- (30) Bryantsev, V. S.; Diallo, M. S.; Van Duin, A. C. T.; Goddard, W. A. Hydration of Copper(II): New Insights from Density Functional Theory and the COSMO Solvation Model. *J. Phys. Chem. A* **2008**, *112*, 9104–9112.
- (31) Waluyo, I.; Huang, C.; Nordlund, D.; Bergmann, U.; Weiss, T. M.; Pettersson, L. G. M.; Nilsson, A. The Structure of Water in the Hydration Shell of Cations from X-Ray Raman and Small Angle x-Ray Scattering Measurements. *J. Chem. Phys.* **2011**, *134*, No. 064513.
- (32) Kiyohara, K.; Kawai, Y. Hydration of Monovalent and Divalent Cations near a Cathode Surface. *J. Chem. Phys.* **2019**, *151*, No. 104704.
- (33) Cunningham, E. M.; Taxer, T.; Heller, J.; Onćák, M.; van der Linde, C.; Beyer, M. K. Microsolvation of Zn Cations: Infrared Multiple Photon Dissociation Spectroscopy of $Zn+(H_2O)_n$ ($n = 2-35$). *Phys. Chem. Chem. Phys.* **2021**, *23*, 3627–3636.
- (34) O'Brien, J. T.; Williams, E. R. Coordination Numbers of Hydrated Divalent Transition Metal Ions Investigated with IRPD Spectroscopy. *J. Phys. Chem. A* **2011**, *115*, 14612–14619.
- (35) Zeng, Y.; Jia, Y.; Yan, T.; Zhuang, W. Binary Structure and Dynamics of the Hydrogen Bonds in the Hydration Shells of Ions. *Phys. Chem. Chem. Phys.* **2021**, *23*, 11400–11410.
- (36) Chen, Y.; Okur, H. I.; Liang, C.; Roke, S. Orientational Ordering of Water in Extended Hydration Shells of Cations Is Ion-Specific and Is Correlated Directly with Viscosity and Hydration Free Energy. *Phys. Chem. Chem. Phys.* **2017**, *19*, 24678–24688.
- (37) Carugo, O. When Proteins Are Completely Hydrated in Crystals. *Int. J. Biol. Macromol.* **2016**, *89*, 137–143.
- (38) Stamboroski, S.; Joshi, A.; Noeske, P.-L. M.; Köppen, S.; Brüggemann, D. Principles of Fibrinogen Fiber Assembly in Vitro. *Macromol. Biosci.* **2021**, *21*, No. 2000412.
- (39) Wnek, G. E.; Carr, M. E.; Simpson, D. G.; Bowlin, G. L. Electrospinning of Nanofiber Fibrinogen Structures. *Nano Lett.* **2003**, *3*, 213–216.
- (40) Mirzaei-Parsa, M. J.; Ghanizadeh, A.; Ebadi, M. T. K.; Faridi-Majidi, R. An Alternative Solvent for Electrospinning of Fibrinogen Nanofibers. *Biomed. Mater. Eng.* **2018**, *29*, 279–287.
- (41) Raoufi, M.; Aslankoochi, N.; Mollenhauer, C.; Boehm, H.; Spatz, J. P.; Brüggemann, D. Template-Assisted Extrusion of Biopolymer Nanofibers under Physiological Conditions. *Integr. Biol.* **2016**, *8*, 1059–1066.
- (42) Wei, G.; Reichert, J.; Bossert, J.; Jandt, K. D. Novel Biopolymeric Template for the Nucleation and Growth of Hydroxyapatite Crystals Based on Self-Assembled Fibrinogen Fibrils. *Biomacromolecules* **2008**, *9*, 3258–3267.
- (43) Rieu, C.; Mosser, G.; Haye, B.; Sanson, N.; Coradin, T.; Trichet, L. Thrombin-Free Polymerization Leads to Pure Fibrin(Ogen) Materials with Extended Processing Capacity. *bioRxiv* **2020**, 1–38.
- (44) Barinov, N. A.; Pavlova, E. R.; Tolstova, A. P.; Dubrovin, E. V.; Klinov, D. V. Myeloperoxidase-Induced Fibrinogen Unfolding and Clotting. *bioRxiv* **2021**, 1–19.
- (45) Wei, G.; Reichert, J.; Jandt, K. D. Controlled Self-Assembly and Templated Metallization of Fibrinogen Nanofibrils. *Chem. Commun.* **2008**, 3903–3905.
- (46) Wang, J.; Wang, H.; Wang, Y.; Li, J.; Su, Z.; Wei, G. Alternate Layer-by-Layer Assembly of Graphene Oxide Nanosheets and Fibrinogen Nanofibers on a Silicon Substrate for a Biomimetic Three-Dimensional Hydroxyapatite Scaffold. *J. Mater. Chem. B* **2014**, *2*, 7360–7368.
- (47) Stapelfeldt, K.; Stamboroski, S.; Mednikova, P.; Brüggemann, D. Fabrication of 3D-Nanofibrous Fibrinogen Scaffolds Using Salt-Induced Self Assembly. *Biofabrication* **2019**, *11*, No. 025010.
- (48) Stapelfeldt, K.; Stamboroski, S.; Walter, I.; Suter, N.; Kowalik, T.; Michaelis, M.; Br, D. Controlling the Multiscale Structure of Nanofibrous Fibrinogen Scaffolds for Wound Healing. *Nano Lett.* **2019**, *19*, 6554–6563.
- (49) Suter, N.; Joshi, A.; Wunsch, T.; Graupner, N.; Stapelfeldt, K.; Radmacher, M.; Müssig, J.; Brüggemann, D. Self-Assembled Fibrinogen Nanofibers Support Fibroblast Adhesion and Prevent *E. coli* Infiltration. *Mater. Sci. Eng., C* **2021**, *126*, No. 112156.
- (50) Dubrovin, E. V.; Barinov, N. A.; Schäffer, T. E.; Klinov, D. V. In Situ Single-Molecule AFM Investigation of Surface-Induced Fibrinogen Unfolding on Graphite. *Langmuir* **2019**, *35*, 9732–9739.
- (51) Chen, G.; Ni, N.; Wang, B.; Xu, B. Fibrinogen Nanofibril Growth and Self-Assembly on Au (1,1,1) Surface in the Absence of Thrombin. *ChemPhysChem* **2010**, *11*, 565–568.
- (52) Feidenhans'l, N. A.; Hansen, P. E.; Pilný, L.; Madsen, M. H.; Bissacco, G.; Petersen, J. C.; Taboryski, R. Comparison of Optical Methods for Surface Roughness Characterization. *Meas. Sci. Technol.* **2015**, *26*, 085208–085217.
- (53) Verband der automobilindustrie E. V., (VDA). *Geometrische Produktspezifikation Oberflächenbeschaffenheit Winkelauflöste Streulichtmesstechnik Definition, Kenngrößen Und Anwendung*; VDA 2009:2010-07; Berlin, 2010.
- (54) Seewig, J.; Beichert, G.; Brodmann, R.; Bodschwinn, H.; Wendel, M. In *Extraction of Shape and Roughness Using Scattering Light*, Optical Measurement Systems for Industrial Inspection VI, 2009; 73890N.
- (55) Jiang, B.; Tsavalas, J. G.; Sundberg, D. C. Water Whitening of Polymer Films: Mechanistic Studies and Comparisons between Water and Solvent Borne Films. *Prog. Org. Coat.* **2017**, *105*, 56–66.
- (56) Pervin, R.; Ghosh, P.; Basavaraj, M. G. Tailoring Pore Distribution in Polymer Films via Evaporation Induced Phase Separation. *RSC Adv.* **2019**, *9*, 15593–15605.
- (57) Liu, C.; Min, F.; Liu, L.; Chen, J. Hydration Properties of Alkali and Alkaline Earth Metal Ions in Aqueous Solution: A Molecular Dynamics Study. *Chem. Phys. Lett.* **2019**, *727*, 31–37.
- (58) Devlin, N. R.; Loehr, K.; Harris, M. T. The Importance of Gravity in Droplet Evaporation: A Comparison of Pendant and Sessile Drop Evaporation with Particles. *AIChE J.* **2016**, *62*, 947–955.
- (59) Dutta Choudhury, M.; Dutta, T.; Tarafdar, S. Growth Kinetics of NaCl Crystals in a Drying Drop of Gelatin: Transition from Faceted to Dendritic Growth. *Soft Matter* **2015**, *11*, 6938–6947.
- (60) Laclair, C. E.; Etzel, M. R. Turbidity and Protein Aggregation in Whey Protein Beverages. *J. Food Sci.* **2009**, *74*, C526–C535.
- (61) Montoya, G.; Lopez, K.; Arenas, J.; Zamora, C.; Hoz, L.; Romo, E.; Jiménez, K.; Arzate, H. Nucleation and Growth Inhibition of Biological Minerals by Cementum Attachment Protein-derived Peptide (CAP-pi). *J. Pept. Sci.* **2020**, *26*, No. e3282.
- (62) McBride, S. A.; Skye, R.; Varanasi, K. K. Differences between Colloidal and Crystalline Evaporative Deposits. *Langmuir* **2020**, *36*, 11732–11741.
- (63) Helbing, C.; Stoeßel, R.; Hering, D. A.; Arras, M. M. L.; Bossert, J.; Jandt, K. D. PH-Dependent Ordered Fibrinogen Adsorption on Polyethylene Single Crystals. *Langmuir* **2016**, *32*, 11868–11877.
- (64) Roach, P.; Farrar, D.; Perry, C. C. Interpretation of Protein Adsorption: Surface-Induced Conformational Changes. *J. Am. Chem. Soc.* **2005**, *127*, 8168–8173.
- (65) Sivaraman, B.; Fears, K. P.; Latour, R. A. Investigation of the Effects of Surface Chemistry and Solution Concentration on the Conformation of Adsorbed Proteins Using an Improved Circular Dichroism Method. *Langmuir* **2009**, *25*, 3050–3056.
- (66) Wingfield, P. T. Use of Protein Folding Reagents. *Curr. Protoc. Protein Sci.* **2016**, *84*, A–3A.
- (67) Huerta-Viga, A.; Woutersen, S. Protein Denaturation with Guanidinium: A 2D-IR Study. *J. Phys. Chem. Lett.* **2013**, *4*, 3397–3401.
- (68) Lim, W. K.; Rösger, J.; Englander, S. W. Urea, but Not Guanidinium, Destabilizes Proteins by Forming Hydrogen Bonds to the Peptide Group. *Proc. Natl. Acad. Sci. U.S.A.* **2009**, *106*, 2595–2600.
- (69) Dong, A.; Randolph, T. W.; Carpenter, J. F. Entrapping Intermediates of Thermal Aggregation in α -Helical Proteins with Low Concentration of Guanidine Hydrochloride. *J. Biol. Chem.* **2000**, *275*, 27689–27693.
- (70) Greene, R. F.; Pace, C. N. Urea and Guanidine Hydrochloride Denaturation of Ribonuclease, Lysozyme, α Chymotrypsin, and β Lactoglobulin. *J. Biol. Chem.* **1974**, *249*, 5388–5393.
- (71) Emadi, S.; Behzadi, M. A Comparative Study on the Aggregating Effects of Guanidine Thiocyanate, Guanidine Hydrochloride and Urea

on Lysozyme Aggregation. *Biochem. Biophys. Res. Commun.* **2014**, *450*, 1339–1344.

(72) Crevenna, A. H.; Naredi-Rainer, N.; Lamb, D. C.; Wedlich-Söldner, R.; Dzubiella, J. Effects of Hofmeister Ions on the α -Helical Structure of Proteins. *Biophys. J.* **2012**, *102*, 907–915.

(73) Baldwin, R. L. How Hofmeister Ion Interactions Affect Protein Stability. *Biophys. J.* **1996**, *71*, 2056–2063.

(74) Xie, W. J.; Gao, Y. Q. A Simple Theory for the Hofmeister Series. *J. Phys. Chem. Lett.* **2013**, *4*, 4247–4252.

(75) Rashid, F.; Sharma, S.; Bano, B. Comparison of Guanidine Hydrochloride (GdnHCl) and Urea Denaturation on Inactivation and Unfolding of Human Placental Cystatin (HPC). *Protein J.* **2005**, *24*, 283–292.

(76) Loreto, S.; Cuypers, B.; Brokken, J.; Van Doorslaer, S.; De Wael, K.; Meynen, V. The Effect of the Buffer Solution on the Adsorption and Stability of Horse Heart Myoglobin on Commercial Mesoporous Titanium Dioxide: A Matter of the Right Choice. *Phys. Chem. Chem. Phys.* **2017**, *19*, 13503–13514.

(77) Long, D.; Yang, D. Buffer Interference with Protein Dynamics: A Case Study on Human Liver Fatty Acid Binding Protein. *Biophys. J.* **2009**, *96*, 1482–1488.

(78) Dér, A.; Kelemen, L.; Fábán, L.; Taneva, S. G.; Fodor, E.; Páli, T.; Cupane, A.; Cacace, M. G.; Ramsden, J. J. Interfacial Water Structure Controls Protein Conformation. *J. Phys. Chem. B* **2007**, *111*, 5344–5350.

(79) Krainer, G.; Welsh, T. J.; Joseph, J. A.; Espinosa, J. R.; Wittmann, S.; de Csilléry, E.; Sridhar, A.; Toprakcioglu, Z.; Gudískyte, G.; Czekalska, M. A.; Arter, W. E.; Guillén-Boixet, J.; Franzmann, T. M.; Qamar, S.; George-Hyslop, P. S.; Hyman, A. A.; Collepardo-Guevara, R.; Alberti, S.; Knowles, T. P. J. Reentrant Liquid Condensate Phase of Proteins Is Stabilized by Hydrophobic and Non-Ionic Interactions. *Nat. Commun.* **2021**, *12*, No. 1085.

(80) Jahn, T. R.; Parker, M. J.; Homans, S. W.; Radford, S. E. Amyloid Formation under Physiological Conditions Proceeds via a Native-like Folding Intermediate. *Nat. Struct. Mol. Biol.* **2006**, *13*, 195–201.

(81) Zuev, Y. F.; Litvinov, R. I.; Sitnitsky, A. E.; Idiyatullin, B. Z.; Bakirova, D. R.; Galanakis, D. K.; Zhmurov, A.; Barsegov, V.; Weisel, J. W. Conformational Flexibility and Self-Association of Fibrinogen in Concentrated Solutions. *J. Phys. Chem. B* **2017**, *121*, 7833–7843.

(82) Koo, J.; Rafailovich, M. H.; Medved, L.; Tsurupa, G.; Kudryk, B. J.; Liu, Y.; Galanakis, D. K. Evaluation of Fibrinogen Self-Assembly: Role of Its AC Region. *J. Thromb. Haemost.* **2010**, *8*, 2727–2735.

(83) Dutta, B.; Vos, B. E.; Rezus, Y. L. A.; Koenderink, G. H.; Bakker, H. J. Observation of Ultrafast Vibrational Energy Transfer in Fibrinogen and Fibrin Fibers. *J. Phys. Chem. B* **2018**, *122*, 5870–5876.

(84) Henschen, A.; Mcdonagh, J. A. N. Fibrinogen, Fibrin and Factor XIII. In *New Comprehensive Biochemistry*; Elsevier, 1986; Vol. 13, pp 171–241.

(85) Milles, L. F.; Unterauer, E. M.; Nicolaus, T.; Gaub, H. E. Calcium Stabilizes the Strongest Protein Fold. *Nat. Commun.* **2018**, *9*, No. 4764.

Supporting information

Influence of divalent metal ions on the precipitation of the plasma protein fibrinogen

Stephani Stamboroski^{1,2}, Kwasi Boateng^{1,2}, Jana Lierath^{1,2}, Thomas Kowalik¹, Karsten Thiel¹, Susan Köppen^{3,4}, Paul-Ludwig Michael Noeske¹ & Dorothea Brüggemann^{2,4}*

¹ Fraunhofer Institute for Manufacturing Technology and Advanced Materials IFAM, Wiener Strasse 12, 28359 Bremen, Germany

² Institute for Biophysics, University of Bremen, Otto-Hahn-Allee 1, 28359 Bremen, Germany

³ Hybrid Materials Interfaces Group, Faculty of Production Engineering and Bremen Center for Computational Materials Science, University of Bremen, Am Fallturm 1, 28359 Bremen, Germany

⁴ MAPEX Center for Materials and Processes, University of Bremen, 28359 Bremen, Germany

* Corresponding author: brueggemann@uni-bremen.de

S1: Overview of ionic properties (on the atomic level)

Table S1: for each cationic ionic species, which is discussed in that work according their effect on protein morphology and conformation are listed. The table contains the ionic properties for mono and divalent ions (described in the Hofmeister series) and divalent transition metal ions (not addressed in the Hofmeister series)

| metal ion species | Hofmeister series | | | | | |
|--|-----------------------|------------------|---------------------|------------------|---|-------------------|
| | monovalent main group | | divalent main group | | divalent transition | |
| | K ⁺ | Na ⁺ | Mg ²⁺ | Ca ²⁺ | Cu ²⁺ | Zn ²⁺ |
| Period | 4 | 3 | 3 | 4 | 4 (3d) | 4 (3d) |
| vdW radii (pm) | 275 ¹ | 227 ¹ | 173 ¹ | 231 ¹ | 140 ² | 139 ² |
| coordination number | 4/ 137 | 4/ 99 | 4/ 57 | | 4/ 57 | 4/ 60 |
| CN / ionic Radii IR (pm) ³ | 6/ 138 | 6/ 102 | 6/ 72 | 6/ 100 | 6/ 73 | 6/ 74 |
| | 8/ 151 | 8/ 118 | 8/ 89 | 8/ 112 | | 8/ 90 |
| | | | | 10/ 123 | | |
| distance d _{IOion} - O _{H2O} (pm) | 283 ⁴ | 244 ⁴ | 209 ⁴ | 237 ⁴ | CN4: 1.942 ⁵ CN5: 2.044 ⁵ CN6:2.07 ⁵ | 1.96 ⁶ |
| Δ (d _{IO} – IR) (pm) | 145 | 142 | 137 | 137 | 134 (CN6) | 122 |
| distance d _{ion-H2O} of 1 st water layer (pm) ⁷ | 260 | 220 | 200 | 250 | -- | -- |
| distance d _{ion-H2O} of 2 nd water layer (pm) ⁷ | 490 | 430 | 410 | 450 | -- | -- |
| Δ 1 st – 2 nd hydration shell | 230 | 210 | 210 | 200 | -- | -- |

*O – O distance in bulk water 275 pm⁸

The Van der Waals (vdW) radius clearly correlates with the number of shells in the cations and decreases with the charge density of the ions, i.e. monovalent ions systematically have a larger vdW radius than divalent ions with the same number of shells. The same trend can be observed for the ionic radius (IR), but this depends on the number (CN) of coordinated water molecules. It increases with increasing CN. This form of radii are established in common handbooks.³

In more recent, largely theoretical works, the CN and the corresponding ion-water distance are increasingly discussed as the distance between the cation (nucleus) and oxygen of the water molecule and are marked in Table S1 as $d_{\text{IO ion} - \text{O}_{\text{H}_2\text{O}}}$.⁴⁻⁶ The difference of ion radius IR and $d_{\text{IO ion} - \text{O}_{\text{H}_2\text{O}}}$ shows the distance of the water molecules independent of the ion radius and reveals that water molecules are closer to the ion at higher charge density than in the case of monovalent ions. This effect is even stronger with transition metal ions. Anyway, all distances are smaller than the bulk water oxygen-oxygen distances⁸ and therefore lead to distortion of the hydrogen bonding network in water.

Furthermore, distances between ion, first and second hydration shell are also found in the literature⁷, whereby the position of the water layers is not normalised to the oxygen positions here. These values differ somewhat from the $d_{\text{IO ion} - \text{O}_{\text{H}_2\text{O}}}$ and show how differently these distances are defined in the literature. This makes it extremely difficult to compare the values from different publications in order to use them to explain the influence of the water structure on the interaction with proteins. The calculation of Kiyohara and Kawai of the first and second hydration shells around ions of the Hofmeister series show that the effect of proximity with the higher charge density is still noticeable in the second water layer.⁷

S2: Methods

Secondary structure analysis

The secondary structure was determined by deconvolution analysis and curve fitting of amide I bands using the Origin 2020 software (OriginLab Northampton, USA). An example of the amide I band deconvolution is shown in Figure S1. First a zero baseline was adjusted over the length of the amide I peak, which was then normalized. The number of underlying peaks in the amide I peak and their positions were determined by second derivative analysis. Curve fitting was performed using a non-linear least squares fitting applying Gaussian band shape. Half height band width was limited between 11 cm^{-1} to 15 cm^{-1} and allowed to assume any height and area. The fitting included 8 to 10 bands with two marginal bands that were included for the fit but excluded from the calculation of the secondary structure. Peak assignments were based on our previous study:⁹ 1614 cm^{-1} , 1625 cm^{-1} , 1636 cm^{-1} and 1691 cm^{-1} were assigned to β -strands, 1655 cm^{-1} to α -helix structures and 1645 cm^{-1} , 1667 cm^{-1} and 1679 cm^{-1} to other secondary structures (random coils, turns and loops). The content of the different secondary structure features was calculated by dividing the area of the peak assigned to a specific component by the total area of the amide I peak. Since a variation between the amide I peak shapes was observed within individual fibrinogen precipitates, more than one deconvolution was performed for each sample. With this routine, after the secondary structure quantification, the average and standard deviation for each fibrinogen-salt-combination was calculated.

Table S2: Range of positions of amide I and II bands for fibrinogen layers prepared after drying 5 mg/mL of fibrinogen with different salts

| Sample | Amide I band position | Amide II band position |
|-------------------------------|-----------------------|------------------------|
| Fg & 375 mM CaCl ₂ | 1630-1680 | 1536-1557 |
| Fg & 375 mM MgCl ₂ | 1647-1671 | 1545-1549 |
| Fg & 375 mM CuCl ₂ | 1630-1680 | 1535-1566 |
| Fg & 375 mM ZnCl ₂ | 1645-1686 | 1538-1560 |
| Fg & 4 M Urea | 1647-1665 | 1542-1551 |
| Fg & 4 M GdnHCl | 1647-1648 | 1539-1542 |
| Fg & 5 mM Tris | 1649-1670 | 1539-1552 |
| Fg & 2.5× PBS | 1653-1656 | 1544-1546 |

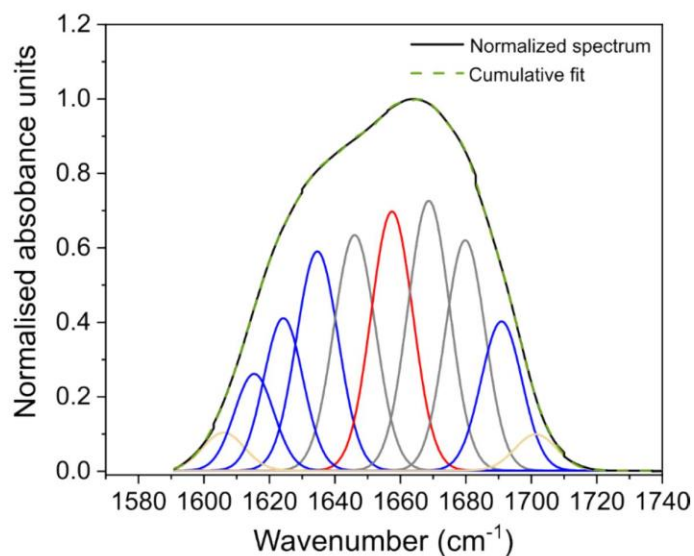


Figure S1: Example of the FTIR deconvolution of an amide I band for 5 mg/mL fibrinogen dried in the presence of 375 mM CaCl₂ after crosslinking and washing. The measured spectrum is shown in black below the cumulative fit (green dashed line). The color code of the contributing bands is based on red for α -helices, blue for β -strands and grey for “others”. The two yellow bands are marginal bands due to side-chain absorption that were included in the deconvolution but were not considered for the secondary structure quantification.

S3: Results

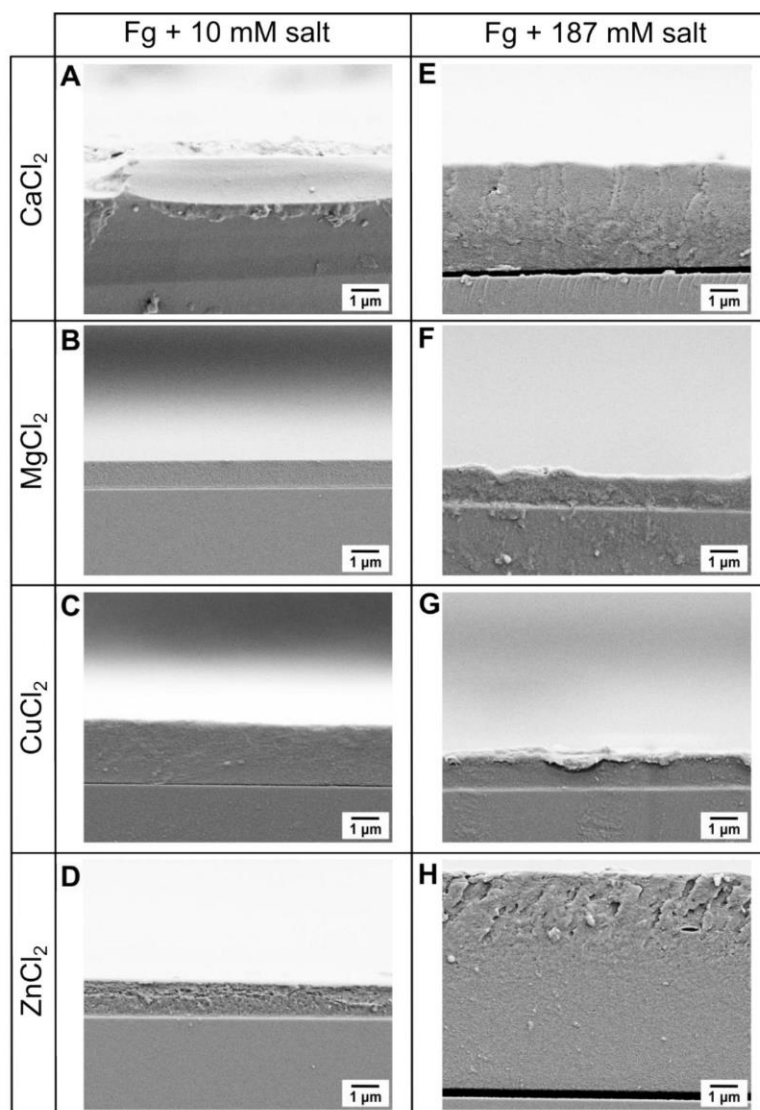


Figure S2: Cross-sectional SEM images of fibrinogen precipitates on APTES-modified glasses after drying in the presence of different divalent metal ions: 5 mg/mL fibrinogen dried with either 10 mM or 187 mM of (A, E) CaCl₂, (B, F) MgCl₂, (C, G) CuCl₂ and (D, H) ZnCl₂. The images revealed a compact film formation without the presence of fibers for all salts in the respective concentrations.

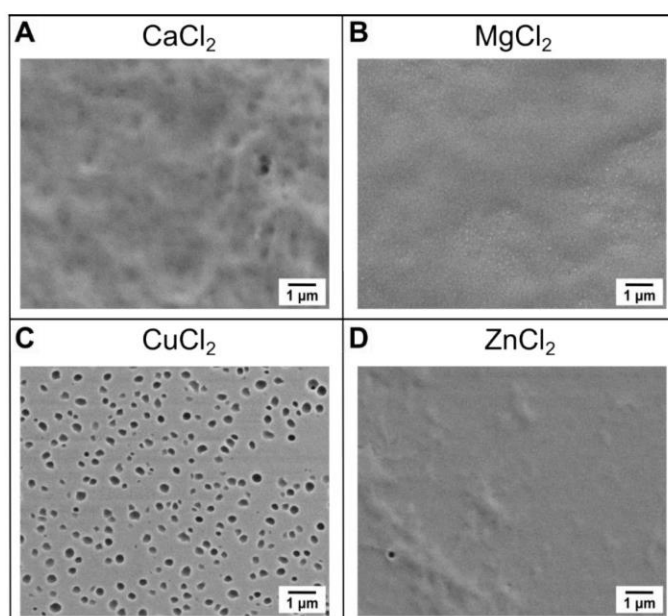


Figure S3: SEM images in top view of fibrinogen precipitates on gold prepared in the presence of different divalent metal ions: 5 mg/mL fibrinogen dried with 375 mM of (A) CaCl_2 , (B) MgCl_2 , (C) CuCl_2 and (D) ZnCl_2 . The fibrinogen precipitates exhibited similar morphology as on APTES-modified glass: CaCl_2 and ZnCl_2 formed rougher fibrinogen films than with MgCl_2 or CuCl_2 . For fibrinogen dried with MgCl_2 a smooth layer was formed while for CuCl_2 evenly distributed holes can be seen.

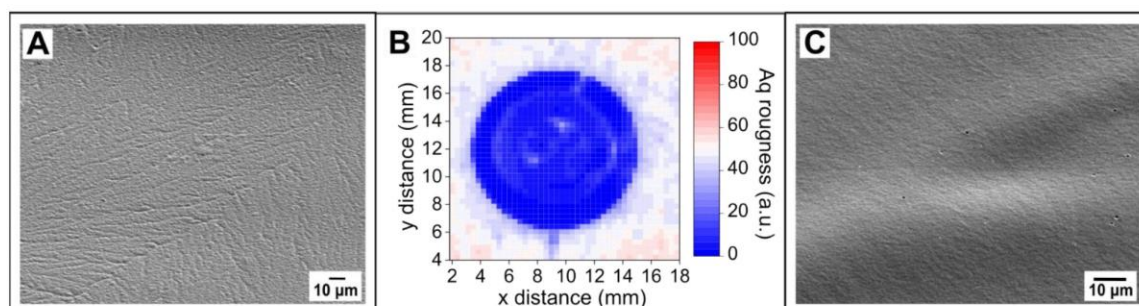


Figure S4: SEM images and Aq mapping of 5 mg/mL fibrinogen dried in the presence of 375 mM CuCl_2 and after crosslinking with vapor formaldehyde. SEM image (A) and Aq mapping (B) before rinsing and (C) SEM image after 5 min rinsing with pure water. Overall, before washing the fibrinogen layer shows a more inhomogeneous and locally rougher surface than after washing as also observed by the Aq mapping (see Fig. 3C in the main manuscript for Aq mapping after washing).

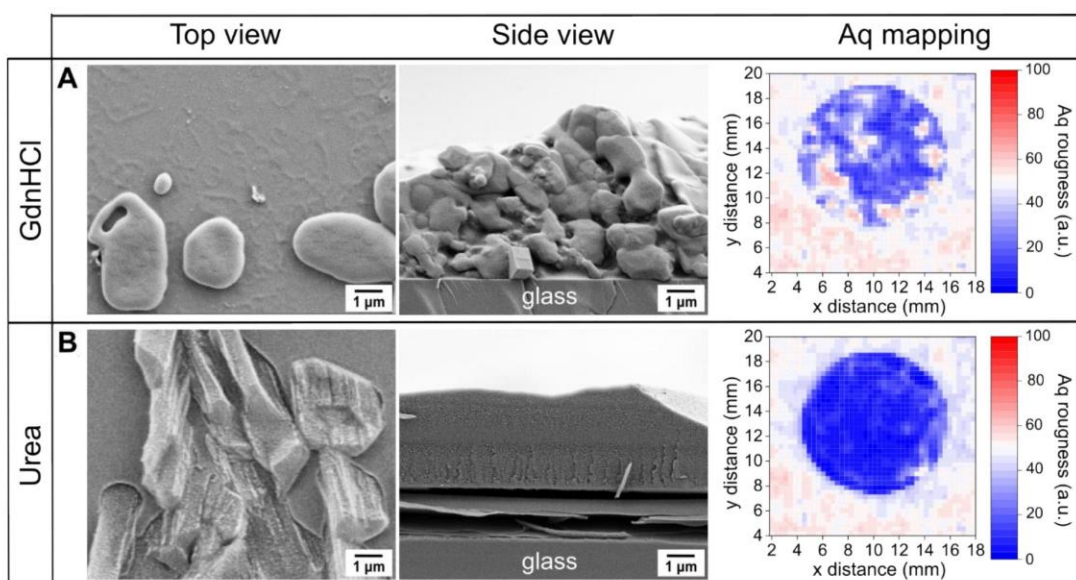


Figure S5: SEM images in top and side view perspective with Aq mappings of 5 mg/mL fibrinogen samples after droplet drying in the presence of denaturing agents: (A) 4 M GdnHCl and (B) 4 M urea. For SEM analysis, the precipitates were prepared on APTES-modified glass while for Aq mapping, fibrinogen precipitates were prepared on gold. From both perspectives fiber formation is not observed. Aq values reveal an inhomogeneous and predominantly rather smooth surface after washing out the denaturing agents.

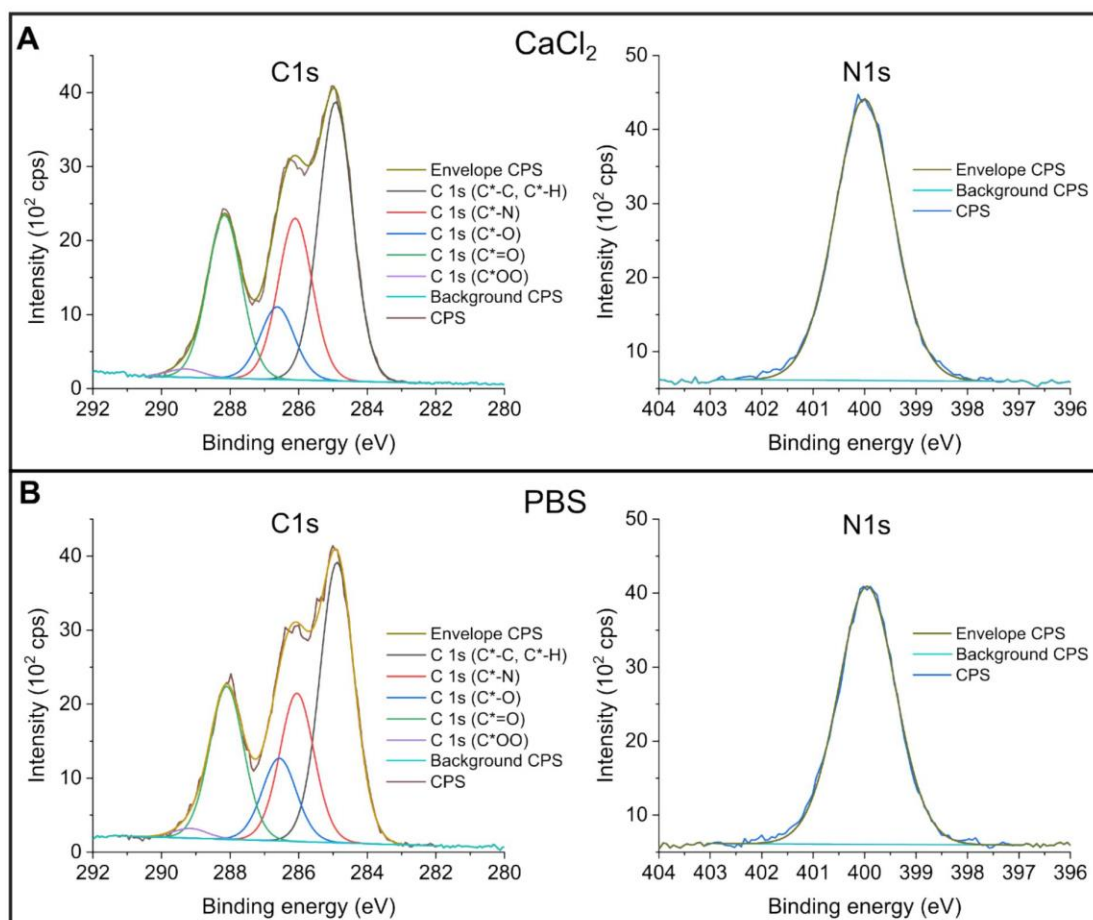


Figure S6: Deconvoluted C1s and fitted N1s XPS spectra of 5 mg/mL fibrinogen dried with 375 mM of (A) CaCl_2 or (B) 2.5xPBS after crosslinking and 30 min rinsing with pure water. The C1s photoelectron emission signals were decomposed according to binding energies of carbon atom cores in proteins. They are well fitted with components at 285.0 eV, corresponding to carbon atom cores envired by C–C and C–H bonds, 286.1 eV, corresponding to C–N bonds, 286.6 eV corresponding to C–O bonds, 288.2 eV corresponding to C=O, O–C–O or CO–N bonds preferentially in peptide groups and the component at 289.5 eV, corresponding to CO–O bonds.

References

- (1) Mantina, M.; Chamberlin, A. C.; Valero, R.; Cramer, C. J.; Truhlar, D. G. Consistent van Der Waals Radii for the Whole Main Group. *J. Phys. Chem. A* **2009**, *113* (19), 5806–5812. <https://doi.org/10.1021/jp8111556>.
- (2) Bondi, A. Van Der Waals Volumes and Radii. *J. Phys. Chem.* **1964**, *68* (3), 441–451.
- (3) David R. Lide. *CRC Handbook of Chemistry and Physics*, 82nd ed.; David R. Lide, Ed.; CRC Press.
- (4) Gagné, O. C.; Hawthorne, F. C. Bond-Length Distributions for Ions Bonded to Oxygen: Alkali and Alkaline-Earth Metals. *Acta Crystallogr. Sect. B Struct. Sci. Cryst. Eng. Mater.* **2016**, *72* (4), 602–625. <https://doi.org/10.1107/S2052520616008507>.
- (5) de Almeida, K. J.; Murugan, N. A.; Rinkevicius, Z.; Hugosson, H. W.; Vahtras, O.; Ågren, H.; Cesar, A. Conformations, Structural Transitions and Visible near-Infrared Absorption Spectra of Four-, Five- and Six-Coordinated Cu(II) Aqua Complexes. *Phys. Chem. Chem. Phys.* **2009**, *11* (3), 508–519. <https://doi.org/10.1039/B806423G>.
- (6) Nimmermark, A.; Öhrström, L.; Reedijk, J. Metal-Ligand Bond Lengths and Strengths: Are They Correlated? A Detailed CSD Analysis. *Zeitschrift für Krist. - Cryst. Mater.* **2013**, *228* (7), 311–317. <https://doi.org/10.1524/zkri.2013.1605>.
- (7) Kiyohara, K.; Kawai, Y. Hydration of Monovalent and Divalent Cations near a Cathode Surface. *J. Chem. Phys.* **2019**, *151* (10). <https://doi.org/10.1063/1.5113738>.
- (8) Waluyo, I.; Huang, C.; Nordlund, D.; Bergmann, U.; Weiss, T. M.; Pettersson, L. G. M.; Nilsson, A. The Structure of Water in the Hydration Shell of Cations from X-Ray Raman and Small Angle x-Ray Scattering Measurements. *J. Chem. Phys.* **2011**, *134* (6), 1–10. <https://doi.org/10.1063/1.3533958>.
- (9) Stapelfeldt, K.; Stamboroski, S.; Walter, I.; Suter, N.; Kowalik, T.; Michaelis, M.; Br, D. Controlling the Multiscale Structure of Nanofibrous Fibrinogen Scaffolds for Wound Healing. *Nano Lett.* **2019**, *49* (0), 1–15. <https://doi.org/https://doi.org/10.1021/acs.nanolett.9b02798>.

4. INFLUENCE OF HIGHLY SALINE AQUEOUS SOLUTIONS OF MONOVALENT ALKALI METAL IONS ON FIBRINOGEN SELF-ASSEMBLY *IN VITRO*

Status: parts of this chapter were prepared for submission.

4.1. MOTIVATION & HYPOTHESIS

Hypothesis addressed: Monovalent ions are a main driving force of fibrinogen fibrillogenesis in an enzyme-free environment.

The self-assembly of fibrinogen into fibers *in vitro* through drying fibrinogen from highly saline solutions seems to be intrinsically related to the composition of the salts. In Chapter 2, the review showed how difficult it is to detangle the influence of different metal ions on the fiber formation of fibrinogen, since they are always present during fibrinogen dissolution in buffers and consequently during fibrinogen precipitation on different surfaces. In Chapter 3 it was shown that the use of buffers comprising divalent metal cations resulted in the formation of smooth fibrinogen layers when fibrinogen was precipitated in the presence of chlorides containing Ca^{2+} , Mg^{2+} , Cu^{2+} , and Zn^{2+} ions. On the other hand, when fibrinogen was precipitated from a PBS solution, which was composed of monovalent salts (NaCl, KCl, Na_2HPO_4 , NaH_2PO_4), rougher and fibrous fibrinogen films were formed. The composition of the fibrinogen layers formed from divalent salts revealed the completely washing out of the ions, while for layers prepared from PBS, sodium was retained even after rinsing with water for 30 min.

Re-evaluation of the already published results in Chapters 3, 5 and 6 showed that the standard concentration to form fibers is optimal at 2.5 mg/ml and not at the reported value of 5 mg/ml. In Chapter 4, that reports research work to be submitted, a concentration of 2.5 mg/ml was used fibrinogen to conduct a systematic study on the ability of different monovalent salts to induce fibrillogenesis of fibrinogen. Different metals ions that are contained in PBS and other monovalent salts were investigated in their ability of forming rough and fibrous fibrinogen layers and how this behavior can be correlated with the salting-in/salting-out characteristic of the salts as well as the fibrinogen layer composition and fibrinogen secondary structure. Moreover, a 2D-Hofmeister series revealing the most suitable combinations of cations and anions in order to obtain rough and fibrous fibrinogen films was presented.

Hypothesis assessment: Confirmed.

Influence of highly saline aqueous solutions of monovalent alkali metal ions on fibrinogen self-assembly *in vitro*

Stephani Stamboroski^{1,2}, Kwasi Boateng^{1,2}, Jana Lierath^{1,2}, Jonas Aniol¹, Peter Schiffels¹, Paul-Ludwig Michael Noeske^{1,3}, Dorothea Brüggemann^{2,4, #, *}

¹ Fraunhofer Institute for Manufacturing Technology and Advanced Materials IFAM, Wiener Strasse 12, 28359 Bremen, Germany

² Institute for Biophysics, University of Bremen, Otto-Hahn-Allee 1, 28359 Bremen, Germany

³ University of Applied Sciences Bremerhaven, An der Karlstadt 8, Bremerhaven 27568, Germany

⁴ MAPEX Center for Materials and Processes, University of Bremen, 28359 Bremen, Germany

Present address: City University of Applied Sciences, Neustadtswall 30, 28199 Bremen, Germany

* Corresponding author: dorothea.brueggemann@hs-bremen.de

Abstract

Fibrinogen nanofiber scaffolds have great potential for tissue engineering and wound healing due to their biochemical and topographical similarity to fibrin blood clots. Here, we study the influence of alkaline salts (Na^+ , K^+) on the *in vitro* precipitation of fibrinogen from highly saline aqueous dispersions. By monitoring roughness (Aq) *in-situ* during drying we observed co-precipitation of monovalent salts and fibrinogen. SEM analysis and Aq-mapping of dried fibrinogen precipitates revealed varying fibrinogen morphologies ranging from smooth (KCl) and faintly fibrous (NaCl) to highly rough and finely fibrous (Na-PO_4 and K-PO_4) topographies. FTIR analysis showed that changes in the secondary structure do not necessarily lead to fiber formation, as has already been established for fibrinogen and divalent salts. XPS analyses demonstrated stronger ion uptake by fibrinogen for Na^+ than for K^+ , particularly with salts forming fine fibrinogen fibers. With highly saline solutions made of different oxygen-containing polyvalent anions that have Na^+ as a counter ion, we found that SO_4^{2-} as a more kosmotropic anion leads to fiber formation, whereas oxalate as a more chaotropic anion leads to smooth fibrinogen films. Combining divalent Mg^{2+} or monovalent K^+ with kosmotropic SO_4^{2-} , did not lead to fiber formation. Based on these findings, we propose a two-dimensional Hofmeister series to tailor fibrinogen fibrillogenesis with monovalent salts based on the selection of anion-cation pairs according to their chaotropic/kosmotropic nature. We conclude that fibrinogen fiber assembly is salt-driven and tailored by the intentional combination of a kosmotropic anion with a kosmotropic cation.

Keywords: fibrinogen, nanofibers, alkali cation absorption, chlorides, hydrogen phosphates

1. Introduction

The blood glycoprotein fibrinogen plays a crucial role in blood coagulation and wound healing contributing to the formation of nanofibrous blood clots^{1,2}, which makes it predestined to prepare fibrous scaffolds for regenerative medicine. Fibrinogen has a molecular weight of 340 kDa and consists of a central globular E region and two identical D regions, both containing three pairs of polypeptide chains ($A\alpha$, $B\beta$, and γ) that are covalently linked by five disulfide bonds in the E region. Fibrinopeptides (FpA and FpB) are located at the ends of the $A\alpha$ and $B\beta$ chains within the E region. Flexible αC domains with disordered structure extend from the distal coiled-coil region of each $A\alpha$ chain to the central region, interacting with each other and the central region of the molecule²⁻⁴.

Fibrinogen is present in blood plasma at concentrations of 1.5 to 4 mg mL⁻¹^{3,5} and surrounded by numerous ions^{6,7}. In healthy humans, the major cations in the blood plasma are Na⁺ (142 mM), K⁺ (5 mM), Mg²⁺ (1.5 mM), Ca²⁺ (2.5 mM), together with the anions Cl⁻ (103 mM), HCO₃⁻ (27 mM), HPO₄²⁻ (1 mM) and SO₄²⁻ (0.5 mM)^{7,8}. In addition to initiating blood coagulation, these ions are important for many biochemical functions, such as buffering the pH of blood and maintaining osmotic pressure or muscle activity^{3,6,9}. Mediated by Ca²⁺ ions, the enzyme thrombin cleaves FpA and FpB from fibrinogen, producing fibrin, the fundamental building block of blood clots³. *In vivo*, this polymerization initiates the formation of an insoluble nanofiber network that serves as scaffold for platelet adhesion, preventing blood loss after injury. Numerous *in vitro* strategies have been developed to reproduce this 3D-nanostructure that serves as provisional extracellular matrix during tissue repair.

Fibrinogen molecules themselves, for instance, can assemble into nanofibrous networks without the presence of thrombin under various *in vitro* conditions that we previously grouped into three categories: substrate interaction, denaturing buffers and non-denaturing buffers¹. Electrospinning, the most common technique, yields fibrinogen nanofibers with good biocompatibility¹⁰⁻¹³. However, high fibrinogen amounts^{14,15} are required with this technique. Moreover, the use of organic solvents or harsher conditions induces fibrinogen denaturation or even amyloid formation¹⁶. Recently, Hense et al. presented fibrin-like fibers that were formed from fibrinogen solution without thrombin¹⁷. They used low/moderate concentrations of multivalent oxoanions (corresponding to multiply deprotonated acids) such as phosphate and citrate at low temperature (5° C) with sodium as a counterion in solution¹⁷. The resulting fibers resembled the native fibrin structure. Similarly to Hense et al., Galanakis et al. reported the formation of fibrin fibers from solutions enriched with soluble fibrin after precipitating fibrin at 4° C and low sodium phosphate concentration^{18,19}. Non-denaturing buffers, thus, facilitate the most promising and cost-effective procedures to prepare fibrin-like fibers from fibrinogen without thrombin *in vitro*.

We also introduced a process for fiber formation under non-denaturing buffer conditions and achieved nanofiber assembly in highly saline aqueous environments by adding phosphate buffered saline (PBS) and a drying step^{20,21}. Dense nanofibers with dimensions resembling native fibrin and the networks prepared by Hense et al.¹⁷ were formed at high salt concentrations without thrombin-induced cleavage. Mild secondary structure changes were found after salt-induced fibrinogen self-assembly without any amyloid transitions²¹. Such 3D-fibrinogen networks presented good mechanical stability when hydrated, supported the co-cultivation of fibroblasts and keratinocytes and prevented *E. coli* infiltration^{22,23}. They also enhanced platelet adhesion while minimizing their procoagulant activity and can therefore be used to steer blood-materials interactions²⁴.

To understand which other salts may trigger fibrinogen fiber formation, we also studied the influence of divalent ions like Ca^{2+} and Mg^{2+} on fibrinogen. While various monovalent ions drive^{17,20} or assist²⁵ fiber formation, divalent ions did not induce fiber assembly in highly saline formulations although they yielded much stronger changes in fibrinogen secondary structure than monovalent PBS²⁶. We showed that fibrinogen self-assembly into nanofibers could be induced by monovalent cations in direct contact with the protein while multivalent cations did not interact specifically with solvent-exposed moieties of fibrinogen²⁶. Hence, we hypothesized that the primary hydration shell of monovalent cations is coordinated looser than the one of divalent cations and that water ligands can be partly detached in contact with certain fibrinogen domains²⁶. So far, nanofibers were observed after drying fibrinogen with sodium or potassium phosphate and to some extent with sodium or potassium chloride²⁰. However, for fibers formed with those pristine salts, no further characterizations of their composition or internal structure have yet been presented.

To establish self-assembly of fibrinogen nanofibers as a reproducible process to prepare large-scale scaffolds for tissue engineering applications with controlled molecular structure, nanoarchitecture and cell-binding properties, we understanding how specific monovalent ions influence this process is crucial. Integrating these influences into a constituting rule like a Hofmeister series for fibrinogen self-assembly is essential. Furthermore, considering the biological relevance of monovalent ions, particularly those present in blood plasma, is vital. Therefore, this study aims to understand the influence of different monovalent cations, anions and polyvalent anions on fibrinogen fiber assembly during drying in highly saline aqueous formulations.

2. Materials & Methods

2.1 Substrate preparation

Round glass slides (VWR, Darmstadt, Germany) with a diameter of 12 mm were used as substrates for fibrinogen self-assembly²⁶ and cleaned for 5 min by immersion in a mixture of

3:1 sulfuric acid (VWR) and 30% hydrogen peroxide solution (VWR). Subsequently, the slides were thoroughly rinsed and kept in deionized water from a TKA water purification system (Thermo Fisher Scientific, Schwerte, Germany). Before fibrinogen self-assembly, glasses were dried with nitrogen. For light scattering and FTIR analysis, cleaned glass slides were coated with a gold layer using an EM ACE600 high vacuum sputter coater (Leica Microsystems, Wetzlar, Germany). First, an adhesion layer of 5 nm of chromium was applied, followed by 25 nm of gold. For scanning electron microscopy (SEM) investigations, cleaned glass slides were modified by immersion in an ethanolic (Honeywell, VWR) solution containing 5% (3-aminopropyl)triethoxysilane (APTES, Sigma-Aldrich, Steinheim, Germany). Before subsequent modification with fibrinogen, APTES-modified glasses were washed with ethanol and dried with N₂.

2.2. Buffers and salt solutions

To directly compare the results obtained for divalent metals with monovalent metals, in the current study we used Tris as a background buffer in the current study, as in our previous report²⁶. All buffers and salt solutions were prepared using deionized water from the TKA water purification system. The pH was monitored and adjusted with a pH meter (Carl Roth GmbH, Karlsruhe, Germany) by adding concentrated solutions of HCl (VWR) or NaOH (VWR) dropwise, as required. Buffer solutions of Tris (Tris(hydroxymethyl)-aminomethane (C₄H₁₁NO₃, Roth) were prepared with a concentration of 10 mM and pH 7.0. Phosphate buffered saline (PBS) (Gibco, Thermo Fisher) solution was used in a concentration of 5x and pH of 7.4. Sodium phosphate (Na-PO₄) buffer with 300 mM, 200 mM and 100 mM concentrations were prepared by mixing NaH₂PO₄ and Na₂HPO₄ (Carl Roth GmbH) solutions in different ratios to the desired pH of 7.0 in ultrapure water. The same concentrations and pH were prepared for potassium phosphate (K-PO₄) by mixing KH₂PO₄ and K₂HPO₄ (Sigma Aldrich). Stock solutions of sodium chloride (NaCl, VWR) and potassium chloride (KCl, Carl Roth GmbH) were prepared with concentrations of 750 mM, 1500 mM and 2250 mM in 10 mM Tris buffer, pH 7.0. Salt solutions of sodium acetate (C₂H₃O₂Na, Honeywell Fluka, Beilstein, Germany), sodium sulfate (Na₂SO₄, Sigma Aldrich), sodium citrate (C₆H₅O₇Na₃, Sigma Aldrich), magnesium sulfate (MgSO₄ · 7 H₂O, Merck KGaA) and potassium sulfate (K₂SO₄, Merck KGaA) were prepared with concentrations of 200 mM by dissolving the salts in ultrapure water. Likewise, disodium oxalate (C₂O₄Na₂, Merck KGaA) solution was prepared with a stock concentration of 100 mM.

2.3 Fibrinogen stock solution and fibrinogen self-assembly

Fibrinogen stock solutions were prepared by dissolving 5 mg/mL of fibrinogen from human plasma (Merck KGaA, Darmstadt, Germany) in 10 mM Tris, followed by overnight dialysis using a 14 kDa cutoff cellulose membrane dialysis tubing (Sigma Aldrich) to remove low

molecular weight compounds²⁰. Fibrinogen precipitation was carried out pipetting 60 μL of the fibrinogen stock solution and 60 μL of the respective salt solution on glass or gold substrates, respectively. For planar samples, instead of salt solutions, 60 μL of deionized water were added. Sample drying was performed overnight in a home-built humidity chamber at 24°C and 30% relative humidity. Subsequently, the dried samples were placed in a petri dish containing one microliter of 37% formaldehyde solution (FA, AppliChem GmbH) per cm^3 and covered with parafilm. Following cross-linking in formaldehyde vapor for 2h, samples were aired in the fume-hood for 30 min and rinsed with deionized water for 30-60 min (exchanging the water every 5 to 15 min), which removed any residual salt crystals.

2.4 *In situ* analysis of fibrinogen fiber assembly

To monitor the drying process of selected fibrinogen samples in real-time, we utilized an optical scattering sensor device, the OS 500 from Optosurf (Ettlingen, Germany) in conjunction with a Sartorius TE 3102 (Göttingen, Germany) or a Kern TGD 50-3C Taschenwaage (Kern & Sohn, Balingen, Germany) mass balance, as previously described²⁶. To maintain a consistent humidity level during the *in-situ* measurements, a continuous flow of dry air was introduced into the chamber. The light scattering sensor was positioned at a distance of 5 mm from the substrate surface, and a light-emitting diode with a wavelength of 676 ± 1 nm was used, generating a focused spot with a width of 0.9 mm that was centrally aligned on the substrate. By analyzing the light scattering patterns, we obtained data on both the overall intensity and the variance of the angle distribution (referred to as Aq roughness) of the detected light for each fibrinogen-coated surface. More details on the Aq parameter can be found in our previous report²⁶. First, baseline signals were established by characterizing gold samples without any liquid deposition. Subsequently, aqueous fibrinogen and salt solutions were applied, and we continuously monitored time-dependent changes in intensity, mass and Aq of the fibrinogen precipitates until the samples reached a completely dry state.

2.6 Morphological and roughness characterization

Roughness maps of cross-linked and washed fibrinogen samples were obtained with the same light scattering sensor device OS 500 used during *in situ* analysis at a measuring distance of 5 mm from the substrate surface, and again a light-emitting diode (wavelength of 676 ± 1 nm) was used. Local roughness findings obtained by scanning a 30 μm light spot over the sample surface were integrated in an Aq map, i.e. a two-dimensional array of measuring spots, with a lateral distance of 50 μm between neighboring measurement regions resulting in a total map width of 20 x 20 mm^2 . Roughness information of fibrinogen precipitates were averaged across the 30 μm light spots and several 100 μm wide regions. The overall surface coverage was analyzed with macroscopic images taken with a Keyence VHX-7000 digital microscope

(Keyence, Neu-Isenburg, Germany). The samples were imaged using 20× magnification in overall survey applying stitching for single partial images.

After cross-linking and washing of the precipitated fibrinogen, the morphology of the samples at the nanoscale was examined by SEM following sputter coating with a 7 nm thick gold layer using our EM ACE600 high vacuum sputter coater. For SEM imaging we used a Phenom XL Desktop SEM (Phenom-World BV, Eindhoven, Netherlands) at acceleration voltages of 10 kV, employing the secondary electron detector. Fiber diameters were manually analyzed with Image J using a total of 50 measurements equally distributed on selected SEM images with 15,000 x magnification. The position of each measurement region within a survey image is given in the Supporting Information (see Table S1).

2.7 Secondary structure analysis

To analyze the secondary structure of dried fibrinogen precipitates on gold, we utilized a Bruker Vertex 70 infrared spectrometer with IR Scope II following our previous routine^{21,26}. Fourier-transform infrared (FTIR) spectra were recorded at 10 to 15 different positions, with a resolution of 4 cm⁻¹ and 64 scans per measurement. At least three samples of each fibrinogen-salt combination were measured. All spectra were processed using the OPUS software package provided by Bruker. The positions of the amide bands were determined by peak integration using the Origin 2020 software from OriginLab Northampton. The secondary structure, i.e. the amount of alpha helices, beta-strands or other structures, was obtained by deconvoluting the amide I band using our previous procedure^{21,26}.

2.8 Chemical composition of fibrinogen precipitates

The surface composition of dried, cross-linked and washed fibrinogen precipitates underwent characterization by X-ray photoelectron spectroscopy (XPS) using a Thermo Scientific™ K-Alpha™ X-ray Photoelectron Spectrometer with monochromatic Al K_α X-ray irradiation. The electron analyzer worked in Constant Analyzer Energy mode (CAE) with 150 eV for overview spectra, 40 eV for detailed scans in the Na 1s, K 2p, Cl 2p, S 2p, P 2p spectral regions and 20 eV for energetic high-resolution line spectra. The applied diameter of the area of analysis was 0.4 mm. The achieved sensitivity depended on the respective elements and allowed for detecting sodium at concentrations as low as 0.1 at% within the information depth of several nanometers. All fibrinogen samples were analyzed after 30 minutes of cross-linking and rinsing with ultrapure water. Our previous rinsing procedure²⁶ was modified by changing the water every five minutes to effectively remove salt deposits. To ensure comparability with our previous results²⁶, samples freshly prepared from 2.5x PBS were analyzed after they had been rinsed with the modified procedure.

All data obtained from the spectra were fitted using the CasaXPS software (Version 2.3.19PR1.0, Casa Software Ltd.). To compensate for electrostatic charging effects, the C1s photoemission line related to hydrocarbonaceous C–C/C–H-species was fixed at 285 eV, and all other lines were respectively shifted. Signal areas were obtained by performing a Shirley background subtraction. Peak components were adjusted using a Gaussian-Lorentzian line shape (GL(30)) for the fitting process.

3. Results and discussion

In our previous studies, drying saline fibrinogen formulations in the presence of PBS or sodium phosphate solutions reproducibly resulted in well-defined fibrous structures on substrates from different materials^{20,21,26}. Minimum starting concentrations of 0.5x PBS or 5 mM Na-PO₄ were necessary to induce self-assembly of fibrinogen nanofibers²⁰ with lower salt concentrations leading to a lower surface coverage with nanofibers. So far, the best fiber coverage was achieved with 50 mM Na-PO₄ and 2.5x PBS, equivalent to 375 mM NaCl²⁰. Therefore, we have now used these concentrations as starting point to investigate fibrinogen precipitation in the presence of, respectively, NaCl, KCl, Na-PO₄ and K-PO₄ and also studied the influence of higher starting concentrations of monovalent salts on fibrinogen fibrillogenesis.

3.1 Precipitation of fibrinogen is altered in the presence of different monovalent salts

As we established for divalent salts and PBS,²⁶ we used angle-resolved light scattering to monitor Aq roughness of the solid below the droplet as a dynamic indicator of surface topography during fibrinogen precipitation until complete evaporation of water (see Figure 1). The time-dependent Aq roughness curves were obtained at the center position in a 0.9 mm wide spot while drying fibrinogen with different monovalent salts at varying concentrations. We used 2.5 mg/mL fibrinogen with varying concentrations of sodium or potassium chloride (375, 750, 1125 mM) and sodium or potassium phosphates (50, 100, 150 mM) before drying. In Figure 1 low Aq values indicate a very smooth surface and small roughness while higher Aq values correspond to higher roughness. At 0 hours, the initial roughness corresponds to the underlying gold substrate before adding fibrinogen and salt solution. After depositing a transparent droplet composed of salt, Tris and fibrinogen, a 30 min initial equilibration phase of relative humidity was observed, followed by an ongoing mass loss, which was attributed to water evaporation during drying (see Figure S1 in the Supporting Information).

Based on the mass variation and calculated solution concentration, arrows in Figure 1 indicate when the fibrinogen-containing droplets achieved salt solubility, expected to get saturated and to precipitate. Moreover, we marked when the maximum fibrinogen solubility of 10 mg/mL in Tris buffer would be reached, based on mass and water evaporation. Salt solubility was typically reached after 80% of the water evaporated. Overall, we observed variations in the drying time

that ranged from 3 to 5.5 hours, depending on the salt type and concentration. Fibrinogen solutions with phosphates dried faster than those with chloride, although chlorides were less hygroscopic.

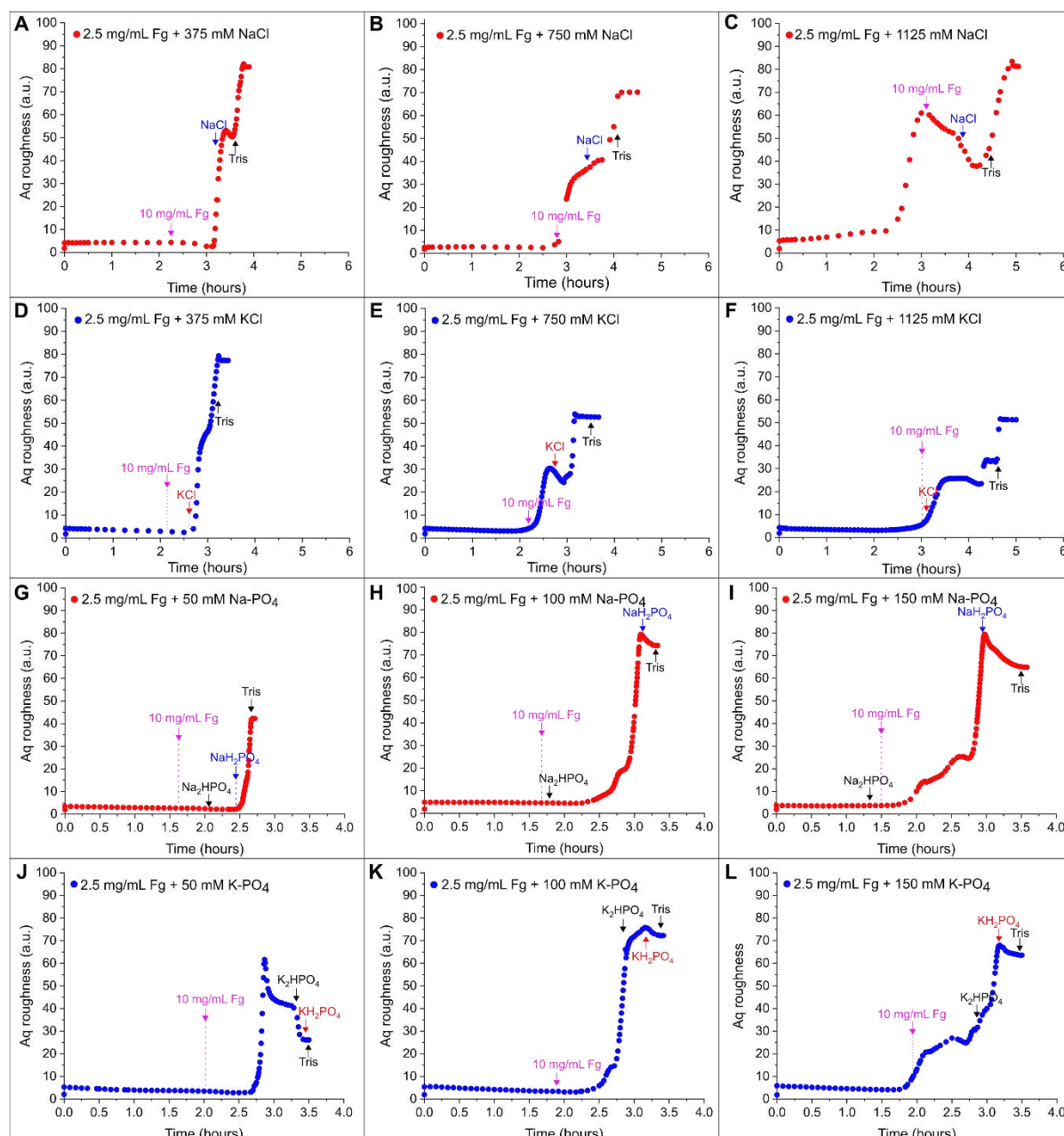


Figure 1: In situ monitoring of the surface roughness of dried fibrinogen precipitates. Aq versus time curves were obtained from light scattering analysis of fibrinogen (Fg) precipitation on gold in the presence of different monovalent salts. In each plot, the round dots represent data points measured until sample drying and indicate the change in Aq surface roughness during the drying of droplets containing 2.5 mg/mL fibrinogen in 5 mM Tris and varying concentrations of (A-C) NaCl, (D-F) KCl, (G-I) Na-PO₄, and (J-L) K-PO₄. The initial Aq values at 0 h represent the roughness of the underlying gold substrate before the fibrinogen and salt solutions were added. The different arrows flag up the time point when the respective salts are expected to reach saturation (following concomitant gravimetrical assessment) and precipitate.

Generally, higher salt concentrations increased the drying times due to a reduction in water vapor pressure. In the first two hours, significant mass loss occurred with minimal change in

Aq values (around 5 or below), indicating no precipitation or a very smooth layer. After two hours, Aq values rose, and solutions became turbid, which coincided with the start of the rise in Aq values. The shape of the Aq curves varied depending on the salt concentration and type, with chloride and phosphate salts showing similar features within their groups.

As shown in Figure 1, the overall change in Aq during drying ($\Delta(\text{Aq})_{\text{total drying}}$) was mostly above 40, reaching up to 90 for fibrinogen with various monovalent salts, except for lower concentrations of K-PO₄ (50 mM) which only reached an Aq of 26. Aq vs. time curves for fibrinogen-free salt solutions only showed minor increases in Aq during drying, with overall $\Delta(\text{Aq})_{\text{total drying}}$ values between 2 and 17 and for Na-PO₄ and K-PO₄ even below 10 (see Figure S2), indicating smoother surfaces without fibrinogen. This is in contrast to divalent chlorides that previously exhibited a $\Delta(\text{Aq})_{\text{total drying}}$ between 20 and 70 when dried without fibrinogen²⁶. The low Aq values for monovalent salts in the sample center also correlate well with optical microscopy images of NaCl and KCl precipitates, which showed that the sample center was mostly free of large salt crystals (see Figure S3).

To understand whether fiber formation occurred at a threshold salt concentration or near complete sample drying, we subsequently increased the initial salt concentration and analyzed the slope in the Aq vs. time plots and roughening inset time related to the first Aq increase. This salt increase allowed us to separate the respective onset times of fibrinogen and salt precipitation during our *in-situ* analysis.

In our reference measurements of both chlorides with 375 mM and both phosphates with 50 mM we did not observe any notable Aq increase during drying (see Supplementary Information, Figure S2). For fibrinogen with 375 mM NaCl or KCl, the Aq roughness showed two steep slopes: the first coinciding with salt saturation and the second with Tris saturation (see Figure 1A and D). Initially, Aq was below 10 and constant until 2.5-3.0 hours, before it sharply increased to around 80 for both salts. With 750 mM chlorides, a less steep two-step Aq rise occurred, reaching final values of 70 for NaCl and 55 for KCl (see Figure 1B and E). For both lower concentrations, the saturation of the salts was reached during the initial changes of the Aq values. At 1125 mM, an additional step appeared between the two already present at lower chloride concentrations, with final Aq values around 85 for NaCl and 55 for KCl (see Figure 1C and F). KCl showed a continuous three-step increase, while NaCl had a decrease between the salt and Tris saturation events.

For fibrinogen and alkali phosphate salts, Aq changes were similar to those for chlorides but with narrower curves. Na-PO₄ and K-PO₄ solutions contain mixtures of phosphates with different solubilities (NaH₂PO₄ and Na₂HPO₄ or KH₂PO₄ and K₂HPO₄) with differently protonated anions and their hydrates showing different solubilities^{37,38}, causing salts to precipitate at different drying times (see arrows in Figure 1G to L). At 50 mM, Na-PO₄ and K-PO₄ with fibrinogen showed distinct Aq vs. time curves. Initially, Aq was low and constant

until a sharp increase at 2.0-2.5 hours occurred in less than 30 minutes. For Na-PO₄, Aq increased when NaH₂PO₄ started precipitating, while Na₂HPO₄ precipitation caused no change. However, we did not observe any corresponding change in the Aq value. This may be attributed to the presence of a pH-dependent mixture of different salts in sub-saturation concentrations. For K-PO₄, the Aq increased earlier than expected and did not coincide with the expected precipitation of any of the phosphate salts. It decreased in two steps, likely due to less soluble hydrates of K₂HPO₄ and KH₂PO₄.

At 100 and 150 mM, both fibrinogen-phosphate mixtures had similar Aq curves. A small shoulder appeared at the initial Aq rise for 100 mM, followed by a steep rise, reaching Aq values of 80 during 1 hour, then decreasing to 75 at the final drying point for both phosphates. At 150 mM, another shoulder appeared, and the curve was less steep, taking 1.5 hours to reach a final Aq of 65. For Na-PO₄, Na₂HPO₄ precipitation was expected before the Aq rise, with NaH₂PO₄ precipitation coinciding with the Aq increase. However, higher concentrations of K-PO₄ showed Aq changes correlating well with the expected precipitation of K₂HPO₄ and KH₂PO₄.

Overall, *in-situ* monitoring of drying fibrinogen solutions revealed that mutual interactions are present during salt and fibrinogen co-precipitation that influence the roughness of the dried precipitates. Comparing all graphs in Figure 1, Aq further increased at the end for NaCl and KCl, when Tris was expected to precipitate, but decreased for the phosphates. This is because Tris forms tris-hydrochlorides with chlorides that have a rough texture, as we reported previously³⁹, causing Aq profiles to increase. With phosphates, Tris-HCl did not precipitate, resulting in decreased roughness. Since fibrinogen saturation was expected before salt saturation – apart from the mixture of 2.5 mg/mL fibrinogen with 150 mM Na-PO₄ – our findings suggest that at lower salt concentrations, major changes in Aq roughness are linked to the onset of salt precipitation. Increasing turbidity during drying indicates protein aggregation and precipitation^{20,40}, possibly due to a lower solubility threshold of fibrinogen that might correspond to salting out in a high-saline environment. This could mean more salt decreases fibrinogen solubility, bringing the Aq increase event closer to the 10 mg/mL saturation limit, suggesting early co-precipitation with salts.

However, increasing salt concentration showed changes in Aq profiles not directly related to salt precipitation, indicating fibrinogen precipitation before the salts. In a nutshell, our time-dependent combined assessment of the Aq roughness of the deposits and the mass loss of the droplet during drying suggest that not only the final phase, but rather an essential period of the solidification process after the onset of a roughness increase is dominated by coprecipitation of fibrinogen and the respective salts. These hypotheses require further analysis of salt-dependent fibrinogen precipitation, including turbidity measurements, as saturation levels may vary with solution composition.

3.2 Variations in fibrinogen morphology and roughness depend on the monovalent salts present during drying

To study whether high surface roughness correlates with fiber formation, as we previously observed for fibrinogen drying with PBS in comparison to divalent salts or Tris ²⁶, we now combined Aq mapping with optical microscopy and SEM analysis of cross-linked and washed fibrinogen precipitates with different monovalent salts (see Figure 2). The macroscopic features found in optical microscopy images of all fibrinogen precipitates correlated precisely with the roughness information in the Aq maps where high Aq values (red) indicate high surface roughness, while low Aq values (blue) indicate smooth regions.

Fibrinogen precipitated with 375 mM NaCl showed dendritic features of 0.1 to 0.2 mm width with high roughness and an average Aq value around 75 (see Figure 2A-B and Figure S4). Similar dendrites were previously observed when fibrinogen, collagen or BSA were precipitated in the presence of NaCl ^{39,41}. SEM analysis of fibrinogen with 375 mM NaCl now revealed nanofibrous deposits only in a few distinguished sample regions (see Figure 2C and Figure S5A-D). Remarkably, those regions were surrounded by elevated areas that appeared rough but did not show a nanofibrous morphology. Detailed analysis revealed domains with flat and apparently smooth fibrinogen layers (see Figure S5A, blue arrow) and domains with rough but not fibrous structures (see Figure S5C, D) were also observed. Comparing our previous SEM analysis of unrinsed fibrinogen-NaCl precipitates (see Figure S6A ³⁹) with the SEM images of washed fibrinogen precipitates where Tris and NaCl crystals had been dissolved (see Figures S5A and S6B), we conclude that fibers had formed underneath the largest branches of the salt dendrites, which consist of crystallites with a width of around 200 μm .

Planar fibrinogen regions were associated with areas between the NaCl dendrites. Interestingly, below small NaCl crystals, fibrinogen showed a rough but not fibrous morphology, contrasting with previous findings where PBS or Na-PO₄ precipitates yielded fibers around and on top of salt crystals ²⁰. Fibrinogen layers formed with 375 mM KCl were shaped by simultaneous salt dendrite formation (see Figure 2D) with an average Aq roughness 40 that was much lower than with NaCl (c.f. Figures 2E and 2B). The highest Aq roughness was detected in the central sample region with the lowest KCl dendrite density. These fibrinogen-KCl precipitates had a thickness of at least 0.1 mm following cross-sectional analysis with 3D-optical microscopy (see Figure S7). Interestingly, no fibers were found with KCl – neither around nor under KCl crystals (see Figure 2F). Detailed SEM analysis revealed both smooth and clumpy domains (see Figure S5G-H), which matches Aq mapping results, showing a less rough surface than fibrinogen films formed from saturated NaCl solutions. Notably, in our previous study we reported fiber formation with 375 mM KCl, but fibers were less defined than those from PBS salt solutions and distributed differently ²⁰. The previous study used NH₄HCO₃ instead of Tris for dialyzing fibrinogen. NH₄HCO₃ decomposes into volatile gases and water during drying ⁴², while Tris is non-volatile with a lower pH ⁴³ and therefore still present at the end of drying. These differences

could indicate an influence of the pH value and the ions in the background buffer on the course and completion of fiber formation upon drying of the fibrinogen solutions. Further studies are required to confirm this hypothesis.

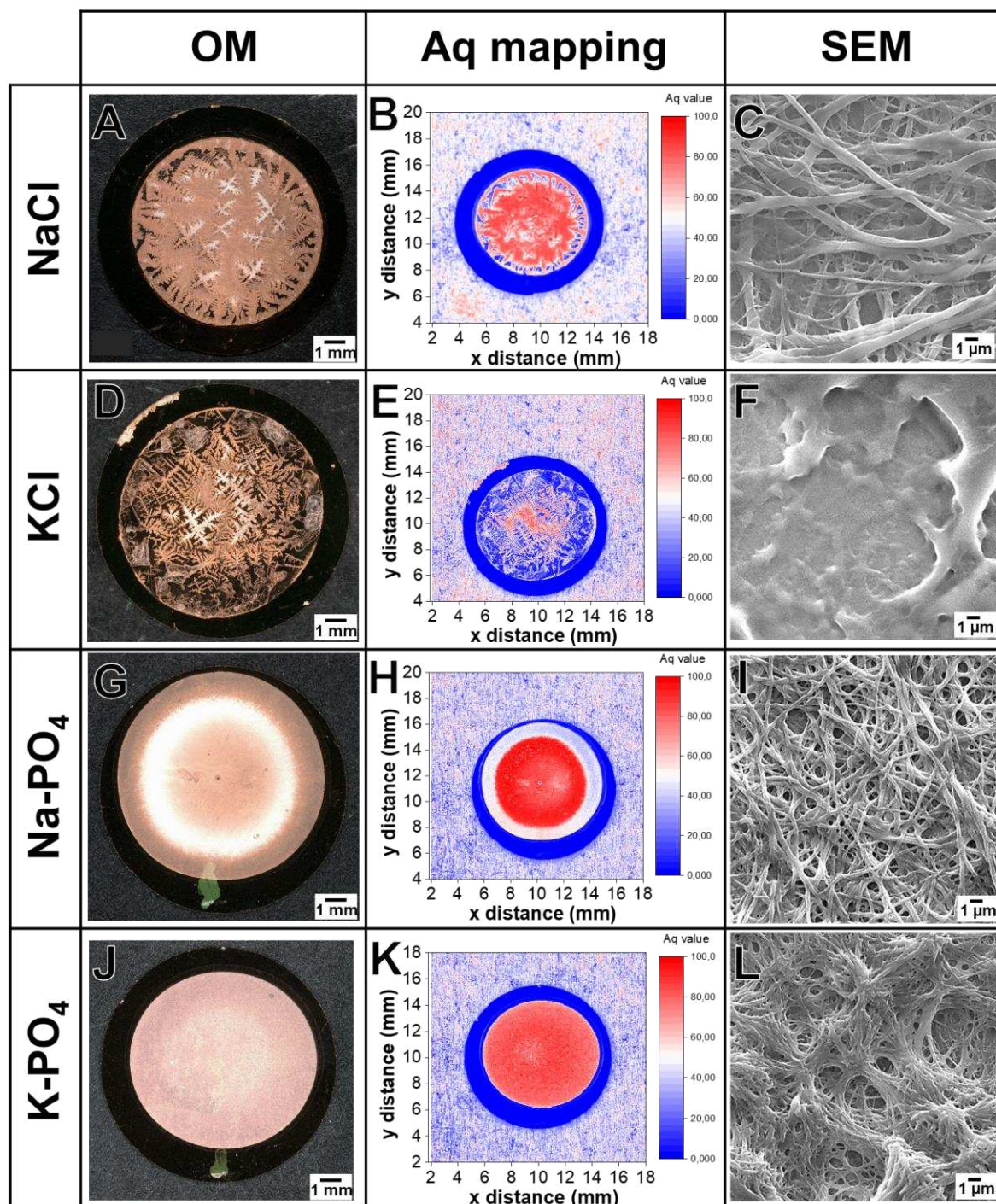


Figure 2: Morphology and roughness of fibrinogen dried in the presence of different monovalent salts. Optical light microscopy (OM), Aq-based survey images and SEM-based local detail images of samples prepared after drying 2.5 mg/mL fibrinogen in the presence of different salts: (A, B, C) 375 mM NaCl, (D, E, F) 375 mM KCl, (G, H, I) 100 mM Na-PO₄, (J, K, L) 100 mM K-PO₄. For SEM analysis, all precipitates were prepared on APTES-modified glass, while for Aq mapping, fibrinogen films were prepared on gold. Light microscopy views correspond to Aq-mapping, with rougher areas (red color) being an indication of fiber formation. SEM-images reveal (C) low density fiber formation for NaCl, (F) no fiber assembly for KCl, (I) high density fiber assembly for Na-PO₄ and (L) assembly of partly coalesced fibers with high density for K-PO₄.

Figures 2G-I show that fibrinogen precipitated with 100 mM Na-PO₄ had rough, homogeneous surfaces with Aq values up to 100, correlating well with microscopic details. Light microscopy showed a flat surface without large salt crystals, but Aq mapping revealed high roughness. SEM analysis after rinsing linked this roughness to dense fibrinogen nanofibers, evenly spread over the surface (see Figures S5E-F). Similar results were seen with 100 mM K-PO₄, but these fibers appeared more coalesced (see Figure 2J-L and S5I-J). Overall, Na-PO₄ resulted in the highest fiber formation and coverage, with no large salt crystals or gaps observed. Our combined analysis suggests that higher roughness ($Aq_{\max} \geq 80$) indicates fiber assembly, especially compared to previous findings with divalent salts, where low Aq values ($Aq_{\max} \leq 80$) corresponded to no fiber formation²⁶.

To analyze the contribution of salt crystals to film roughness, we additionally compared Aq values of droplets directly after drying with those after crosslinking and dissolving salts and Tris by washing. Before cross-linking and rinsing, Aq values were 80.8 for NaCl, 77.3 for KCl, 74.2 for Na-PO₄, and 72.3 for K-PO₄, matching the average Aq roughness in 1 mm regions around the center of cross-linked and washed fibrinogen precipitates (see Figure S4). Aq values slightly decreased for NaCl and KCl after washing, while they slightly increased for Na-PO₄ and K-PO₄. This suggests chloride crystals add roughness on top of fibrinogen (see Figures S3 and S4), while phosphate crystals fill valleys in the undulated fibrinogen topography^{22,24}. Differences in Aq values before and after rinsing were within the standard deviation, indicating the roughness is mainly due to fibrinogen content. Apparently, the mobile anions and monovalent cations of the fibrinogen-salt solutions shape the fibrinogen microstructure, while precipitated salt crystals act as a template for the dried macroscopic fibrinogen films.

For future applications in tissue engineering, lateral scaffold homogeneity is crucial. Therefore, we analyzed the average $\langle Aq \rangle$ value and standard deviation of the Aq roughness in a 1 mm wide central region of cross-linked and washed fibrinogen films presented in the center column of Figure 2 (see Figure S4). The lowest $\langle Aq \rangle$ values were found for KCl (68.2) and NaCl (77.9). Na-PO₄ and K-PO₄ had higher, similar $\langle Aq \rangle$ values (81.7 and 81.3). The highest standard deviations in the central region were observed for NaCl and KCl, indicating the highest variation in Aq mapping. This lower homogeneity for chloride salts is attributed to their larger crystal size and potential gaps in water-rinsed films (c.f. Figures 2, S5, and S6). Moreover, KCl yielded no fibers, and NaCl fibers were not uniformly distributed, with gaps filled by salt crystals before rinsing (see Figure S6). Hence, monovalent salts with phosphates will be best suited in future to produce nanofibrous fibrinogen scaffolds for regenerative medicine in the future.

An important parameter to steer cell-scaffold interactions is the diameter of individual fibers in the scaffold. Therefore, we analyzed average fiber diameters from SEM images (see Figure S8 and Table S1) and found the lowest diameter of 228 ± 49 nm for fibrinogen with 100 mM Na-PO₄, followed by 233 ± 67 nm for 100 mM K-PO₄ and 301 ± 76 nm for 2.5x PBS. With 375 mM

NaCl only few regions with fibers were found that yielded an average diameter of 371 ± 131 nm. These results show that more fibrinogen was converted into persistently thin fibers with phosphates than with chlorides (c.f. Figure 2). For K-PO₄ in particular, the coalesced fibers indicate that self-assembled fibrinogen fibers were also prone to some ripening effect as it is known from the Ostwald ripening of intersecting fibers⁴⁴. We suggest that material exchange between neighboring fibers is ruled by a salt-dependent transport-related barrier that counteracts coalesce with the following order: KCl < NaCl < K-PO₄ < Na-PO₄. This barrier, effective in highly saline environments, is likely influenced by attractive hydrophobic and repulsive hydrophilic Lifshitz–van der Waals interactions rather than electrostatic effects⁴⁵.

Recently, Hense et al. studied the effect of different salts on fibrinogen fiber formation at lower concentrations (15 mM) than we used¹⁷. Interestingly, in their study NaCl was considered to hinder fiber formation, while Na-PO₄ promoted fiber formation, similar to our findings with protonated phosphates using sodium or potassium alkali counterions. They focused on sodium salts at pH 7.0, concluding that oxygen-containing, multivalent anions like phosphate or citrate best support fiber formation. Wei et al. previously also observed how ions in PBS influence fibrinogen aggregation and fiber assembly under when acidic conditions at pH 2, noting increased fiber yield with PBS present and they observed an increased fiber yield when PBS was present²⁵. Based on our findings, we conclude that fibrinogen precipitates into different fibrous or non-fibrous morphologies under varying environmental conditions, indicating that specific ion-protein interactions initiate and promote fibrinogen aggregation and consequently fiber assembly. Moreover, we studied the effect of higher salt starting concentrations on fibrinogen precipitation. We obtained Aq maps and SEM images similar to those with lower salt concentrations for all salts (c.f. Figure S9 and S10 with Figure 2). Higher NaCl and KCl concentrations did not increase surface roughness or coverage, nor did they produce fibers for KCl. For phosphates, fibrinogen coverage increased from 50 to 100 mM but remained unchanged at 150 mM, with no change in fiber morphology. Therefore, we focused our further analyses of ion uptake and secondary structure on the lowest salt concentrations providing sufficient coverage: 375 mM for KCl and NaCl, and 100 mM for K-PO₄ and Na-PO₄.

3.3 Ion uptake is stronger for Na⁺ and only observed for fibrous fibrinogen

Previously, we observed for fibrinogen dried with PBS that sodium cations were present in washed fibrinogen fibers while divalent cations were completely rinsed away²⁶. Hence, we hypothesized that ion-protein interactions may be affected by the hydration shells of both the ions and the protein and that sodium ions were bound to anionic sites within fibrinogen²⁶. To confirm this hypothesis, we now analyzed the elemental surface composition of cross-linked and rinsed fibrinogen precipitates that were dried with different monovalent salts (375 mM of NaCl or KCl and 100 mM of Na-PO₄ or K-PO₄) using XPS.

The atomic surface concentrations from XPS inspection are presented in Table 1. The nitrogen surface concentration [N] remained around 17 at% for all samples, similar to our previous study²⁶. In the presence of NaCl and KCl, no metallic cation or Cl-based moieties were detected, suggesting that chloride salts macroscopically shaped the fibrinogen films but were subsequently washed away. Fibrinogen samples prepared with PBS showed some scattering and lower [Na]/[N] concentration ratios between 1.3 % and 2.6 % compared to the previously detected 4.9 %, i.e. 0.049²⁶. Although the modified rinsing process not only dissolved salt deposits, but also dissolved sodium cations from the fibrinogen, the sodium was not completely rinsed out. We attribute the decrease in [Na]/[N] concentration ratio to the shorter washing steps in which we now exchanged water every 5 min instead of every 15 min²⁶. When we rinsed one of the samples that had a [Na]/[N] ratio of 0.026 after 30 minutes of rinsing for additional 15 minutes (see Table 1, second row), we found that the concentration decreased by slightly more than half. This confirmed our hypothesis that Na⁺ can be leached from sodium-fibrinogen compounds. We attribute this partial and incremental leaching effect to the interface regions of fibrinogen deposits and to the formation of a complete hydration shell around Na⁺ cations in diluted aqueous solutions. Moreover, we suppose that Na⁺ ions were replaced by (originally hydrated) H⁺ ions from water following an ion exchange process. Although PBS also contains KCl and K-PO₄ in its formulation, we did not detect potassium species in either of the rinsed samples, agreeing well with our previous results²⁶. Moreover, XPS results showed no Tris residues on the surface, neither in overall nitrogen surface concentration [N] nor in the contribution of C*-O species to the C1s signal. This agrees well with the Aq maps and SEM images (see Figure 2), which showed no clear indication of Tris salts after rinsing cross-linked and dried fibrinogen films.

Since fibrinogen precipitates prepared with NaCl did not show any Na⁺ after washing, we presume that for PBS samples, exchangeable sodium-fibrinogen moieties originated from dissolved sodium phosphate salt. Remarkably, XPS analysis of fibrinogen layers prepared with Na-PO₄ showed a [Na]/[N] concentration ratio of about 1.2 %, with no detectable phosphate species. This confirms our hypothesis that Na⁺ in fibrinogen-PBS samples originated from Na⁺ counterbalanced by (protonated) phosphate ions. Since K⁺ was not detected in fibrinogen-PBS samples, we did not expect any potassium in fibrinogen-K-PO₄ either, which was confirmed by our XPS findings.

With these results we hypothesize that nanofibrous fibrinogen preferentially captures Na⁺ rather than K⁺, preferentially in the presence of O-containing counterions in solution, like (protonated) phosphates. Presumably, this preference is due to the smaller van der Waals radius of Na⁺ (227 pm) compared to K⁺ (275 pm)⁴⁶. The preferential sorption of sodium over potassium on protein surfaces was studied by Vrbka et al.⁴⁷ *via* molecular dynamics simulations for actin, bovine pancreatic trypsin inhibitor, ubiquitin and ribonuclease. They suggested that interactions between the carbonyl oxygen of the amide group and Na⁺ are responsible for this preference.

Table 1: Composition of fibrinogen-salt precipitates on APTES-coated glass slides after crosslinking fibrinogen with FA vapor and rinsing with pure water for 30 min obtained from XPS analysis and given in atomic % (at%) in case of [N] and in % in case of ratios normalized to [N]. ___/___ represents one position of one measurement per sample.

| Sample | Metal ion in starting solution | Rinsing time (min) | [N] | [Metal]/[N] | [Cl]/[N] | [S]/[N] | [P]/[N] |
|--|---|-----------------------|---------------------------------|----------------------|---------------------|-----------------------------|------------------------------|
| | Na ⁺ , K ⁺ | | | Metal = Na | | | |
| Fg & 2.5× PBS pH 7 | Morphology: highly fibrous | 30 min | 14.7/ 17.5/ 17.2 | 4.9*/ 1.3/ 2.4 | 0.9/ 0/ 0 | 2.5/ 2.8/ 3 | -/ 0.1/ 0.08 |
| Time series rinsing for PBS (Na ⁺ leaching) | Morphology: highly fibrous | 30 min 30 + 15 min | 16.5/ 17.06 | 2.6 1.1 | 0/ 0 | 3.1/ 3.2 | 0.07/ 0.04 |
| | Na ⁺ | | | Metal = Na | | | |
| Fg & 375 mM NaCl, pH 7 | Morphology: low fibrous | 30 min | 17.5/ 17.7/ 17.3/ 17.3 | 0/ 0/ 0/ 0 | 0/ 0/ 0/ 0 | 2.9/ 2.6/ 2.8/ 2.4 | 0.1/ 0.2/ 0.08/ 0.1 |
| | Na ⁺ | | | Metal = Na | | | |
| Fg & 100 mM Na-PO ₄ , pH 7 | Morphology: highly fibrous | 30 min | 17.2/ 17.0/ 17.6 | 1.2/ 1.0/ 1.1 | 0/ 0/ 0 | 3.1/ 2.7/ 2.7 | 0.09/ 0.2/ 0.06 |
| | K ⁺ | | | Metal = K | | | |
| Fg & 375 mM KCl, pH 7 | Morphology: rough with smooth domains. No fibers. | 30 min | 17.7/ 16.5 | 0 / 0 | 0/ 0 | 2.8/ 2.5 | 0.1/ 0.1 |
| | K ⁺ | | | Metal = K | | | |
| Fg & 100 mM K-PO ₄ , pH 7 | Morphology: highly fibrous | 30 min | 17.2/ 17.3 | 0/ 0 | 0/ 0 | 2.7/ 3.3 | 0.2/ 0.2 |

* result from previous publication ²⁶

We previously hypothesized that sodium ions can disrupt their hydration layer to establish direct protein contact to integrate into the protein structure²⁶. As the concentration of peptide groups exceeds the maximum detected Na⁺ concentration by more than one order of magnitude we suggested carboxylate groups in fibrinogen side-chains as potential binding sites for monovalent cations²⁶. Based on our results, we now suggest that such integration can induce structural changes and promote fibrinogen fiber assembly.

However, our SEM findings reveal fiber formation with K-PO₄, even though K⁺ was not detected on thoroughly washed fibrinogen films. A possible explanation, that would still allow for considerable potassium-fibrinogen interactions, could be that monovalent cations as Na⁺ and K⁺ can indeed interact directly with the protein in solution, but that Na⁺, due to its preference for a cation-fibrinogen interaction, may not as easily be fully hydrated and exchanged by the H⁺ ions when dried fibrinogen precipitates are rinsed with water after drying. This higher affinity might be due to thermodynamic effects like a stronger cation-carboxylate interaction or kinetic effects like a three-dimensional complexation that exceeds a single cation-carboxylate interaction⁴⁸. As a more pronounced 3D complexation might be associated with changes in intramolecular or intermolecular protein-protein interactions, we subsequently also analyzed fibrinogen films by vibrational spectroscopy.

3.4 Secondary structure of fibrinogen precipitates does not indicate fiber formation

To study whether specific ion-protein interactions are associated with conformational changes, we conducted FTIR analysis of cross-linked and washed fibrinogen precipitates that were dried with NaCl, KCl, Na-PO₄ and K-PO₄ (see Figure 3).

The resulting FTIR histograms were ordered following the SEM-based structural characteristics, starting from non-fibrous fibrinogen films prepared in Tris (left) to the most nanofibrous films with Na-PO₄ (right). The α -helix content decreased from smooth fibrinogen with Tris (21% \pm 4%) via fibrinogen with KCl (18% \pm 3%) and NaCl (17% \pm 1%), which did not necessarily result in fiber assembly to fibrinogen fibers with PBS (17% \pm 0%). The α -helix content was highest for K-PO₄ (19% \pm 1%), and Na-PO₄ (22% \pm 4%), the most fibrous fibrinogen precipitates. β -strand content was lowest for Tris (33% \pm 5%) and both phosphate samples (Na-PO₄: 37% \pm 1% and K-PO₄: 35% \pm 3%) and highest for PBS (42% \pm 1%) and both chlorides (NaCl: 43% \pm 4%, KCl: 42% \pm 4%), all showing more β -strand than the smooth samples prepared with Tris. Despite the strong differences in morphology, fibrinogen with Tris and K-PO₄ had the highest amounts of other structures around 46%, while for all other salts the percentage of other structures was between 40% and 41%. Overall, more fibrous fibrinogen precipitates assembled with phosphates had less β -strand and more α -helix content than the less fibrous chloride precipitates (c.f. Figure 3 and 4). PBS, which contains 10 times as much NaCl as phosphates, had a secondary structure that resembled NaCl rather than phosphates. This

conformational similarity is also reflected by the similar fiber diameters obtained from SEM analysis (see Figure S8).

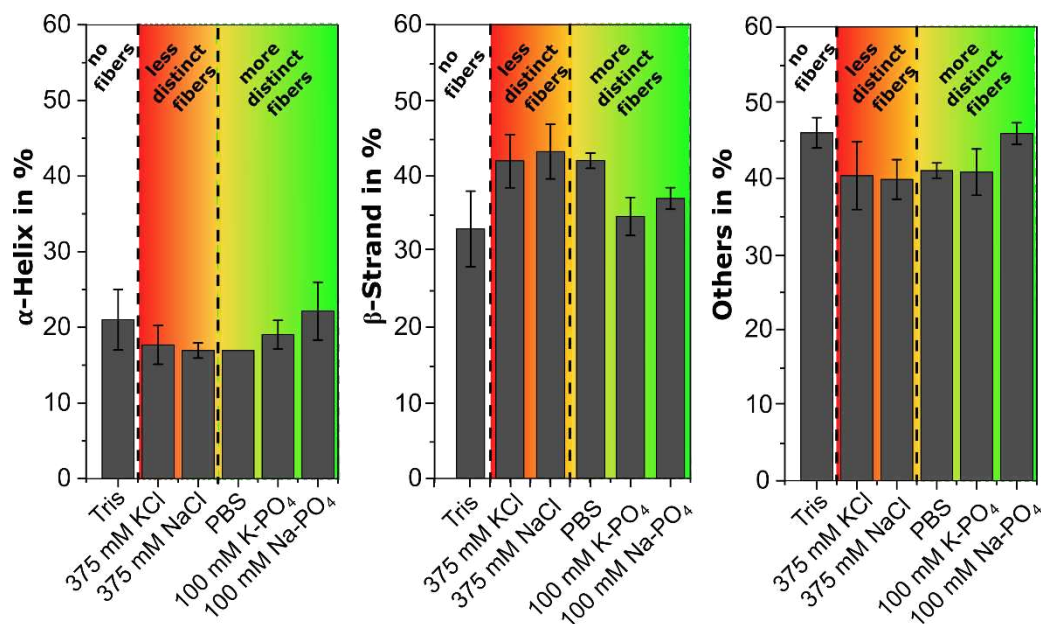


Figure 3: Secondary structure of fibrinogen precipitates. 2.5 mg/mL fibrinogen were dried with different monovalent salts, cross-linked and washed. The histogram presents the results from the deconvolution applied to the amide I bands of the FTIR spectra (average of $n=3$ independently prepared samples). For comparison, the results for fibers assembled with PBS from our previous study²⁶ are also shown. No clear correlation between β -strand and fiber formation was observed. Non-fibrous fibrinogen samples (KCl) yielded a higher amount of β -strands than dense fiber networks of fibrinogen (Na-PO₄).

Overall, the secondary structure profiles show that both chlorides are similar to the addition of PBS to fibrinogen, for which we had previously reported a decrease in α -helix and an increase in β -strand content^{20,21}. We had suggested that the increase in β -strand structures in fibrous fibrinogen layers prepared with PBS correlated with a transition from smooth to fibrous layers²¹. However, further studies with divalent ions had showed that an increase in β -strand content does not necessarily result in fibrinogen fiber assembly²⁶. This finding is corroborated here, since although there was an increase in β -strands for NaCl and KCl, the assembly of fibrinogen into fibers was limited or even suppressed.

For fibrinogen with both phosphates, we also obtained similar conformational trends. Interestingly, these secondary structure profiles were close to that of native fibrinogen in aqueous solution as we had previously measured by CD spectroscopy (26% α -helices, 27% β -strands, and 47% other structures)²¹. With serine and threonine located in the A α chain, native fibrinogen contains many phosphorylation sites that play an important role *in vivo* during ageing or surgery⁴⁹. Therefore, we hypothesize that these phosphorylation sites are involved during *in vitro* fiber assembly with K-PO₄ or Na-PO₄ by supporting the attachment of phosphate, which presumably promotes the disruption of the hydration shell. In particular, for Na-PO₄ with the smaller van der Waals radius of Na⁺, this disruption may lead to direct contact between the Na⁺ ions and the fibrinogen molecule, allowing the Na⁺ ions to be captured during fiber assembly.

Further atomistic studies are needed to confirm these hypotheses and to understand whether binding of Na^+ is a prerequisite for or a consequence of fiber assembly.

Comparing results from divalent salts with monovalent salts, the β -strand content for phosphates matched that of divalent chlorides²⁶. This reinforces that secondary structure changes alone cannot explain why fibrinogen assembles into fibers with phosphate salts during drying, or why fibers form inconsistently with monovalent chlorides. Additionally, it does not explain why monovalent chlorides yield some roughness while divalent chlorides result in smooth layers. However, as discussed previously²⁶, FTIR findings can indicate or exclude fibrinogen denaturation during fiber assembly, which is important for the future use of these scaffolds in regenerative medicine. With our previous results^{21,26} and current findings, we confirm that fibrinogen probably assembles into fibers in the presence of certain monovalent salts only when its tertiary or quaternary structure - rather than its secondary structure - changes, similar to fibrin^{50,51}.

3.5 Fiber conversion with polyvalent anions depends on cation/anion pairing

So far, we did not detail why more fibrinogen is converted into fibers or potentially why its tertiary and quaternary structures change more with monovalent cations and (protonated) phosphates instead of chlorides. The most defined fibers were observed with hydrogen phosphates ($[\text{HPO}_4]^{2-}$ and $[\text{H}_2\text{PO}_4]^-$), which are polyvalent and amphoteric anions that act as both acid or base and can form several hydrogen bonds and salt bridges⁵². With reference to the Hofmeister series, several polyvalent anions, classified as kosmotropic, may have similar effects. To further understand fibrinogen fiber assembly with phosphates and the reaction of the monovalent cations Na^+ and K^+ with other kosmotropic anions, we therefore studied the capability of different polyvalent anions to promote fibrinogen fiber formation.

First, we tested Na^+ with different polyvalent anions using sodium sulfate and three different sodium carboxylates, namely the monocarboxylate anion acetate, the dicarboxylate anion oxalate, and the tricarboxylate anion citrate as ordered in the sequence of increasing steric demand and efficiency for multidentate chelation of (partially) hydrated cations. Then, sulfate was paired with K^+ to establish a comparison with its smaller homologue Na^+ . Finally, we combined sulfate with the divalent cation Mg^{2+} to verify the hypothesis that the observed inhibiting effect of divalent chloride salts on the formation of nanofibers in highly saline aqueous environment²⁶ is not only due to the presence of chloride anions but also affected by the presence of divalent cations. Figure 4 shows SEM images of the six salt-fibrinogen precipitates mentioned.

Fibrinogen films formed with 50 mM Na-oxalate (see Figure 4A) and 100 mM Na-acetate (Figure 4B) resulted in rough precipitates. For Na-acetate, the fibrinogen morphology showed some porosity, suggesting seamless coalescence of previously formed and precipitated fibers.

On the other hand, films with 100 mM of Na-citrate (see Figure 4C) displayed localized fiber-like structures between elevated smooth, potentially coalescent domains, indicating citrate's greater tendency to induce fibrinogen fiber assembly compared to acetate, as observed by Hense et al.¹⁷.

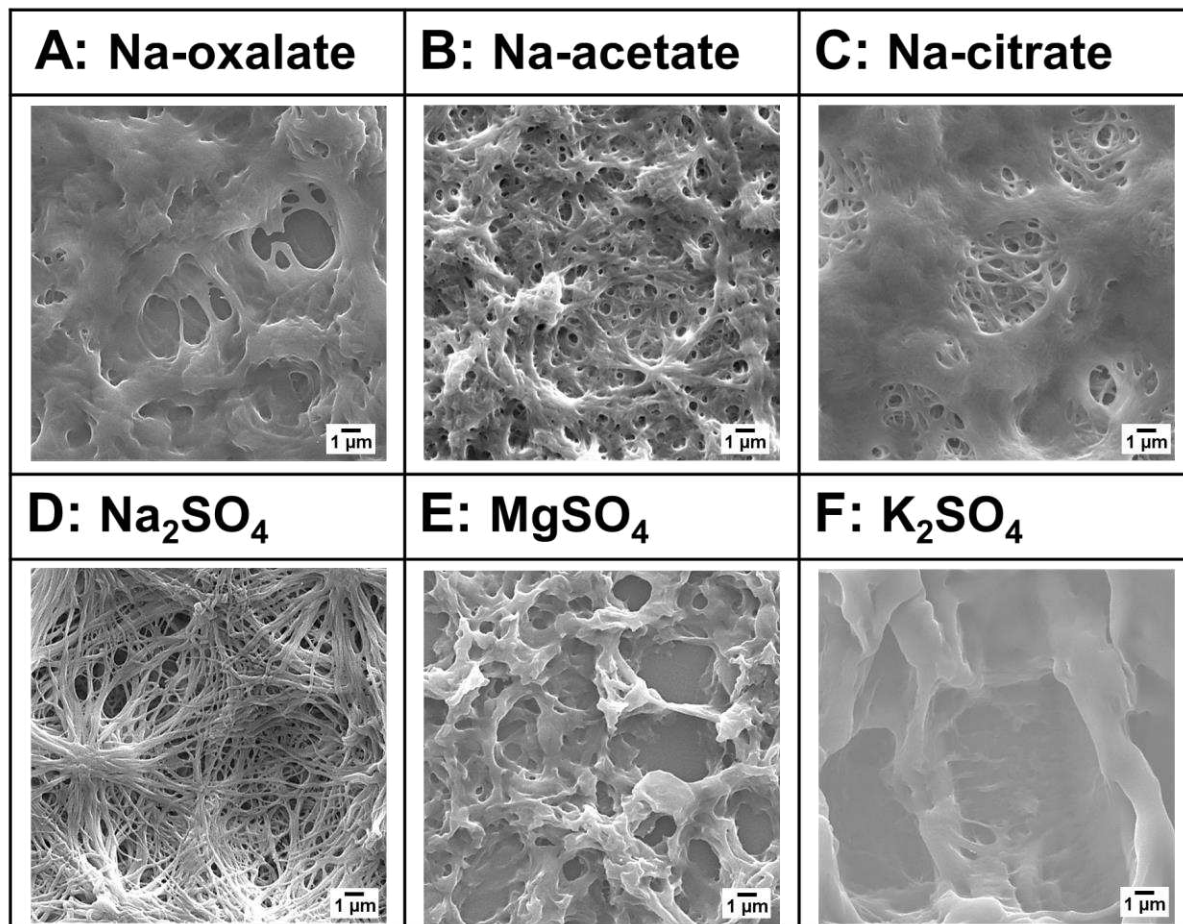


Figure 4: Morphology of fibrinogen precipitates dried with different polyvalent anions. SEM images of samples prepared after drying 2.5 mg/mL fibrinogen with different salts using the following starting concentrations: (A) 50 mM Na-oxalate, rough without fibers; (B) 100 mM Na-acetate, rough without fibers; (C) 100 mM Na-citrate, fiber-like structures between smooth domains; (D) 100 mM Na₂SO₄, fiber-like structure with star-shaped profile; (E) 100 mM MgSO₄, rough without fibers; (F) K₂SO₄, smooth. Salts with Na⁺ are more favorable to form fibers than the ones with K⁺.

Further investigations, e.g., applying sodium soaps⁵³, might reveal if the length of terminal alkyl chains in acetate-homologue mono-carboxylates affects the shape of co-precipitated fibrinogen deposits. In contrast to the tested sodium salts of carboxylic acids, 100 mM sodium sulfate induced fiber formation with a star-shaped fibrinogen morphology (see Figure 4D), similar to that reported for PBS^{20,21}. Previously, we showed that divalent salts form smooth films when the counterion was chloride²⁶. However, when we combined with the divalent cation Mg²⁺ with sulfate at 100 mM concentration, a rough fibrinogen surface without nanofibrous regions was found (see Figure 4E). Finally, 100 mM of potassium sulfate also created rough fibrinogen structures (see Figure 4F), similar to those of 375 mM KCl. These results suggest that the alkali metal ions Na⁺ and K⁺ and the divalent cation Mg²⁺ in combination with sulfate lead to rough

fibrinogen structures, differing from smooth films. Hence, we speculate that varying cation exchanges influence the size and structure of fibrinogen-based precipitates. They might also affect the surface mobility of fibrinogen growth units attaching to the forming film, as seen in halite growth models and exemplarily expressed by a Damköhler number³⁹.

Our SEM-based morphology analysis of dried fibrinogen precipitates shows the following pattern for sodium salts (c.f. Figure 2 and Figure 4):

- Na-PO₄ and Na₂SO₄: full coverage with dense fibers;
- NaCl: fiber formation only below crystals;
- Na-citrate: fiber formation at localized spots surrounded by confluent regions;
- Na-acetate: rough regions with coarsely fibrous features;
- Na-oxalate: rough regions without defined fibers.

We conclude that SO₄²⁻ anions lead to denser and more defined fiber networks than Cl⁻ anions as seen in Figure 2C for NaCl and Figure 4D for Na₂SO₄. Previously, Dumetz et al. showed that sulfate increases attractive interactions of proteins in concentrated salt solutions more than chloride, attributing this to water-mediated effects⁵⁴. Similarly, Metrick II and MacDonald showed that SO₄²⁻ ions decrease protein solvation, increasing protein stability and favoring salting-out effects (i.e. protein aggregation) while Cl⁻ ions enhance protein solvation and decrease protein stability in solution⁵⁵. These reports agree well with the trends in fiber assembly we observed for fibrinogen in the presence of SO₄²⁻ and Cl⁻.

Our findings suggest that not all polyvalent anions with sodium induce fiber formation. Neither Na⁺ or K⁺ cations nor SO₄²⁻ anions alone can fully explain the formation or absence of fibrinogen nanofibers. Comparing Na₂ SO₄ to K₂ SO₄, we found that the latter results in a much flatter fibrinogen film, despite both cations sharing the same counter anion. This may be due to sodium's higher affinity for protein surfaces⁴⁷, and its more ordered hydration shell compared to potassium⁵⁶. This might indicate that sodium provides a more kosmotropic environment for fibrinogen than potassium and promotes nanofiber formation by altering protein self-assembly.

3.6 Mechanism of salt-induced fiber assembly from highly saline fibrinogen solutions

In our recent review, we showed that ions play a more significant role than substrate surface properties during *in vitro* fiber assembly of fibrinogen¹. Although many studies previously included metal ions during different fiber assembly routines, their effect on fiber formation remained unclear and no classification of fibrinogen solidification based on the Hofmeister series has yet been presented. Therefore, we investigated the fundamental role of monovalent ions, commonly present in aqueous fibrinogen solutions during fiber formation^{20,21,25,57–66}. Thereby, we found that the sole consideration of cations or anions, as they would occur in a one-dimensional Hofmeister series, is not sufficient to explain the relevant driving forces for

fibrinogen fibrillogenesis. These findings and our earlier work on the influence of divalent ions on fibrinogen precipitation²⁶ now led to a two-dimensional Hofmeister series that summarizes the tendency of fibrinogen to form fibers based on the anions and cations present during drying (see Figure 5). Ordinate and abscissa order anions and cations by their kosmotropic and chaotropic effects, respectively. Exemplary SEM images included in the 2D-Hofmeister series illustrate fibrinogen morphology when precipitated from various salt solutions. Thus, the two axes also arrange the impact of different an- or cations on forming distinct, thin and dense fibers. Moreover, the ordinate arranges the cation retention tendency after rinsing fibrinogen films assembled with various salts and their secondary structure. Thus, it can be seen that the appropriate combination of monovalent cations with anions is key to fiber formation during fibrinogen drying and to controlling the three-dimensional structure and roughness of fibrinogen precipitates from highly saline aqueous solutions.

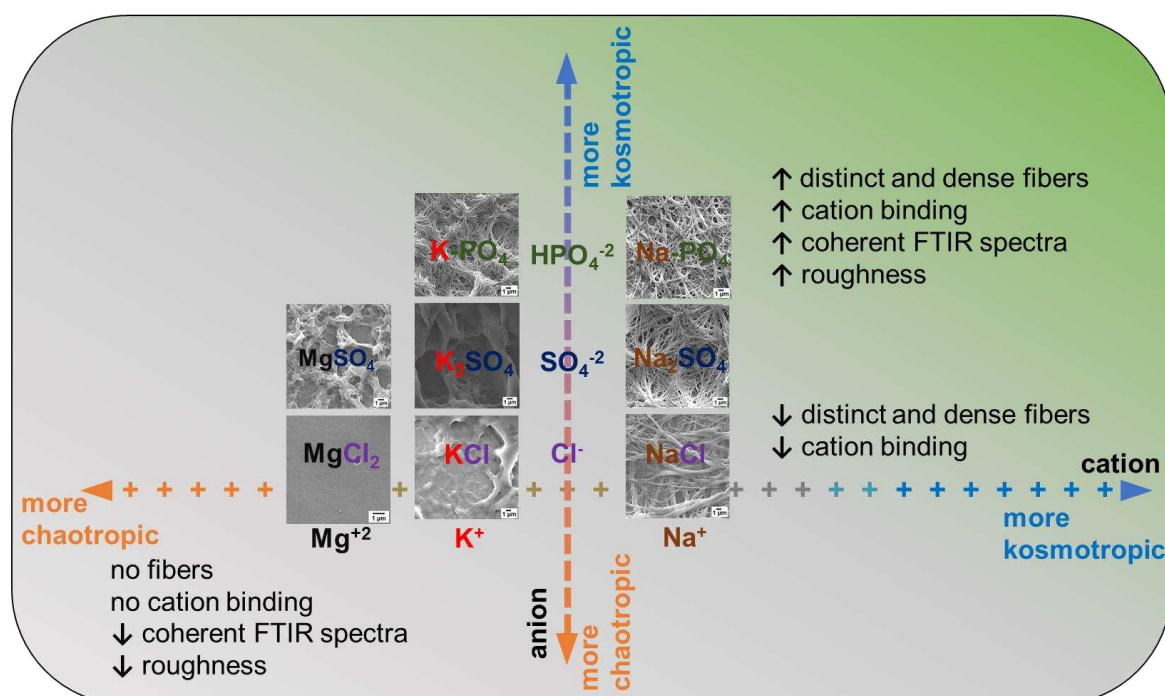


Figure 5: Two-dimensional Hofmeister series describing the influence of different ions on the morphology of fibrinogen precipitates. The abscissa ranges from chaotropic cations on the left to kosmotropic cations on the right, the ordinate ranges from chaotropic anions at the bottom to kosmotropic anions on the top. The combination of a kosmotropic cation with a kosmotropic anion (e.g. Na-PO₄) leads to very dense fiber networks as shown in the green shaded quadrant at the top right, whereas a chaotropic cation combined with a chaotropic anion (e.g. MgCl₂) yields a very smooth structure as indicated by red shading at the bottom left. An intermediate state with the combination of a kosmotropic cation with a chaotropic anion (e.g. KCl) leads to a rough surface with no clear fiber formation. Image of fibrinogen dried in presence of MgCl₂ is modified and reproduced with permission from²⁶ Copyright © 2021, American Chemical Society.

Kosmotropic ions stabilize and salt out proteins, while chaotropic ions have a salting-in effect⁶⁷. Here, we correlate kosmotropic/chaotropic ions with their capacity to assemble or inhibit fibrinogen fibers. Sulfate and (protonated) phosphate exhibit a more pronounced salting-out effect than chlorides⁶⁸. In our study, this is reflected by the higher molar concentrations of alkali chlorides needed to precipitate fibrinogen compared to Na-PO₄ and K-PO₄ (see Figure

1). Monovalent kosmotropic cations like Na^+ can form fibers with slightly kosmotropic anions like Cl^- , while monovalent chaotropic cations like K^+ only form fibers with strongly kosmotropic anions like HPO_4^{2-} . Divalent salts do not form fibers regardless of the anion, even if highly kosmotropic (e.g. SO_4^{2-}). Therefore, fibrinogen forms a dense, highly defined fiber network only when both cations and anions have kosmotropic characteristics. These results underline the importance of both cations and anions in fibrinogen fiber formation, countering previous studies that suggested anions alone^{17,67,69,70} or cations alone²⁵ are more relevant. In this way, our results complement those of Hense et al.¹⁷, who studied the influence of different Hofmeister salts on fibrinogen fiber formation by varying the anions while using only Na^+ cations. Moreover, they did not study highly saline fibrinogen formulations where salting-out effects may dominate. This may explain why, unlike our findings, Hense et al. observed that more chaotropic anions like acetate resulted in fewer and thinner fibers. In contrast, we found that the chaotropic nature of Cl^- resulted in thicker and more coalesced fibers due to a ripening effect. This highlights how important it is to consider the ion pairs during fibrinogen precipitation and not just variations of the cation or anion alone.

In contrast to our previous study²⁶, Hense et al. recently demonstrated fibrinogen fiber formation with CaCl_2 and MgSO_4 at low temperature (5°C) without external triggers (e.g. water evaporation) allowing long aggregation times^{71,72}. Although Na_2SO_4 was initially reported as a strong fiber former¹⁷, this later study showed more defined fibrinogen fibers when Na_2SO_4 was used with MgCl_2 ⁷². Similarly, spontaneous self-assembly of protofibrils and fibers at 4°C was reported for fibrin-rich fibrinogen solutions with low sodium phosphate concentration^{18,19}. Conversely, at 37°C Hense et al. could only assemble fibrinogen fibers when NaCl was added to CaCl_2 to increase fibrinogen solubility and reach concentrations of 40 mg/mL . This suggests two regimes of salt-induced fibrinogen fiber assembly: one at low salt concentration and low temperature with slow kinetics that also works with divalent salts and is triggered by soluble fibrin that is also present in the blood¹⁹ and another faster regime, requiring higher monovalent salt and fibrinogen concentrations to significantly shorten fiber formation time.

Many authors have studied how Hofmeister salts influence self-assembly systems, proposing various explanations^{67,69,70,73}, but recent evidence shows that this complex phenomenon cannot be explained by a single theory^{67,70}. Understanding the hydration properties of ions in salt solutions, their interactions with protein surfaces (here fibrinogen) and the effects on protein-protein interactions is essential for a comprehensive understanding of fibrinogen solidification based on the Hofmeister series. Thereby, it needs to be considered that the observed phase transitions were studied *in vitro* and not *in vivo* and that solute–solute, water–water, and solute–water interactions need to be considered⁷⁰ to explain salt-induced fibrinogen fiber formation. For example, divalent chlorides were not detected in our previous XPS or EDX studies because divalent salts have higher binding forces to water than for monovalent salts^{26,74}. However, this does not explain why potassium was undetected, although fibrous structures formed with

potassium phosphate. This suggests specific interactions between ions and fibrinogen must be considered. Sodium has a higher affinity to proteins than potassium⁴⁷ but was only detected when phosphate was present during fiber formation, indicating the role of counter-ions is crucial. Furthermore, fibers were more defined and denser with phosphate and sulfate salts, especially with monovalent Na⁺ cations, but not with K⁺. Therefore, the equilibrium between ion and counter-ion pairing in water significantly influences their interaction with fibrinogen.

We suppose that during weak ion pairing in solution, such as sodium with more chaotropic anions or sulfate with more chaotropic cations⁷⁰, the ions are facilitated to interact with fibrinogen. This interaction results in a more pronounced salting-in effect, affecting the intramolecular and intermolecular interactions between protein moieties and preventing protein-protein contact through attractive hydrophobic interactions. In contrast, for salts with strong ion pairing in solution, salting-out predominates and fibrinogen-fibrinogen interaction becomes effective. Considering all these aspects and our recent results on the targeted fibrinogen fiber formation from highly saline aqueous formulations, we believe that sodium phosphate at higher concentrations provides the best ion/counter-ion combination for fibrinogen fiber assembly, as it favors all possible interactions of the water-fibrinogen-salt triad in a synergic way for self-assembly. Therefore, our study offers insight into optimal selection of monovalent salts for the assembly of fibrinogen nanofibers scaffolds for tissue engineering by considering for the first time the two-dimensional relationship between fibrinogen and salt based on their chao-/kosmotropic nature.

4. Conclusions

When studying the influence of monovalent salts with Na⁺ and K⁺ as cations on the salt-induced fibrillogenesis of fibrinogen, *in situ* analysis of the Aq surface roughness indicated a co-precipitation of salts and fibrinogen. By combining fibrinogen with four different salts with monovalent cations (NaCl, KCl, Na-PO₄, and K-PO₄), SEM-imaging and Aq-mapping analysis revealed varying fibrinogen morphologies ranging from smooth (KCl), rough and locally fibrous (NaCl), to highly and ubiquitously rough/fibrous (Na-PO₄ and K-PO₄) topography, with the latter forming the densest network with the smallest fiber diameters. FTIR analysis of fibrinogen precipitates assembled with various monovalent salts showed that conformational changes are not always associated with fiber assembly. Unlike divalent salts, which were rinsed out of the fibrinogen precipitates upon washing, XPS analysis for monovalent salts showed that ion uptake by fibrinogen is only detectable for samples with clear fiber formation and more persistent for Na⁺ than for K⁺. Fibrinogen fibrillogenesis was more pronounced for polyvalent partly protonated phosphate anions (i.e., H-PO₄) than for unmixed chloride anions. Using Na⁺ with the kosmotropic anion SO₄²⁻ led to fiber formation, while the more chaotropic anion oxalate yielded a rough surface without fibers. However, combining divalent Mg²⁺ or monovalent K⁺ cations with the kosmotropic anion (SO₄²⁻) did not produce fibers. We conclude

that fibrinogen salts out of solution at neutral pH and high ionic strength to form fibers, depending on the kosmotropic or chaotropic nature of the cations and anions present during drying. We conclude that fibrinogen forms fibres in the presence of monovalent salts at neutral pH and high ionic strength, which depends on the kosmotropic or chaotropic nature of the cations and anions present during drying. Based on our findings, we propose a two-dimensional Hofmeister series to summarize the fibrinogen fibrillogenesis with monovalent and divalent salts, where fiber formation is obtained by combining kosmotropic anions and kosmotropic cations, revealing that the driver for fibrillogenesis essentially is the composition of the salt.

Acknowledgements

D.B. gratefully acknowledges funding by the Emmy Noether program of the German Research Council (DFG) via grant number 267326782. S.St. was financially supported by the program Fraunhofer TALENTA start.

Declaration of competing interests

The authors declare no competing financial interest.

References

- (1) Stamboroski, S.; Joshi, A.; Noeske, P.-L. M.; Köppen, S.; Brüggemann, D. Principles of Fibrinogen Fiber Assembly in Vitro. *Macromol. Biosci.* **2021**, *21* (5), 2000412. <https://doi.org/10.1002/mabi.202000412>.
- (2) Weisel, J. W. Fibrinogen and Fibrin. In *Advances in Protein Chemistry*; 2005; Vol. 70, pp 247–299. [https://doi.org/10.1016/S0065-3233\(05\)70008-5](https://doi.org/10.1016/S0065-3233(05)70008-5).
- (3) Weisel, J. W.; Litvinov, R. I. Fibrin Formation, Structure and Properties. In *Sub-Cellular Biochemistry*; Springer, 2017; Vol. 82, pp 405–456. https://doi.org/10.1007/978-3-319-49674-0_13.
- (4) Medved, L.; Weisel, J. W. Recommendations for Nomenclature on Fibrinogen and Fibrin. *J. Thromb. Haemost.* **2009**, *7* (2), 355–359. <https://doi.org/10.1111/j.1538-7836.2008.03242.x>.
- (5) Doolittle, R. F. Fibrinogen and Fibrin. *Sci. Am.* **1981**, *245* (6), 126–135. <https://doi.org/https://doi.org/10.1038/scientificamerican1281-126>.
- (6) Kellum, J. A. Determinants of Blood PH in Health and Disease. *Crit. Care* **2000**, *4* (1), 6–14. <https://doi.org/10.1186/cc644>.
- (7) Nezafati, N.; Moztarzadeh, F.; Hesaraki, S. Surface Reactivity and in Vitro Biological Evaluation of Sol Gel Derived Silver/Calcium Silicophosphate Bioactive Glass. *Biotechnol. Bioprocess Eng.* **2012**, *17* (4), 746–754. <https://doi.org/10.1007/s12257-012-0046-x>.

- (8) Covington, A. K.; Robinson, R. A. References Standards for the Electrometric Determination, with Ion-Selective Electrodes, of Potassium and Calcium in Blood Serum. *Anal. Chim. Acta* **1975**, 78 (1), 219–223. [https://doi.org/10.1016/S0003-2670\(01\)84768-1](https://doi.org/10.1016/S0003-2670(01)84768-1).
- (9) Berend, K.; Van Hulsteijn, L. H.; Gans, R. O. B. Chloride: The Queen of Electrolytes? *Eur. J. Intern. Med.* **2012**, 23 (3), 203–211. <https://doi.org/10.1016/j.ejim.2011.11.013>.
- (10) Mcmanus, M.; Boland, E.; Sell, S.; Bowen, W.; Koo, H.; Simpson, D.; Bowlin, G. Electrospun Nanofibre Fibrinogen for Urinary Tract Tissue Reconstruction. *Biomed. Mater.* **2007**, 2, 257–262. <https://doi.org/10.1088/1748-6041/2/4/008>.
- (11) Gugutkov, D.; Gustavsson, J.; Ginebra, M. P.; Altankov, G. Fibrinogen Nanofibers for Guiding Endothelial Cell Behavior. *Biomater. Sci.* **2013**, 1 (10), 1065. <https://doi.org/10.1039/c3bm60124b>.
- (12) Forget, J.; Awaja, F.; Gugutkov, D.; Gustavsson, J.; Ferrer, G. G.; Coelho-sampaio, T.; Hochman-mendez, C.; Salmeron-sánchez, M.; Altankov, G. Differentiation of Human Mesenchymal Stem Cells Toward Quality Cartilage Using Fibrinogen-Based Nanofibers. *Macromol. Biosci.* **2016**, 16, 1348–1359. <https://doi.org/https://doi.org/10.1002/mabi.201600080>.
- (13) McManus, M. C.; Boland, E. D.; Simpson, D. G.; Barnes, C. P.; Bowlin, G. L. Electrospun Fibrinogen: Feasibility as a Tissue Engineering Scaffold in a Rat Cell Culture Model. *J. Biomed. Mater. Res. Part A* **2007**, 81A (2), 299–309. <https://doi.org/10.1002/jbm.a.30989>.
- (14) Wnek, G. E.; Carr, M. E.; Simpson, D. G.; Bowlin, G. L. Electrospinning of Nanofiber Fibrinogen Structures. *Nano Lett.* **2003**, 3 (2), 213–216. <https://doi.org/10.1021/nl025866c>.
- (15) McManus, M. C.; Boland, E. D.; Koo, H. P.; Barnes, C. P.; Pawlowski, K. J.; Wnek, G. E.; Simpson, D. G.; Bowlin, G. L. Mechanical Properties of Electrospun Fibrinogen Structures. *Acta Biomater.* **2006**, 2 (1), 19–28. <https://doi.org/10.1016/j.actbio.2005.09.008>.
- (16) Wei, G.; Reichert, J.; Jandt, K. D. Controlled Self-Assembly and Templated Metallization of Fibrinogen Nanofibrils. *Chem. Commun.* **2008**, No. 33, 3903–3905. <https://doi.org/10.1039/b806316h>.
- (17) Hense, D.; Büngeler, A.; Kollmann, F.; Hanke, M.; Orive, A.; Keller, A.; Grundmeier, G.; Huber, K.; Strube, O. I. Self-Assembled Fibrinogen Hydro- And Aerogels with Fibrin-like 3D Structures. *Biomacromolecules* **2021**, 22 (10), 4084–4094. <https://doi.org/10.1021/acs.biomac.1c00489>.
- (18) Galanakis, D. K.; Protopopova, A.; Zhang, L.; Li, K.; Marmorat, C.; Scheiner, T.; Koo, J.; Savitt, A. G.; Rafailovich, M.; Weisel, J. Fibers Generated by Plasma Des-AA Fibrin Monomers and Protofibril/Fibrinogen Clusters Bind Platelets: Clinical and Nonclinical Implications. *TH Open* **2021**, 05 (03), e273–e285. <https://doi.org/10.1055/s-0041-1725976>.
- (19) Galanakis, D. K.; Protopopova, A.; Li, K.; Yu, Y.; Ahmed, T.; Senzel, L.; Heslin, R.; Gouda, M.; Koo, J.; Weisel, J.; Manco-Johnson, M.; Rafailovich, M. Novel Characteristics of Soluble Fibrin: Hypercoagulability and Acceleration of Blood Sedimentation Rate Mediated by Its Generation of Erythrocyte-Linked Fibers. *Cell Tissue Res.* **2022**, 387 (3), 479–491. <https://doi.org/10.1007/s00441-022-03599-9>.
- (20) Stapelfeldt, K.; Stamboroski, S.; Mednikova, P.; Brüggemann, D. Fabrication of 3D-Nanofibrous Fibrinogen Scaffolds Using Salt-Induced Self Assembly. *Biofabrication* **2019**, 11 (2), 025010. <https://doi.org/10.1088/1758-5090/ab0681>.
- (21) Stapelfeldt, K.; Stamboroski, S.; Walter, I.; Suter, N.; Kowalik, T.; Michaelis, M.; Br, D. Controlling the Multiscale Structure of Nanofibrous Fibrinogen Scaffolds for Wound Healing.

- Nano Lett.* **2019**, 49 (0), 1–15. <https://doi.org/https://doi.org/10.1021/acs.nanolett.9b02798>.
- (22) Suter, N.; Joshi, A.; Wunsch, T.; Graupner, N.; Stapelfeldt, K.; Radmacher, M.; Müssig, J.; Brüggemann, D. Self-Assembled Fibrinogen Nanofibers Support Fibroblast Adhesion and Prevent E. Coli Infiltration. *Mater. Sci. Eng. C* **2021**, 126, 112156. <https://doi.org/https://doi.org/10.1016/j.msec.2021.112156>.
- (23) Joshi, A.; Nuntapramote, T.; Brüggemann, D. Self-Assembled Fibrinogen Scaffolds Support Cocultivation of Human Dermal Fibroblasts and HaCaT Keratinocytes. *ACS Omega* **2023**, 8 (9), 8650–8663. <https://doi.org/10.1021/acsomega.2c07896>.
- (24) Kenny, M.; Stamboroski, S.; Taher, R.; Brüggemann, D.; Schoen, I. Nanofiber Topographies Enhance Platelet-Fibrinogen Scaffold Interactions. *Adv. Healthc. Mater.* **2022**, 2200249, 2200249. <https://doi.org/10.1002/adhm.202200249>.
- (25) Wei, G.; Reichert, J.; Bossert, J.; Jandt, K. D. Novel Biopolymeric Template for the Nucleation and Growth of Hydroxyapatite Crystals Based on Self-Assembled Fibrinogen Fibrils. *Biomacromolecules* **2008**, 9 (11), 3258–3267. <https://doi.org/10.1021/bm800824r>.
- (26) Stamboroski, S.; Boateng, K.; Lierath, J.; Kowalik, T.; Thiel, K.; Köppen, S.; Noeske, P.-L. M.; Brüggemann, D. Influence of Divalent Metal Ions on the Precipitation of the Plasma Protein Fibrinogen. *Biomacromolecules* **2021**, In press. <https://doi.org/10.1021/acs.biomac.1c00930>.
- (27) Kostelansky, M. S.; Betts, L.; Gorkun, O. V.; Lord, S. T. 2.8 Å Crystal Structures of Recombinant Fibrinogen Fragment D with and without Two Peptide Ligands: GHRP Binding to the “b” Site Disrupts Its Nearby Calcium-Binding Site. *Biochemistry* **2002**, 41 (40), 12124–12132. <https://doi.org/10.1021/bi0261894>.
- (28) Anandkrishnan, R.; Aguilar, B.; Onufriev, A. V. H++ 3.0: Automating PK Prediction and the Preparation of Biomolecular Structures for Atomistic Molecular Modeling and Simulations. *Nucleic Acids Res.* **2012**, 40 (W1), W537–W541. <https://doi.org/10.1093/nar/gks375>.
- (29) Myers, J.; Grothaus, G.; Narayanan, S.; Onufriev, A. A Simple Clustering Algorithm Can Be Accurate Enough for Use in Calculations of p K s in Macromolecules. *Proteins Struct. Funct. Bioinforma.* **2006**, 63 (4), 928–938. <https://doi.org/10.1002/prot.20922>.
- (30) Gordon, J. C.; Myers, J. B.; Folta, T.; Shoja, V.; Heath, L. S.; Onufriev, A. H++: A Server for Estimating PKas and Adding Missing Hydrogens to Macromolecules. *Nucleic Acids Res.* **2005**, 33 (Web Server), W368–W371. <https://doi.org/10.1093/nar/gki464>.
- (31) Kashfolgheta, S.; Vila Verde, A. Developing Force Fields When Experimental Data Is Sparse: AMBER/GAFF-Compatible Parameters for Inorganic and Alkyl Oxoanions. *Phys. Chem. Chem. Phys.* **2017**, 19 (31), 20593–20607. <https://doi.org/10.1039/C7CP02557B>.
- (32) Jo, S.; Kim, T.; Iyer, V. G.; Im, W. CHARMM-GUI: A Web-based Graphical User Interface for CHARMM. *J. Comput. Chem.* **2008**, 29 (11), 1859–1865. <https://doi.org/10.1002/jcc.20945>.
- (33) Lee, J.; Hitzenberger, M.; Rieger, M.; Kern, N. R.; Zacharias, M.; Im, W. CHARMM-GUI Supports the Amber Force Fields. *J. Chem. Phys.* **2020**, 153 (3). <https://doi.org/10.1063/5.0012280>.
- (34) Humphrey, W.; Dalke, A.; Schulten, K. VMD: Visual Molecular Dynamics. *J. Mol. Graph.* **1996**, 14 (1), 33–38. [https://doi.org/10.1016/0263-7855\(96\)00018-5](https://doi.org/10.1016/0263-7855(96)00018-5).
- (35) Michaud-Agrawal, N.; Denning, E. J.; Woolf, T. B.; Beckstein, O. MDAAnalysis: A Toolkit for the Analysis of Molecular Dynamics Simulations. *J. Comput. Chem.* **2011**, 32 (10), 2319–2327. <https://doi.org/10.1002/jcc.21787>.
- (36) Gowers, R.; Linke, M.; Barnoud, J.; Reddy, T.; Melo, M.; Seyler, S.; Domański, J.; Dotson, D.;

- Buchoux, S.; Kenney, I.; Beckstein, O. MDAnalysis: A Python Package for the Rapid Analysis of Molecular Dynamics Simulations; 2016; pp 98–105. <https://doi.org/10.25080/Majora-629e541a-00e>.
- (37) Hammick, D. L.; Goadby, H. K.; Booth, H. CLXXV.—Disodium Hydrogen Phosphate Dodecahydrate. *J. Chem. Soc. Trans.* **1920**, 117 (0), 1589–1592. <https://doi.org/10.1039/CT9201701589>.
- (38) El, S. M. A.; Ghallali, A. L.; Guendouzi, M. E. L. Solubility and Thermodynamic Properties of Dipotassium or Disodium Hydrogenphosphates in Aqueous Solutions at Various Temperatures. *J. Solution Chem.* **2022**, 51 (7), 802–815. <https://doi.org/10.1007/s10953-022-01172-0>.
- (39) Stamboroski, S.; Boateng, K.; Leite Cavalcanti, W.; Noeske, M.; Beber, V. C.; Thiel, K.; Grunwald, I.; Schiffels, P.; Dieckhoff, S.; Brüggemann, D. Effect of Interface-Active Proteins on the Salt Crystal Size in Waterborne Hybrid Materials. *Appl. Adhes. Sci.* **2021**, 9 (1). <https://doi.org/10.1186/s40563-021-00137-8>.
- (40) Laclair, C. E.; Etzel, M. R. Turbidity and Protein Aggregation in Whey Protein Beverages. *J. Food Sci.* **2009**, 74 (7), C526–C535. <https://doi.org/10.1111/j.1750-3841.2009.01260.x>.
- (41) Goto, M.; Oaki, Y.; Imai, H. Dendritic Growth of NaCl Crystals in a Gel Matrix: Variation of Branching and Control of Bending. *Cryst. Growth Des.* **2016**, 16 (8), 4278–4284. <https://doi.org/10.1021/acs.cgd.6b00323>.
- (42) Espada, A.; Rivera-Sagredo, A. Ammonium Hydrogencarbonate, an Excellent Buffer for the Analysis of Basic Drugs by Liquid Chromatography–Mass Spectrometry at High PH. *J. Chromatogr. A* **2003**, 987 (1–2), 211–220. [https://doi.org/10.1016/S0021-9673\(02\)01819-8](https://doi.org/10.1016/S0021-9673(02)01819-8).
- (43) van Wijk, A. M.; Muijselaar, P. G.; Stegman, K.; de Jong, G. J. Capillary Electrophoresis-Mass Spectrometry for Impurity Profiling of Basic Pharmaceuticals Using Non-Volatile Background Electrolytes. *J. Chromatogr. A* **2007**, 1159 (1–2), 175–184. <https://doi.org/10.1016/j.chroma.2007.05.070>.
- (44) Streets, A. M.; Quake, S. R. Ostwald Ripening of Clusters during Protein Crystallization. *Phys. Rev. Lett.* **2010**, 104 (17), 178102. <https://doi.org/10.1103/PhysRevLett.104.178102>.
- (45) Van Oss, C. J. Long-Range and Short-Range Mechanisms of Hydrophobic Attraction and Hydrophilic Repulsion in Specific and Aspecific Interactions. *J. Mol. Recognit.* **2003**, 16 (4), 177–190. <https://doi.org/10.1002/jmr.618>.
- (46) Mantina, M.; Chamberlin, A. C.; Valero, R.; Cramer, C. J.; Truhlar, D. G. Consistent van Der Waals Radii for the Whole Main Group. *J. Phys. Chem. A* **2009**, 113 (19), 5806–5812. <https://doi.org/10.1021/jp8111556>.
- (47) Vrbka, L.; Vondrasek, J.; Jagoda-cwiklik, B.; Vacha, R.; Jungwirth, P. Quantification and Rationalization of the Higher Affinity of Sodium over Potassium to Protein Surfaces. **2006**. <https://doi.org/10.1073/pnas.0606959103>.
- (48) Kherb, J.; Flores, S. C.; Cremer, P. S. Role of Carboxylate Side Chains in the Cation Hofmeister Series. *J. Phys. Chem. B* **2012**, 116 (25), 7389–7397. <https://doi.org/10.1021/jp212243c>.
- (49) De Vries, J. J.; Snoek, C. J. M.; Rijken, D. C.; De Maat, M. P. M. Effects of Post-Translational Modifications of Fibrinogen on Clot Formation, Clot Structure, and Fibrinolysis: A Systematic Review. *Arterioscler. Thromb. Vasc. Biol.* **2020**, 40 (3), 554–569. <https://doi.org/10.1161/ATVBAHA.119.313626>.
- (50) Mosesson, M. W.; Siebenlist, K. R.; Meh, D. A. The Structure and Biological Features of Fibrinogen and Fibrin. *Ann. N. Y. Acad. Sci.* **2001**, 936 (1), 11–30. <https://doi.org/10.1111/j.1749-6632.2001.tb03491.x>.

- (51) Weisel, J. W.; Litvinov, R. I. Mechanisms of Fibrin Polymerization and Clinical Implications. *Blood* **2013**, *121* (10), 1712–1719. <https://doi.org/10.1182/blood-2012-09-306639>.
- (52) Hunter, T. Why Nature Chose Phosphate to Modify Proteins. *Philos. Trans. R. Soc. B Biol. Sci.* **2012**, *367* (1602), 2513–2516. <https://doi.org/10.1098/rstb.2012.0013>.
- (53) Lin, B.; McCormick, A. V.; Davis, H. T.; Strey, R. Solubility of Sodium Soaps in Aqueous Salt Solutions. *J. Colloid Interface Sci.* **2005**, *291* (2), 543–549. <https://doi.org/10.1016/j.jcis.2005.05.036>.
- (54) Dumetz, A. C.; Snellinger-O'Brien, A. M.; Kaler, E. W.; Lenhoff, A. M. Patterns of Protein-Protein Interactions in Salt Solutions and Implications for Protein Crystallization. *Protein Sci.* **2007**, *16* (9), 1867–1877. <https://doi.org/10.1110/ps.072957907>.
- (55) A Metrick II, M.; Macdonald, G. Colloids and Surfaces A : Physicochemical and Engineering Aspects Hofmeister Ion Effects on the Solvation and Thermal Stability of Model Proteins Lysozyme and Myoglobin. *Colloids Surfaces A Physicochem. Eng. Asp.* **2015**, *469*, 242–251. <https://doi.org/10.1016/j.colsurfa.2015.01.038>.
- (56) Mancinelli, R.; Botti, A.; Bruni, F.; Ricci, M. A.; Amaldi, F. E.; Uni, V. Hydration of Sodium , Potassium , and Chloride Ions in Solution and the Concept of Structure Maker / Breaker. **2007**, 13570–13577.
- (57) Chen, G.; Ni, N.; Wang, B.; Xu, B.; Chen, G., Ni, N., Wang, B., & Xu, B. Direct Observation of Self-Assembled Fibrinogen Fiber Formation on Au (1, 1, 1) in the Absence of Thrombin. *Chemphyschem a Eur. J. Chem. Phys. Phys. Chem.* **2011**, *11* (3), 565–568. <https://doi.org/10.1002/cphc.200900916>.
- (58) Raoufi, M.; Aslankoochi, N.; Mollenhauer, C.; Boehm, H.; Spatz, J. P.; Brüggemann, D. Template-Assisted Extrusion of Biopolymer Nanofibers under Physiological Conditions. *Integr. Biol. (United Kingdom)* **2016**, *8* (10), 1059–1066. <https://doi.org/10.1039/c6ib00045b>.
- (59) Barinov, N. A.; Pavlova, E. R.; Tolstova, A. P.; Dubrovin, E. V.; Klinov, D. V. Myeloperoxidase-Induced Fibrinogen Unfolding and Clotting. *bioRxiv* **2021**, 1–19. <https://doi.org/10.1101/2021.01.06.425586>.
- (60) Reichert, J.; Wei, G.; Jandt, K. D. Formation and Topotactical Orientation of Fibrinogen Nanofibrils on Graphite Nanostructures. *Adv. Eng. Mater.* **2009**, *11* (11), B177–B181. <https://doi.org/10.1002/adem.200900084>.
- (61) Zhang, L.; Casey, B.; Galanakis, D. K.; Marmorat, C.; Skoog, S.; Vorvolakos, K.; Simon, M.; Rafailovich, M. H. The Influence of Surface Chemistry on Adsorbed Fibrinogen Conformation, Orientation, Fiber Formation and Platelet Adhesion. *Acta Biomater.* **2017**, *54*, 164–174. <https://doi.org/10.1016/j.actbio.2017.03.002>.
- (62) Koo, J.; Galanakis, D.; Liu, Y.; Ramek, A.; Fields, A.; Ba, X.; Simon, M.; Rafailovich, M. H. Control of Anti-Thrombogenic Properties: Surface-Induced Self- Assembly of Fibrinogen Fibers. *Biomacromolecules* **2012**, *13*, 1259–1268.
- (63) Barinov, N. A.; Protopopova, A. D.; Dubrovin, E. V.; Klinov, D. V. Thermal Denaturation of Fibrinogen Visualized by Single-Molecule Atomic Force Microscopy. *Colloids Surfaces B Biointerfaces* **2018**, *167*, 370–376. <https://doi.org/10.1016/j.colsurfb.2018.04.037>.
- (64) Helbing, C.; Stoeßel, R.; Hering, D. A.; Arras, M. M. L.; Bossert, J.; Jandt, K. D. PH-Dependent Ordered Fibrinogen Adsorption on Polyethylene Single Crystals. *Langmuir* **2016**, *32* (45), 11868–11877. <https://doi.org/https://pubs.acs.org/doi/10.1021/acs.langmuir.6b03110>.
- (65) Koo, J.; Rafailovich, M. H.; Medved, L.; Tsurupa, G.; Kudryk, B. J.; Liu, Y.; Galanakis, D. K. Evaluation of Fibrinogen Self-Assembly: Role of Its AC Region. *J. Thromb. Haemost.* **2010**, *8*

- (12), 2727–2735. <https://doi.org/10.1111/j.1538-7836.2010.04072.x>.
- (66) Dubrovin, E. V.; Barinov, N. A.; Schäffer, T. E.; Klinov, D. V. In Situ Single-Molecule AFM Investigation of Surface-Induced Fibrinogen Unfolding on Graphite. *Langmuir* **2019**, *35* (30), 9732–9739. <https://doi.org/10.1021/acs.langmuir.9b01178>.
- (67) Okur, H. I.; Hladílková, J.; Rembert, K. B.; Cho, Y.; Heyda, J.; Dzubiella, J.; Cremer, P. S.; Jungwirth, P. Beyond the Hofmeister Series: Ion-Specific Effects on Proteins and Their Biological Functions. *J. Phys. Chem. B* **2017**, *121* (9), 1997–2014. <https://doi.org/10.1021/acs.jpcc.6b10797>.
- (68) Collins, K. D. Why Continuum Electrostatics Theories Cannot Explain Biological Structure, Polyelectrolytes or Ionic Strength Effects in Ion-Protein Interactions. *Biophys. Chem.* **2012**, *167*, 43–59. <https://doi.org/10.1016/j.bpc.2012.04.002>.
- (69) Iscen, A.; Schatz, G. C. Hofmeister Effects on Peptide Amphiphile Nanofiber Self-Assembly. *J. Phys. Chem. B* **2019**, *123* (32), 7006–7013. <https://doi.org/10.1021/acs.jpcc.9b05532>.
- (70) Gibb, B. C. Supramolecular Assembly and Binding in Aqueous Solution: Useful Tips Regarding the Hofmeister and Hydrophobic Effects. *Isr. J. Chem.* **2011**, *51* (7), 798–806. <https://doi.org/10.1002/ijch.201100058>.
- (71) Hense, D.; Strube, O. I. Fibrillogenesis and Hydrogel Formation from Fibrinogen Induced by Calcium Salts. *Gels* **2023**, *9* (3). <https://doi.org/10.3390/gels9030175>.
- (72) Hense, D.; Strube, O. I. Thrombin-Free Fibrillogenesis and Gelation of Fibrinogen Triggered by Magnesium Sulfate. *Gels* **2023**, *9* (11), 892. <https://doi.org/10.3390/gels9110892>.
- (73) Zhang, Y.; Cremer, P. S. Interactions between Macromolecules and Ions: The Hofmeister Series. *Current Opinion in Chemical Biology*. Elsevier Current Trends December 1, 2006, pp 658–663. <https://doi.org/10.1016/j.cbpa.2006.09.020>.
- (74) Kiyohara, K.; Kawai, Y. Hydration of Monovalent and Divalent Cations near a Cathode Surface. *J. Chem. Phys.* **2019**, *151* (10), 104704. <https://doi.org/10.1063/1.5113738>.

SUPPORTING INFORMATION

Influence of highly saline aqueous solutions of monovalent alkali metal ions on fibrinogen self-assembly *in vitro*

Stephani Stamboroski^{1,2}, *Kwasi Boateng*^{1,2}, *Jana Lierath*^{1,2}, *Jonas Aniol*¹, *Peter Schiffels*¹, *Paul-Ludwig Michael Noeske*^{1,3}, *Dorothea Brüggemann*^{2,4, #, *}

¹ Fraunhofer Institute for Manufacturing Technology and Advanced Materials IFAM, Wiener Strasse 12, 28359 Bremen, Germany

² Institute for Biophysics, University of Bremen, Otto-Hahn-Allee 1, 28359 Bremen, Germany

³ University of Applied Sciences Bremerhaven, An der Karlstadt 8, Bremerhaven 27568, Germany

⁴ MAPEX Center for Materials and Processes, University of Bremen, 28359 Bremen, Germany

Present address: City University of Applied Sciences, Neustadtswall 30, 28199 Bremen, Germany

* Corresponding author: Dorothea.brueggemann@hs-bremen.de

Table S1:

Table S1: Details of fiber diameter analysis from representative SEM images. Fibrinogen fibers were prepared by drying mixtures of 2.5 mg/mL fibrinogen with (A) 375 mM NaCl, (B) 2.5x PBS, (C) 100 mM Na-PO₄ and (D) 100 mM K-PO₄. Average fiber diameter measurements were conducted by measuring 50 randomized positions per SEM image (indicated by red lines) with the ImageJ Software. The thinnest average fiber diameters were obtained with Na-PO₄, followed by K-PO₄, PBS and NaCl. For 375 mM KCl no fiber diameters were obtained because no fibers had formed during fibrinogen precipitation.

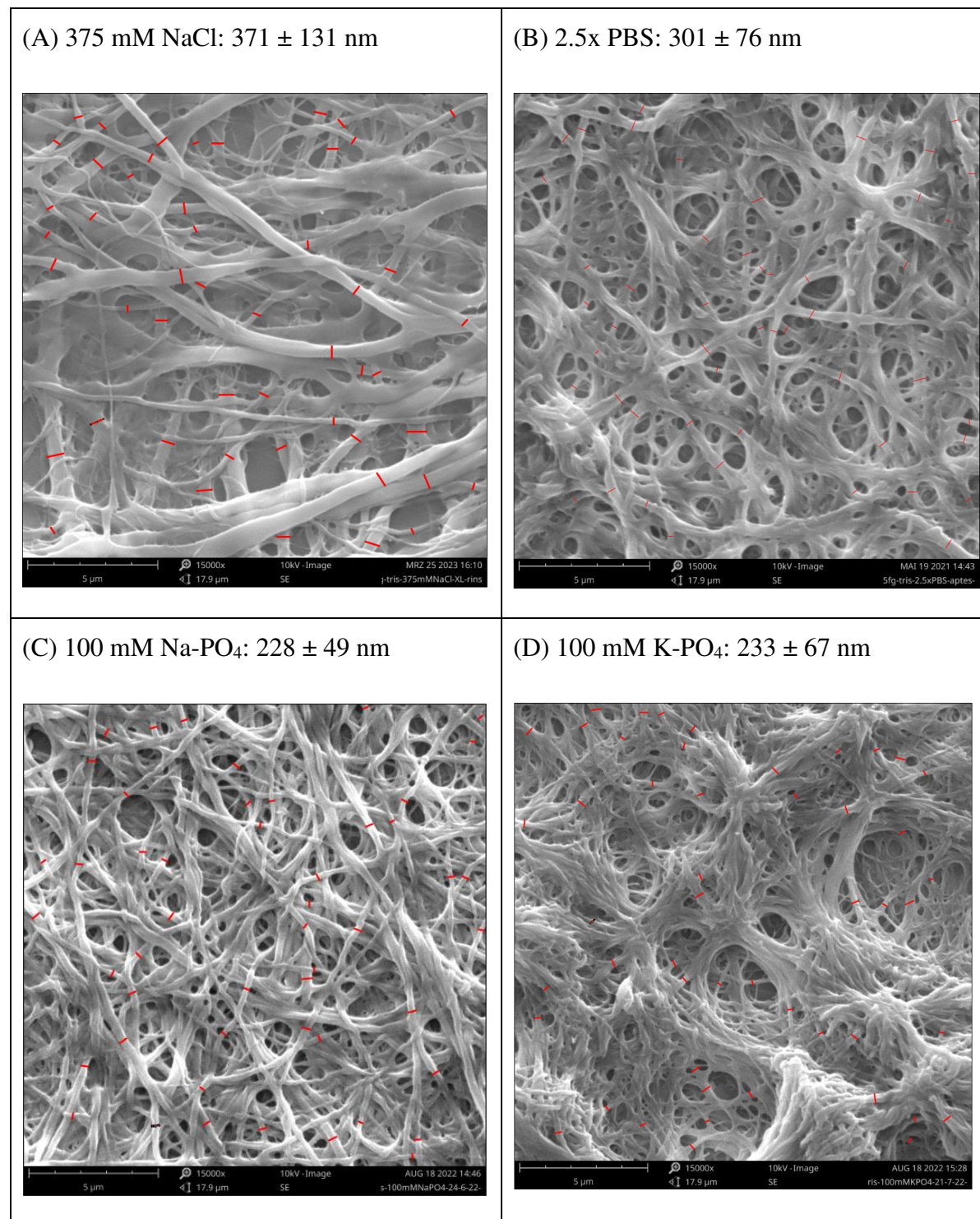


Figure S1:

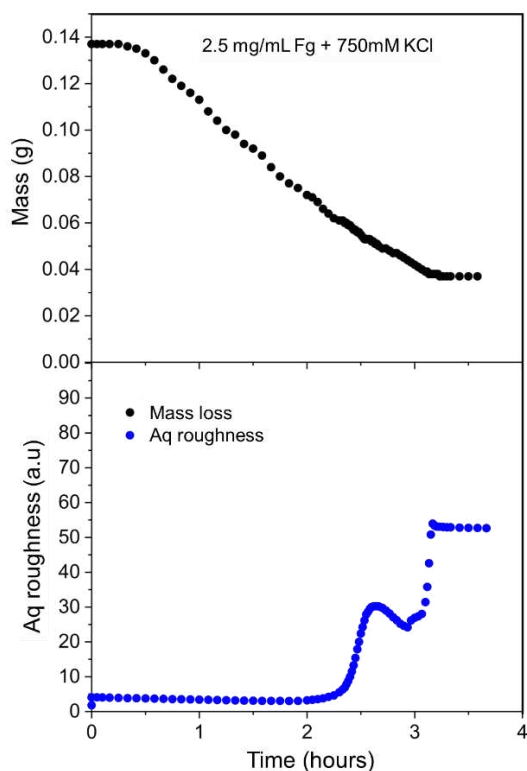


Figure S1: Mass loss correlation with Aq roughness during fibrinogen drying. Example of the linear mass decrease during drying (water evaporation) and in situ measurement of the Aq roughness as a function of time of one droplet containing a mixture of 2.5 mg/mL fibrinogen (Fg) and 750 mM KCl applied on the surface of a gold substrate. The first increase in Aq roughness happened when 75-80% of the water had evaporated, and the last increase was observed when most of the water had evaporated (95%)

Figure S2:

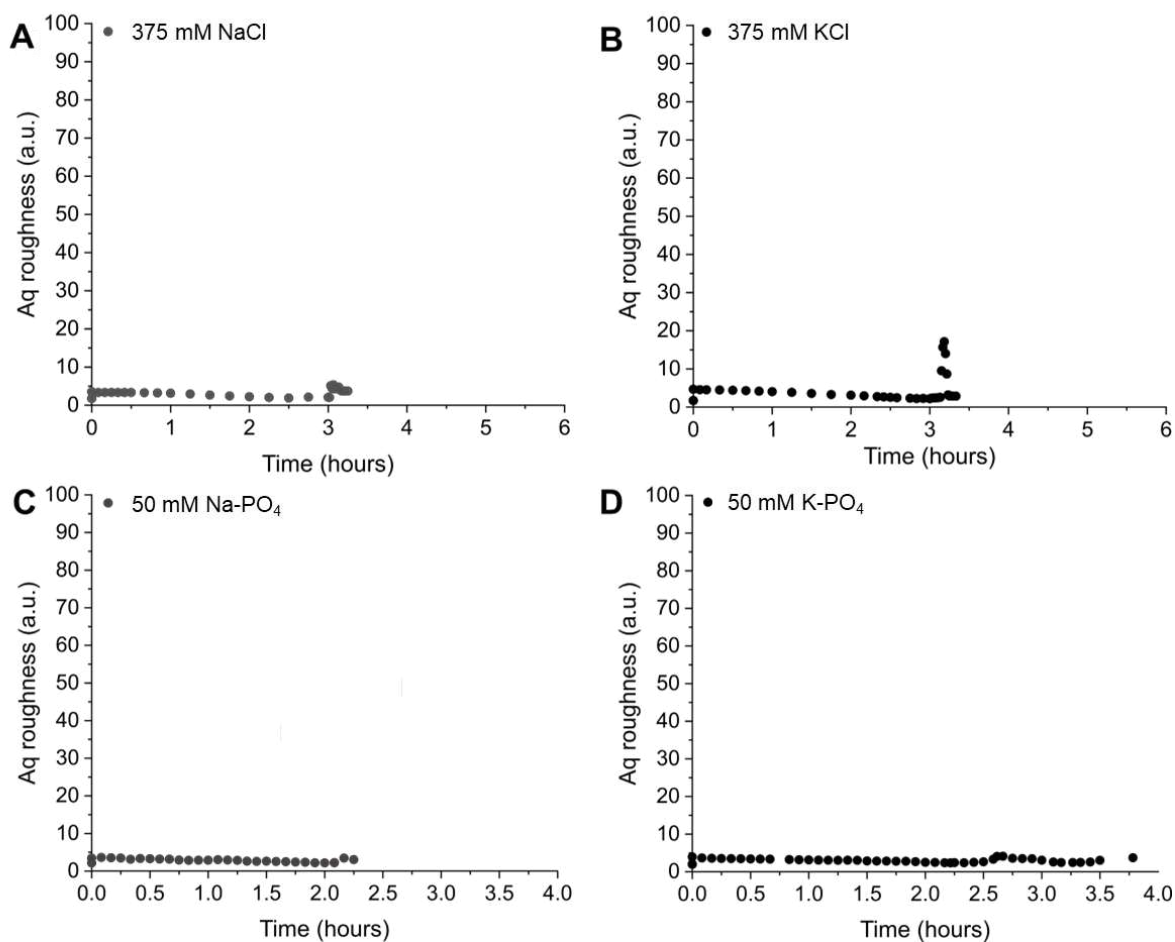


Figure S2: Aq curve profiles from light scattering analysis of monovalent salt precipitation on gold. In each plot, the round dots represent the change in Aq surface roughness during the drying of droplets containing (A) 375 mM NaCl (in Tris), (B) 375 mM KCl (in Tris), (C) 50 mM Na-PO₄, and (D) 50 mM K-PO₄. The initial Aq values at 0 h represent the roughness of the underlying gold substrate before the salt solutions were added. For all tested salts, no significant change in the Aq roughness was observed during drying. The final Aq roughness values around 1-2 indicate very smooth surfaces. When compared to Figure S3, we can infer that at the center of the samples no bigger salt crystals were formed and therefore no high Aq roughness was recorded.

Figure S3:

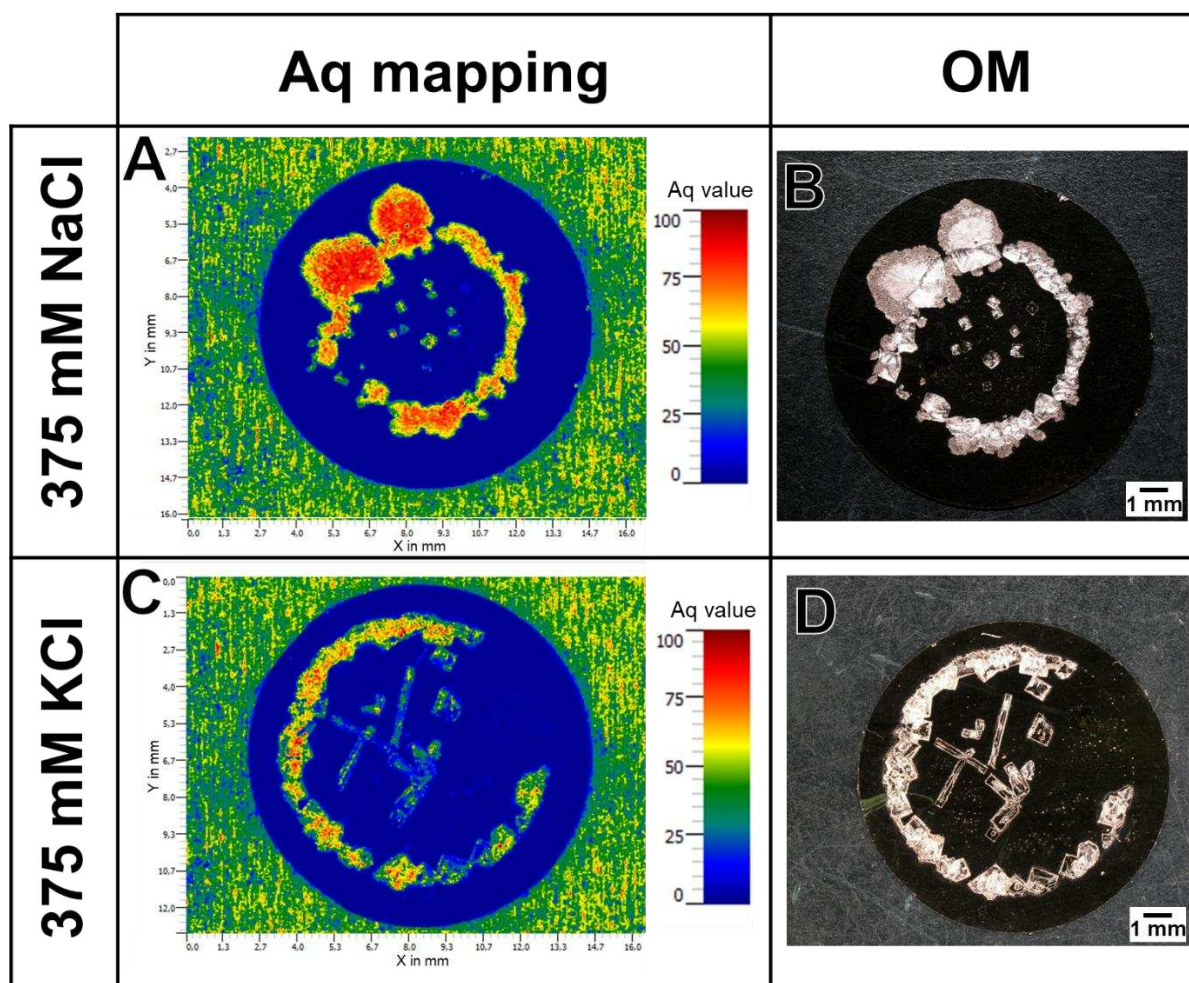


Figure S3: Surface features of dried salt crystals on gold substrates. (A) Aq based survey images and (B) optical light microscopy (OM) images of 375 mM NaCl, (C) Aq based survey images and (B) OM images of 375 mM KCl. For both salts, light microscopy images correspond to Aq-mapping with red color being an indication of rougher and more elevated areas. Salt crystals precipitated at the outer edges of the droplet, i.e., at the pinning line while the center was free of bigger salt crystals, revealing a very low Aq value at the center of both samples, corresponding well with the data obtained for in situ analysis of drying of salts alone without fibrinogen as presented in Figure S2.

Figure S4:

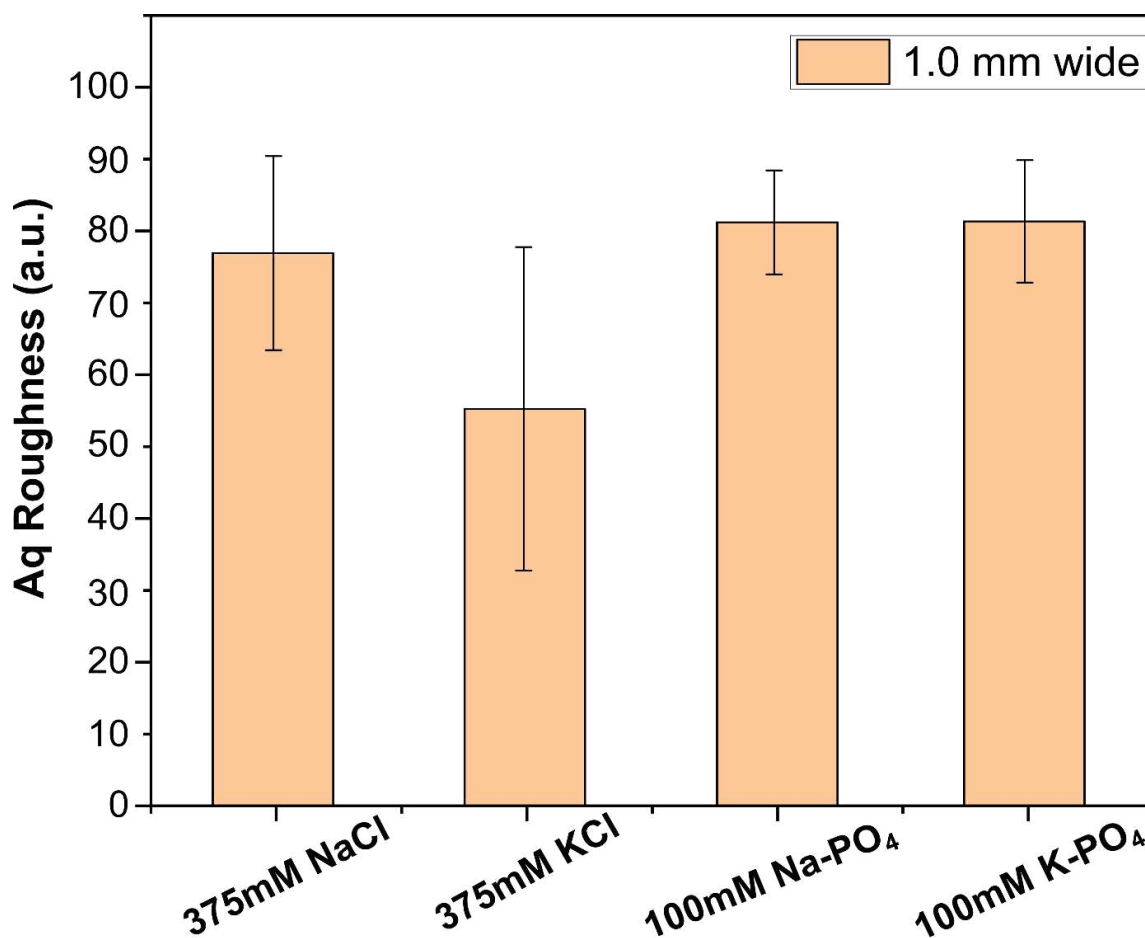


Figure S4: Average Aq roughness for 2.5 mg/mL fibrinogen dried in the presence of different monovalent salts after cross-linking and washing. The average Aq roughness was recorded in a 1 mm wide central regions of the samples presented in Figure 2. A smooth surface morphology (375 mM KCl, no fibers) led to the lowest Aq value, low density fiber (375 mM NaCl) yielded the second lowest Aq values, whereas more dense fibers (Na-PO₄ and K-PO₄) were associated with the highest Aq values and the lowest standard deviations.

Figure S5:

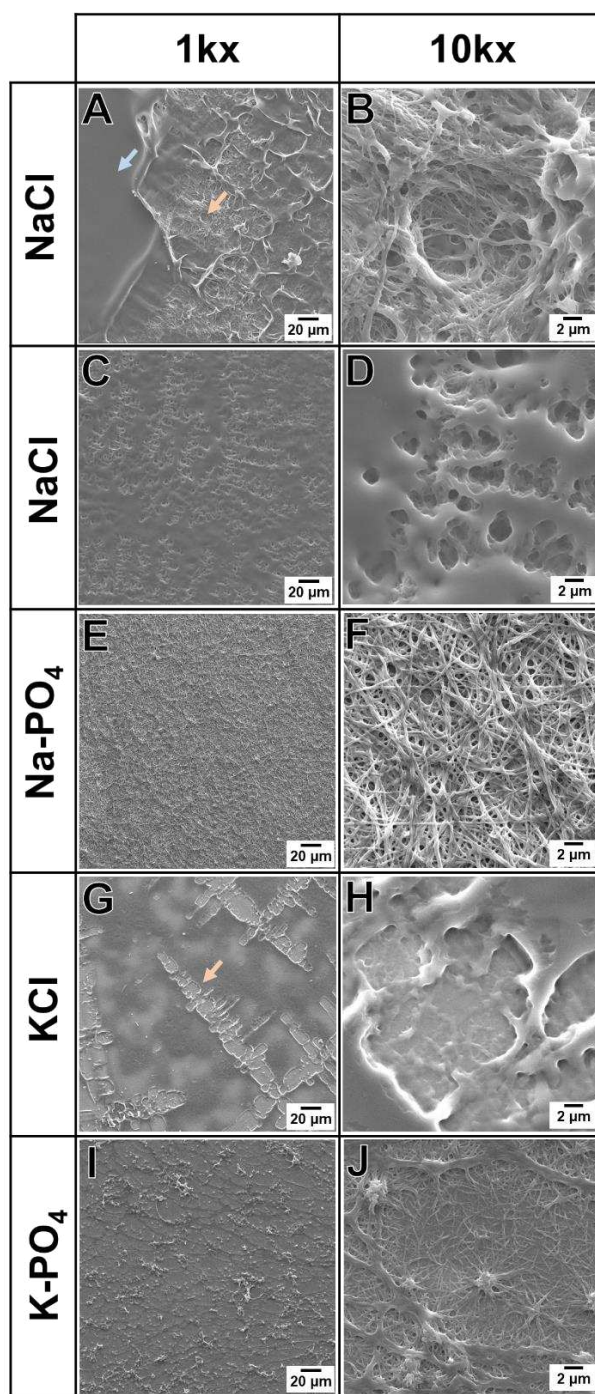


Figure S5: SEM-based local detail images of fibrinogen samples after drying, crosslinking and washing mixtures of 2.5 mg/mL fibrinogen and different salts. (A, B, C, D) 375 mM NaCl, (E, F) 100 mM Na-PO₄, (G, H) 375 mM KCl and (I, J) 100 mM K-PO₄. Image on the left show bigger regions of the samples at 1 kx magnification, while images on the right side show detailed parts at 10 kx magnification of a zoomed area of the same region. For NaCl, two different regions are presented to show the different morphologies observed along the same sample. The blue arrow in A indicates the elevated smooth region and the orange one shows the fibrous region, which is then shown in detail in B. For Na-PO₄ and K-PO₄, the fibers were distributed evenly across the sample. For KCl, the orange arrow in G points to the zoomed region presented in H.

Figure S6:

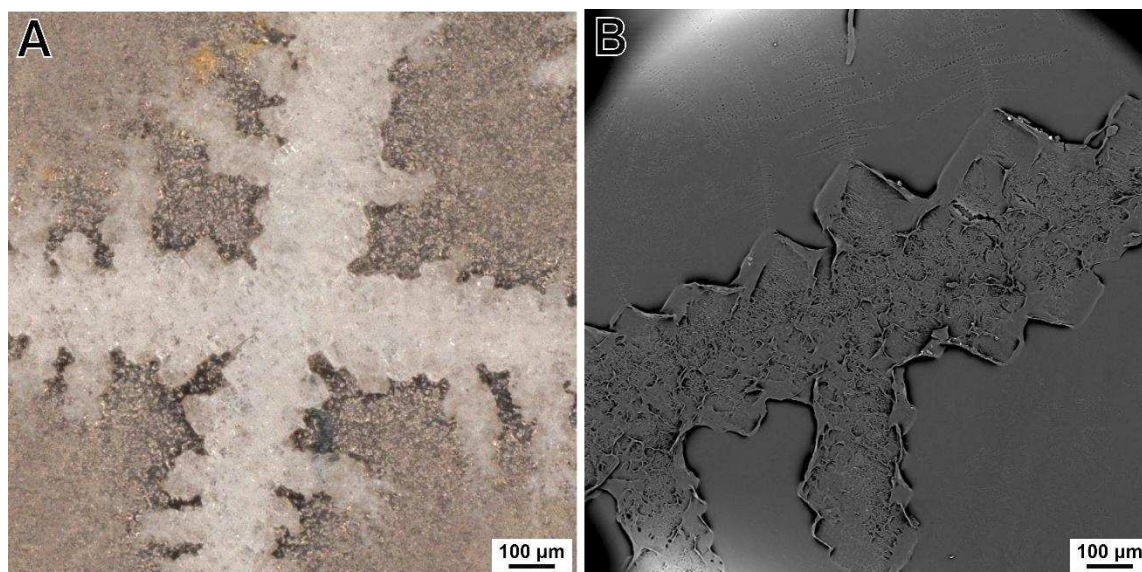


Figure S6: Fibrinogen precipitation in the presence of NaCl. (A) Optical microscopy image of 2.5 mg/mL fibrinogen with NaCl after drying and crosslinking (adapted from (Stamboroski et al., 2021), licensed under a Creative Commons Attribution 4.0 International License), (B) Back scattered SEM image of 2.5 mg/mL fibrinogen with NaCl after drying, crosslinking and an additional rinsing step. The optical microscopy image in (A) shows the NaCl dendrites crystals formed during drying, and the SEM image in (B) shows the morphology of the fibrinogen layer below the NaCl dendrite crystals after washing, which preserved the fibrinogen nanofibers that had formed below the salt crystals. Morphological details of the fibrinogen sample shown in (B) are shown in Figure S5A-D.

Figure S7:

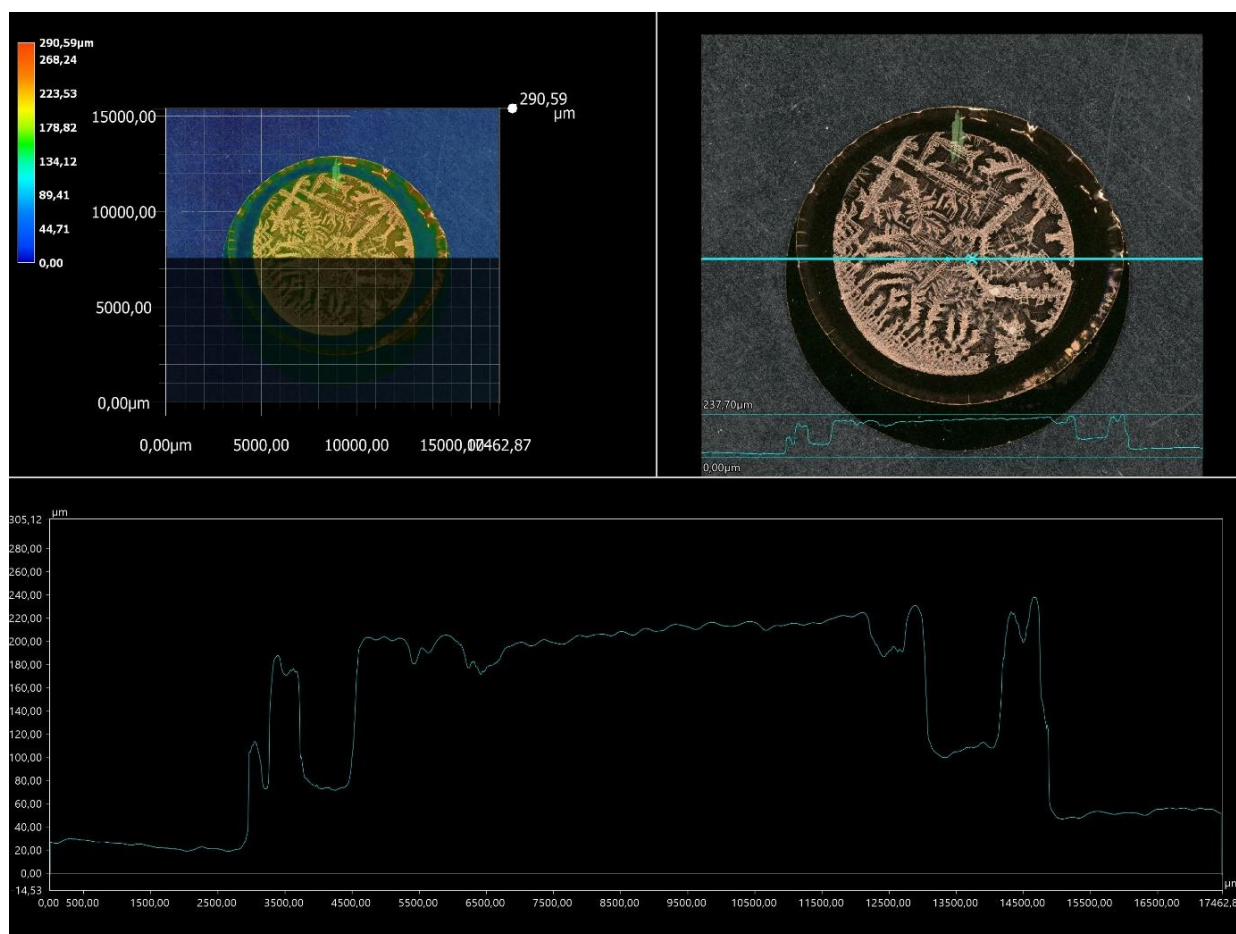


Figure S7: Surface topography of 2.5 mg/mL fibrinogen dried with 375 mM KCl in 5 mM Tris. Sample height profiles obtained from 3D optical microscopy after drying a mixture of 2.5 mg/mL fibrinogen and 375 mM KCl (in 10 mM Tris) showed how the thickness and salt crystal size varied along a representative horizontal line across the sample. The precipitated fibrinogen film has a thickness of at least a 100 μm .

Figure S8:

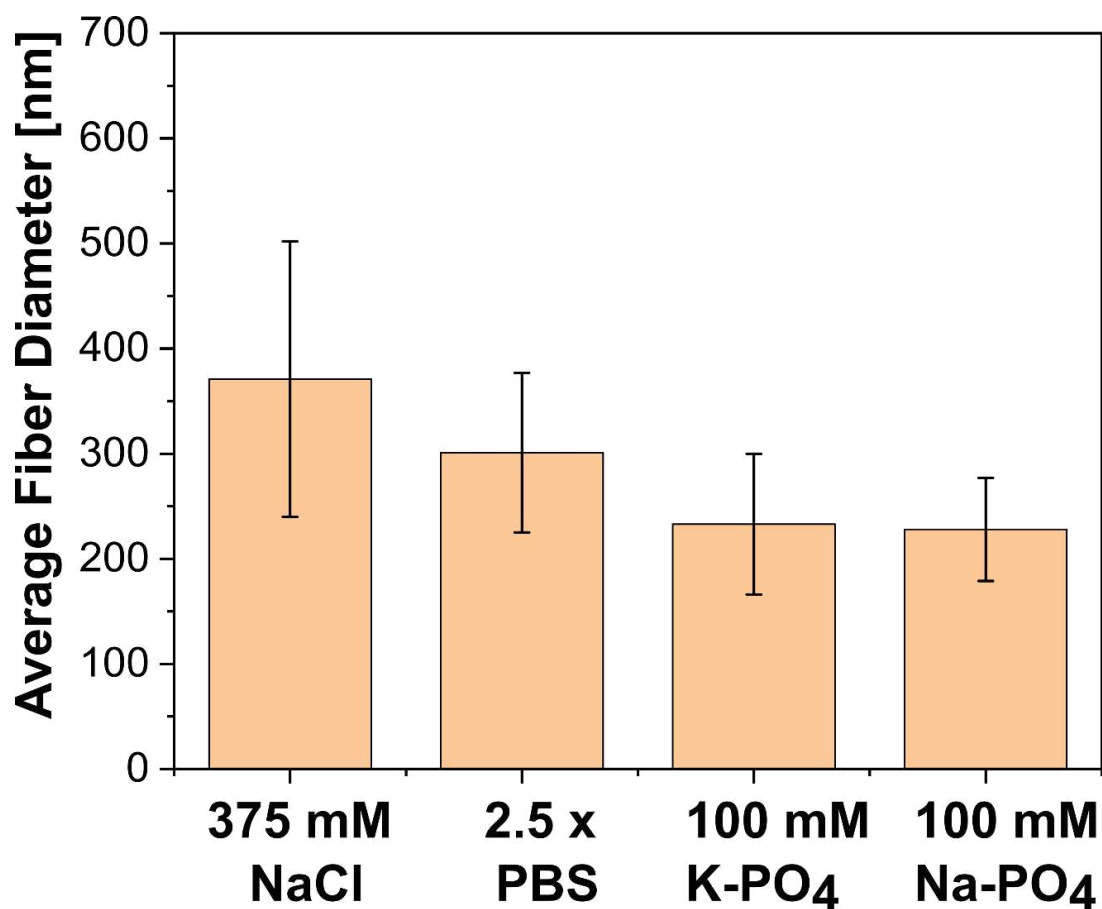


Figure S8: Average diameter of fibrinogen fibers assembled with varying monovalent salts. Average fiber diameters of samples prepared after drying 2.5 mg/mL fibrinogen in the presence of different salts were obtained from manual measurements with the Image J software at 50 distinct positions of SEM images (see Table S1). Fibrinogen precipitated from Na-PO₄ had the densest fiber network with the smallest average fiber diameter and lowest standard deviation, K-PO₄ resulted in the second densest fiber network with the second smallest fiber diameter, while PBS showed the third densest fiber network and second thicker fiber diameter, and NaCl yielded the least dense fiber network with the largest average fiber diameter and highest standard deviation.

Figure S9:

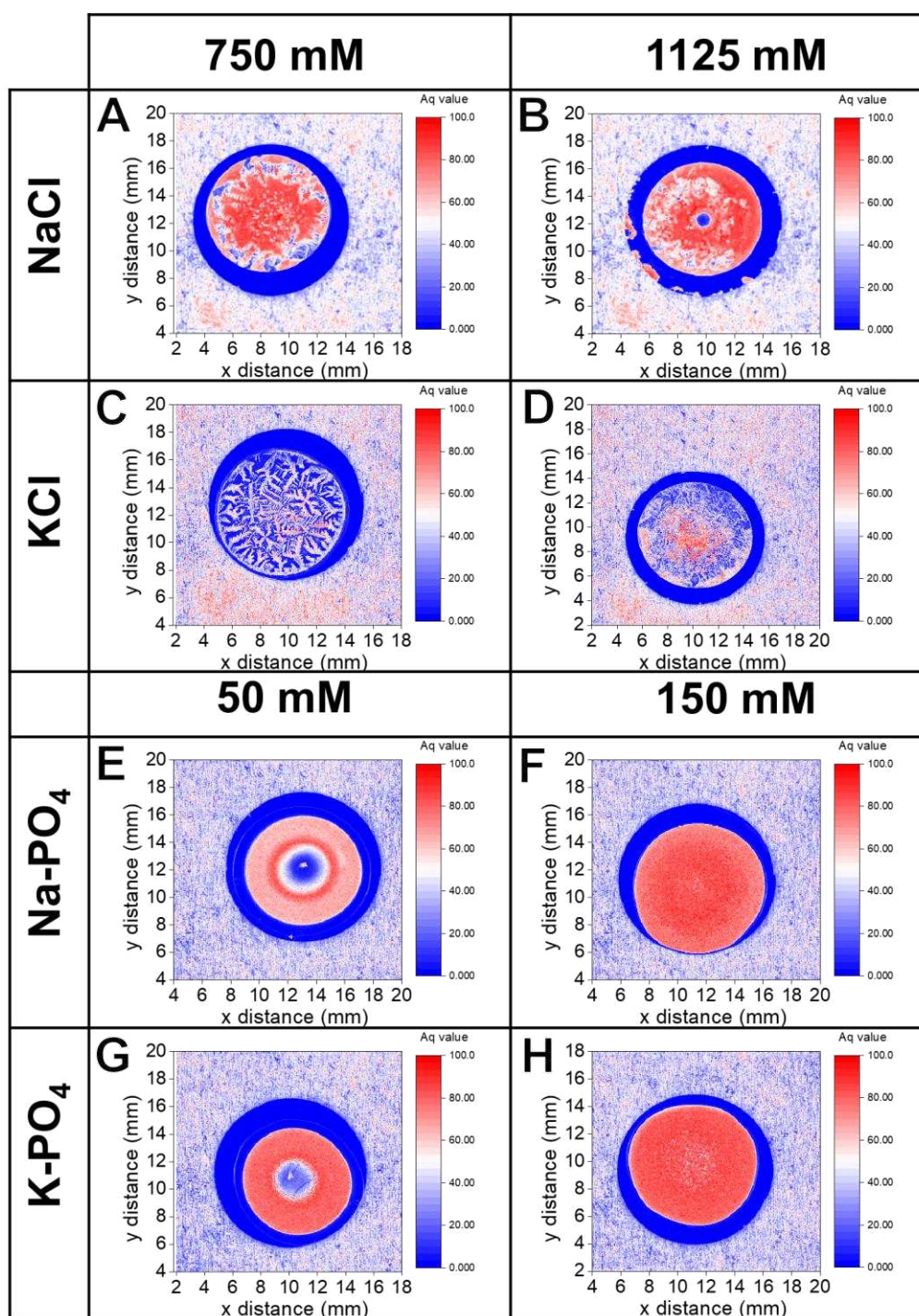


Figure S9: Influence of increased salt concentration on the surface roughness. Aq-based survey images of samples prepared after drying 2.5 mg/mL fibrinogen in the presence of (A) 750 mM and (B) 1125 mM NaCl, (C) 750 mM and (D) 1125 mM KCl, (E) 50 mM and (F) 150 mM Na-PO₄, (G) 50 mM and (H) 150 mM K-PO₄. For NaCl, no significant increase in the Aq value at the center of the sample could be observed when increasing the salt concentration. For KCl, the increase in salt concentration seemed to slightly increase the Aq value at the center of the sample. For Na-PO₄ and K-PO₄, the sample coverage was clearly increased, and the Aq value increased significantly when increasing the salt concentration.

Figure S10:

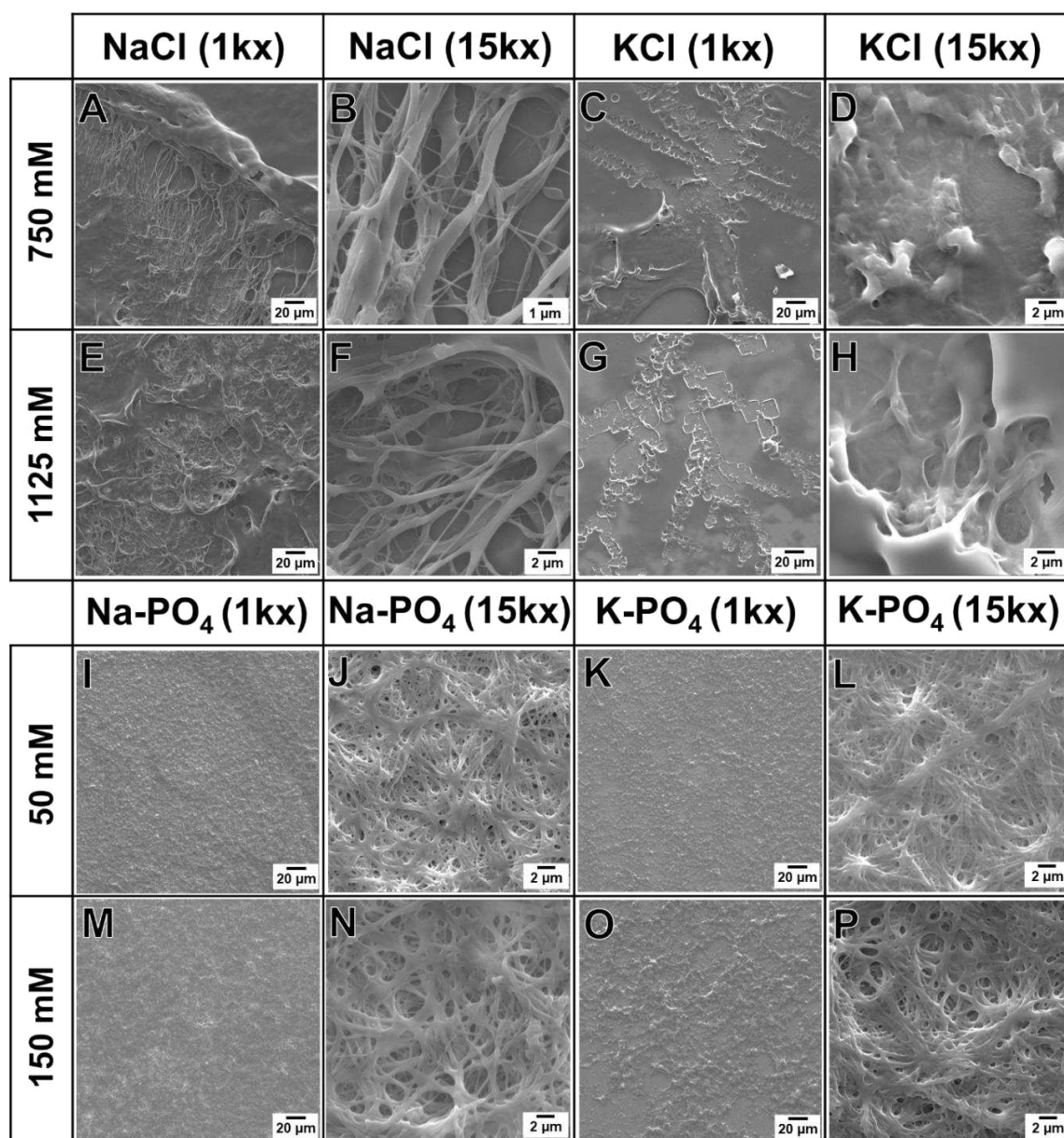


Figure S10: Effect of increased salt concentration on the surface roughness. SEM-based local detail images of fibrinogen samples after drying, crosslinking and washing mixtures of 2.5 mg/mL fibrinogen and different monovalent salts: (A, B) 750 mM NaCl, (C, D) 750 mM KCl, (E, F) 1125 mM NaCl, (G, H) 1125 mM KCl, (I, J) 50 mM Na-PO₄, (K, L) 50 mM K-PO₄, (M, N) 150 mM Na-PO₄ and (O, P) 150 mM K-PO₄. All left images of the same salt show bigger regions of the samples at 1 kx magnification, while right side images show detailed parts of a zoomed area of the same region with 15 kx magnification. In general, the increase in salt concentration did not increase or suddenly trigger fibrinogen fiber formation. Similar structures/morphologies are seen for all samples prepared with the same salt, independently of the used salt concentration. 750 mM and 1125 mM NaCl yielded fibrous and planar regions comparable to the 375 mM NaCl sample presented in **Figure S5**. For KCl, no fiber formation was observed even by increasing the salt concentration, and the morphology of the fibrinogen layers was similar to the ones obtained for 375 mM KCl. Both concentrations of Na-PO₄ and K-PO₄ samples induced fiber formation with dense fiber networks.

5. EFFECT OF INTERFACE-ACTIVE POLYMERS ON THE SALT CRYSTAL SIZE IN WATERBORNE HYBRID MATERIALS

Status: Paper published at Applied Adhesion Science (2021)

Stamboroski, S., Boateng, K., Leite Cavalcanti, W., Noeske, M., Beber, V. C., Thiel, K., Grundwald, I., Schiffels, P., & Brüggemann, D. (2021). Effect of interface-active proteins on the salt crystal size in waterborne hybrid materials. Applied Adhesion Science, 9(1), 1-22

DOI: <https://doi.org/10.1186/s40563-021-00137-8>

5.1. MOTIVATION & HYPOTHESIS

Hypothesis addressed: Presence of proteins influences the precipitation behavior of the monovalent salt NaCl.

Previous studies showed that polymers and proteins can affect the shape of sodium chloride crystals. Goto et al. (Goto et al., 2016) observed a variety of dendritic morphologies of NaCl crystallization from a gel matrix containing gelatin. In Chapter 4, it was shown that salt crystals leave holes on the fibrinogen layer when dissolved again in water, during rinsing. Interestingly, during the study of fibrinogen precipitation from solutions containing high concentrations of NaCl or KCl, a completely different salt crystal pattern than the salts crystallized from only water solutions was observed. This behavior shows that not only fibrinogen is affected by the presence of salt, but that this is a mutual influence and fibrinogen also affects the behavior of the crystallization of salts. In Chapter 5 the variation on the crystallization morphology of the alkali metal salt sodium chloride upon drying protein-containing saline water is presented. Bearing in mind that under high NaCl concentration fibrinogen can form fibers, a globular protein (BSA) and another fibrous protein (collagen) were also studied on their influence on sodium chloride precipitation for comparison.

Hypothesis assessment: Confirmed.

RESEARCH

Open Access

Effect of interface-active proteins on the salt crystal size in waterborne hybrid materials



Stephani Stamboroski^{1,2,6*} , Kwasi Boateng^{1,2}, Welchy Leite Cavalcanti¹, Michael Noeske¹, Vinicius Carrillo Beber¹, Karsten Thiel¹, Ingo Grunwald^{3,4}, Peter Schiffels¹, Stefan Dieckhoff¹ and Dorothea Brüggemann^{2,5}

*Correspondence: stephani.stamboroski@ifam.fraunhofer.de
⁶ Department Adhesion and Interface Research, Fraunhofer Institute for Manufacturing Technology and Advanced Materials, Wiener Straße 12, 28359 Bremen, Germany
Full list of author information is available at the end of the article

Abstract

Aqueous processes yielding hybrid or composite materials are widespread in natural environments and their control is fundamental for a multiplicity of living organisms. Their design and in vitro engineering require knowledge about the spatiotemporal evolution of the interactions between the involved liquid and solid phases and, especially, the interphases governing the development of adhesion during solidification. The present study illustrates the effects of distinct proteins on the precipitation of sodium chloride encompassing the size, shape and distribution of halite crystals formed during the drying of droplets containing equally concentrated saline protein solutions. The precipitates obtained from aqueous sodium chloride formulations buffered with tris(hydroxymethyl)aminomethane (Tris) contained either bovine serum albumin (BSA), fibrinogen or collagen and were characterized with respect to their structure and composition using optical and electron microscopy as well as x-ray analysis. The acquired findings highlight that depending on the protein type present during droplet drying the halite deposits predominantly exhibit cubic or polycrystalline dendritic structures. Based on the phenomenological findings, it is suggested that the formation of the interphase between the growing salt phase and the highly viscous saline aqueous jelly phase containing protein governs not only the material transport in the liquid but also the material exchange between the solid and liquid phases.

Keywords: Protein-based composites, Sodium chloride, Bovine serum albumin, Collagen, Fibrinogen, Crystallization, Spatiotemporal development of adhesion, Damköhler number

Introduction

Natural hybrid or composite materials that are composed in aqueous environments and consist of organic and inorganic components or constituents are highly visible and frequent. Seashells, nacre, and bone are protein-based composite materials known for their high functionality at low weight, and their remains from geological eras long ago still shape the landscape in many regions of the world [1]. Moreover, understanding biomineralization processes and characterizing the properties of biomineralized organic/inorganic hybrid materials provide inspiration for materials development following biomimetic principles [2].



© The Author(s), 2021. **Open Access** This article is licensed under a Creative Commons Attribution 4.0 International License, which permits use, sharing, adaptation, distribution and reproduction in any medium or format, as long as you give appropriate credit to the original author(s) and the source, provide a link to the Creative Commons licence, and indicate if changes were made. The images or other third party material in this article are included in the article's Creative Commons licence, unless indicated otherwise in a credit line to the material. If material is not included in the article's Creative Commons licence and your intended use is not permitted by statutory regulation or exceeds the permitted use, you will need to obtain permission directly from the copyright holder. To view a copy of this licence, visit <http://creativecommons.org/licenses/by/4.0/>.

Protein-based composite materials with multi-level hierarchical structures and manifold functions form the basis of many living organisms [3]. Studies of prokaryotes, probably the oldest life-form on Earth, reveal that biomineralization is found in halophiles living in environments governed by high pH and high salt concentrations [4]. These extremophiles are able to attach ions to their outer surface to form minerals [5, 6]. This ability is attributed to a two-dimensional protein assembly, the so-called S-layer (surface layer) of such bacteria and archaea [5]. While the vast majority of biominerals found on Earth are inorganic compounds with oxoanions like carbonates, silicates or phosphates, the crystallization of the evaporite mineral halite, which is based on sodium chloride, is reportedly influenced by the presence of organic entities. These entities include, synthetically produced nanoparticles proposed as an analog to protocellular material [7], surface layers of *Haloarcula* strain SP8807 or the presence of halobacteria [8], the synthetic peptide ATEA [9], and also gelatin [10, 11]. The crystallization of calcium oxalate or phosphate salts during urolithogenesis in urine or in vitro may be influenced by both dissolved salts and the presence of proteins that contribute to the organic matrix of urinary stones up to several millimeters in width [12, 13]. Hence, in addition to illustrating the effect of organic compounds on salt crystallization, the reciprocal effect of salts on the solidification of organic materials can be highlighted. For example, many proteins precipitate in the presence of highly concentrated salt solutions, like sodium chloride. This effect is known as salting out and its distinctness is reflected by the position of the salt-forming ions in the Hofmeister series [14], which elucidate the tendency of proteins to form aggregates in the presence of different ions [15]. Sodium chloride has also been reported to govern the solubility of lysozyme, α -chymotrypsin and BSA [16]; drive the nucleation and the polymorphic transformation of the amino acid glycine [17]; influence specific attractive interactions relevant for the crystallization and precipitation behaviour of proteins like lysozyme [18]; and affect the aggregation of pork myofibrillar protein [19]. Moreover, sodium chloride can influence the tendency of proteins to hierarchically assemble into superstructures like fibers, such as with spider silk protein [20], the extracellular matrix protein collagen [21], and the blood plasma protein fibrinogen [22]. Submicroscopic protein crystals based on dense aggregates of macromolecular protein units were found in equine chondrocyte cells [23], and, nanoparticulate or crystalline structures composed of proteins and carbohydrates, and containing traces of metals like Na, K, Mg, Ca, Al, and Si were identified in secretions [24].

Notably, the development of adhesion during natural processes occurring at dynamic interphases around solids is in the focus of a growing research area. Acquiring knowledge relating to anti-freeze proteins (AFP) [25, 26] or peptide-based bioadhesives [27] in terms of composition, structural design, and interaction with surfaces is essential for the implementation of underlying concepts based on biochemical and mechanical principles in trendsetting medical and technical applications [28, 29]. In the view of adhesion research, solid formation from an originally continuous fluid phase is an essential scenario during physical hardening [30] and even chemical curing [31]. Rätzke et al. highlighted that a causal sequence of process steps following nucleation and growth may start from sites governing the formation of interphases between the fluid and hardened phases [31]. These locally developing interphases may be perceived as the centerpiece of growth around centers. In these boundary regions, a balance evolves between

the arrangement of material entities upon solid formation and the transport of entities towards the shifting solid/fluid interface [31]. The ratio between the reaction or incorporation flux and the mass transport flux can be represented by the Damköhler number (Da), which correlates transport phenomena, e.g. based on solutes, with time-dependent reaction rates [32] and facilitates the assessment of spatiotemporal distribution of the reaction rate under local non-equilibrium conditions as observed in precipitation/dissolution processes [33]. For NaCl precipitation from an aqueous solution during water evaporation, the Damköhler number was, for instance, shown to drastically change when the growth of sodium chloride crystals was observed [34]. Desarnaud et al. recently highlighted that in nature crystals are rarely found only in their equilibrium state [35]. Rather, many minerals and salts, like notably calcite and halite, form hopper crystals composed of clusters of interconnected crystalline regions. These authors point out that little fundamental work had been done on understanding hopper crystal shapes resulting from an anisotropic growth that is due to the edges of a crystal growing faster than the centers of its faces. With kinetics of growth being an important factor in determining the overall shape of a solid, a transition between cubic and hopper growth at a high supersaturation of around 1.5 was reported when the growth rate of the cubic crystal reached a maximum of around $7 \mu\text{m/s}$ [35]. Goto et al. presented dendritic morphologies of sodium chloride when grown in a thin gelatin gel matrix in which the mass transport is governed by diffusion. Furthermore, the authors demonstrated a significant influence of the [salt]/[gelatin] concentration ratio and the humidity around a drying aqueous solution on the halite crystal shape and growth velocity ranging from approximately 1 to $20 \mu\text{m/s}$ [11]. Choudhury et al. used a simple simulation algorithm incorporating aggregation and evaporation to reproduce the observed well-defined cross-over from a compact NaCl crystal morphology in aqueous gelatin to a dendritic pattern as water evaporation proceeded [10]. Lately, Yang et al. [36] reviewed self-assembly in hopper-shaped crystals and described the change of crystal morphology according to a change of the interfacial instability. They established the role of capping agents that may inhibit the adsorption of a newly added building block on the surface of a growing solid. With respect to crystalline evaporative deposition, McBride et al. [37] showed that the energetics between all the three phases involved in the crystallization of solutes, namely substrate, crystal, and liquid, contribute to the nucleation barrier, and the authors elucidated that salt solutions with lower nucleation barriers will pin-drop substrate/drop contact lines to form rings.

Based on these studies and recent reports [38], it becomes clear that exploiting the mutual influences between proteins and salts for material design is an approach that is gaining increasing technological relevance. Thus, it is important to gain a fundamental understanding of the protein/salt or peptide/salt interactions when solid materials are formed from an aqueous phase. Such knowledge on liquid-solid transitions in the presence of different salts will be of great relevance for controlling the formation and multifunctional properties of new protein-based composite materials. In natural and biotechnical processes, the respective solid formation often starts from a liquid formulation comprising a solvent, an inorganic solute, and an organic co-solute and proceeds via the formation of growth units [11] as relevant entities, their assembly into nuclei, and the growth of metastable or stable solid phases [17]. Alternatively, processes allocating

inorganic and organic moieties from different formulations may be engineered, e.g. using layer-by-layer [39] or sol–gel processes [40]. Recently, within the scope of tailoring biomimetic hybrid collagen/chitosan hydrogels with a dual network structure [38], an immersion in a highly concentrated 5 wt% aqueous sodium sulfate solution was reported to result in an opaque gel during a universal soaking step following a UV-induced crosslinking step.

Based on knowledge from experimental or simulation approaches, target-oriented strategies can be framed not only for the synthesis of bio-inspired materials, e.g. nacre-like composites [41], or surfactants for interface engineering [42, 43], but also for assessing environmental, agricultural, alimentary, medical or pharmaceutical challenges [17, 19, 38, 42, 44–46], e.g. avoiding the formation of renal stones [44]. Systematic material development is significantly promoted by applying scale-comprehensive simulation, e.g. of growth processes [30, 47], and access to databases facilitated by data and metadata interoperability [48].

Lately, our group demonstrated how salt-driven self-assembly can be applied for the physiological preparation of nanofibrous fibrinogen scaffolds to support cell adhesion [49–51] and compared relevant approaches for fibrinogen fiber assembly *in vitro* [22]. By precipitating a water-soluble mixture of salts in the presence of fibrinogen, the salts enabled the formation of dense nanofiber networks upon drying. On the other hand, chloride salts of calcium, magnesium, copper and zinc hamper fibrinogen fiber formation [52]. Moreover, we routinely used highly concentrated salt solutions to assemble the extracellular matrix protein collagen into nanofibers to control the growth of different cell types [53, 54]. In view of the hierarchy for hybrid materials presented by Saveleva et al. [55], such self-assembly processes start from an organic molecule-modified inorganic material (organics-*in*-inorganics) and end with a potentially inorganic-modified organic material (inorganics-*in*-organics). In the present contribution, we therefore focus on revealing the interface-active action of the proteins BSA, fibrinogen and collagen type I in the organics-*in*-inorganics approach for directing the crystallization of the alkali metal salt sodium chloride upon drying protein-containing saline water. While BSA and fibrinogen are both blood plasma proteins, collagen contributes to the assembly of an extracellular matrix during the early stages of wound healing [56]. In detail, we present microscopic images for evaluating the crystal size distribution and energy dispersive x-ray analysis (EDX) studies for disclosing the presence of an organic surface film.

Materials and experimental procedure

Sample preparation

All solutions were prepared using ultrapure water from a TKA water purification system (Thermo Fisher Scientific, Schwerte, Germany). A sufficient amount of tris(hydroxymethyl)aminomethane (Tris, $C_4H_{11}NO_3$, Carl Roth GmbH, Karlsruhe, Germany) to obtain a 10 mM concentration was dissolved in ultrapure water and the pH of the solution was adjusted to 7.4 with hydrochloric acid (aqueous HCl, VWR, Darmstadt, Germany). Likewise, sodium chloride (NaCl, VWR) was dissolved in the Tris–HCl buffer to obtain a stock solution concentration of 1.5 M. Fibrinogen stock solutions were prepared by dissolving 10 mg/mL fibrinogen (100% clottable, Merck, Darmstadt,

Germany) in a 10 mM Tris–HCl solution. The fibrinogen stock solution was dialyzed against a 10 mM Tris–HCl solution overnight using cellulose membrane dialysis tubing with 14 kDa cut-off (Sigma, Steinheim, Germany) to remove low molecular weight compounds. The BSA stock solution was prepared by dissolving 10 mg/mL BSA (Sigma Aldrich Munich, Germany) in 10 mM Tris–HCl buffer. Collagen stock solutions were prepared by dissolving 10 mg/mL collagen type I from calf skin (Sigma Aldrich, Munich, Germany) in 5% aqueous acetic acid (Carl Roth GmbH, Karlsruhe, Germany). Round glass coverslips with a diameter of 12 mm (VWR, Darmstadt, Germany) were sputter-coated with a 5 nm thin adhesion layer of chrome, followed by 25 nm of gold, using an EM ACE600 high vacuum sputter coater (Leica Microsystems, Wetzlar, Germany). A volume of 70 μ L of the respective protein solution was pipetted onto the gold-coated glass substrates, followed by the addition of 70 μ L salt solution to the protein drop. For the preparation of samples without protein, 70 μ L of the salt solution was pipetted onto the gold-coated glass followed by 70 μ L of ultra-pure water to adjust the salt and Tris–HCl concentrations. The samples were placed in a container purged with dry N₂ gas, and after the droplet drying process the samples were transferred to a home-built humidity chamber to be incubated at 24 °C and 30% relative humidity overnight.

Microscopic surface analysis

All optical microscopy images were obtained with a Keyence VHX-7000 digital microscope (Keyence, Neu-Isenburg, Germany). The samples were imaged in overall survey applying stitching and using magnification from 20 \times for single partial images. Details of the precipitated salt or the protein deposits were imaged with magnifications varying from 80 \times to 500 \times . Moreover, after depositing a thin electrically conductive carbon layer more detailed inspection was performed with Scanning Electron Microscopy (SEM) using a field emission device (FESEM), type FEI Helios 600 (Dual Beam, FEI, Eindhoven, Netherlands). The resolution was 0.9 nm at 15 kV at optimal working distance and 1 nm at 15 kV at the coincidence point. The images of the sample surface were obtained at acceleration voltages between 0.35 and 30 kV and at working distances between 1 and

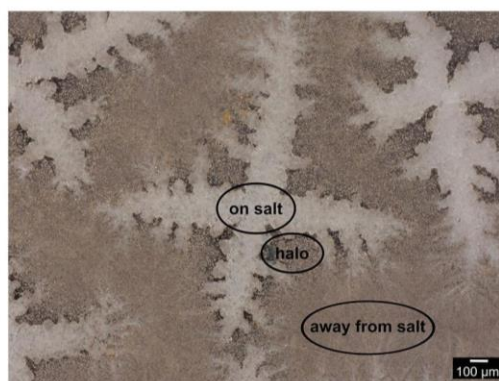
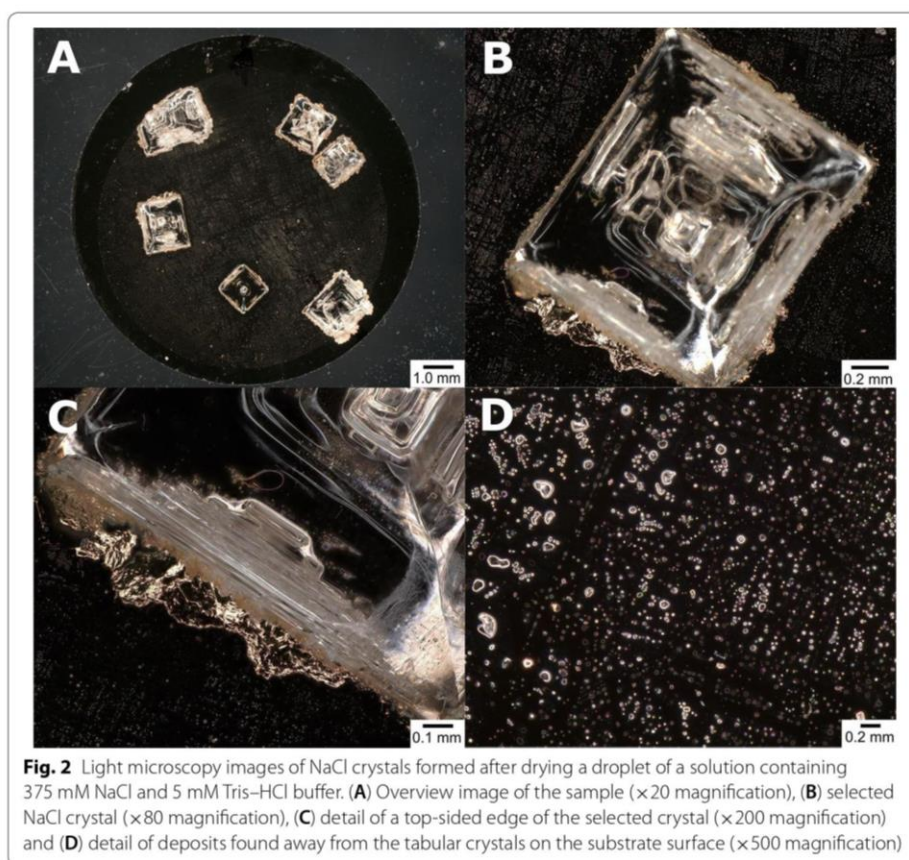


Fig. 1 Light microscopy image of deposits containing NaCl, fibrinogen and Tris moieties. Introduction of the terminology applied for surface areas imaged with higher magnification and SEM analysis: the surface of apparently crystalline salt deposits (labelled “on salt”), the halo close to the salt deposits (labelled “halo”), and regions beyond the halo (labelled “away from salt”)



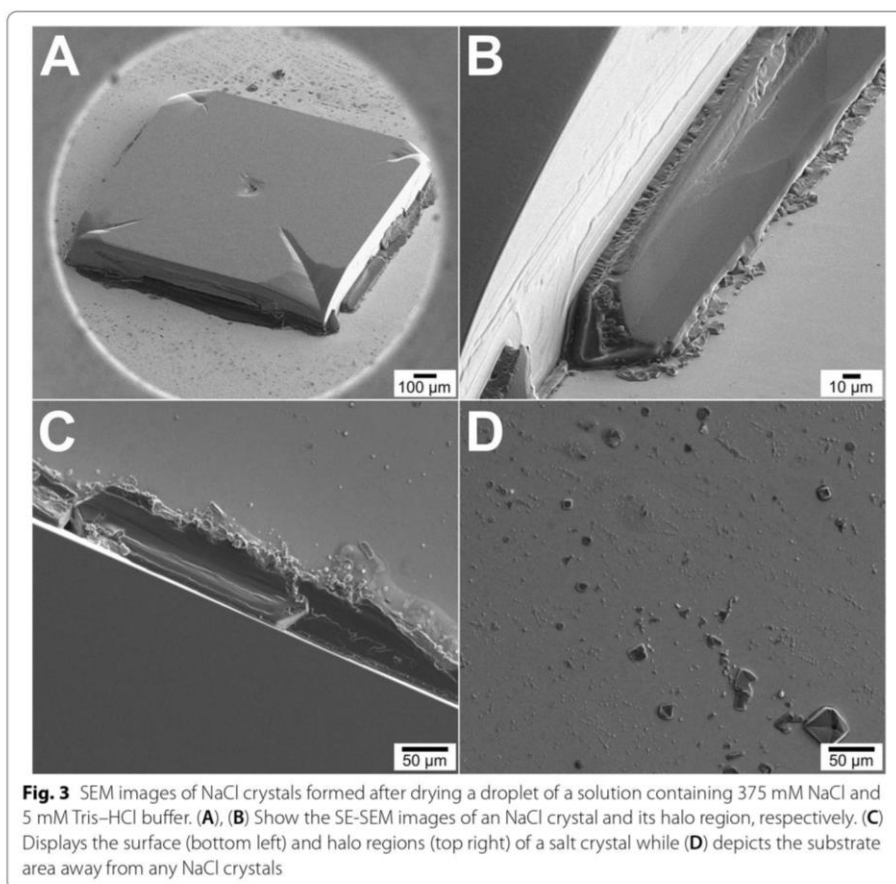
10 mm. For the detection of secondary or backscattered primary electrons an Everhart–Thornley or an in-lens detector was used.

EDX investigations

EDX measurements were performed with the same FESEM of type FEI Helios 600 (DualBeam) equipped with an Oxford X-Max80 silicon drift detector (SDD) for x-rays, an ATW2-window and an energy resolution down to 129 eV. The detection angle of the detector was 52° .

Results and discussion

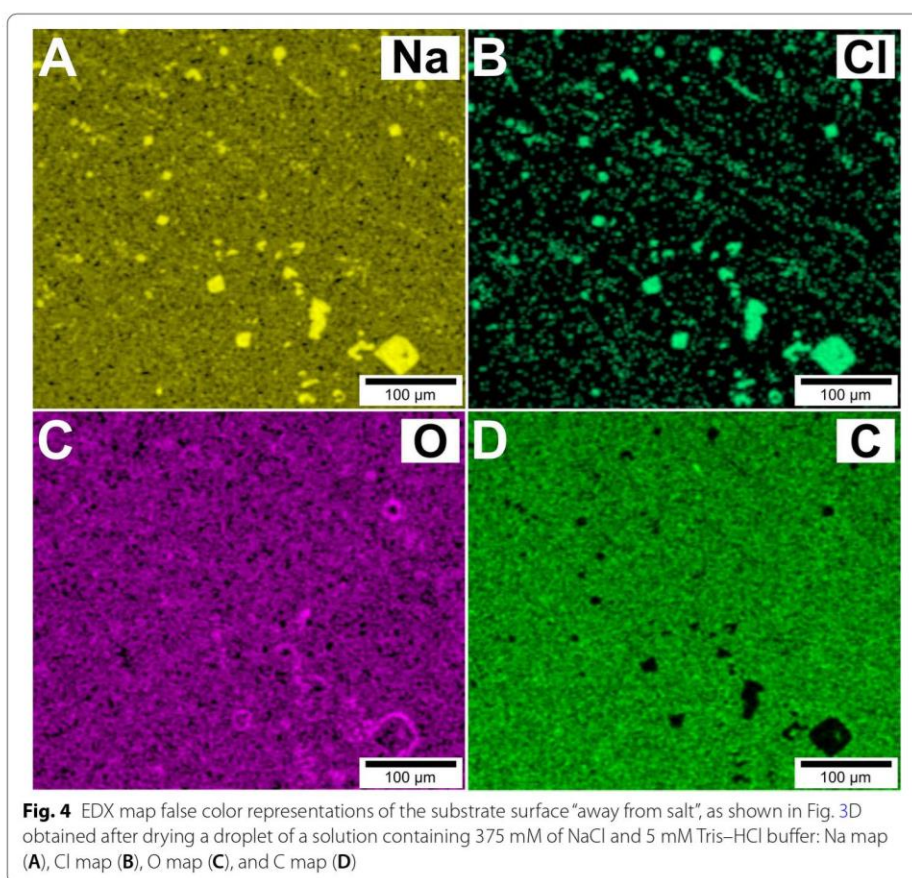
The following discusses, the structure and arrangement of the NaCl crystals formed upon droplet drying as well as the composition of the deposits revealed in their surroundings. Hereby, the results of four scenarios are considered; namely the deposits resulting from water evaporation from Tris–HCl buffered aqueous formulations free of biopolymers in comparison with those obtained in the presence of BSA, fibrinogen or collagen, respectively. The Tris–HCl buffer was used to maintain the same physiological pH (7.4) for all four starting formulations involved in this study. In detail, three characteristic regional sections within the laterally inhomogeneous drying patterns were considered, as displayed in Fig. 1; these comprise the surface of apparently crystalline salt



deposits (called “on salt”), the halo close to the salt deposits (called “halo”), and regions beyond the halo (called “away from salt”).

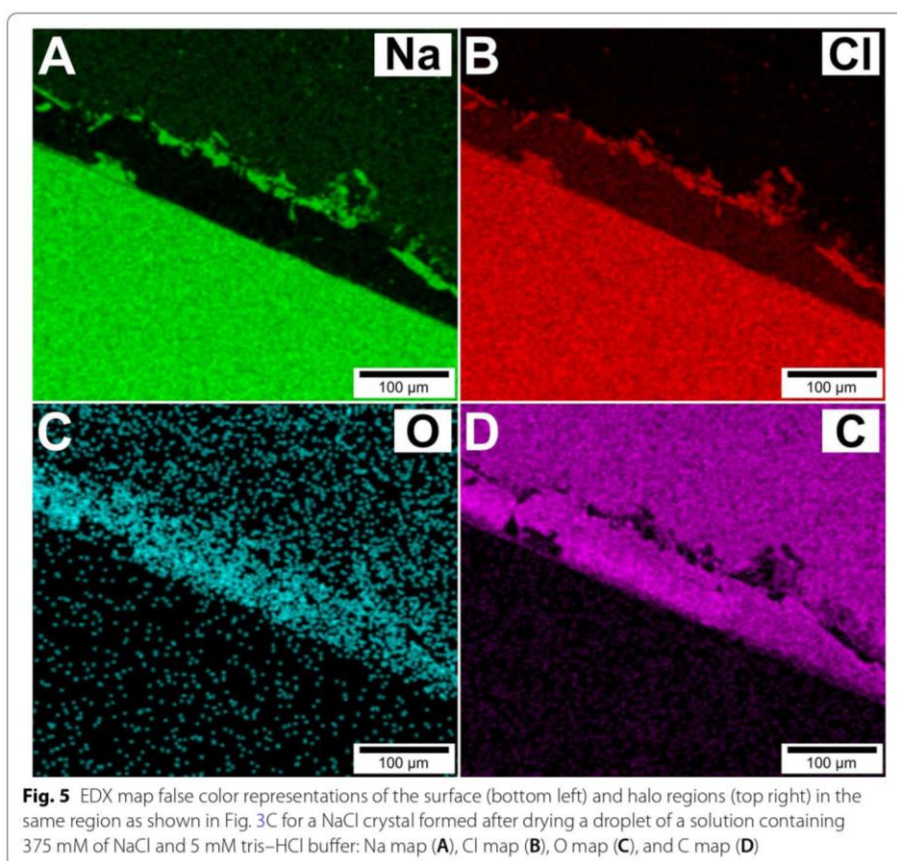
Macrostructure variation of NaCl crystals precipitated in the absence of proteins

After sodium chloride was dried in the absence of proteins the precipitated NaCl crystals were imaged with light microscopy and SEM. Figure 2 depicts the top view light microscopy images obtained after drying a droplet that was initially about 2 mm narrower than the substrate slide, as can be inferred from the approx. 1 mm wide dark rim shown in the light microscopic image in Fig. 2A. Water evaporation occurring over the course of two hours gave rise to the formation of six NaCl crystals with a rectangular, almost square base. While the width of these crystals varied between 1.3 and 2.5 mm, the heights of up to 0.2 mm were approximately one order of magnitude smaller. The tabular shape of the NaCl crystals was confirmed by the SEM in Fig. 3A, which illustrates that the crystal plateau height does not exceed the droplet height. Most of these crystals exhibited one edge that was less than 1 mm away from the initial contact line and the central substrate region was free from such distinct salt crystals. This finding can be explained by the observation that the decline of the liquid volume primarily resulted in a reduction of the droplet height rather than the droplet width. Details of the surface and the



shape of a 3D crystal can be seen in Fig. 2B, C. The crystal growth seemed to be faster at the crystal edges than at the crystal center or corners since steps and depressions were observed in the central region and at the corners of the crystals. The basal corners of the crystals show 90° angles, as expected for the growth morphology of halite, yet the topmost corners were not complete and exposed unfilled steps. In regions between the bigger crystals, and notably around the sample center, deposits of tiny NaCl crystals up to 30 μm in width can be observed as suggested by the light microscopy (see Fig. 2D) and SEM analyses (see Fig. 3D) and substantiated by the element contrast revealed in the EDX maps highlighting locally elevated Na and Cl concentrations (Fig. 4A, B). The bases of the halite crystals are bordered by amorphous deposits that are comparatively poor in Na or Cl species but rich in O and C containing moieties based on the contrast in the EDX maps shown in Figs. 4 and 5. Due to this elemental composition, these deposits can be attributed to solid Tris moieties.

As Tris-based deposits were observed and as they revealed a laterally inhomogeneous distribution we infer that Tris constitutes not only a buffer but also a co-solute of sodium chloride. Moreover, Taha et al. reported interactions between Na⁺ and Cl⁻ ions and Tris



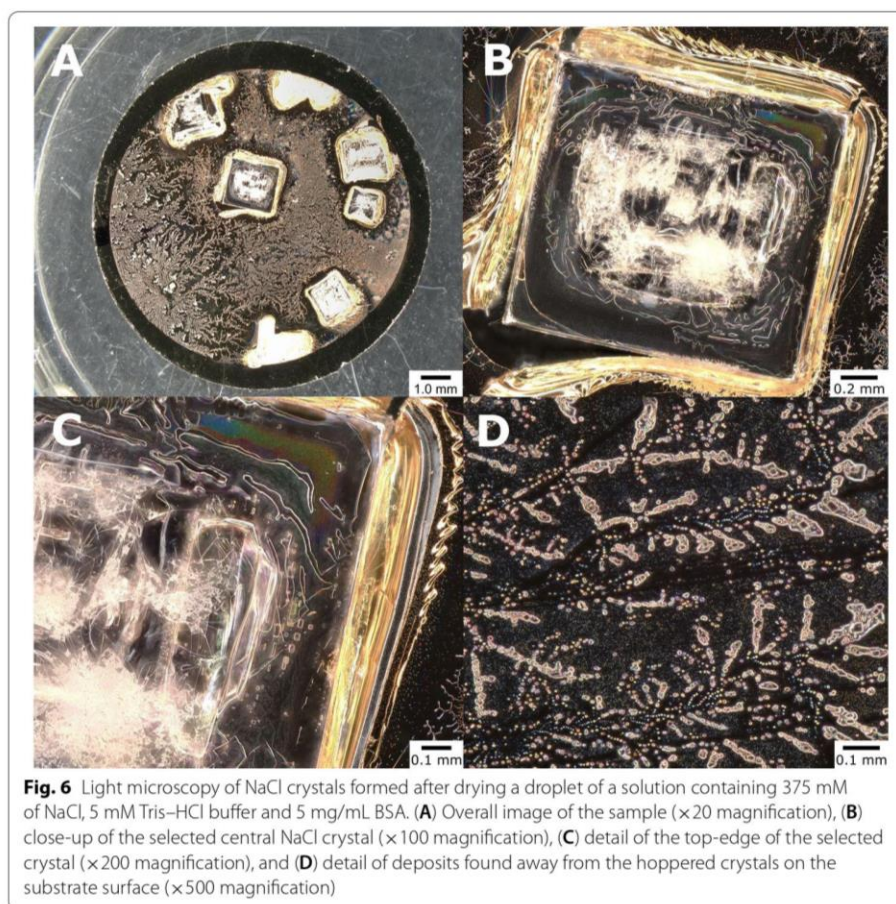
molecules [57]. The crystallization-related effects of the interactions between Tris, salt and water at interfaces are subject to ongoing studies.

Macrostructure variation of NaCl crystals precipitated in the presence of proteins

The following sections highlight the effects resulting from the presence of the proteins BSA, fibrinogen or collagen on the structure of sodium chloride precipitates as well as the arrangement and composition of organic deposits.

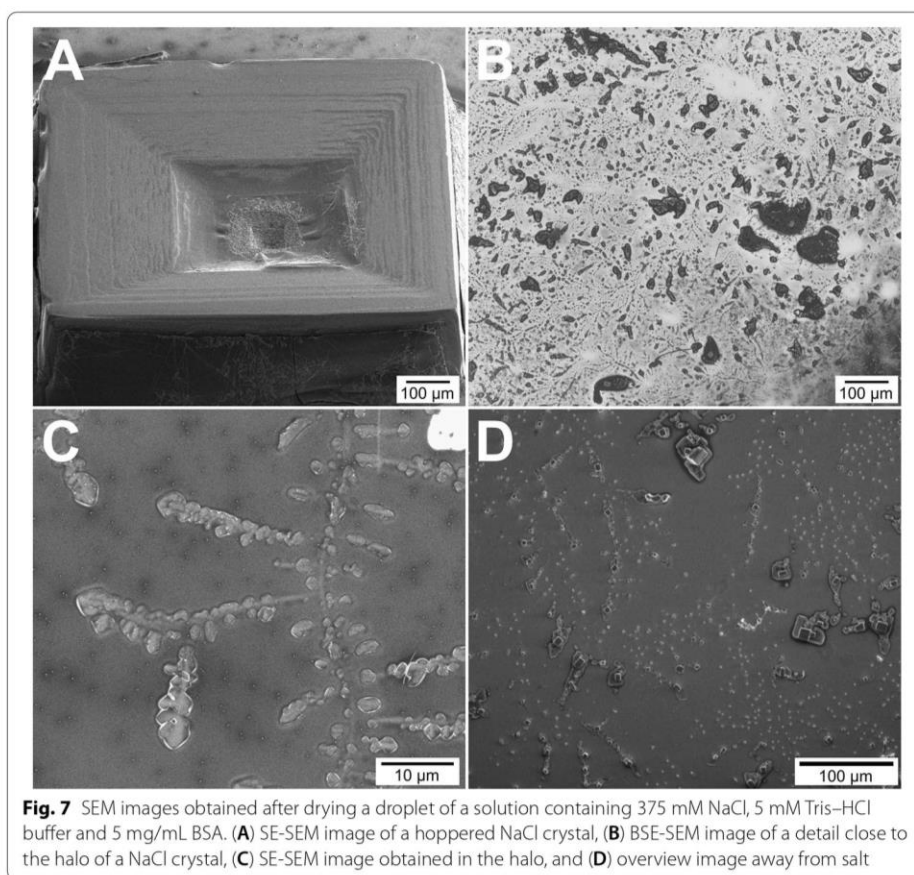
Effect of BSA

When 5 mg/mL BSA as a starting concentration was adjusted in the solution left for drying, seven bigger NaCl crystals with widths varying from 1 to 1.8 mm and a rectangular base were observed (Figs. 6A and 7A), similar to the salt precipitates obtained after drying the droplet without any protein. Similarly to Figs. 2B, C and 6B, C show more surface topography details of the central NaCl crystal. Figure 6D, in particular, shows the formation of more tiny crystals and dendrite growth from the edges towards the center of the substrate. However, the crystal shape formed in the presence of BSA was significantly different from NaCl deposits formed in the absence of protein since the bigger halite crystals were hopped. In contrast, numerous arrangements of dendritic NaCl crystallites were found in regions away



from salt (see Figs. 6D and 7B–D), with their sizes varying between approximately 1 and 100 μm . This finding indicates that the nucleation of salt crystals is not a limiting step within a nucleation and growth scenario. Rather, the observed multiplicity of small crystallites is attributed to a hindered transport of NaCl growth units in the BSA-containing fluid and, therefore, the dendrite formation may be inferred to occur in a later stage of the droplet drying than the growth of huge hoppered halite crystals. As such prevalence of salt dendrites was not observed upon the drying of protein-free droplets, we suggest that in this ultimate drying stage the viscosity of the remaining liquid was higher due to the presence of BSA and its self-assembly by the increase in salt concentration. Previously, similar aspects were addressed with respect to drying aqueous gelatin formulations resulting in a viscous gel film upon water evaporation [10, 58]. Such a protein-related effect may be in addition to the effect experienced by the salt growth units through the successively increasing salt concentration upon water evaporation [59].

As revealed by light microscopy, SEM analysis and the EDX maps obtained from the surface of halite hoppers (cf. Figs. 6B, C and 8), the central hopper region acted



as a pool for the remaining liquid during droplet drying. The thus provided micro-environment featured deposits that were dominated by Tris and its hydrochloride (Tris–HCl), as can be concluded from the EDX findings listed in Table 1. In detail, the corresponding EDX maps not only showed a significant atomic concentration of chloride without revealing any metal cations but also revealed an [N]/[O] concentration ratio around 0.45, which is similar to the stoichiometrically expected ratio for Tris, i.e. $[N]/[O] = 0.33$, or possibly mixtures resulting from interactions of Tris with BSA [60], which are expected to be closer to 1 in view of the predominant ratio of $[N]/[O] = 1$ of the peptide groups in proteins. Moreover, the organic deposits visible via light microscopy and SEM seem to decorate and wrap the salt hoppers as well as the smaller crystallites around their borders (see Figs. 6B, 7B and 9C).

Effect of fibrinogen

When 5 mg/mL fibrinogen as a starting concentration was added to the NaCl solution and left to drying, no apparently single crystalline halite deposits more than 1 mm wide were observed. Rather, the original contact line was decorated by a rim of NaCl deposits less than 0.5 mm wide. Around the initial droplet center, a dozen crosswise salt dendrites with maximum lengths between 1 and 2 mm and maximum

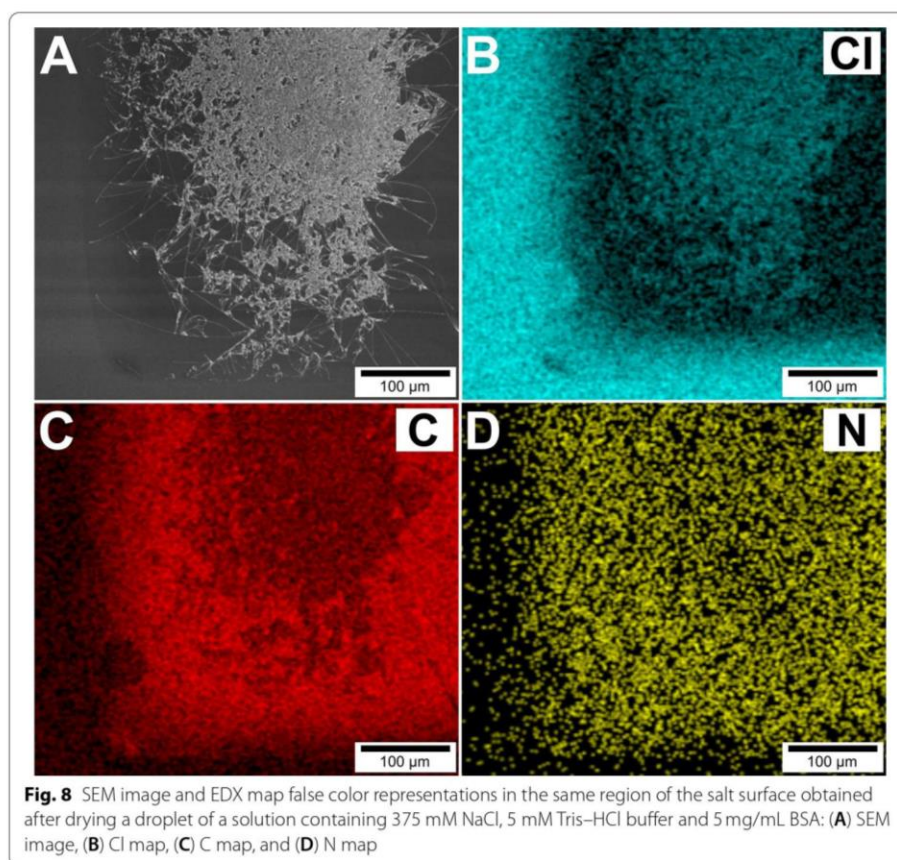
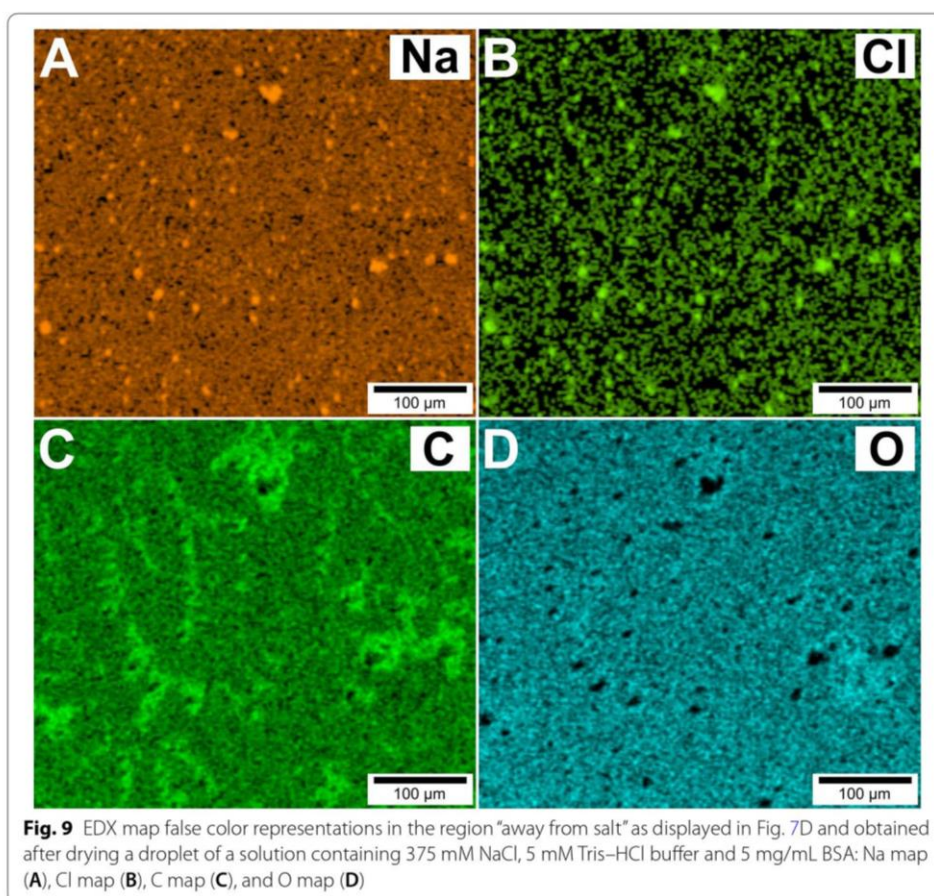


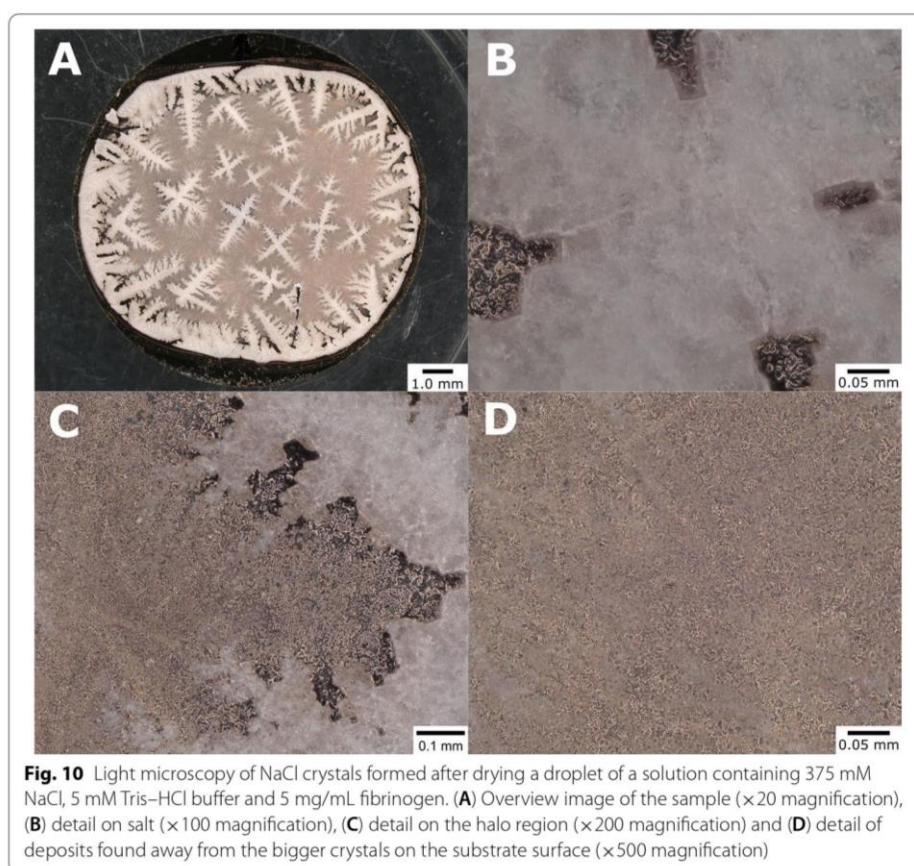
Table 1 Evaluation of the EDX investigations for distinct surface regions of deposits from NaCl with and without different proteins obtained from Tris-buffered droplets

| Sample | [C] (at%) | [N] (at%) | [O] (at%) | [Na] (at%) | [Cl] (at%) | [S] (at%) | [N]/[O] |
|--|-----------|-----------|-----------|------------|------------|-----------|---------|
| Surface of tabular NaCl crystal, without protein (10 kV) | 21.1 | – | 0.3 | 40.2 | 38.4 | – | – |
| Surface of hopped NaCl crystal, with BSA (10 kV) like in Fig. 8 | 56.2 | 12.2 | 27.0 | – | 4.6 | – | 0.45 |
| Beading in halo of hopped NaCl crystal, with BSA (10 kV) | 57.7 | 18.5 | 23.3 | 0.3 | 0.9 | 0.3 | 0.79 |
| Overall dendritic NaCl crystal and halo, with fibrinogen (10 kV) | 61.6 | 6.5 | 7.1 | 12.9 | 11.7 | 0.1 | 0.92 |
| Around center of dendritic NaCl crystal, with fibrinogen (10 kV) | 53.7 | 3.6 | 2.9 | 20.2 | 19.4 | 0.1 | 1.2 |
| Away from dendritic NaCl crystal, with fibrinogen (10 kV) | 69.4 | 8.4 | 8.8 | 6.9 | 6.0 | 0.2 | 0.95 |
| Overall dendritic NaCl crystal and surrounding, with collagen (10 kV) like in Fig. 14B | 59.8 | 12.1 | 22.4 | 2.5 | 3.2 | 0.05 | 0.54 |
| Tris, according to stoichiometric composition | 50 | 12.5 | 37.5 | – | – | – | 0.33 |

The atomic concentrations (at%) and the [N]/[O] concentration ratio are given as obtained with an electron acceleration voltage of 10 kV



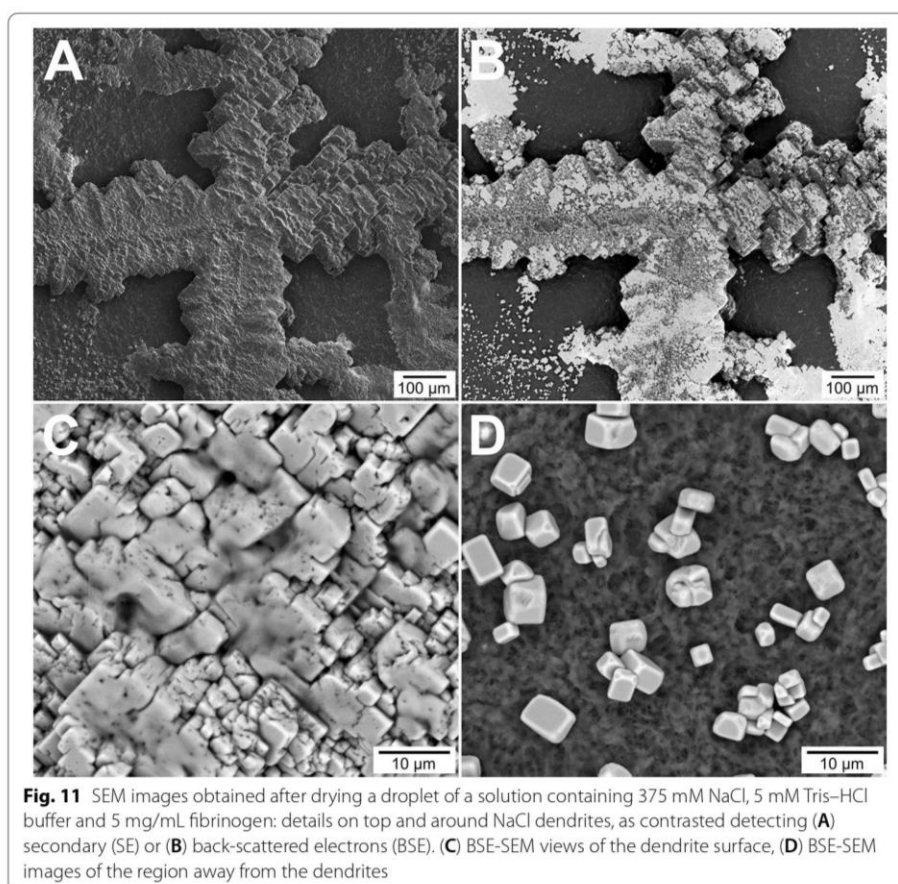
widths between 0.2 and 0.3 mm were observed (see Fig. 10A). The compact packing within the manifestly polycrystalline dendritic NaCl deposits (see Fig. 11C) indicates that the heterogeneous nucleation of the up to several micrometer wide cubic grains on the surface took place, while the lateral growth stopped at the grain boundaries. The near-surface material contrast achieved by the detection of back-scattered electrons (BSE) as shown in Fig. 11B, C and the elemental distribution revealed by the EDX maps (see Fig. 12) recorded on top and around the intersection area of the two orthogonal branches constituting the crosswise NaCl dendrite revealed three distinct characteristics. First, the elevated regions of the salt deposits are covered by patches of an organic substance composed of elements with a lower atomic number than Na or Cl. The findings from the EDX analysis listed in Table 1 reveal a significant attenuation of Na and Cl signals from the underlying sodium chloride and an [N]/[O] atomic concentration ratio around 1. Correspondingly, the organic deposits are interpreted to be predominantly composed of fibrinogen multilayers. Second, an approximately 100 μm wide halo that is depleted in NaCl is visible close to the central intersection area of the crosswise dendritic crystals. Third, in comparison to the central dendrite regions, the lower extensions adjacent to the principal branch revealed a lower coverage by such organic moieties.



Since we did not detect any noticeable X-ray emission from the underlying gold substrate we conclude that the respective NaCl moieties were deposited on top of an organic film. This film is thicker than that on top of the NaCl dendrites. Similar findings were obtained in regions away from the salt dendrites, as shown in Fig. 11D and in Table 1, which once again revealed an [N]/[O] atomic concentration ratio of around 1. In these regions, NaCl crystallites a few micrometer wide and with a cubic or cubo-octahedral shape due to exposed {100} or partially {111} faces were observed (Fig. 11D). Therefore, we suggest that the halite formation contributing to the aforementioned extensions and the deposits in the last-mentioned regions proceeded after the precipitation of the principal NaCl branch in the ultimate phase of the droplet drying process.

Effect of collagen

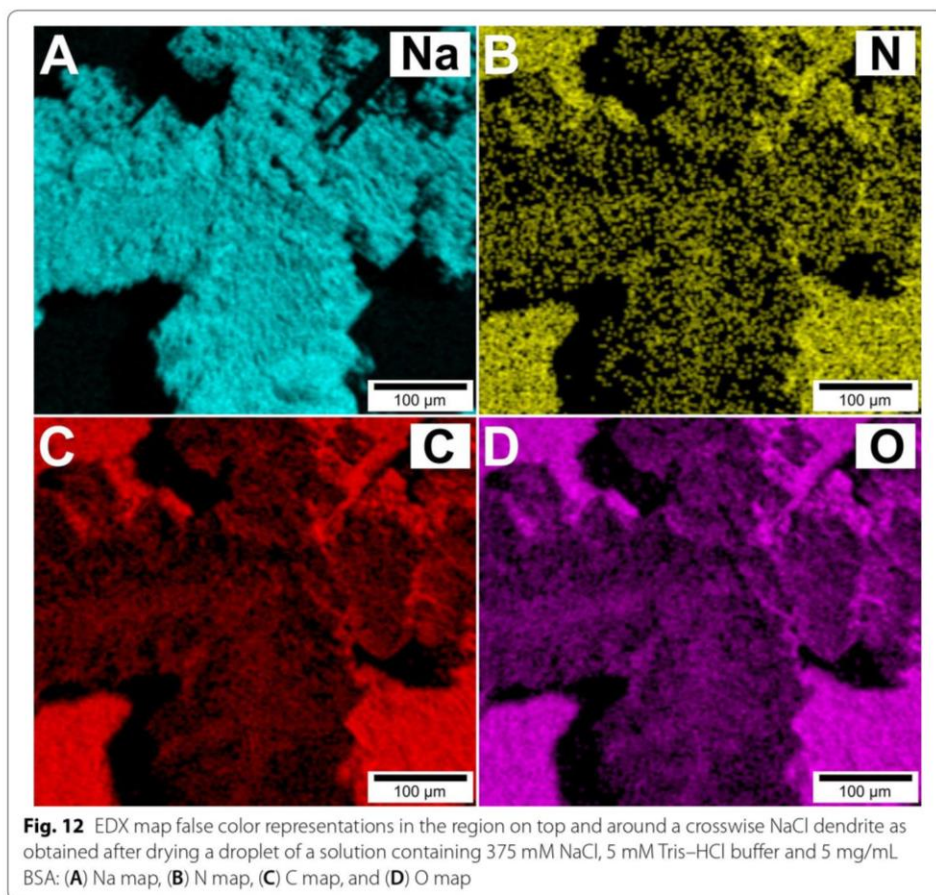
The final investigation focused on the precipitates formed when drying droplets containing 5 mg/mL collagen as a starting concentration. The findings obtained by light microscopy (see Fig. 13), SEM (see Fig. 14), and EDX mapping (see Fig. 15) revealed the formation of polycrystalline crosswise dendrites extending from the initial contact line towards the sample center. Similarly, orthogonal dendrites with straight branches of sodium chloride were observed when grown in a thin gel matrix made of gelatin



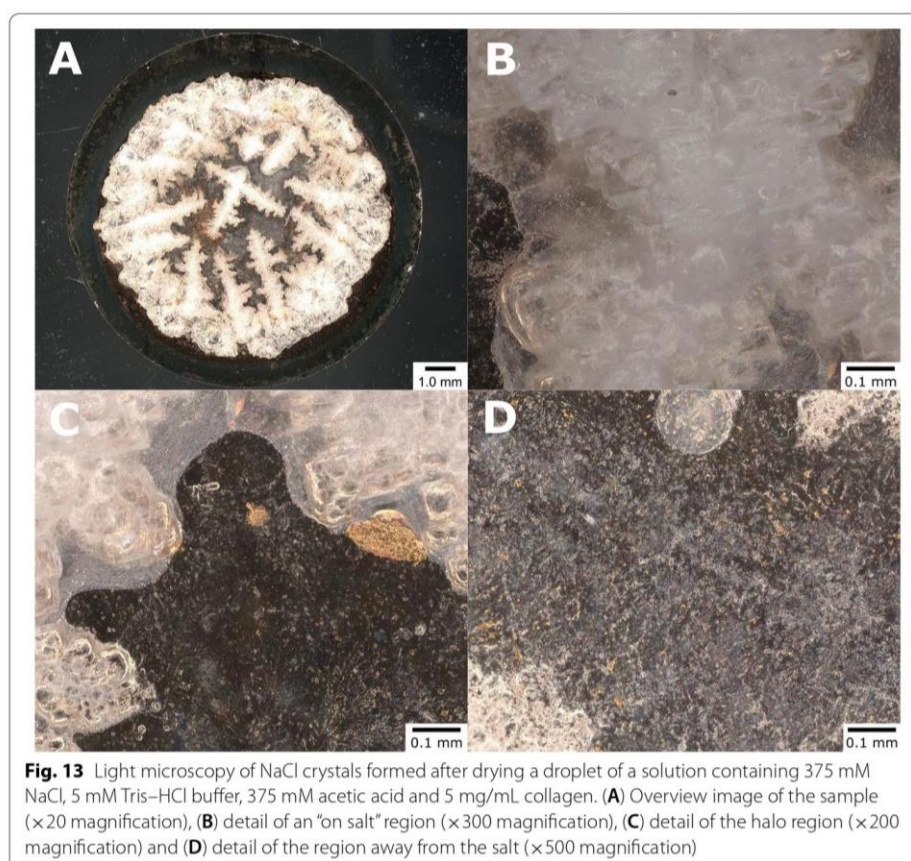
[11], a collagen hydrolysate, at mass concentration ratios $[\text{gelatin}]/[\text{NaCl}]$ of around 0.5; meanwhile, we used a mass concentration ratio of 0.23 in the Tris buffer. In the dendrites, the sizes of the elevated halite grains on top of the approximately 0.2 mm high central NaCl crystallite ranged from 30 to 50 μm (see Fig. 14A–C), meaning they were significantly bigger than the ones obtained in the presence of fibrinogen.

Effects of distinct proteins in direct comparison

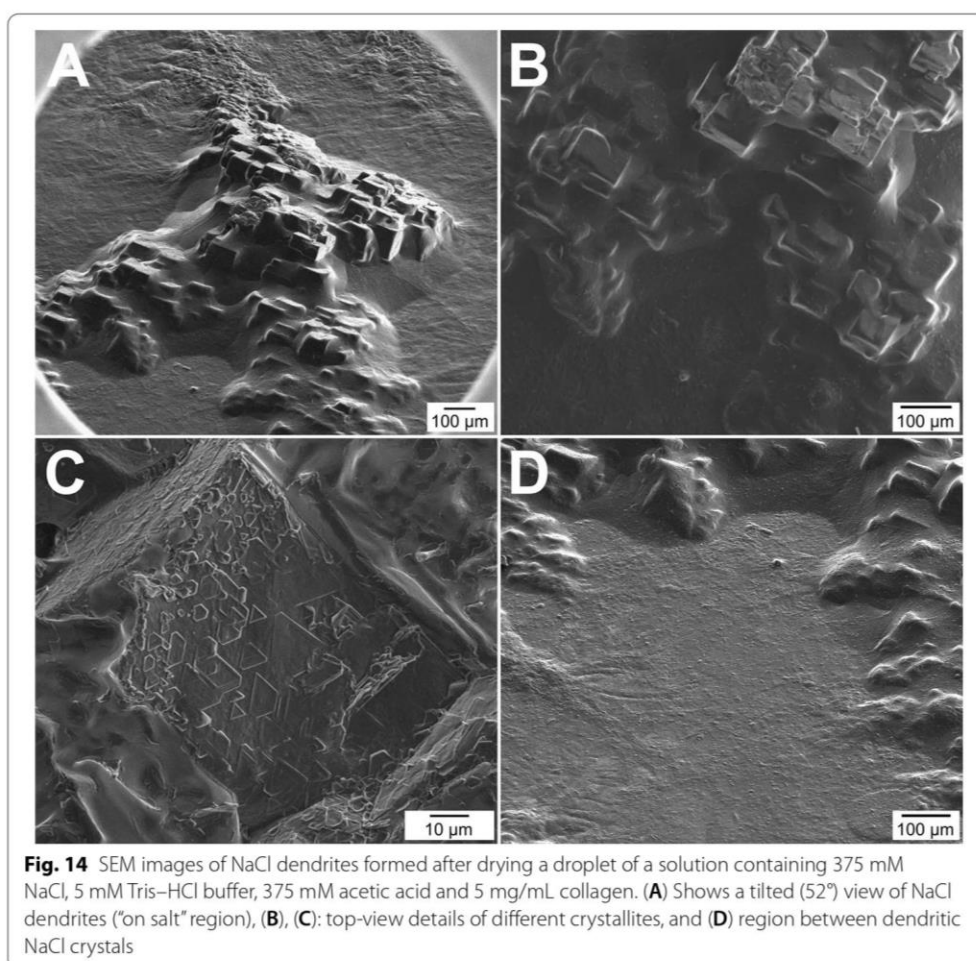
By comparing the microscopic findings for the structure and arrangement of halite crystallites formed during the drying of droplets containing aqueous formulations buffered with 5 mM Tris and a given NaCl concentration of 22 mg/mL we found that adding an initial 5 mg/mL concentration of a protein chosen among BSA, fibrinogen or collagen significantly and specifically changed the obtained drying pattern on gold-coated glass slides. On the one hand, the addition of the globular protein BSA did not strongly affect the overall drying pattern and—as also observed in the absence of proteins—still gave rise to the formation of approximately 1 mm wide halite crystals with a clear and transparent optical appearance. However, in the presence of BSA, the crystal shape was not tabular as in the absence of any protein, but hopped. On the



other hand, adding the fibrillar proteins fibrinogen or collagen resulted in the formation of polycrystalline dendritic NaCl deposits with halite grain sizes clearly below 0.1 mm and an opaque optical appearance. Hence, the very nature of a specific protein and its complex interactions with the co-solutes NaCl and Tris significantly govern the formation of halite grain boundaries. We suppose that in the case of fibrinogen and collagen, the resulting salt crystals are shaped by persisting interphases between the salt and the circumjacent aqueous formulation, impeding an Ostwald ripening of neighboring halite crystallite grains over distances exceeding 0.1 mm. Facilitating such longer-range transport in the liquid phase or even water monolayers [61] would be expected to result in a reduction of the number of smaller sodium chloride deposits for the benefit of bigger crystals with an energetically more favorable faceting of their habits. We thus rather infer that the rate of solute transport may be affected by the viscosity of the concentrated mobile phase, while the restructuring of the halite grain surfaces by the loss and gain of growth units may be influenced by protein-containing films and adsorbates. In this way, both the transport and the surface-related reaction term contributing to the Damköhler number characterizing the dynamics between the stationary and mobile phases will depend on the presence of a specific protein.

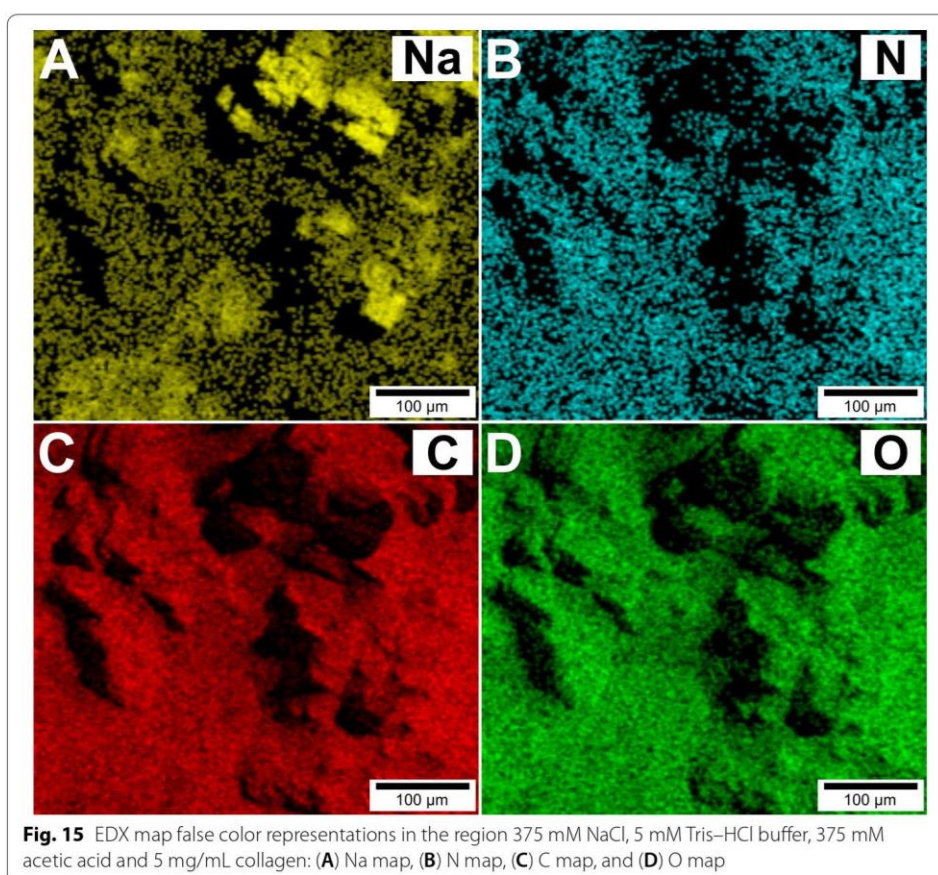


Based on our findings, we suggest that the specific protein–NaCl interactions are guided by the behaviour of the respective protein at the salt/liquid interphase, with the effect of collagen being rather more similar to that of fibrinogen than to that of BSA. Globular proteins on the one hand, and fibrous proteins, on the other hand, not only differ in the principles of their topology but also in the relative abundance of apolar and polar side chains in the amino acids constituting these proteins and the molecular flexibility [62]. For example, Cacace et al. highlighted that at pH 7 in the hydrated state the surface tension of human serum albumin (HSA) features a lower contribution from apolar Lifschitz–van der Waals interactions and a higher share of polar electron acceptor and electron donor potentials than the surface tension of fibrinogen. Therefore, we hypothesize that the specific interactions between a protein and the halite surface significantly influence the observed drying pattern. In detail, the reaction-related contributions to adhesion development within the frame of the macrokinetic approach based on a characteristic Damköhler number may be manifold. The process steps governing the formation of the interphase between the growing solid phase, e.g. salt crystals or solidified protein, and the highly viscous saline aqueous jelly phase containing protein may be related to two principal reaction-type binding events [63]: firstly, the often exothermic binding between cations or anions and the solid phase and, secondly, the entropy-driven and often endothermic water



replacement—e.g. upon dehydration of inorganic or organic moieties—in interphases, such as at highly dynamic salt crystal or protein interfaces in contact with the fluid environment.

In this way, acquiring knowledge on the formation of hybrid or composite materials in droplets of saturated aqueous solutions composed of several co-solutes in environments involving salts and proteins may be inspired by nature and promote medical, pharmaceutical or technological innovation. As highlighted by Lohse and Zhang [64], the spatiotemporal development of multicomponent fluid dynamical systems out of equilibrium is governed by concentration gradients inducing a transport concurring with phase transitions. These complex and interwoven phenomena and the challenges and opportunities related to them may be dealt with by the experimental, numerical and methodical tools and procedures provided by implementing the digital transformation not only in industry but also in research and development. Hence, exploring and designing the spatiotemporal evolution of adhesion is a topic that shows great promise in profiting from advanced materials modelling.



Conclusions

In this study on the drying patterns formed from aqueous saline formulations, we found that the NaCl crystal arrangements and morphologies varied with the composition of the initial solution. Depending on the type of the protein chosen, among BSA, fibrinogen and collagen, the halite deposits predominantly exhibited cubic or polycrystalline dendritic structures. Based on these results, we hypothesize that the process steps in the formation of the interphase between the growing solid phase and the highly viscous saline aqueous jelly phase containing protein govern not only the material transport in the liquid but also the material exchange between solid and liquid phases. In the future, the synthesis of bio-inspired, protein-based composite materials will benefit immensely from understanding fundamental solid-liquid phase interactions to successively tailor these scale-comprehensive dynamic processes.

Abbreviations

BSA: Bovine serum albumin; Tris: Tris(hydroxymethyl)aminomethane; Da: Damköhler number; EDX: Energy dispersive X-ray analysis; SEM: Scanning electron microscopy.

Acknowledgements

The authors thankfully acknowledge the peers for in-depth assessment and comments on the manuscript and Andreas Volkman for technically supporting light microscopic investigations.

Authors' contributions

StS prepared the samples and set up the light microscopy experiments supported by KB and VCB, and contributed to the lay-out, drafting and formatting of the article; KB and VCB also contributed to the discussion of microscopic characterization; KT performed the SEM and EDX measurements and contributed to the discussion of microscopic characterization; WLC and MN took part in defining and setting up the experiments, discussing and merging the obtained data and in drafting the manuscript; IG, PS and SD took part in defining and setting up the experiments based on emerging material design challenges; DB contributed in planning the conceptual approach for joint research and in discussing results and drafting the manuscript. All authors read and approved the final manuscript.

Funding

Open Access funding enabled and organized by Projekt DEAL. DB: Emmy Noether program of the German Research Council (DFG), Grant Number 267326782. St.S.: Fraunhofer TALENTA start program.

Availability of data and materials

The datasets used and/or analyzed during the current study are available from the corresponding author upon reasonable request.

Declarations

Competing interests

The authors declare that they have no competing interests.

Author details

¹Fraunhofer Institute for Manufacturing Technology and Advanced Materials IFAM, Wiener Straße 12, 28359 Bremen, Germany. ²Institute for Biophysics, University of Bremen, Otto-Hahn-Allee 1, 28359 Bremen, Germany. ³Hochschule Bremen, City University of Applied Sciences, Neustadtswall 30, 28199 Bremen, Germany. ⁴Purenum GmbH, Fahrenheitstraße 1, 28359 Bremen, Germany. ⁵MAPEX Center for Materials and Processes, University of Bremen, 28359 Bremen, Germany. ⁶Department Adhesion and Interface Research, Fraunhofer Institute for Manufacturing Technology and Advanced Materials, Wiener Straße 12, 28359 Bremen, Germany.

Received: 20 August 2021 Accepted: 18 October 2021

Published online: 03 November 2021

References

1. Bruckschen P, Neuser RD, Richter DK (1992) Cement stratigraphy in Triassic and Jurassic limestones of the Weserbergland (northwestern Germany). *Sediment Geol* 81:195–214
2. Arakaki A, Shimizu K, Oda M, Sakamoto T, Nishimura T, Kato T (2015) Biomineralization-inspired synthesis of functional organic/inorganic hybrid materials: organic molecular control of self-organization of hybrids. *Org Biomol Chem R Soc Chem* 13:974–989
3. Hu X, Cebe P, Weiss AS, Omenetto F, Kaplan DL (2012) Protein-based composite materials. *Mater Today* 15:208–215. [https://doi.org/10.1016/S1369-7021\(12\)70091-3](https://doi.org/10.1016/S1369-7021(12)70091-3)
4. Yin J, Chen JC, Wu Q, Chen GQ (2015) Halophiles, coming stars for industrial biotechnology. *Biotechnol Adv* 33(7):1433–1442
5. Ma Y, Galinski EA, Grant WD, Oren A, Ventosa A (2010) Halophiles 2010: life in saline environments. *Appl Environ Microbiol* 76:6971–6981
6. DasSarma S, DasSarma P (2017) Halophiles. eLS. Wiley, Chichester, pp 1–13. <https://doi.org/10.1002/9780470015902.a0000394.pub3>
7. Pasteris JD, Freeman JJ, Wopenka B, Qi K, Ma Q, Wooley KL (2006) With a grain of salt: what halite has to offer to discussions on the origin of life. *Astrobiology* 6:625–643
8. Lopez-Cortes A, Ochoa J, Vazquez-Duhalt R (1994) Participation of halobacteria in crystal formation and the crystallization rate of NaCl. *Geomicrobiol J* 12:69–80. <https://doi.org/10.1080/01490459409377973>
9. Zhou M, Yi RJ, Gu Y, Zou J, Guo X (2019) Characterization and evaluation of synthesized ammonia triethyl amide (ATEA) for removing sodium chloride deposition. *J Pet Sci Eng* 179:136–142. <https://doi.org/10.1016/j.petrol.2019.04.005>
10. Dutta Choudhury M, Dutta T, Tarafdar S (2015) Growth kinetics of NaCl crystals in a drying drop of gelatin: transition from faceted to dendritic growth. *Soft Matter R Soc Chem* 11:6938–6947
11. Goto M, Oaki Y, Imai H (2016) Dendritic growth of NaCl crystals in a gel matrix: variation of branching and control of bending. *Cryst Growth Des* 16:4278–4284. <https://doi.org/10.1021/acs.cgd.6b00323>
12. Pramanik R, Asplin JR, Jackson ME, Williams JC (2008) Protein content of human apatite and brushite kidney stones: significant correlation with morphologic measures. *Urol Res* 36:251–258
13. Kovacevic L, Lu H, Kovacevic N, Lakshmanan Y (2020) Effect of bisphosphonates on the crystallization of stone-forming salts in synthetic urine. *Investig Clin Urol* 61:310–315
14. Dumetz AC, Snellinger-O'Brien AM, Kaler EW, Lenhoff AM (2007) Patterns of protein–protein interactions in salt solutions and implications for protein crystallization. *Protein Sci* 16:1867–1877
15. Hyde AM, Zultanski SL, Waldman JH, Zhong YL, Shevlin M, Peng F (2017) General principles and strategies for salting-out informed by the Hofmeister series. *Org Process Res Dev* 21(9):1355–1370
16. Shih Y-C, Prausnitz JM, Blanch HW (1992) Some characteristics of protein precipitation by salts. *Biotechnol Bioeng* 40:1155–1164

17. Yang X, Lu J, Wang XJ, Ching CB (2008) Effect of sodium chloride on the nucleation and polymorphic transformation of glycine. *J Cryst Growth* 310:604–611
18. Takahashi D, Nishimoto E, Murase T, Yamashita S (2008) Protein–protein interaction on lysozyme crystallization revealed by rotational diffusion analysis. *Biophys J* 94:4484–4492. <https://doi.org/10.1529/biophysj.107.111872>
19. Kang ZL, Zhang XH, Li X, Song ZJ, Ma HJ, Lu F et al (2020) The effects of sodium chloride on proteins aggregation, conformation and gel properties of pork myofibrillar protein running head: relationship aggregation, conformation and gel properties. *J Food Sci Technol*. <https://doi.org/10.1007/s13197-020-04736-4>
20. Gronau G, Qin Z, Buehler MJ (2013) Effect of sodium chloride on the structure and stability of spider silk's N-terminal protein domain. *Biomater Sci* 1:276–284
21. Kadler KE, Holmes DF, Trotter JA, Chapman JA (1996) Review article: collagen fibril formation Karl. *Biochem J* 11:1–11
22. Stamboroski S, Joshi A, Noeske PL-M, Köppen S, Brüggemann D (2021) Principles of fibrinogen fiber assembly in vitro. *Macromol Biosci* 21(5):2000412
23. Nürnberger S, Rentenberger C, Thiel K, Schädler B, Grunwald I, Ponomarev I et al (2017) Giant crystals inside mitochondria of equine chondrocytes. *Histochem Cell Biol* 147:635–649
24. Corrales-Urena YR, Sanchez A, Pereira R, Rischka K, Kowalik T, Vega-Baudrit J (2017) Extracellular micro and nano-structures forming the velvet worm solidified adhesive secretion. *Mater Res Express* 4:125013
25. Gaede-Koehler A, Kreider A, Canfield P, Kleemeier M, Grunwald I (2012) Direct measurement of the thermal hysteresis of antifreeze proteins (AFPs) using sonocrystallization. *Anal Chem* 84:10229–10235. <https://doi.org/10.1021/ac301946w>
26. He Z, Wu C, Hua M, Wu S, Wu D, Zhu X et al (2020) Bioinspired multifunctional anti-icing hydrogel. *Matter Cell Press* 2:723–734
27. Rathi S, Saka R, Domb AJ, Khan W (2019) Protein-based bioadhesives and bioglues. *Polym Adv Technol* 30:217–234. <https://doi.org/10.1002/pat.4465>
28. Richter K, Grunwald I, von Byern J (2018) Bioadhesives. Handbook of adhesive technology, 2nd edn. Springer International Publishing, Cham, pp 1597–640. https://doi.org/10.1007/978-3-319-55411-2_53
29. Deng Y, Ediriwickrema A, Yang F, Lewis J, Girardi M, Saltzman WM (2015) A sunblock based on bioadhesive nanoparticles. *Nat Mater* 14:1278–1285
30. Cavalcanti WL, Noeske PL-M (2014) Investigating dynamic interactions by multi-scale modelling: from theory to applications. *Chem Model* 11:175–200. <https://doi.org/10.1039/9781782620112-00175>
31. Raetzke K, Shaikh MQ, Faupel F, Noeske PLM (2010) Shelf stability of reactive adhesive formulations: a case study for dicyandiamide-cured epoxy systems. *Int J Adhes Adhes* 30:105–110. <https://doi.org/10.1016/j.ijadhadh.2009.09.004>
32. Sanchez-Vila X, Dentz M, Donado LD (2007) Transport-controlled reaction rates under local non-equilibrium conditions. *Geophys Res Lett* 34:1–5
33. Yu F, Hunt AG (2017) Damköhler number input to transport-limited chemical weathering calculations. <https://pubs.acs.org/sharingguidelines>. Accessed 5 Aug 2021
34. Naillon A, Joseph P, Prat M (2017) Sodium chloride precipitation reaction coefficient from crystallization experiment in a microfluidic device. *J Cryst Growth* 463:201–210
35. Desarnaud J, Derluyn H, Carmeliet J, Bonn D, Shahidzadeh N (2018) Hopper growth of salt crystals. *J Phys Chem Lett* 9:2961–2966. <https://doi.org/10.1021/acs.jpclett.8b01082>
36. Yang Z, Zhang J, Zhang L, Fu B, Tao P, Song C et al (2020) Self-assembly in hopper-shaped crystals. *Adv Funct Mater* 30:1–26
37. McBride SA, Skye R, Varanasi KK (2020) Differences between colloidal and crystalline evaporative deposits. *Langmuir* 36:11732–11741. <https://doi.org/10.1021/acs.langmuir.0c01139>
38. Huang L, Zhang Z, Guo M, Pan C, Huang Z, Jin J et al (2021) Biomimetic hydrogels loaded with nanofibers mediate sustained release of pDNA and promote in situ bone regeneration. *Macromol Biosci*. <https://doi.org/10.1002/mabi.202000393>
39. Perez FMU, Corrales Ureña YR, Rischka K, Cavalcanti WL, Noeske PLM, Safari AA et al (2019) Bio-interfacants as double-sided tapes for graphene oxide. *Nanoscale* 11:4236–4247. <https://doi.org/10.1039/c8nr08607a>
40. Rauti MG, Guarino V, Ambrosio L (2010) Hybrid composite scaffolds prepared by sol–gel method for bone regeneration. *Compos Sci Technol* 70:1861–1868
41. Zhao H, Yang Z, Guo L (2018) Nacre-inspired composites with different macroscopic dimensions: strategies for improved mechanical performance and applications. *NPG Asia Mater* 10:1–22. <https://doi.org/10.1038/s41427-018-0009-6>
42. Rillig MC (2005) A connection between fungal hydrophobins and soil water repellency? *Pedobiologia (Jena)* 49:395–399
43. Berger BW, Sallada ND (2019) Hydrophobins: multifunctional biosurfactants for interface engineering. *J Biol Eng*. <https://doi.org/10.1186/s13036-018-0136-1>
44. Montoya G, Lopez K, Arenas J, Zamora C, Hoz L, Romo E et al (2020) Nucleation and growth inhibition of biological minerals by cementum attachment protein-derived peptide (CAP-pi). *J Pept Sci*. <https://doi.org/10.1002/psc.3282>
45. Mao J, Nierop KGJ, Dekker SC, Dekker LW, Chen B (2019) Understanding the mechanisms of soil water repellency from nanoscale to ecosystem scale: a review. *J Soils Sediments*. <https://doi.org/10.1007/s11368-018-2195-9>
46. Nguyen PH, Ramamoorthy A, Sahoo BR, Zheng J, Faller P, Straub JE et al (2021) Amyloid oligomers: a joint experimental/computational perspective on Alzheimer's disease, Parkinson's disease, Type II diabetes, and amyotrophic lateral sclerosis. *Chem Rev* 121:2545–2647. <https://doi.org/10.1021/acs.chemrev.0c01122>
47. Cavalcanti W, Santos M, Figueiredo W (2004) Growth model with a finite number of orientations on a linear substrate. *Phys Rev E* 69:021608. <https://doi.org/10.1103/PhysRevE.69.021608>
48. Horsch MT, Niethammer C, Boccardo G, Carbone P, Chiacchiera S, Chiricotto M et al (2020) Semantic interoperability and characterization of data provenance in computational molecular engineering. *J Chem Eng Data* 65:1313–1329. <https://doi.org/10.1021/acs.jced.9b00739>

49. Stapelfeldt K, Stamboroski S, Mednikova P, Brüggemann D (2019) Fabrication of 3D-nanofibrous fibrinogen scaffolds using salt-induced self assembly. *Biofabrication* 11:025010. <https://doi.org/10.1088/1758-5090/ab0681>
50. Stapelfeldt K, Stamboroski S, Walter I, Suter N, Kowalik T, Michaelis M et al (2019) Controlling the multiscale structure of nanofibrous fibrinogen scaffolds for wound healing. *Nano Lett* 49:1–15
51. Suter N, Joshi A, Wunsch T, Graupner N, Stapelfeldt K, Radmacher M et al (2021) Self-assembled fibrinogen nanofibers support fibroblast adhesion and prevent *E. coli* infiltration. *Mater Sci Eng C* 126:112156
52. Stamboroski S, Boateng K, Lierath J, Kowalik T, Thiel K, Köppen S et al (2021) Influence of divalent metal ions on the precipitation of the plasma protein fibrinogen. *Biomacromolecules*. <https://doi.org/10.1021/acs.biomac.1c00930>
53. Dutta D, Markhoff J, Suter N, Rezwan K, Brüggemann D (2021) Effect of collagen nanofibers and silanization on the interaction of HaCaT keratinocytes and 3T3 fibroblasts with alumina nanopores. *ACS Appl Bio Mater* 4:1852–1862
54. Suter N, Stebel S, Rianna C, Radmacher M, Brüggemann D (2021) Spatial patterning of nanofibrous collagen scaffolds modulates fibroblast morphology. *Biofabrication* 13:015007–015018
55. Saveleva MS, Eftekhari K, Abalymov A, Douglas TEL, Volodkin D, Parakhonskiy BV et al (2019) Hierarchy of hybrid materials—the place of inorganics-in-organics in it, their composition and applications. *Front Chem* 7:1–21
56. Rodrigues M, Kosaric N, Bonham CA, Gurtner GC (2019) Wound healing: a cellular perspective. *Physiol Rev* 99:665–706
57. Kamasa P, Bokor M, Pyda M, Tompa K (2007) DSC approach for the investigation of mobile water fractions in aqueous solutions of NaCl and Tris buffer. *Thermochim Acta* 464:29–34
58. Giri A, Choudhury MD, Dutta T, Tarafdar S (2013) Experiment and simulation of multifractal growth of crystalline NaCl aggregates in aqueous gelatin medium. *Colloids Surf A Physicochem Eng Asp* 432:127–131
59. Shahidzadeh N, Schut MFL, Desarnaud J, Prat M, Bonn D (2015) Salt stains from evaporating droplets. *Sci Rep* 5:1–9
60. Taha M, Lee M-J (2010) Interactions of TRIS [tris(hydroxymethyl)aminomethane] and related buffers with peptide backbone: thermodynamic characterization. *Phys Chem Chem Phys* 12:12840
61. Oliva-Ramirez M, Macías-Montero M, Borrás A, González-Elipe AR (2016) Ripening and recrystallization of NaCl nanocrystals in humid conditions. *RSC Adv* 6:3778–3782
62. Cacace MG, Landau EM, Ramsden JJ (1997) The Hofmeister series: salt and solvent effects on interfacial phenomena. *Q Rev Biophys* 30:241–277
63. Darby SJ, Platts L, Daniel MS, Cowieson AJ, Falconer RJ (2017) An isothermal titration calorimetry study of phytate binding to lysozyme: a multisite electrostatic binding reaction. *J Therm Anal Calorim* 127:1201–1208
64. Lohse D, Zhang X (2020) Physicochemical hydrodynamics of droplets out of equilibrium. *Nat Rev Phys* 2:426–443

Publisher's Note

Springer Nature remains neutral with regard to jurisdictional claims in published maps and institutional affiliations.

Submit your manuscript to a SpringerOpen[®] journal and benefit from:

- Convenient online submission
- Rigorous peer review
- Open access: articles freely available online
- High visibility within the field
- Retaining the copyright to your article

Submit your next manuscript at ► [springeropen.com](https://www.springeropen.com)

6. NANOFIBER TOPOGRAPHIES ENHANCE PLATELET-FIBRINOGEN SCAFFOLD INTERACTIONS

- Status: Paper published at Advanced Healthcare Materials (2022)

Kenny, M., Stamboroski, S., Taher, R., Brüggemann, D., & Schoen, I. (2022). Nanofiber Topographies Enhance Platelet-Fibrinogen Scaffold Interactions. *Advanced Healthcare Materials*, 11(14), 2200249

DOI: [10.1002/adhm.202200249](https://doi.org/10.1002/adhm.202200249)

6.1. MOTIVATION & HYPOTHESIS

Hypothesis addressed: Self-assembled fibrinogen nanofibers influence blood platelet adhesion due to their special topography.

Fibrinogen nanofibers have already shown good biocompatibility with human bladder cells (Mcmanus et al., 2007), cardiac fibroblasts (McManus et al., 2007), endothelial cells (Gugutkov et al., 2013) and human mesenchymal stem cells (Forget et al., 2016). The salt-induced fibrinogen nanofibers presented in the previous chapters have also demonstrated good support to dermal fibroblasts and keratinocytes growth (Joshi et al., 2023; Suter et al., 2021). Aiming at using the developed *in vitro* salt-induced fibrinogen nanofibers as a scaffold material for *in vivo* future tissue engineering or wound dressing applications, Chapter 6 presents the results of the interaction of blood platelets with nanofibers produced from the precipitation of fibrinogen in the presence of 2.5x PBS. For comparison, also smooth fibrinogen scaffolds were exposed to platelets. The influence of the different fibrinogen topographies/morphologies were assessed in terms of promoting or hindering cell adhesion.

Hypothesis assessment: Confirmed.

RESEARCH ARTICLE

ADVANCED
HEALTHCARE
MATERIALS

www.advhealthmat.de

Nanofiber Topographies Enhance Platelet-Fibrinogen Scaffold Interactions

Martin Kenny, Stephani Stamboroski, Reem Taher, Dorothea Brüggemann,*
and Ingmar Schoen*

The initial contact with blood and its components, including plasma proteins and platelets, directs the body's response to foreign materials. Natural scaffolds of extracellular matrix or fibrin contain fibrils with nanoscale dimensions, but how platelets specifically respond to the topography and architecture of fibrous materials is still incompletely understood. Here, planar and nanofiber scaffolds are fabricated from native fibrinogen to characterize the morphology of adherent platelets and activation markers for phosphatidylserine exposure and α -granule secretion by confocal fluorescence microscopy and scanning electron microscopy. Different fibrinogen topographies equally support the spreading and α -granule secretion of washed platelets. In contrast, preincubation of the scaffolds with plasma diminishes platelet spreading on planar fibrinogen surfaces but not on nanofibers. The data show that the enhanced interactions of platelets with nanofibers result from a higher locally accessible surface area, effectively increasing the ligand density for integrin-mediated responses. Overall, fibrinogen nanofibers direct platelets toward robust adhesion formation and α -granule secretion while minimizing their procoagulant activity. Similar results on fibrinogen-coated polydimethylsiloxane substrates with micrometer-sized 3D features suggest that surface topography could be used more generally to steer blood-materials interactions on different length scales for enhancing the initial wound healing steps.

Recent wound healing approaches have benefited immensely from advances in nanotechnology,^[2] where a wide range of engineered nanomaterials has been explored.^[3,4] When synthetically prepared materials are used for wound treatment, they come into direct contact with blood, resulting in adsorption of various proteins and subsequent adhesion of blood cells.^[5,6] These blood-material interactions depend on the particular surface chemistry and topography of a scaffold material and have a direct effect on its hemocompatibility.^[7] Although consensus on some general design principles for medical device coatings in contact with blood has been reached, the specific requirements for wound dressings have received much less attention, and the influence of nanoscale topography on protein adsorption and cell adhesion is incompletely understood.^[6,7]

When a blood vessel gets injured, platelets (i.e., thrombocytes) adhere to the subendothelial matrix and form a thrombus through fibrinogen-mediated platelet-platelet aggregation.^[8] The plasma protein fibrinogen then is enzymatically cleaved by thrombin at the wound site and a nanofibrous fibrin clot is formed during secondary hemostasis.^[9] This fibrin mesh serves as a provisional extracellular matrix to support the migration of fibroblasts, endothelial cells, and immune cells involved in wound repair.^[10,11]

1. Introduction

The treatment of acute and chronic wounds has evolved into one of the greatest challenges of our rapidly aging population.^[1]

secondary hemostasis.^[9] This fibrin mesh serves as a provisional extracellular matrix to support the migration of fibroblasts, endothelial cells, and immune cells involved in wound repair.^[10,11]

M. Kenny, R. Taher, I. Schoen
School of Pharmacy and Biomolecular Sciences
Royal College of Surgeons in Ireland (RCSI)
123 St Stephen's Green, Dublin D02 YN77, Ireland
E-mail: ingmarschoen@rcsi.ie

M. Kenny, I. Schoen
Irish Centre for Vascular Biology
Royal College of Surgeons in Ireland (RCSI)
123 St Stephen's Green, Dublin D02 YN77, Ireland
S. Stamboroski, D. Brüggemann
Institute for Biophysics
University of Bremen
Otto-Hahn-Allee 1, Bremen 28359, Germany
E-mail: brueggemann@uni-bremen.de

 The ORCID identification number(s) for the author(s) of this article can be found under <https://doi.org/10.1002/adhm.202200249>

© 2022 The Authors. Advanced Healthcare Materials published by Wiley-VCH GmbH. This is an open access article under the terms of the Creative Commons Attribution-NonCommercial License, which permits use, distribution and reproduction in any medium, provided the original work is properly cited and is not used for commercial purposes.

S. Stamboroski
Fraunhofer Institute for Manufacturing Technology and Advanced Materials (IFAM)
Wiener Strasse 12, Bremen 28359, Germany
D. Brüggemann
MAPEX Center for Materials and Processes
University of Bremen
Bremen 28359, Germany

DOI: 10.1002/adhm.202200249

Platelets attach to fibrin(ogen) via the highly abundant platelet integrin $\alpha_{IIb}\beta_3$ whose activation is tightly regulated to avoid erroneous thrombosis.^[12] Immobilized, but not soluble fibrinogen, is sufficient to induce platelet adhesion, spreading and contraction which is strictly dependent on functional $\alpha_{IIb}\beta_3$ integrins^[13] and further modulated by ligand density,^[14] substrate stiffness,^[15,16] glycoprotein VI signaling,^[17] as well as by other platelet agonists such as thrombin. In native 3D nanofibrous fibrin clots, platelets extend filopodia along fibrin fibers to pull on them to drive clot compaction.^[18] Platelets can foster thrombin generation by exposing “procoagulant” phosphatidylserine (PS) on their surface^[19] which serves as platform for the assembly of the intrinsic tenase and prothrombinase complexes. Platelet activation can also lead to the secretion of α -granules which contain “prohemostatic” adhesion proteins and clotting factors, but also growth factors, cytokines, and antimicrobial peptides important for wound healing.^[20,21] How local microenvironmental cues selectively tune platelet activation to differentially regulate these diverse platelet functions is incompletely understood.^[8,20] A detailed characterization of a scaffold’s ability to steer platelet responses is thus important to evaluate its suitability for wound healing applications.

So far, the role of surface topography on platelet-material interactions has been investigated predominantly in the context of dental implants. Microtextured titanium disks with rough surfaces led to enhanced platelet adhesion from platelet rich plasma (PRP)^[22,23] as well as to elevated P-selectin expression^[23] or growth factor release^[24] as a consequence of α -granule secretion. The coarser the microtexture, the higher was the platelet activation, independent of calcium or phosphate ions on the surface.^[24] However, such synthetic microtextures were fabricated by different techniques and potential differences in surface chemistry^[25] could affect the composition of the adsorbed protein layer^[6] and therefore complicate the interpretation of platelet-topography interactions. Polydimethylsiloxane (PDMS) substrates with approximately micrometer-sized holes and well-defined fibrinogen coating revealed two distinct modes of how platelets touch, sense, and bridge the holes,^[26] leading to more irregular platelet shapes but similar spreading area compared to flat surfaces.^[27] Despite these isolated insights obtained on different synthetically prepared surfaces, an overarching mechanistic understanding of how platelets sense and respond to different topographies is missing.

Fibrin gels can be readily fabricated from (autologous) plasma or from purified fibrinogen by the addition of thrombin and calcium. While fibrin gels offer a simple route to 3D nanofibrous scaffolds for tissue engineering applications,^[28] human thrombin is costly, and its retention can cause thrombotic complications^[29] when not counter-acted, e.g., by their modification with heparin.^[30] As a better-defined alternative to fibrin gels, synthetically prepared fibrinogen nanofibers have become of particular interest as scaffolds to support wound healing.^[31] Techniques to prepare fibrinogen nanofibers include electrospinning,^[32] template-assisted extrusion^[33] or various self-assembly approaches.^[34] While electrospun fibrinogen fibers have been shown to promote the growth of fibroblasts,^[35–37] endothelial cells,^[38] smooth muscle cells,^[39] and mesenchymal stem cells,^[40,41] their preparation involves organic solvents and high electric fields, which may affect their bioactivity.^[42] For fib-

rinogen in particular, electrospinning requires very high protein concentrations up to 200 mg mL⁻¹,^[32,38] which renders the production of large wound healing scaffolds very resource intensive. To overcome these limitations, we have recently introduced salt-induced self-assembly as a physiological process to prepare fibrinogen nanofibers using fibrinogen concentrations of only 5 mg mL⁻¹.^[43,44] These self-assembled fibrinogen nanofibers resemble the architecture of native fibrin clots, exhibit mechanical properties similar to fibrin upon rehydration, promote fibroblast adhesion, and prevent infiltration with *Escherichia coli* bacteria.^[45] To further explore the potential of self-assembled fibrinogen nanofibers as new scaffold material for the treatment of acute and chronic wounds, we here assessed the interaction of different fibrinogen topographies with human platelets in the absence or presence of plasma proteins. Unlike fibrin which offers only limited tuning of fibril dimensions,^[46,47] the salt-induced self-assembly of fibrinogen can be controlled to yield planar 2D films or nanofibrous 3D scaffolds with nearly identical surface chemistries, as previously characterized by circular dichroism and Fourier-Transform Infrared (FTIR) spectroscopy.^[43,44] Our unique approach thus allowed us to specifically investigate the effect of (nano)topography on platelet activation in terms of adhesion and spreading, α -granule secretion, and PS exposure.

2. Results

2.1. Nanofibers Promote Platelet Adhesion and Spreading on Fibrinogen Scaffolds in the Presence of Plasma

We first characterized the surface topography of nanofibrous versus planar fibrinogen scaffolds. As a reference to facilitate comparisons with previous platelet studies, we included coverslips that were coated with fibrinogen by physisorption from solution. Scanning electron microscopy (SEM) images and confocal microscopy images showed flat, almost featureless surfaces for the physisorbed glass and planar scaffolds, with an increased fibrinogen staining density on planar scaffolds (Figure 1a,b). Nanofibrous scaffolds had the strongest fibrinogen staining (Figure S1, Supporting Information) and exhibited fibrils with submicrometer diameters piled up into bundles which formed an ca. 6 μ m high, mountainous landscape with undulated microtopography (Figure 1c), in agreement with previous studies.^[43–45]

Static incubation of PRP from healthy donors on the three different surfaces resulted in platelet adsorption and spreading to different degrees. SEM images showed mainly round platelets without or with filopodia on physisorbed and planar fibrinogen surfaces, whereas platelets appeared denser and more spread on fibrinogen nanofibers (Figure 1d–f and Figure S2, Supporting Information). Accordingly, platelets on physisorbed and planar scaffolds showed mainly cortical f-actin staining with some filopodia protrusions, while on fibrinogen nanofibers, the actin cytoskeleton exhibited clear f-actin bundles spanning across spread platelets or small platelet aggregates (Figure 1g–i). Counting of platelets revealed a trend toward more adhered platelets on nanofiber scaffolds which did not reach statistical significance (Figure 1j). In contrast, the surface area covered by platelets was highly significantly larger on nanofibers compared to both flat fibrinogen surfaces (Figure 1k). A visual evaluation of the adhesion morphology revealed that about 50% of adherent platelets

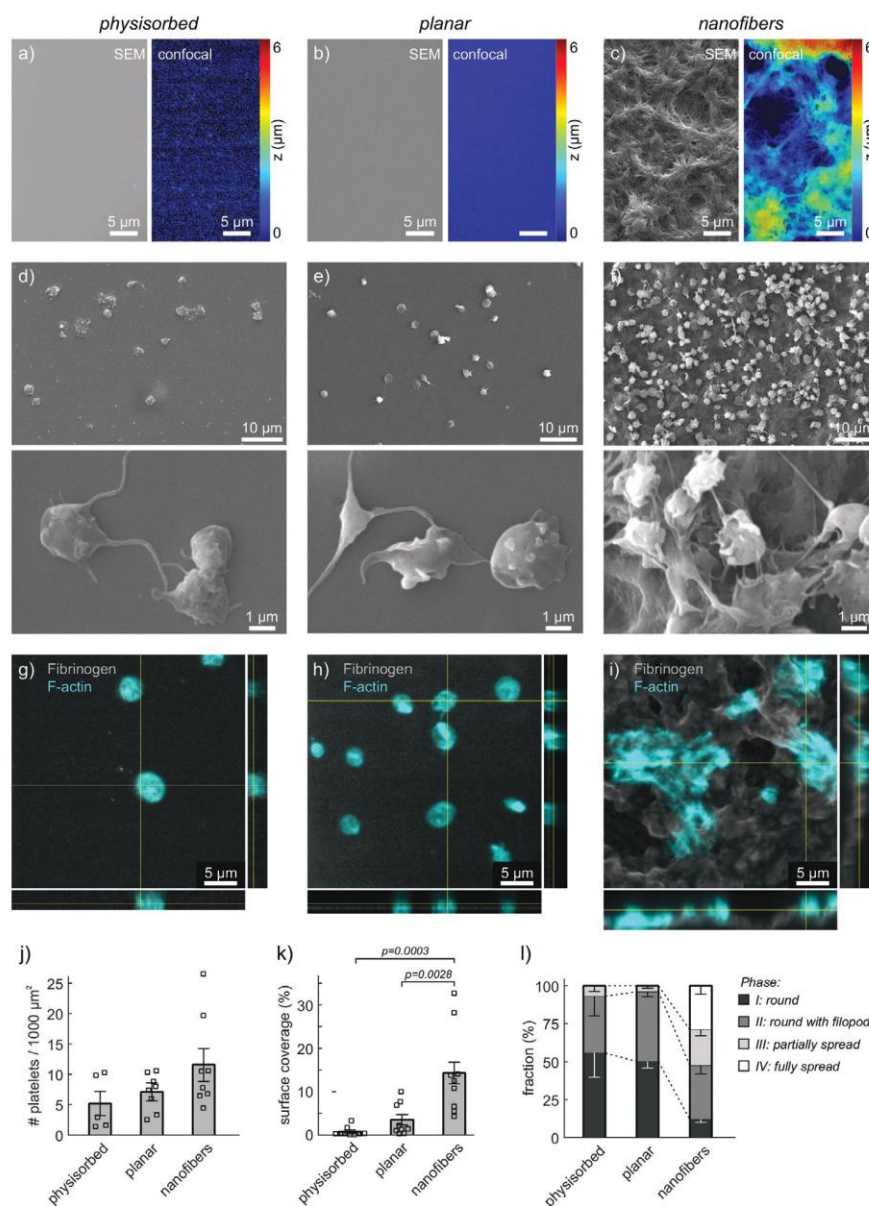


Figure 1. Interactions of human platelet-rich plasma (PRP) with fibrinogen scaffolds of different topographies. Samples comprised: a,d,g) physisorbed fibrinogen on glass coverslips; b,e,h) planar or c,f,i) nanofibrous fibrinogen scaffolds prepared by salt-induced self-assembly. a–c) Characterization of surface topography by scanning electron microscopy (SEM; left) or by confocal z-stacks (color-coded; right). Note that SEM and confocal images show different sample regions. d–f) PRP from citrated blood was incubated for 1 h at 37 °C on the surfaces before fixation and sample processing for imaging. d–f) Representative SEM images of fixed, dehydrated, and gold-coated adherent platelets on the three different scaffolds. g–i) Representative confocal images and orthogonal views of adhered platelets on the three different scaffolds. Gray: fibrinogen stain. Cyan: phalloidin stain. j–l) Quantitative comparison of platelet interactions with the three different scaffolds with respect to j) number of adhered platelets, k) surface coverage by platelets, and l) spreading phase of platelets. Each data point in (j,k) represents one image. Bars and error bars show mean and standard error of the mean (s.e.m.) of replicates, respectively. For (j,k), differences between conditions were assessed by one-way ANOVA with Tukey post hoc multiple comparison. Only *p*-values smaller than 0.05 are displayed.

were partially or fully spread on nanofibers, whereas more than 90% of platelets on flat surfaces remained round or were round with filopodia (Figure 1l). In summary, platelets from PRP adhered and spread much more strongly on nanofibrous scaffolds than on planar scaffolds or on physisorbed fibrinogen control surfaces.

2.2. Washed Platelets Adhere and Spread Normally on All Fibrinogen Surfaces

The failure of platelets from PRP to spread on flat fibrinogen surfaces was unexpected considering that fibrinogen is the primary ligand of the most abundant integrin on platelets, $\alpha_{IIb}\beta_3$. Since plasma proteins can affect cell-material^[7] and receptor-ligand^[48] interactions, we next tested how washed platelets interact with the three different fibrinogen surfaces in the absence of plasma proteins. Washed platelets adhered and spread on all three substrates (Figure 2a–c and Figure S3, Supporting Information). On flat surfaces, platelets formed extensive flat lamellipodia outward from a central, slightly elevated granulomere region (Figure 2a,b), resulting in the prototypic and commonly reported “fried egg” appearance.^[49] On nanofibers, platelets spread over the rough surface and further extended finger-like protrusions along fibrinogen fibers (Figure 2c, asterisks), similar to platelets in native fibrin meshes.^[18] Platelets on all substrates showed pronounced bundled f-actin filaments spanning the cell (Figure 2d–f). Vinculin, an adaptor protein re-enforcing focal adhesions under mechanical tension,^[50] localized to the ends of these f-actin bundles, as well as to the outer rim of the lamellipodium on flat fibrinogen surfaces (Figure 2d,e), in agreement with previous findings.^[49] On nanofibers (Figure 2f), focal adhesions and f-actin bundles appeared more distinct than on flat surfaces; however, a systematic analysis of f-actin cytoskeletal morphology^[49] did not show significant differences in the self-alignment of actin filaments within single platelets (Figure 2j). Interestingly, this pronounced formation of f-actin bundles on nanofiber scaffolds contrasts with our previous study in which fibroblasts exhibited a more diffuse cytoskeleton on fibrinogen fibers compared with aligned actin filaments on planar fibrinogen.^[45] An analysis of platelet outlines revealed a comparable spreading area and overall elliptical platelet shape on all surfaces (Figure 2g,h), whereas the circularity revealed significantly more irregular cell shapes on nanofibers (Figure 2i), as explained by the protrusions seen on SEM images (Figure 2c). Taken together, the interaction of platelets alone with fibrinogen surfaces of different topography resulted in comparable activation of platelet adhesion and spreading, indicating a diminished spreading of platelets on planar surfaces in the presence of plasma proteins.

2.3. Nanofibers Steer Platelets toward a Noncoagulant Biomechanical Phenotype

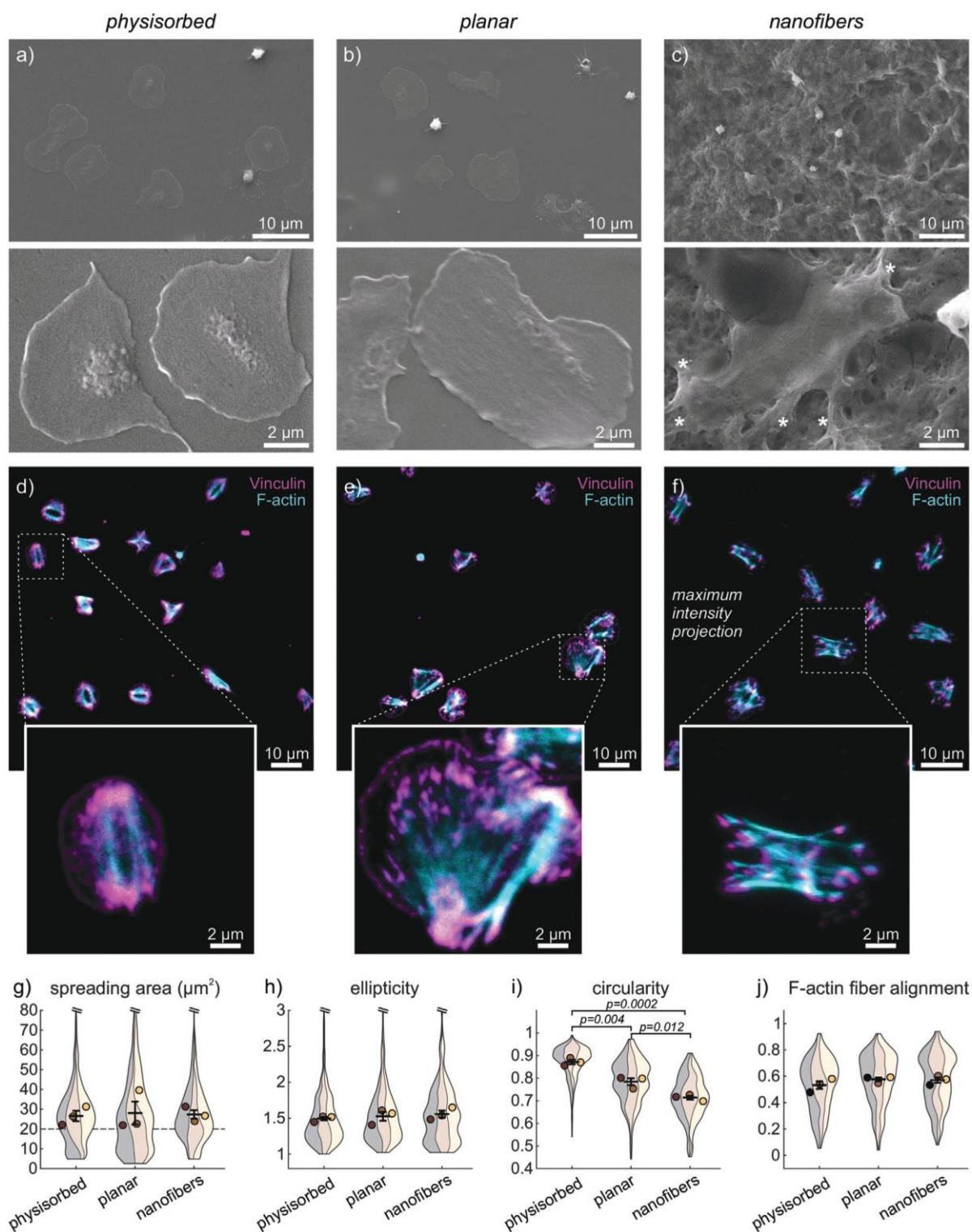
To investigate how platelet functions beyond adhesion, spreading and aggregation were affected by fibrinogen scaffold topography, we assessed P-selectin expression as a marker for α -granule secretion, and Annexin-V binding as a marker for PS exposure, in the presence and absence of plasma (Figure 3). An f-actin

counterstain showed adhesion morphologies similar to previous experiments (cf. Figures 1 and 2), with predominantly non-spread platelets from PRP on planar scaffolds and partially or fully spread platelets in other conditions (Figure 3a–d). About 50% of platelets expressed P-selectin on their surface, irrespective of the fibrinogen topography (Figure 3e). PS exposure was considerable (>60%) on planar substrates in the presence of plasma but significantly reduced to <12% on nanofibrous scaffolds, with no significant difference for washed platelets (Figure 3f). Most pronounced in PRP on nanofibers was the reduction for PS+ only platelets (Figure 3g) which typically had a dissolved f-actin cytoskeleton (cf. Figure 3a for a comparison to planar). Accordingly, the proportion of double negative platelets increased (Figure 3g) which was also seen in the images on nanofibers as platelets containing only the f-actin stain (Figure 3b). We thus conclude that nanofiber topographies limited the amount of PS exposure on platelets by promoting their spreading, while equally allowing for the secretion of α -granules.

2.4. Nanofibers Promote Platelet Spreading by Locally Increasing the Accessible Surface Area

We next investigated how different aspects of the nanofiber topography contributed to platelet responses. We first assessed whether the micrometer-scale substrate curvature affected platelet adhesion and spreading. Platelets on nanofibers were found to spread in both, convex regions (“peaks”) or in concave regions (“valleys”) of the undulated 3D landscape (Figure 4a). While platelets on peaks were relatively flat (ca. 1 μm), platelets in valleys often spanned a larger z-range (2–4 μm) or bridged gaps by forming pronounced focal adhesions on opposing mountain sides interconnected by f-actin bundles (arrows). To distinguish between peaks and valleys, we obtained a height profile of the surface topography from confocal z-stacks and used a Laplace filter with a scale of 2 μm to separate convex from concave regions (Figure 4b). A statistical analysis of the surface coverage of platelets in peak versus valley regions, relative to the total surface coverage in the whole image, revealed no preference for convex or concave regions for washed platelets, but a pronounced preference of platelets from PRP for peak regions (Figure 4c).

Apart from forming a mountainous landscape on the micrometer scale, fibrinogen nanofibers offer a substantially increased surface area due to their thin diameter and porous network architecture (cf. Figure 1c). To estimate the increase in surface area associated with this undulated submicrometer topography, we deconvolved high-resolution confocal z-stacks, determined a detailed height profile and calculated the fold-increase of the local surface area (compared to a flat surface) following standard procedures.^[52] The involved nanofiber architecture locally resulted in a more than 10x increased surface area (Figure 4d), with an average fold-increase of 6.9 ± 3.5 (mean \pm std) compared to a planar surface (Figure 4e). Note that this simplistic analysis underestimates the true surface area because finest structural details are not resolved by diffraction-limited confocal imaging, and any overhanging regions are not accounted for. The surface area accessible to platelets for adhesion and spreading thus might well be >10x larger than on the planar scaffold, an estimate which is



further supported by the measured increase in surface roughness of nanofiber scaffolds by 15-fold compared to planar.^[45]

Based on this analysis, we hypothesized that an increased locally accessible surface area due to the mountainous 3D topography directly modulated platelet spreading by offering more immobilized fibrinogen molecules that can be bound by platelet integrins. To test our hypothesis in a more generic setting, we turned toward PDMS micropost arrays as a geometrically well-defined 3D topography model. We compared two cases: arrays in which only the tops of posts were microcontact-printed with fibrinogen while the surfaces between posts were passivated, restricting platelet adhesion and spreading to the printed post tops, versus arrays that were uniformly coated with fibrinogen by physisorption, allowing platelets to adhere on posts or in the gaps between posts (Figure 4f). The uniformly coated arrays offer a ca. 13-fold larger local surface area covered by fibrinogen than the printed arrays, which can be compared to the fold-increase of the surface area on nanofiber versus planar fibrinogen scaffolds. Washed platelets adhered and spread on the tops of the fibrinogen-printed posts (Figure 4g), as exploited commonly in traction force measurements,^[53,54] while they engulfed single posts or adhered between posts to maximize their contact area with the homogeneously fibrinogen-coated substrate (Figure 4h). Incubation of the top-printed arrays with PRP resulted in very little platelet adsorption and rounded morphologies, similar to the printed flat support structures next to the micropost arrays (Figure 4i). In stark contrast, PRP incubation on homogeneously coated arrays resulted in an extended mesh of interconnected platelets covering posts and filling the gaps in between (Figure 4j). The surface coverage by platelets from PRP was highly significantly increased on homogeneously coated arrays versus printed arrays (Figure 4k), with only a slight preference of platelets for (convex) posts (Figure 4l). In summary, the 3D topography of homogeneously coated microposts led to strong interactions with platelets in PRP while the 2D printed post tops failed to do so, analogous to the interactions of 3D nanofiber and 2D planar fibrinogen scaffolds with PRP.

2.5. Priming of Scaffolds by Plasma Reduces Platelet Adhesion and Spreading

It is well established that the activation threshold of platelets in solution depends on plasma components,^[55] but how plasma-material interactions might affect the activation threshold of platelets is less well understood. To further investigate how plasma modulated platelet activation in response to different scaffold topographies, we pretreated planar and nanofiber scaffolds with platelet-poor plasma (PPP) before thorough wash-

ing and seeding of washed platelets in plasma-free spreading buffer. Comparable to the effect of plasma during seeding (Figure 5a, cf. Figure 1), preincubation of the scaffolds with PPP inhibited platelet spreading on planar scaffolds but much less so on nanofibers (Figure 5b). PPP-pretreatment can thus be understood to result in a general reduction of the activating stimulus strength of scaffolds for platelet adhesion. Since the reduction of platelet spreading was much more pronounced on planar scaffolds, we conclude that the nanotopography of fibrous scaffolds provided an effectively stronger stimulus. This general line of reasoning could explain why the spreading of washed platelets was differentially affected by plasma pretreatment, without the necessity of postulating a topography-specific interaction of scaffolds with plasma proteins.

To test whether the reduction in platelet adhesion was due to a blocking effect, we preincubated the scaffolds with albumin, a major component of plasma commonly used to reduce unspecific protein adsorption or cell adhesion to artificial surfaces. Washed platelets spread normally on albumin-blocked planar and nanofibrous scaffolds (Figure 5c), comparable to untreated scaffolds (cf. Figure 2), ruling out that albumin was responsible for the observed reduced platelet spreading. Fibrinogen is another major component of plasma which competes to bind activated $\alpha_{IIb}\beta_3$ integrins that are required for platelet spreading on immobilized fibrinogen, and soluble fibrinogen has been shown to prevent adsorption of platelets to fibrinogen coatings under flow.^[56] However, pretreatment of scaffolds with soluble fibrinogen (Figure 5d) did not significantly reduce spreading of washed platelets (Figure 5h) while it mainly reduced the number of adhered platelets on nanofibers (Figure S4, Supporting Information). A potential preferential adsorption of fibrinogen from plasma to curved regions^[57] that could enhance interactions on nanofiber scaffolds did thus not play a significant role. These results and the similar behavior of platelets on both physisorbed fibrinogen and planar scaffolds (Figures 1 and 2) further demonstrate that the formaldehyde vapor treatment of scaffolds did not affect plasma-scaffold and platelet-scaffold interactions.

The thrombogenicity of materials often is an indirect effect mediated by activation of coagulation,^[6,7] potentially depending on surface topography.^[58] Thrombin is a potent activator of platelets^[59] that is found in plasma in its inactive form but can be activated via the contact-mediated coagulation cascade initiated by binding of factor XII to negatively charged surfaces.^[60] To investigate whether thrombin positively or negatively modulated the response of platelets to the fibrinogen scaffolds, we blocked thrombin activity using the selective inhibitor hirudin, which abolished thrombin-induced aggregation of washed platelets in solution (Figure S5, Supporting Information). Adding hirudin to PPP during the preincubation of scaffolds before seeding

Figure 2. Interactions of washed human platelets with fibrinogen scaffolds of different topographies. Samples comprised: a,d) physisorbed fibrinogen on glass coverslips; b,e) planar or c,f) nanofibrous fibrinogen scaffolds prepared by salt-induced self-assembly. Washed platelets were incubated for 1 h at 37 °C on the surfaces before fixation and sample processing for imaging. a–c) Representative SEM images of adhered platelets on the three different scaffolds. Asterisks denote pseudopodia. d,e) Representative confocal slices or f) maximum intensity projections of z-stacks of adhered platelets on the three different scaffolds. Cyan: phalloidin stain. Magenta: vinculin stain. g–j) Comparison of platelet interactions with the three different scaffolds. Shown are Violin SuperPlots^[51] representing the (non-normal) distribution of parameters within each biological replicate (band) of three independent experiments, overlaid with the replicate means (circles) and the means' mean and s.e.m. (error bars). g) Spreading area of single platelets. The number n of platelets per replicate was between 56 and 288. k) Ellipticity, i) circularity, and j) α -actin fiber alignment of platelets with a spreading area larger than $20 \mu\text{m}^2$ (dashed line in (g)). The number n of platelets per replicate was between 46 and 234. Differences between conditions were assessed by one-way ANOVA with Tukey post hoc multiple comparison. Only p -values smaller than 0.05 are displayed.

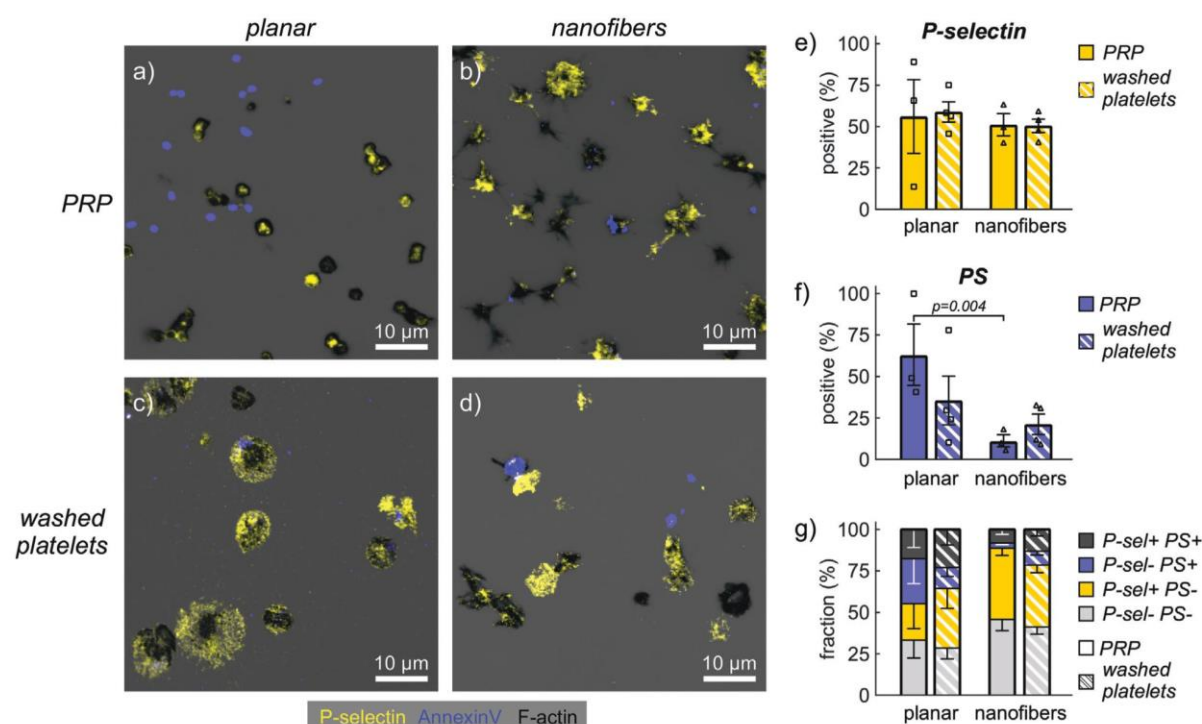


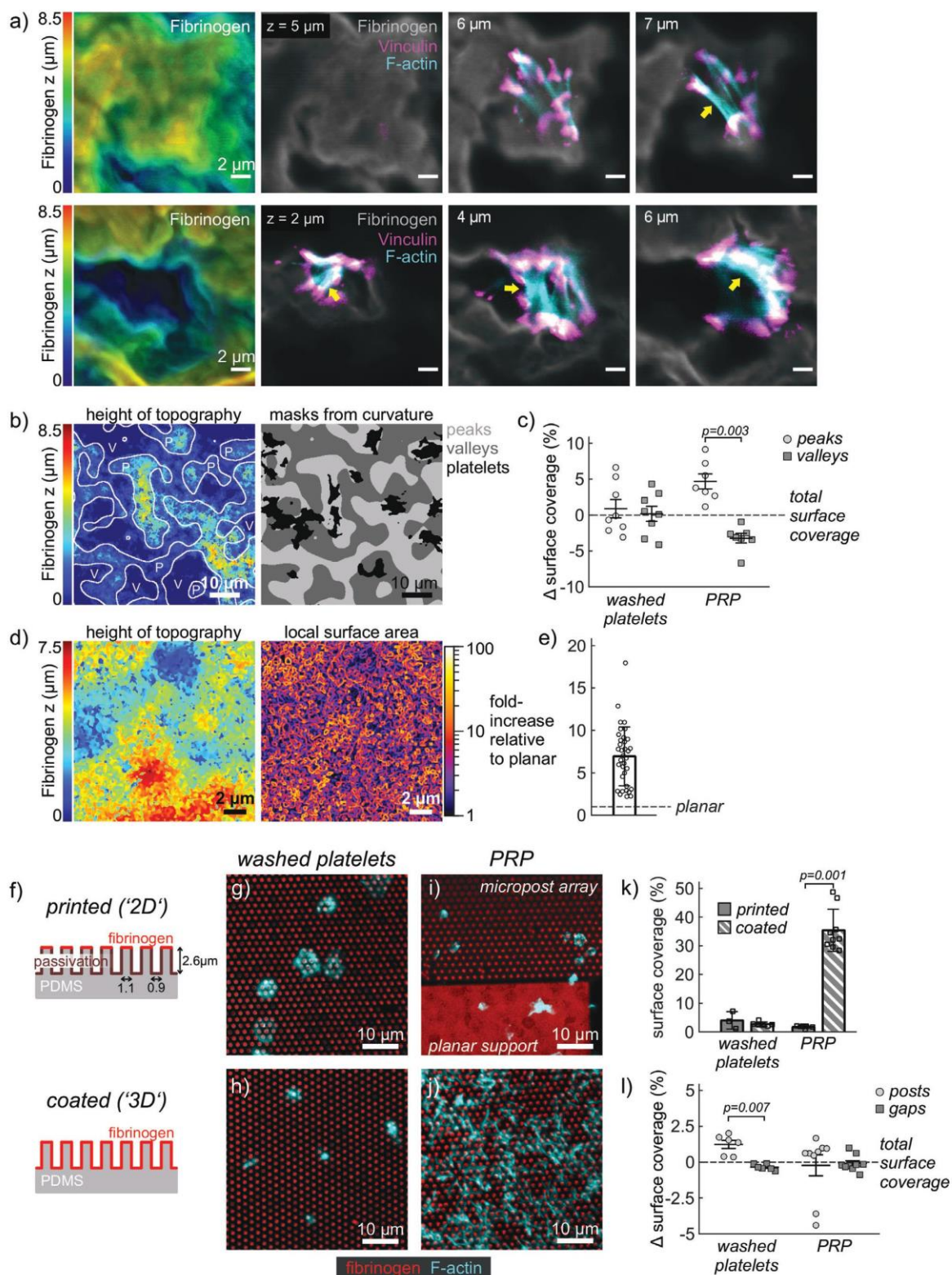
Figure 3. Platelet activation markers on fibrinogen scaffolds of different topographies. a,c) Representative confocal slices on planar scaffolds or b,d) maximum intensity projections of z-stacks on nanofibrous scaffolds of human platelets stained for phalloidin (black), P-selectin (yellow), and Annexin-V (blue). a,b) PRP or c,d) washed platelets were incubated for 45 min at 37 °C on the surfaces and then for 30 min in the presence of fluorescently labeled Annexin-V before fixation and sample processing for imaging. e–g) Comparison of e) P-selectin expression, f) PS exposure, and g) combinations thereof by scaffold topography and by absence/presence of plasma. Bars and error bars show mean and s.e.m. of replicates, respectively. For (e,f), differences between topographies were assessed by a ratio paired t-test. Only *p*-values smaller than 0.05 are displayed.

(Figure 5e) or seeding washed platelets on PPP-pretreated scaffolds in the presence of hirudin (Figure 5f) had similar effects, indicating that any action of thrombin was mediated by its interaction with the scaffold rather than its direct action on platelets. Thrombin inhibition by hirudin did not change the trend of more platelets being found on nanofibers than on planar fibrinogen, even though numbers on planar substrates were tendentially increased (Figure S4, Supporting Information). Thrombin inhibition slightly decreased platelet spreading, and thus surface coverage, on nanofiber scaffolds but did not affect these parameters on planar scaffolds (Figure 5g,h). These opposing trends only partially reduced the differences in platelet behavior between different topographies. Since thrombin inhibition only had a minor effect on platelet adhesion and spreading, a potential activation of the contact pathway on scaffolds, although not directly tested here, did not account for the main inhibitory effect seen with plasma.

2.6. Nanofiber Topographies Facilitate Platelet Adhesion under Shear Flow

Many blood-biomaterial interactions take place under shear flow which is known to affect platelet-surface interactions through ad-

hesion receptor mechanotransduction.^[16] We thus extended the investigation of platelet-scaffold interactions to a previously described flow assay using whole blood.^[61] At arterial shear rates (1500 s^{-1}) where resting platelets do not bind fibrinogen^[56,62] but depend on von Willebrand Factor (vWF) capture by the surface and vWF-GPIIb signaling to activate firm platelet adhesion,^[63] no interactions of platelets with planar fibrinogen scaffolds occurred (Figure 6a,b), in stark contrast to platelet accumulation on vWF-coated channels (Figure S6a, Supporting Information). Very short transient binding of single platelets on planar fibrinogen was observed at elevated venous shear rate (300 s^{-1}), while transient small aggregates formed at 100 s^{-1} (Figure 6a). At low venous shear rate (50 s^{-1}), platelet interactions with planar scaffolds remained sparse, and when microaggregates formed, they remained smaller than ca. $10 \mu\text{m}$ and persisted in the field of view for typically less than a minute before detaching or disassembling (Figure 6c, cf. also Figure S6b, Supporting Information). Platelets also adhered transiently and formed microaggregates on nanofiber scaffolds, with a tendency for more prolonged platelet-surface interactions (see kymographs in Figure 6d and Figure S6c, Supporting Information), resulting in more platelets accumulating over time than on planar scaffolds (Figure 6e). The growth, sliding, and rupture of small aggregates occurred repeatedly at different locations on both planar and nanofiber surfaces



and always locally aligned with the flow direction (Movie S1, Supporting Information), which is typical for platelet adhesion to vWF strings. These data indicate that the underlying nanofibrous fibrinogen topography might be more efficient than planar surfaces to capture vWF from blood which mediates the adhesion of platelets to fibrinogen scaffolds under flow. These findings match published results that showed increased platelet adhesion from whole blood at 300 s^{-1} shear to 3D polymer surfaces with dimensions similar to the peaks and valleys of our mountainous nanofiber topographies, compared to 2D polymer surfaces.^[64]

3. Discussion

The two major findings of our study are that a 3D nanofiber topography facilitates platelet interactions with fibrinogen scaffolds by increasing the local surface area (Figures 1, 2, and 4), and that plasma components interacting with the scaffolds differentially modulate platelet activation responses (Figures 3 and 5). Our approach complements previous works on platelet-scaffold interactions using organic or inorganic materials with different microtextures^[5,24,57,25] and exceeds these in several aspects. Fibrinogen scaffolds ensure well-defined binding interactions through $\alpha_{\text{IIb}}\beta_3$ integrins alone, in contrast to arginine-glycine-aspartic acid (RGD) peptides which are bound by many different integrins, thereby ensuring physiological signaling responses of platelets and facilitating the investigation of topography effects independent of composition. Moreover, dissecting blood into its components allowed us to differentiate between platelet-intrinsic responses versus responses which were mediated by plasma-scaffold interactions.

Different platelet activation outcomes, most importantly proadhesive integrin activation (enabling attachment at wound sites and platelet aggregation), procoagulant PS exposure (contributing to thrombin-driven coagulation), as well as prohemostatic and proangiogenic α -granule secretion (providing a source of adhesion molecules and growth factors at the wound site) are regulated through numerous activation and inhibitory pathways^[13,55,65,66] and contribute critically to the thrombotic risk and the healing response in blood-material interactions.^[7] The observed counter-regulation of proadhesive and procoagulant platelet activation responses, as here induced by the nanofiber topography (Figure 3), agrees with previous findings which showed that PS exposing platelets are noncontractile,^[67,68] and that PS exposure is upregulated upon inhibition of platelet contractility^[69] or upon reduced platelet spreading on nonadhesive topographies.^[70] Previous reports also observed the highest levels of platelet adhesion and α -granule secretion on surfaces with a roughness of 105 nm ^[71] which is comparable to the ca.

120 nm roughness of fibrinogen nanofibers.^[45] It has been proposed that the conformation of physisorbed fibrinogen on planar surfaces influences platelet binding and activation.^[72,73] The preparation of fibrinogen scaffolds using different salt concentrations results in very similar protein conformations, with a slight increase in β -sheets for nanofibers as compared to more α -helical content in planar fibrinogen.^[44] Although we thus cannot exclude that the conformation of fibrinogen molecules in our scaffolds differentially affects platelet binding, the qualitatively similar response of platelets to artificial 3D topographies (Figure 4f–l) that were coated with fibrinogen under physiological conditions strongly indicates that the observed enhanced interaction with 3D environments does not depend on fibrinogen conformation, but rather is an intrinsic property of 3D topographies.

Immobilized fibrinogen is a well-known activating stimulus that induces platelet spreading.^[13] The spreading of platelets depends on integrin clustering and downstream signaling, which are strongly influenced by ligand density of flat fibrinogen coatings.^[14] A tight spacing of binding sites for $\alpha_{\text{IIb}}\beta_3$ integrins, and the concomitant avidity effect, has recently been proposed to enable fibrin to overcome an elevated activation threshold for platelet aggregation in the presence of integrin inhibitors.^[74] Due to the high surface-to-volume ratio of nanofibers and their dense packing, a single platelet on fibers can bind many more fibrinogen molecules in its vicinity than on planar fibrinogen. Our data suggest that the 3D presentation of a larger number of binding sites, as present on nanofibers but also on coated micropost arrays (Figure 4f–l), can enhance platelet responses analogously to reduced ligand spacing. This concept of a locally accessible surface area^[75] as the relevant parameter for platelet adhesion and spreading is also consistent with a reduced platelet adhesion on nanopost^[57] or nanopore^[76] substrates with gaps that are too narrow for platelets to squeeze into.

The interaction of plasma components with the fibrinogen scaffolds that happened before platelet adhesion, rather than their direct action on platelets, led to reduced platelet-scaffold interactions (Figure 5). The observed reduced interactions could in principle be explained by a competitive inhibition of integrin binding to the fibrinogen scaffolds by a plasma component.^[56] More studies are needed to identify which plasma component might bind to, or mask, integrin binding sites on the fibrinogen scaffolds, since we could exclude a role for soluble fibrinogen and albumin by our experiments. Based on the available data, we speculate that a reduced adhesiveness of plasma-exposed scaffolds could not only explain the reduced spreading on planar scaffolds,^[14,77] but also the preference of platelets in PRP, but not of washed platelets, for peak regions (Figure 4b,c). By engulfing

Figure 4. Influence of scaffold curvature and locally accessible surface area on platelet interactions. a) Representative confocal slices of single platelets on nanofiber scaffolds. Gray: fibrinogen stain. Cyan: phalloidin stain. Magenta: vinculin stain. b) Determination of masks for concave (valley) versus convex (peak) regions. c) Difference in platelet surface coverage of valley versus peak regions relative to the overall surface coverage in the respective image. The mean overall surface coverage was 18% for washed platelets and 28% for PRP. d) Detailed height profile of nanofiber scaffolds (left) and corresponding actual local surface area (right). Data analysis was based on high-resolution deconvolved confocal z-stacks. e) Fold-increase of surface area averaged over $10\text{ }\mu\text{m} \times 10\text{ }\mu\text{m}$ regions ($n = 35$) on four different scaffolds. f) Schematic and dimensions of microcontact printed (top) or homogeneously coated (bottom) micropost arrays as 2D and 3D topography models. g,h) Washed platelet and i,j) PRP interactions with g,i) printed or h,i) coated micropost arrays. Red: fluorescently labeled fibrinogen. Cyan: phalloidin stain. k) Comparison of surface coverage by platelets. l) Difference in surface coverage of platelets on posts or in gaps relative to the overall surface coverage. Bars and error bars in (c,k,l) show mean and s.e.m. of replicates, respectively, while bars and error bars in (e) show mean and standard deviation. For (k,l), differences between substrate topographies were assessed by a paired t-test. Only p-values smaller than 0.05 are displayed. Scale bars: a,d) $2\text{ }\mu\text{m}$, b,g–j) $10\text{ }\mu\text{m}$.

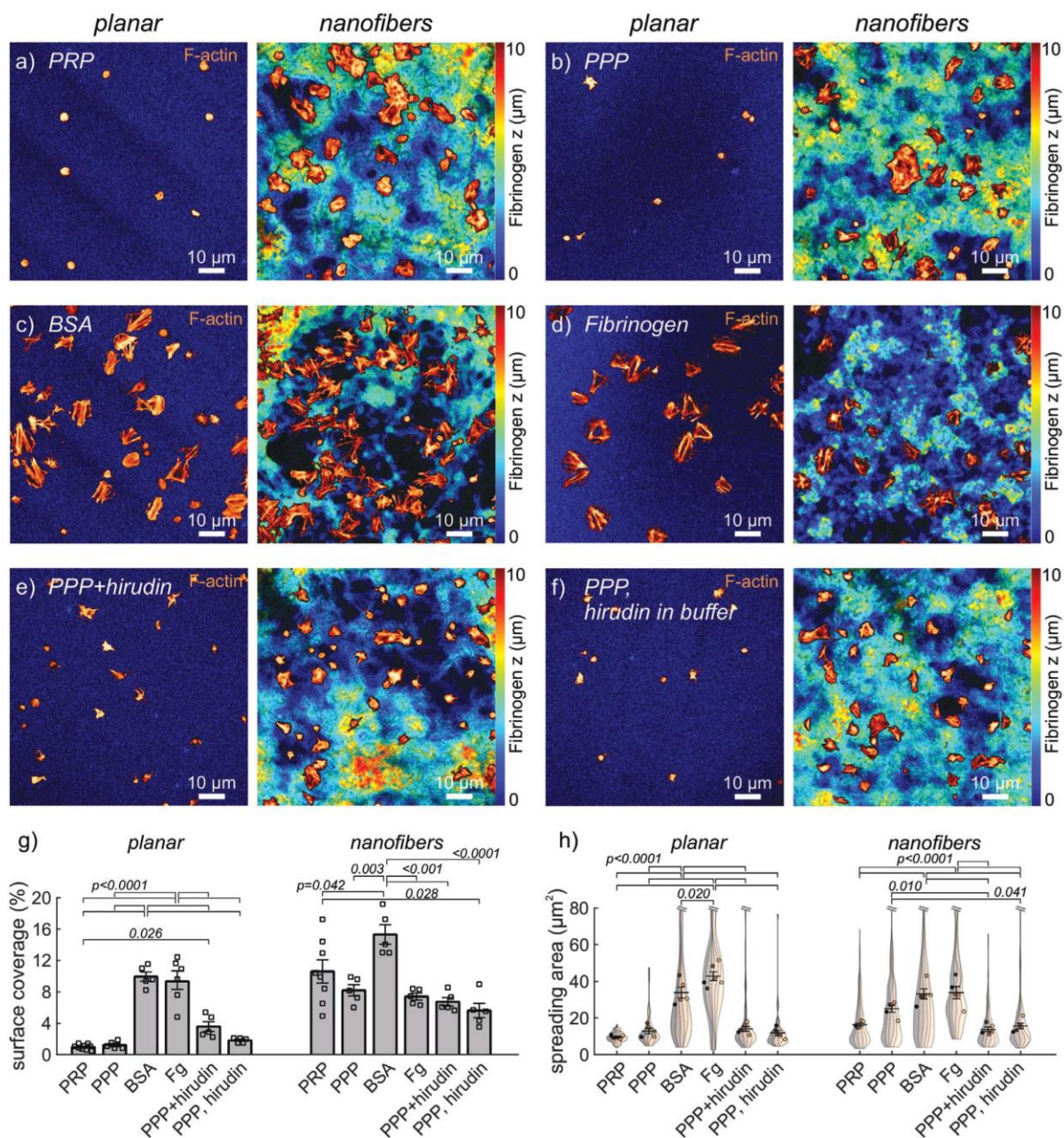


Figure 5. Modulation of platelet adhesion on fibrinogen scaffolds by plasma components. a–f) Representative confocal images of a) PRP on untreated scaffolds or b–f) washed platelets on scaffolds preincubated with b) platelet-poor plasma (PPP), c) bovine serum albumin (BSA, 1 mg mL⁻¹), d) fibrinogen (1.5 mg mL⁻¹), e) PPP and hirudin (1 U mL⁻¹), and f) PPP while hirudin (1 U mL⁻¹) was added to the spreading buffer. Shown are overlays of the f-actin stain (orange-hot) with the fibrinogen stain (color-coded from blue to red according to z-position). g) Surface coverage for different treatments on planar or nanofiber fibrinogen scaffolds. h) Violin SuperPlots of platelet spreading area by scaffold topography. The number *n* of platelets per replicate was between 5 and 32 on planar or between 12 and 129 on nanofiber scaffolds, respectively. Bars and error bars in (g,h) show mean and s.e.m. of replicates, respectively. Differences between treatments on the same topography were assessed by one-way ANOVA with Tukey post hoc multiple comparison. Only adjusted *p*-values smaller than 0.05 are displayed.

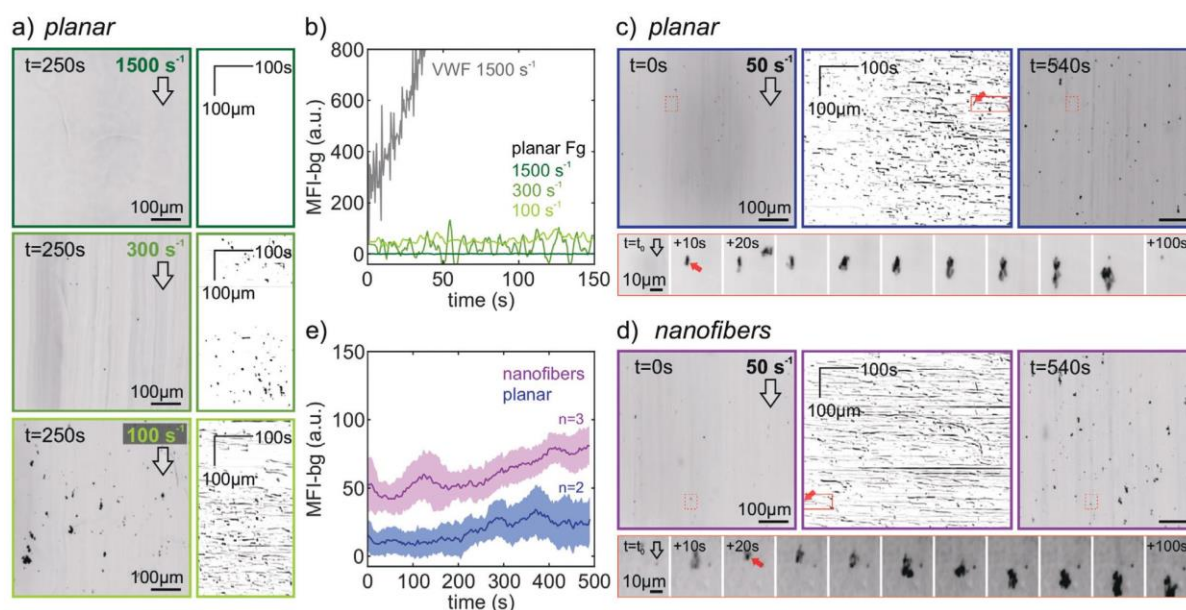


Figure 6. Interactions of whole blood with planar or nanofiber fibrinogen scaffolds under flow. Scaffolds were integrated into a flow channel and whole blood was flown over the scaffolds using a defined flow rate. Platelets were visualized by the fluorescent DiOC6 membrane stain in epifluorescence at two frames per second. a) End frame (left, inverted colormap) and kymographs (right) of time-lapse acquisitions at shear rates of 1500 s^{-1} (top), 300 s^{-1} (middle), or 100 s^{-1} (bottom). Direction of flow is indicated by an arrow. Kymographs were obtained by performing a maximum intensity projection of each frame onto the direction of flow (y-axis) and plotting this over time (x-axis). b) Background-subtracted mean fluorescence intensity of platelet accumulation over time. Shown are the different shear rates (color coded) on planar fibrinogen scaffolds (see (a)). For comparison, platelet accumulation on a vWF-coated surface is shown at arterial shear (gray). c,d) Kymographs with start and end frames (top) at a shear rate of 50 s^{-1} on c) planar or d) nanofiber fibrinogen scaffolds. The exemplary interaction event series (bottom) shown corresponds to the red arrow and boxed regions in the movie frames and kymographs. e) Comparison of platelet accumulation over time on planar (blue) or nanofiber (magenta) fibrinogen scaffolds. Shown are the mean and s.e.m. (40 s moving average) of the background-subtracted mean fluorescence intensity of platelet accumulation over time.

substrate protrusions, less integrin-mediated friction is needed to hold on to and spread over the surface, compared to platelets attaching to two opposing sides of a valley and pulling transversally at the substrate (cf. Figure 4a), since a similar mechanism has been shown to underlie the sensing of nanowire topographies by fibroblasts using filopodia.^[78]

4. Conclusions

Altogether, our study clearly demonstrates the feasibility of employing self-assembled biomimetic nanofibrous fibrinogen scaffolds to enhance platelet adhesion and spreading as compared to planar fibrinogen surfaces. Further studies are required to elucidate the interactions of plasma proteins with these scaffolds and their capacity to modulate platelet-scaffold interactions. It is expected that these differential blood-scaffold interactions based on topography also change the interactions of other cells with the material. This opens up the opportunity to employ fibrinogen scaffolds with defined topography-function relationships for various tissue engineering applications, e.g., as novel wound dressing materials or implant coatings. Toward future applications in wound healing where platelets are known to recruit and instruct immune cells, it will be critical to assess the interactions of immune cells with nanostructured fibrinogen scaffolds, ide-

ally taking PRP exposure into account. Targeted modulation of platelet responses by topography may have potential to enhance responses in patients who suffer from impaired wound healing. Other avenues for fibrous fibrinogen scaffolds are the cocultivation of skin cells to develop new biomaterials for skin tissue engineering or the tailoring of the topography of fibrinogen-based biomaterials for stem cell differentiation or blood vessel replacement.

Our more general finding that surface topography on the nanometer to micrometer scale differentially affected certain platelet activation pathways suggests that topography could be exploited as a design parameter for new biomaterials to prevent excessive clotting while supporting the physiological function of platelets. In this respect, we speculate that (nano)topography might be usable as an alternative to heparin coatings of implants.

Generally, the comprehensive methodology used in this study could be applied to delineate the particular contributions of plasma proteins and platelets to define blood-material interactions also for other (bio)materials. Improved understanding of how the interactions of plasma and/or PRP with tissue engineered scaffolds, either by design^[79] or during implantation, direct the responses of immune cells, stem cells, and tissue forming cells could aid the successful translation of in vitro findings into better in vivo outcomes.

5. Experimental Section

Substrates, Buffers, and Protein Solution Preparation: Glass slides coated with (3-aminopropyl)triethoxysilane (APTES) were used as substrate to prepare nanofibrous and planar fibrinogen scaffolds following a previously published routine.^[45] Fifteen millimeter round glass coverslips (VWR, Darmstadt, Germany) were first cleaned with freshly prepared piranha solution for 5 min by immersion. For the piranha solution, sulfuric acid (95%; VWR) was mixed with hydrogen peroxide solution (30%; VWR) in a ratio of 3:1 v/v. After piranha treatment the glass slides were washed five times with deionized water from a water purification system (TKA MicroPure UV; Thermo Fisher Scientific, Schwerte, Germany). Cleaned glass coverslips were dried with nitrogen and modified with APTES by overnight immersion in ethanol (Honeywell, VWR) containing APTES (5% v/v; Sigma-Aldrich, Steinheim, Germany) at room temperature. The modified APTES glasses were washed with ethanol and dried with N₂ for subsequent modification with fibrinogen. Fibrinogen stock solutions (10 mg mL⁻¹) were prepared by dissolving fibrinogen from human plasma (Merck KGaA, Darmstadt, Germany) in ammonium hydrogen carbonate solution (10 × 10⁻³ M; Roth, Karlsruhe, Germany). Subsequently, dialysis was carried out overnight to remove low molecular weight compounds with 14 kDa cutoff cellulose membrane dialysis tubing (Sigma-Aldrich). Phosphate buffered saline (PBS, Thermo Fischer Scientific) was prepared by dissolving PBS tablets in deionized water.

Preparation of Fibrinogen Scaffolds: As previously introduced,^[45] planar scaffolds were prepared by adding fibrinogen stock solution (100 μL) and deionized water (100 μL) onto APTES-coated glass slides. For fibrous scaffolds instead of water, PBS (5x; 100 μL) was added to yield the final concentration of fibrinogen on the scaffolds (5 mg mL⁻¹ in 2.5x PBS). All fibrinogen scaffolds were dried in a home-built humidity chamber overnight at 24 °C and 30% relative humidity. After drying, scaffolds were crosslinked for 2 h by incubation in a sealed beaker containing formaldehyde solution (1 μL cm⁻³, 37%; AppliChem, Darmstadt, Germany). After crosslinking, all scaffolds were washed with deionized water four times for 15 min each. Washed samples were dried at room temperature for further analysis. To enable visualization of substrate topography by confocal microscopy, the substrates were labeled directly before use with ATTO647N-NHS dye (1 × 10⁻⁶ M in 50 × 10⁻³ M NaHCO₃; AttoTec, Germany) for 1 h at room temperature, washed with PBS.

Preparation of Micropost Arrays: Micropost arrays containing micropillars of 2.65 μm in height and 1 μm in diameter arranged in hexagonal arrays between solid supports were prepared as previously described.^[54] Briefly, hard PDMS base and crosslinker (Gelest Inc, Germany) were mixed 1:1 w/w, degassed under vacuum for 5 min, placed on an air plasma-treated (PDC-32G-2; Harrick, USA) 20 mm round coverslips (Hecht Assistant, Germany) and brought into contact with a negative mold. Samples were degassed under vacuum for 30 min, baked at 80 °C for 16 h, and then unmolded. Prior to surface functionalization with labeled fibrinogen, micropost arrays were treated by UV ozone for 7 min (Novascan PSD PRO-UV4). Human fibrinogen (Sigma-Aldrich) was labeled with Alexa Fluor 488 N-hydroxysuccinimide (NHS) ester (Thermo Fisher Scientific). To restrict fibrinogen coating to the tops of posts and the support structures, a mixture of labeled and unlabeled fibrinogen (1:1 molar ratio, final concentration 100 μg mL⁻¹) was physisorbed onto flat PDMS stamps (1:10 base:crosslinker w/w, Sylgard 184; Dow Corning Inc, USA) for 1 h at room temperature, stamps were dried under nitrogen, and protein was transferred by microcontact printing. Alternatively, to achieve homogeneous fibrinogen coverage of the micropost arrays, a droplet of the same fibrinogen mixture was placed directly onto the substrate for 1 h at room temperature. Unbound fibrinogen was removed by washing with PBS. Uncoated surfaces of the micropost arrays were blocked with bovine serum albumin (BSA, 0.5 mg mL⁻¹ in PBS; 9647; Sigma-Aldrich) conjugated to DyLight405 NHS ester (Thermo Fisher Scientific) for 1 h at room temperature. Pluronic F127 (0.5% in distilled water; Sigma-Aldrich) was added to the substrates for a further 1 h at room temperature. Multiple PBS exchanges were performed to remove unbound BSA or Pluronic F127.

Preparation of Flow Chambers: Fibrinogen scaffolds were directly prepared on 24 mm × 50 mm rectangular glass coverslips. A small drop of

Alexa Fluor 488 NHS ester (0.5 μL; 10 × 10⁻⁶ M in 10 × 10⁻³ M NaHCO₃) was placed in the center and air dried in an oven at 80 °C for 1 min. Previously described flow chambers^[61] (EF Engineering; Dublin, Ireland) with channel width 1.5 mm and height 50 μm were assembled onto these coverslips. As a control, plain coverslips were coated with von Willebrand factor (vWF, Haemate-P; CSL Behring) for 1 h at room temperature. All chambers were rinsed with PBS (2 mL), blocked with BSA (1 mL; 1% in PBS) for 1 h at room temperature, then rinsed with PBS.

Preparation of Platelets from Whole Blood: Whole blood samples were collected from healthy consenting volunteers in accordance with RCSI research ethics (REC1391 and REC1504) and the Declaration of Helsinki. A 20-gauge butterfly needle was used to draw blood into a 2.7 mL ethylenediaminetetraacetic acid (EDTA) tube (S-Monovette; Sarstedt) followed by 2–4 10 mL tubes containing sodium citrate (S-Monovette; Sarstedt). Blood collected in EDTA was used to get a full blood count (Sysmex KX-21N). 5 mL citrated whole blood was placed in 15 mL Falcon tubes and centrifuged at 170 relative centrifugal force (RCF) for 10 min at room temperature without deceleration. Platelet-rich plasma (PRP) was transferred into a clean Falcon tube and recalcified with CaCl₂ (1.8 × 10⁻³ M final concentration) for 10 min prior to seeding on substrates. PPP was prepared by centrifugation of PRP at 1000 RCF for 10 min. To prepare washed platelets, PRP was transferred into a clean Falcon tube, and acid-citrate-dextrose solution (0.4 mL; 124 × 10⁻³ M dextrose, 85 × 10⁻³ M sodium citrate tribasic, 38 × 10⁻³ M citric acid) and prostaglandin E1 (PGE1; 2 μL; 1 × 10⁻³ M in ethanol; Sigma-Aldrich) were added. The time between PGE1 treatment and seeding on substrates was at least 1 h to ensure normal platelet responsiveness. The tubes were centrifuged at 900 RCF for 5 min without deceleration. A micropipette was used to remove as much supernatant as possible without disturbing the pellet. Platelets were resuspended in washing buffer (1 mL; 10 × 10⁻³ M sodium citrate, 150 × 10⁻³ M NaCl, 1 × 10⁻³ M EDTA, 1% (w/v) dextrose, pH 7.4), and two Falcon tubes of platelets were combined into a clean Falcon tube and centrifuged at 720 RCF without deceleration. After removal of supernatant, platelets were resuspended in Tyrode's buffer (134 × 10⁻³ M NaCl, 2.68 × 10⁻³ M KCl, 0.4 × 10⁻³ M Na₂HPO₄, 11.9 × 10⁻³ M NaHCO₃, pH 6.5) containing dextrose (5 × 10⁻³ M; Sigma-Aldrich) and apyrase (0.5 U mL⁻¹; from potato; Sigma-Aldrich). Platelet count was determined and adjusted to 3–3.5 × 10⁵ μL⁻¹ with Tyrode's buffer containing dextrose (5 × 10⁻³ M). Washed platelets were recalcified to 1.8 × 10⁻³ M CaCl₂ at least 10 minutes before use in experiments.

Platelet-Material Interaction Experiments: Five million washed platelets in spreading buffer (1 mL; Tyrode's buffer containing 1.8 × 10⁻³ M CaCl₂ and 5 × 10⁻³ M adenosine diphosphate) were added to fibrinogen-coated coverslips, planar or nanofibrous fibrinogen scaffolds, or micropost arrays in a 12-well plate. Alternatively, undiluted recalcified PRP (0.8 mL) was added. These samples were incubated at 37 °C with 5% CO₂ for 1 h, before washing with Tyrode's buffer, and fixing in paraformaldehyde (3% in PBS) at room temperature for 15 min. For Annexin-V staining, platelets were spread for 45 min, and the spreading solution was replaced with Annexin-V binding buffer (100 μL) containing Annexin-V (Alexa Fluor 555 conjugate; Thermo Fisher Scientific). The samples were incubated at 37 °C with 5% CO₂ for a further 30 min before washing and fixation.

Scanning Electron Microscopy: Fixed platelets on fibrinogen substrates were washed with MilliQ water to prevent salt crystals appearing as artifacts. Fixed samples in 12-well plates were incubated with 50% ethanol:water v/v for 2.5 h at room temperature or at 4 °C overnight. The plates were sealed with parafilm at all stages to reduce evaporation. Samples were incubated with 75% ethanol overnight at 4 °C, followed by 15 min sequential incubations with 87.5%, 93.8%, 96.9%, and 98.4% ethanol. Samples were placed in plastic boxes and allowed to air dry in a fume hood. Before SEM analysis all samples were sputter coated with 7 nm of gold using an EM ACE600 high vacuum sputter coater (Leica Microsystems, Wetzlar, Germany). SEM analysis was conducted with a Desktop SEM (Phenom XL, Phenom-World BV, Eindhoven, the Netherlands) with acceleration voltages of 10 kV.

Fluorescence Staining: Fixed samples containing fluorescently labeled Annexin-V were blocked with BSA (3% in PBS) for 45 min at room temperature and incubated with mouse anti-P-selectin monoclonal antibody

(1:100 in 3% PBS; Abcam Ltd, Cambridge, UK) overnight at 4 °C. Unbound antibody was washed off and samples were incubated with goat anti-mouse Alexa Fluor 647 (1:100; Fisher Scientific) and Alexa Fluor 488 Phalloidin (1:40; F-actin stain; Thermo Fisher Scientific) for 2 h at room temperature. Samples containing ATTO647N-NHS pre-stained scaffolds were permeabilized with 0.5% Triton X-100 for 5 min, incubated with Alexa Fluor 488 Phalloidin (1:40; F-actin stain; Thermo Fisher Scientific) for 2 h at room temperature, washed three times in PBS for 5 min, and mounted in Mowiol® 4-88 containing 1,4-Diazabicyclo 2.2.2 octane (DABCO; 4%; Sigma-Aldrich) on glass object slides. Samples of washed platelets for morphological analysis were permeabilized with 0.5% Triton X-100 for 15 min, blocked with 3% BSA in PBS for 45 min at room temperature and incubated with mouse anti-vinculin monoclonal antibody (1:100; Sigma-Aldrich) overnight at 4 °C. Unbound antibody was washed off and samples were incubated with goat anti-mouse Alexa Fluor 546 (1:100; Fisher Scientific) and Alexa Fluor 488 Phalloidin (1:40) for 2 h at room temperature. All samples were washed three times and mounted as described above.

Confocal Microscopy: Samples were imaged on two confocal microscopes. Data for Figures 1, 2, 3, and 4a,g–j were imaged with a 40x Plan-Apochromat oil objective lens on an Examiner Z1 confocal microscope (Zeiss, Oberkochen, Germany) with 70 nm pixel size in *xy* and 0.3 μm steps for *z*-stacks, which was increased to 280 nm in *xy* and 1 μm in *z* for P-selectin and PS stainings on nanofibrous scaffolds to avoid bleaching. The pinhole was set to 1 Airy unit and laser intensity was adjusted to exploit the full dynamic range. Data for Figures 4b,d and 5 were imaged on a Stellaris confocal microscope (Leica, Mannheim, Germany) using excitation lines at 488, 561, and 638 nm of a white light laser and a 100x oil immersion objective (HC PL APO CS2, 1.40 NA). *Z*-stacks for Figures 4b and 5 were acquired with 178 nm pixel size and 1 μm step size in *z*. *Z*-stacks for Figure 4d were acquired with 46 nm pixel size and 124 nm step size in *z* and further processed by adaptive deconvolution (Lightning; Leica).

Image Analysis: A morphometric analysis of the platelet actin cytoskeleton was performed as previously described.^[49] Briefly, platelet actin images were used to segment individual platelets and single platelet parameters (spreading area, circularity, F-actin alignment, and vinculin adhesion morphology) were calculated. Single platelet P-selectin and Annexin-V stainings were categorized in a blinded fashion as either negative or positive by three independent individuals to achieve an unbiased quantification of the data. For the analysis of effective surface area of the nanofiber scaffolds (Figure 4d,e), deconvolved stacks were upsampled 5x in the *z*-direction and an argmax *z*-projection was performed using the CLIJ2 plugin in Fiji.^[80] From these digital height maps, the calculation of the surface area per pixel was performed according to a published procedure^[52] and implemented in a custom MATLAB (Mathworks) script.

Flow Assay and Analysis: Whole blood samples were stained with 3,3'-dihexyloxacarbocyanine iodide (1×10^{-3} M; DiOC₆) for 5 min before connecting via a ca. 10 cm long tubing to the flow chamber. Flow was driven through the flow chamber by suction using a 10 mL glass syringe (Micro-mate) using a syringe pump (PHD 2000, Harvard apparatus). The flow rate was adapted to achieve the desired shear rate of 50 s⁻¹ (or higher, as indicated) at the bottom of the rectangular channel. The chambers were mounted on the stage of an inverted epifluorescence microscope (Nikon Eclipse Ti2) in an incubation chamber (Okolab) at 37 °C. Illumination around 470 nm (CoolLED) was used together with a green fluorescence protein (GFP) filter set and a 525/50 bandpass emission filter. The bottom of chambers was prefocused using the fluorescently marked spot on the scaffold before turning on the perfect focus system and moving ca. 3–5 mm upstream. This pre-focussing allowed acquisitions to be started within 3–6 s after the blood entered the channel. Images were acquired on an sCMOS camera (Orca Fusion BT; Hamamatsu) at 2 frames s⁻¹ at 15x magnification (pixel size 0.653 μm) for 9 min. Movies were processed using an anisotropic 3D median filter in ImageJ to remove fluorescence of fast-moving labeled platelets in the blood stream. 2D kymographs were obtained from filtered movies by a maximum intensity projection in the transverse direction and postfiltering by an anisotropic 2D median filter before a background subtraction. To measure fluorescence intensity of platelet accumulation on scaffolds over time, the filtered movies were resized 0.25-fold to speed up processing and then a 3D median-filtered

background movie was subtracted to remove the increasing background fluorescence which occurred due to DiOC₆ binding to the scaffolds, before measuring the mean intensity of each frame. Mean and standard deviation of experimental replicates were determined over a 40 s moving window before rescaling the standard deviation by the square root of the replicate number to obtain mean \pm s.e.m. (cf. Figure 6e).

Statistical Analysis: Continuous variables are expressed as mean \pm s.e.m. Mean values from different replicates were treated as normally distributed with equal variances. Paired *t*-tests were used to determine differences between two conditions. One-way analysis of variance (ANOVA) was used to determine differences between three or more experimental conditions, followed by Tukey's post hoc test for multiple comparisons. The significance level was set at $p \leq 0.05$. Results below this value were considered statistically significant. All analyses were conducted using GraphPad Prism (version 8.0.0). Violin SuperPlots were generated using the MATLAB implementation from the respective publication.^[51]

Supporting Information

Supporting Information is available from the Wiley Online Library or from the author.

Acknowledgements

The authors would like to thank Thomas Lukaszczuk (Fraunhofer IFAM) for access to the SEM device. The authors gratefully acknowledge the super-resolution image consortium (SRIC) at the Royal College of Surgeons in Ireland for equipment access and technical expertise. D.B. gratefully acknowledges funding by the Emmy Noether program of the German Research Foundation (DFG) via grant number 267326782. St.S. was financially supported by the internal program Fraunhofer TALENTA start. This work was further supported by RCSI under a StAR lecturership and through the MPharm student-selected projectP scheme (I.S.).

Open access funding provided by IReL.

Conflict of Interest

The authors declare no conflict of interest.

Data Availability Statement

The data that support the findings of this study are available from the corresponding author upon reasonable request.

Keywords

hemocompatibility, platelet-rich plasma, self-assembly, thrombogenicity, wound healing

Received: January 29, 2022

Revised: April 5, 2022

Published online:

[1] M. B. Dreifke, A. A. Jayasuriya, A. C. Jayasuriya, *Mater. Sci. Eng., C* **2015**, *48*, 651.

[2] I. Kalashnikova, S. Das, S. Seal, *Nanomedicine* **2015**, *10*, 2593.

[3] M. Parani, G. Lokhande, A. Singh, A. K. Gaharwar, *ACS Appl. Mater. Interfaces* **2016**, *8*, 10049.

- [4] N. K. Rajendran, S. S. D. Kumar, N. N. Houreld, H. Abrahamse, *J. Drug Delivery Sci. Technol.* **2018**, *44*, 421.
- [5] M. Weber, H. Steinle, S. Golombek, L. Hann, C. Schlensak, H. P. Wendel, M. Avci-Adali, *Front. Bioeng. Biotechnol.* **2018**, *6*, 99.
- [6] J. L. Brash, T. A. Horbett, R. A. Latour, P. Tengvall, *Acta Biomater.* **2019**, *94*, 11.
- [7] M. Gorbet, C. Sperling, M. F. Maitz, C. A. Siedlecki, C. Werner, M. V. Sefton, *Acta Biomater.* **2019**, *94*, 25.
- [8] P. E. J. van der Meijden, J. W. M. Heemskerk, *Nat. Rev. Cardiol.* **2019**, *16*, 166.
- [9] M. W. Mosesson, *J. Thromb. Haemostasis* **2005**, *3*, 1896.
- [10] J. M. Reinke, H. Sorg, *Eur. Surg. Res.* **2012**, *49*, 35.
- [11] M. Rodrigues, N. Kosaric, C. A. Bonham, G. C. Gurtner, *Physiol. Rev.* **2019**, *99*, 665.
- [12] T. N. Durrant, M. T. Van Den Bosch, I. Hers, *Blood* **2017**, *130*, 1607.
- [13] B. Savage, S. J. Shattil, Z. M. Ruggeri, *J. Biol. Chem.* **1992**, *267*, 11300.
- [14] M. Jirouskova, J. K. Jaiswal, B. S. Collier, *Blood* **2007**, *109*, 5260.
- [15] Y. Qiu, A. C. Brown, D. R. Myers, Y. Sakurai, R. G. Mannino, R. Tran, B. Ahn, E. T. Hardy, M. F. Kee, S. Kumar, G. Bao, T. H. Barker, W. Lam, *Proc. Natl. Acad. Sci. USA* **2014**, *111*, 14430.
- [16] C. E. Hansen, Y. Qiu, O. J. T. McCarty, W. A. Lam, *Annu. Rev. Biomed. Eng.* **2018**, *20*, 253.
- [17] P. H. Mangin, M.-B. Onseleer, N. Receveur, N. Le Lay, A. T. Hardy, C. Wilson, X. Sanchez, S. Loyau, A. Dupuis, A. K. Babar, J. L. C. Miller, H. Philippou, E. Craig, A. B. Herr, R. A. S. Ariens, D. Mezzano, *Haematologica* **2018**, *103*, 898.
- [18] O. V. Kim, R. I. Litvinov, M. S. Alber, J. W. Weisel, *Nat. Commun.* **2017**, *8*, 1274.
- [19] S. M. Schoenwaelder, Y. Yuan, E. C. Josefsson, M. J. White, Y. Yao, K. D. Mason, L. A. O'Reilly, K. J. Henley, A. Ono, S. Hsiao, A. Willcox, A. W. Roverts, D. C. S. Huang, H. H. Salem, B. T. Kile, S. P. Jackson, *Blood* **2009**, *114*, 663.
- [20] E. M. Golebiewska, A. W. Poole, *Blood Rev.* **2015**, *29*, 153.
- [21] A. T. Nurden, P. Nurden, M. Sanchez, I. Andia, E. Anitua, *Front. Biosci.* **2008**, *13*, 3532.
- [22] P. W. Kämmerer, M. Gabriel, B. Al-Nawas, T. Scholz, C. M. Kirchmaier, M. O. Klein, *Clin. Oral Implants Res.* **2012**, *23*, 504.
- [23] J. Y. Park, C. H. Gemmell, J. E. Davies, *Biomaterials* **2001**, *22*, 2671.
- [24] L. Kikuchi, J. Y. Park, C. Victor, J. E. Davies, *Biomaterials* **2005**, *26*, 5285.
- [25] V. Milleret, S. Tugulu, F. Schlottig, H. Hall, *Eur. Cells Mater.* **2011**, *21*, 430.
- [26] R. Sandmann, S. Köster, *Sci. Rep.* **2016**, *6*, 22357.
- [27] R. Sandmann, S. S. G. Henriques, F. Rehfeldt, S. Köster, *Soft Matter* **2014**, *10*, 2365.
- [28] F. M. Shaikh, A. Callanan, E. G. Kavanagh, P. E. Burke, P. A. Grace, T. M. McGloughlin, *Cells Tissues Organs* **2008**, *188*, 333.
- [29] L. Frost-Arner, W. D. Spotnitz, G. T. Rodeheaver, D. B. Drake, *Plast. Reconstr. Surg.* **2001**, *108*, 1655.
- [30] O. Kaplan, T. Hierlemann, S. Krajewski, J. Kurz, M. Nevorolová, M. Houska, T. Riedel, Z. Riedelová, J. Zárubová, H. P. Wendel, et al., *J. Biomed. Mater. Res., Part A* **2017**, *105*, 2995.
- [31] T. Rajangam, S. S. A. An, *Int. J. Nanomed.* **2013**, *8*, 3641.
- [32] G. E. Wnek, M. E. Carr, D. G. Simpson, G. L. Bowlin, *Nano Lett.* **2003**, *3*, 213.
- [33] M. Raoufi, N. Aslankoochi, C. Mollenhauer, H. Boehm, J. P. Spatz, D. Brüggemann, *Integr. Biol.* **2016**, *8*, 1059.
- [34] S. Stamboroski, A. Joshi, P.-L. M. Noeske, S. Köppen, D. Brüggemann, *Macromol. Biosci.* **2021**, *21*, 2000412.
- [35] T. T. Yuan, A. M. DiGeorge Foushee, M. C. Johnson, A. R. Jockheck-Clark, J. M. Stahl, *Nanoscale Res. Lett.* **2018**, *13*, 88.
- [36] M. C. McManus, E. D. Boland, D. G. Simpson, C. P. Barnes, G. L. Bowlin, *J. Biomed. Mater. Res., Part A* **2007**, *81A*, 299.
- [37] S. A. Sell, M. P. Francis, K. Garg, M. J. McClure, D. G. Simpson, G. L. Bowlin, *Biomed. Mater.* **2008**, *3*, 045001.
- [38] D. Gugutkov, J. Gustavsson, M. P. Ginebra, G. Altankov, *Biomater. Sci.* **2013**, *1*, 1065.
- [39] M. McManus, E. Boland, S. Sell, W. Bowen, H. Koo, D. Simpson, G. Bowlin, *Biomed. Mater.* **2007**, *2*, 257.
- [40] J. Forget, F. Awaja, D. Gugutkov, J. Gustavsson, G. Gallego Ferrer, T. Coelho-Sampaio, C. Hochman-Mendez, M. Salmerón-Sánchez, G. Altankov, M. Salmeron-Sánchez, G. Altankov, *Macromol. Biosci.* **2016**, *16*, 1348.
- [41] S. Nedjari, F. Awaja, G. Altankov, *Sci. Rep.* **2017**, *7*, 15947.
- [42] R. N. Palchesko, Y. Sun, L. Zhang, J. M. Szymanski, Q. Jallerat, A. W. Feinberg, in *Springer Handbook of Nanomaterials*, Springer, Berlin, Heidelberg **2013**.
- [43] K. Stapelfeldt, S. Stamboroski, P. Mednikova, D. Brüggemann, *Bio-fabrication* **2019**, *11*, 025010.
- [44] K. Stapelfeldt, S. Stamboroski, I. Walter, N. Suter, T. Kowalik, M. Michaelis, D. Brüggemann, *Nano Lett.* **2019**, *19*, 6554.
- [45] N. Suter, A. Joshi, T. Wunsch, N. Graupner, K. Stapelfeldt, M. Radmacher, J. Müssig, D. Brüggemann, *Mater. Sci. Eng., C* **2021**, *126*, 112156.
- [46] C. B. Herbert, C. Nagaswami, G. D. Bittner, J. A. Hubbell, J. W. Weisel, *J. Biomed. Mater. Res.* **1998**, *40*, 551.
- [47] S. L. Rowe, S. Y. Lee, J. P. Stegemann, *Acta Biomater.* **2007**, *3*, 59.
- [48] L. Nicolai, K. Schiefelbein, S. Lipsky, A. Leunig, M. Hoffknecht, K. Pekayvaz, B. Raude, C. Marx, A. Ehrlich, J. Pircher, Z. Zhang, I. Saleh, A. K. Marel, A. Löf, T. Petzold, M. Lorenz, K. Stark, R. Pick, G. Rosenberger, L. Weckbach, B. Uhl, S. Xia, C. A. Reichel, B. Walzog, C. Schulz, V. Zheden, M. Bender, R. Li, S. Massberg, F. Gaertner, *Nat. Commun.* **2020**, *11*, 5778.
- [49] S. Lickert, S. Sorrentino, J. D. Studt, O. Medalia, V. Vogel, I. Schoen, *Sci. Rep.* **2018**, *8*, 5428.
- [50] P. Atherton, B. Stutchbury, D. Jethwa, C. Ballestrom, *Exp. Cell Res.* **2016**, *343*, 21.
- [51] M. Kenny, I. Schoen, *Mol. Biol. Cell* **2021**, *32*, 1333.
- [52] J. S. Jenness, *Wildl. Soc. Bull.* **2004**, *32*, 829.
- [53] S. Feghhi, A. D. Munday, W. W. Tooley, S. Rajsekar, A. M. Fura, J. D. Kulman, J. A. López, N. J. Sniadecki, *Biophys. J.* **2016**, *111*, 601.
- [54] S. Lickert, K. Selcuk, M. Kenny, J. L. Mehl, M. Bender, S. M. Früh, M. A. Burkhardt, J. D. Studt, B. Nieswandt, I. Schoen, V. Vogel, *Sci. Adv.* **2022**, *8*, eabj8331.
- [55] A. Veninga, C. C. F. M. J. Baaten, I. De Simone, B. M. E. Tullemans, M. J. E. Kuijpers, J. W. M. Heemskerk, P. E. J. van der Meijden, *Thromb. Haemostasis* **2021**, Online ahead of print, <https://doi.org/10.1055/s-0041-1735972>.
- [56] S. C. Endenburg, L. Lindeboom-Blokzijl, J. J. Zwaginga, J. J. Sixma, P. G. de Groot, *Arterioscler. Thromb. Vasc. Biol.* **1996**, *16*, 633.
- [57] L. B. Koh, I. Rodriguez, S. S. Venkatraman, *Biomaterials* **2010**, *31*, 1533.
- [58] N. Ferraz, B. Nilsson, J. Hong, M. K. Ott, *J. Biomed. Mater. Res., Part A* **2008**, *87*, 575.
- [59] Y. Sang, M. Roest, B. de Laat, P. G. de Groot, D. Huskens, *Blood Rev.* **2021**, *46*, 100733.
- [60] M. Samuel, R. A. Pixley, M. A. Villanueva, R. W. Colman, G. B. Villanueva, *J. Biol. Chem.* **1992**, *267*, 19691.
- [61] N. J. Kent, L. Basabe-Desmonts, G. Maede, B. D. MacCraith, B. G. Corcoran, D. Kenny, A. J. Ricco, *Biomed. Microdevices* **2010**, *12*, 987.
- [62] A. Bonnefoy, Q. Liu, C. Legrand, M. M. Frojmovic, *Biophys. J.* **2000**, *78*, 2834.
- [63] B. Savage, E. Saldívar, Z. M. Ruggeri, *Cell* **1996**, *84*, 289.
- [64] H. Chen, W. Song, F. Zhou, Z. Wu, H. Huang, J. Zhang, Q. Lin, B. Yang, *Colloids Surf., B* **2009**, *71*, 275.
- [65] D. Altschuler, E. G. Lapetina, *J. Biol. Chem.* **1993**, *268*, 7527.

- [66] M. Eigenthaler, H. Ullrich, J. Geiger, K. Horstrup, P. Honig-Liedl, D. Wiebecke, U. Walter, *J. Biol. Chem.* **1993**, *268*, 13526.
- [67] D. Y. Nechipurenko, N. Receveur, A. O. Yakimenko, T. O. Shepelyuk, A. A. Yakusheva, R. R. Kerimov, S. I. Obydenny, A. Eckly, C. Léon, C. Gachet, E. L. Brishchuk, F. I. Ataulakhanov, P. H. Mangin, M. A. Panteleev, *Arterioscler. Thromb. Vasc. Biol.* **2019**, *39*, 37.
- [68] Y. Zhang, Y. Qiu, A. T. Blanchard, Y. Chang, J. M. Brockman, V. P.-Y. Ma, W. A. Lam, K. Salaita, *Proc. Natl. Acad. Sci. USA* **2018**, *115*, 325.
- [69] E. O. Agbani, M. T. J. Van Den Bosch, E. Brown, C. M. Williams, N. J. A. Mattheij, J. M. E. M. Cosemans, P. W. Collins, J. W. M. Heemskerk, I. Hers, A. W. Poole, *Circulation* **2015**, *132*, 1414.
- [70] N. Ferraz, J. Hong, M. Karlsson Ott, *J. Biomater. Appl.* **2010**, *24*, 675.
- [71] M. Ahmed, H. Ghanbari, B. G. Cousins, G. Hamilton, A. M. Seifalian, *Acta Biomater.* **2011**, *7*, 3857.
- [72] I. Firkowska-Boden, K. D. Jandt, C. Helbing, T. J. Dauben, M. Pieper, *Langmuir* **2020**, *36*, 11573.
- [73] L. Zhang, B. Casey, D. K. Galanakis, C. Marmorat, S. Skoog, K. Vorvolakos, M. Simon, M. H. Rafailovich, *Acta Biomater.* **2017**, *54*, 164.
- [74] L. Buitrago, S. Lefkowitz, O. Bentur, J. Padovan, B. Collier, *Blood Adv.* **2021**, *5*, 3986.
- [75] L. Chen, D. Han, L. Jiang, *Colloids Surf., B* **2011**, *85*, 2.
- [76] N. Ferraz, J. Carlsson, J. Hong, M. K. Ott, *J. Mater. Sci.: Mater. Med.* **2008**, *19*, 3115.
- [77] A. Elozegui-Artola, R. Oria, Y. Chen, A. Kosmalska, C. Pérez-González, N. Castro, C. Zhu, X. Trepate, P. Roca-Cusachs, *Nat. Cell Biol.* **2016**, *18*, 540.
- [78] J. Albuschies, V. Vogel, *Sci. Rep.* **2013**, *3*, 1658.
- [79] R. J. F. C. do Amaral, N. M. A. Zayed, E. I. Pascu, B. Cavanagh, C. Hobbs, F. Santarella, C. R. Simpson, C. M. Murphy, R. Sridharan, A. González-Vázquez, et al., *Front. Bioeng. Biotechnol.* **2019**, *7*, 371.
- [80] J. Schindelin, I. Arganda-Carreras, E. Frise, V. Kaynig, M. Longair, T. Pietzsch, S. Preibisch, C. Rueden, S. Saalfeld, B. Schmid, J.-Y. Tinevez, D. J. White, V. Hartenstein, K. Eliceiri, P. Tomancak, A. Cardona, *Nat. Methods* **2012**, *9*, 676.

WILEY-VCH

Supporting Information

Nanofiber topographies enhance platelet-fibrinogen scaffold interactions

Martin Kenny, Stephani Stamboroski, Reem Taher, Dorothea Brüggemann, Ingmar Schoen**

Supplementary Figures

| | |
|--|--------|
| Figure S1. Immunostainings of fibrinogen scaffolds. | Page 3 |
| Figure S2. Interactions of platelet-rich plasma (PRP) with fibrinogen scaffolds. | Page 4 |
| Figure S3. Interactions of washed platelets with fibrinogen scaffolds. | Page 5 |
| Figure S4. Modulation of platelet adhesion by plasma components. | Page 6 |
| Figure S5. Inhibition of thrombin-induced platelet aggregation by hirudin. | Page 7 |
| Figure S6. Interactions of platelets in whole blood with different surfaces. | Page 8 |

WILEY-VCH

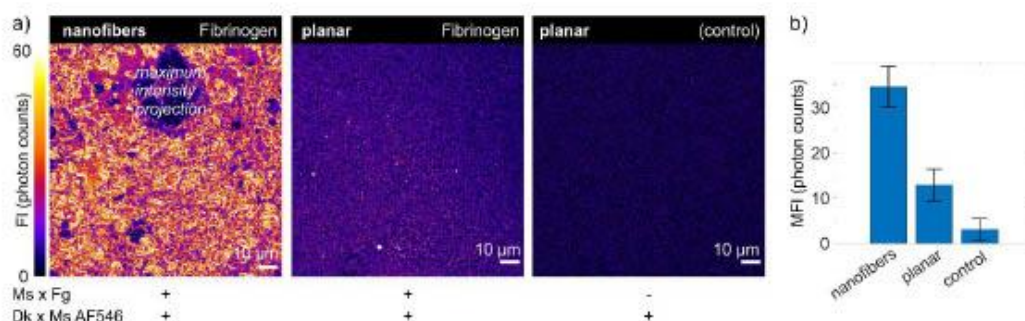


Figure S1. Immunostainings of fibrinogen scaffolds. Fibrinogen samples were prepared as described under materials and methods. To verify the presence of fibrinogen, samples were incubated with mouse anti-fibrinogen antibodies (Sigma F9902; 1:200 dilution in PBS containing 0.02% Tween-20) for 4 hours, washed 3x in PBS, incubated with donkey anti-mouse IgG (Alexa546 conjugate, Jackson ImmunoResearch, 1:100 dilution in PBS containing 0.02% Tween-20) for 2 hours, washed 3x in PBS, and mounted in MOWIOL. As a control, a planar substrate was processed without the addition of primary antibodies. Fluorescence images were obtained on a confocal microscope (Leica Stellaris) using a 100x oil immersion objective (NA 1.46) under identical settings (2% excitation at 488 nm, emission window 498-550 nm, HyD X detector in photon counting mode, 1x magnification, 4x line accumulation). (a) Representative images of fluorescence intensity (FI) of fibrinogen nanofibers (left) and planar fibrinogen films (middle and right) showed specific staining for fibrinogen. (b) Quantification of mean fluorescence intensity (MFI) from 5 images per condition showed ~2.5x stronger antibody stainings on nanofibers as compared to planar scaffolds, indicating a higher accessibility of fibrinogen epitopes on nanofibers.

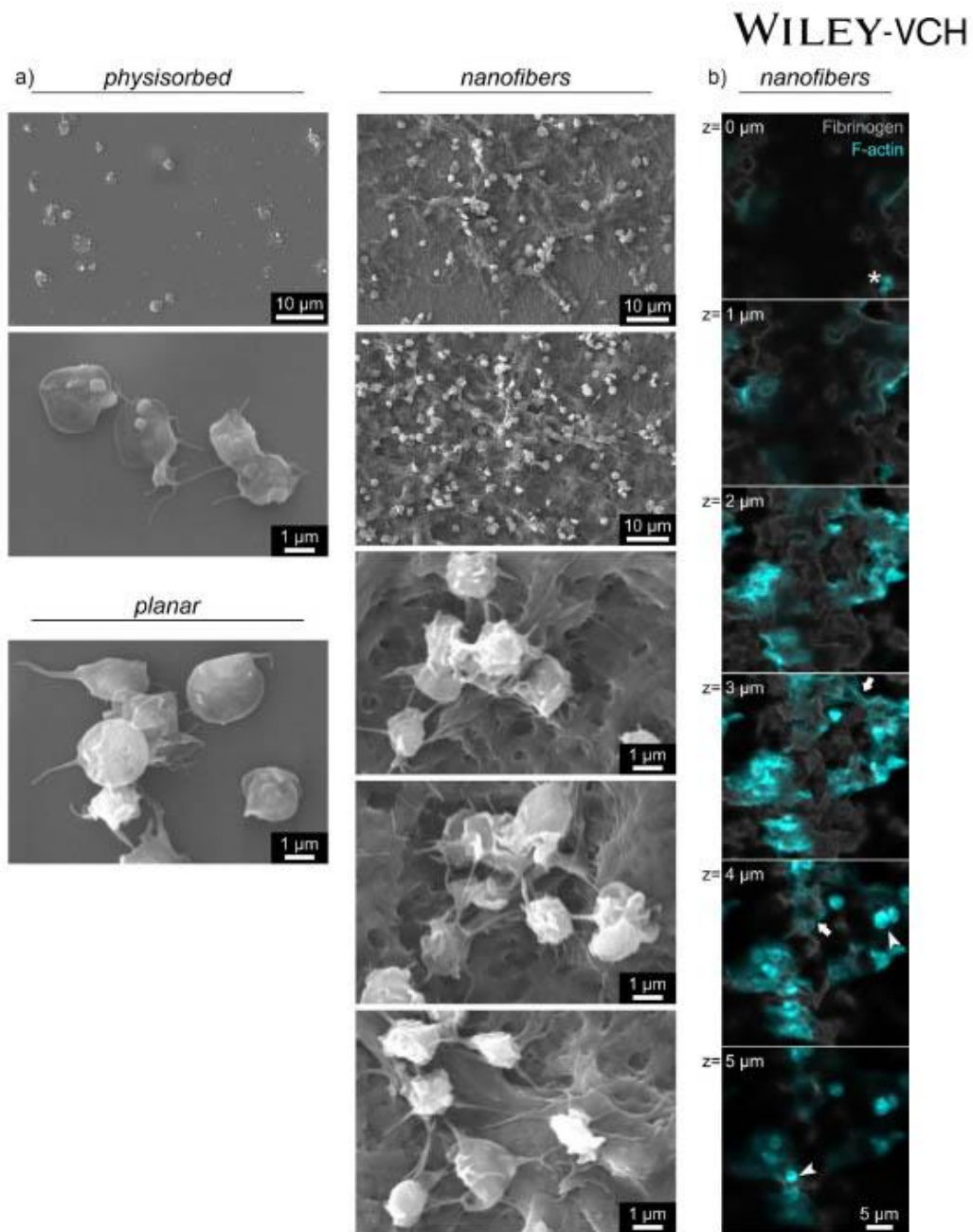


Figure S2. Interactions of platelet-rich plasma (PRP) with fibrinogen scaffolds. (a) Further examples of SEM images on physisorbed, planar, or nanofibrous fibrinogen. (b) Confocal z-stack from 0...6 μm of the F-actin cytoskeleton in platelets (cyan) on nanofibrous fibrinogen (gray). Symbols indicate: asterisk – single platelet spanning hole between two sides; arrow – stress fibers of platelets bridging a larger gap; arrowhead: rounded non-activated platelets on top of small platelet aggregates.

WILEY-VCH

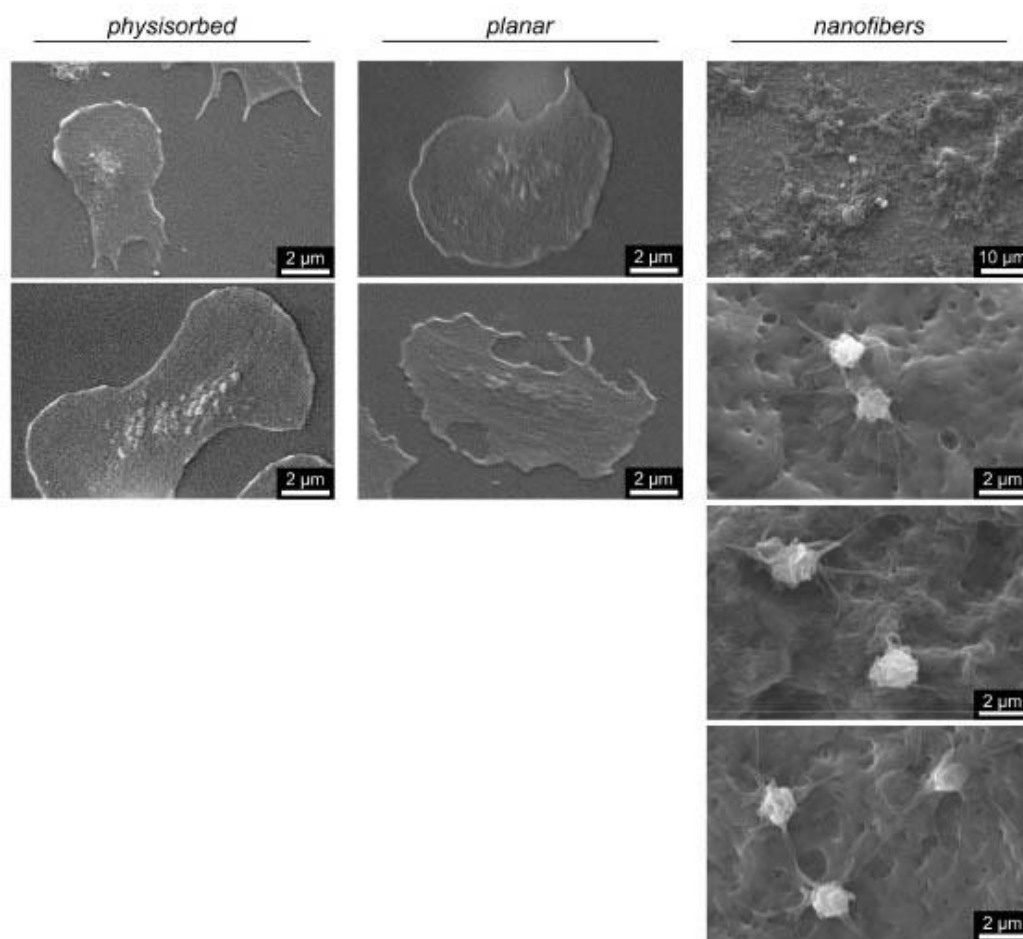


Figure S3. Interactions of washed platelets with fibrinogen scaffolds. Further examples of SEM images on physisorbed, planar, or nanofibrous fibrinogen.

WILEY-VCH

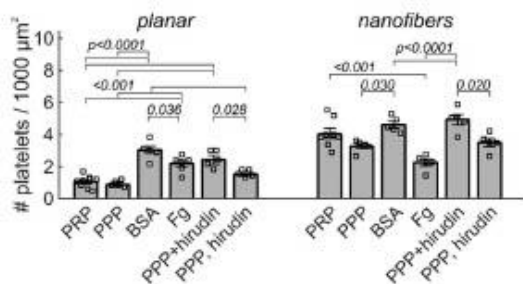


Figure S4. Modulation of platelet adhesion by plasma components. Experiments were performed as described in Figure 5. Bars and error bars show mean and s.e.m. of replicates, respectively. Differences between treatments on the same topography were assessed by one-way ANOVA with Tukey post-hoc multiple comparison. Only adjusted p -values smaller than 0.05 are displayed.

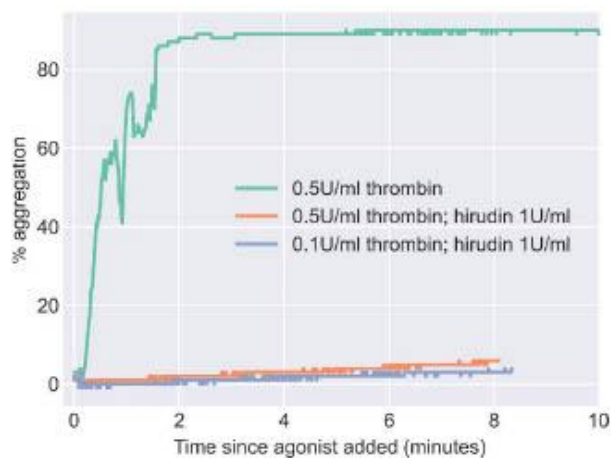


Figure S5. Inhibition of thrombin-induced platelet aggregation by hirudin. Light transmission aggregometry (LTA) was performed with washed platelets supplemented with 0.5 mg ml⁻¹ fibrinogen. Platelet aggregation was induced by addition of thrombin (0.5 U ml⁻¹). In the presence of the thrombin inhibitor hirudin (1 U ml⁻¹), the aggregation response to thrombin was abolished.

WILEY-VCH

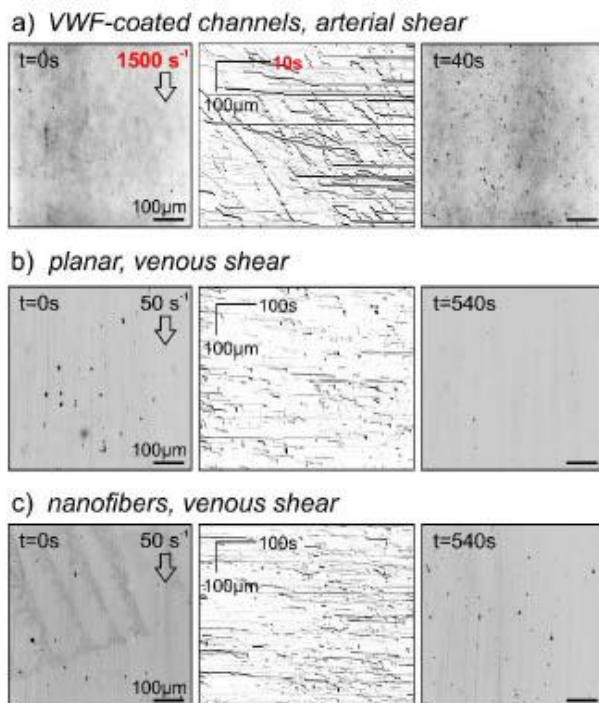


Figure S6. Interactions of platelets in whole blood with different surface. Whole blood was flown over (a) vWF-coated surface at a shear rate of 1500 s⁻¹ or over (b) planar or (c) nanofiber scaffolds at a shear rate of 50 s⁻¹. Platelets were visualized by the fluorescent DiOC₆ membrane stain in epifluorescence at 25 frames per second (a) or 2 frames per second (b+c). Shown are kymographs (*center*) with start and end frames (*left & right*). Note the different time scaling on the kymographs between (a) and (b+c).

7. SUMMARIZING DISCUSSION & FUTURE PERSPECTIVES

The involvement of fibrinogen in many key biological functions as the blood coagulation cascade makes it widely used in the development of new biological materials for tissue engineering and regeneration. The thrombin-induced transformation of fibrinogen into fibrin, initiating the formation of a 3D-nanofibrous matrix that serves as a provisional ECM, has been investigated many times in laboratories around the world.

In existing literature, fibrinogen fiber formation *in vitro* without the addition of thrombin has also been studied, and different methods to form fibrin-like networks of fibrinogen have been developed to date. However, the underlying principles of salt-induced fibrinogen fiber formation *in vitro* and a general mechanism for this phenomenon are still to be elucidated. In this thesis, four studies were conducted to understand the fibrinogen-salt interactions during fibrinogen self-assembly under *in vitro* conditions and to bring new insights into the driving mechanism of fibrinogen fiber formation under non-denaturing conditions. An additional study aiming to demonstrate the application of fibrous fibrinogen formed from highly saline solutions as a scaffold biomaterial was also presented. A schematic representation with the main findings of all thesis chapters is presented in Figure 7-1.

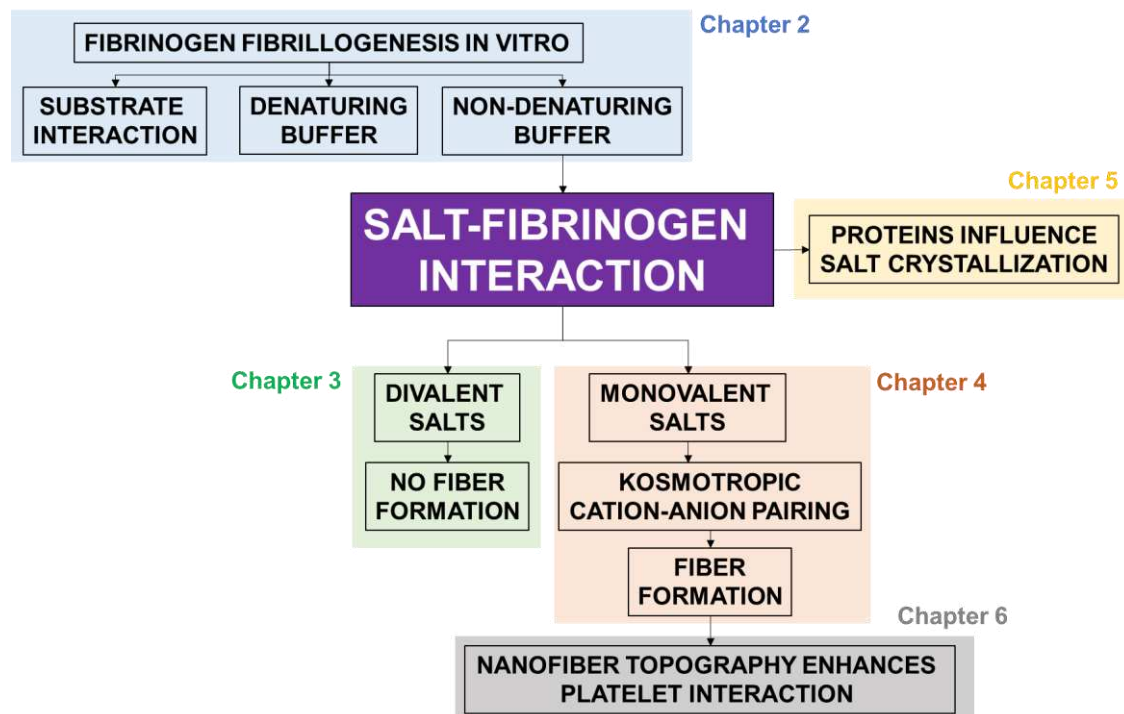


Figure 7-1: Schematic representation of the main findings from this PhD thesis according to their Chapters

The main objective of understanding the molecular interactions of fibrinogen with salt ions under *in vitro* conditions to produce salt-induced fibrinogen nanofibers was evaluated in a literature review in combination with experimental studies. The first study (Chapter 2) intended to determine which are the major factors influencing fibrinogen fiber formation and whether there is a predominant factor in fibrinogen self-assembly *in vitro*. There are many experimental conditions and parameters found to influence fibrinogen self-assembly. The main factors were divided into three main categories:

- substrate interaction;
- denaturing buffer conditions;
- non-denaturing buffer conditions.

Among those, the importance of salts in the non-denaturing buffers category can be highlighted. Salts are important factors to dissolve fibrinogen and are always present in many of the techniques used to prepare fibrinogen fibers. The evaluation made in the review showed that monovalent metal ions play a major role when fibrinogen fibers assemble upon drying. Nonetheless, the particular role of divalent ions in comparison to monovalent ions is also of fundamental importance to be investigated, since they are all involved in many biological processes.

Therefore, the second study (Chapter 3) focused on the influence of metal divalent ions into fibrinogen precipitation and fiber formation. Divalent ions mediate various biological reactions and are therefore essential to the body function. Calcium ions, for instance, are involved at the initial stage of clot formation and therefore it was believed that calcium and other divalent ions could also mediate fibrinogen self-assembly *in vitro*. On the contrary of what was expected, none of the divalent salts tested containing Ca^{2+} , Mg^{2+} , Zn^{2+} or Cu^{2+} ions formed fibrous fibrinogen layers. In summary, this second study reinforced the conclusion drawn from the review in Chapter 2, that monovalent ions are especially important for the assembly of fibrinogen fibers.

Thus, the influence of different monovalent cations in combination with different anions was investigated in the third study of this PhD thesis (Chapter 4). Similarly to divalent ions, monovalent ions are also key electrolytes to maintain well-balanced body functions. A diversity of monovalent salts was tested in their capacity of forming fibrous fibrinogen layers. Depending on the combination between cation and anion, various fibrinogen morphologies, consequently resulting in varying topographies, could be observed. Additionally, a direct correlation between

the surface composition of the fibrinogen layers after washing and removing salt crystals and the formed morphologies could be drawn. Hofmeister effects and protein-salt interactions were taken into account to explain the different fibrinogen layers obtained.

Up to now, it was shown how different salts affect fibrinogen morphology. However, protein-salt interaction is a reciprocal interaction. Salts influence fibrinogen as much as fibrinogen influences the surrounding salts. For this reason, the fourth study (Chapter 5) focused on investigating how fibrinogen and, for comparison, other proteins influence the precipitation and morphology of sodium chloride crystals. The examination of the change in crystal shape of the salt depending on the added protein showed how important and complex this dual interaction between proteins and salts is.

The fifth and final study of this thesis (Chapter 6), is related to the response of blood platelets to different fibrinogen topographies. Here, it is shown that increased topography by, for instance, fiber formation, activates blood platelets more prominently than smooth fibrinogen layers. The study on how blood platelets interact with fibrinogen nanofibers formed from highly saline solutions opens up the opportunity to employ self-assembled fibrinogen nanofibers for tissue engineering and wound healing applications.

The next sections present a summary discussion and the correlation between the chapters presented in this thesis.

7.1. IN VITRO FIBRILLOGENESIS OF FIBRINOGEN

7.1.1. Main factors contributing to fibrinogen fibrillogenesis in vitro

Protein nanofibers have been long studied as a strategy to mimic the microenvironment of the ECM and therefore as a possible solution for the development of tissue engineering scaffolds and wound repair (Barnes et al., 2007). Fibrinogen especially is a protein circulating in blood of all vertebrates and closely involved in the blood coagulation cascade and other biological functions (Weisel, 2005; Weisel & Litvinov, 2017) as presented in Chapter 1. Additionally, fibrinogen molecules possess important binding sites for cell adhesion (Weisel, 2005) and are able to form fibers even without the addition of thrombin (as presented in the review paper in Chapter 2). In this way, fibrinogen nanofibers combine two essential characteristics for a scaffold: biochemical cues for normal cell growth and differentiation and a three-dimensional orientation and space for the cells (Barnes et al., 2007; Rajangam & An, 2013). Similarly to a fibrin clot formed *in vivo* (described in detail in Chapter 2, Section 2.3), fibrinogen nanofibers

formed *in vitro* can act as a provisional ECM to cells and support cell growth and tissue regeneration.

Diverse strategies to produce fibrinogen nanofibers were presented in Chapter 1, Section 1.6. Among them, undoubtedly electrospinning is the most used technique since it allows high nanofiber yield for the production of 3D-fibrous matrices (McManus et al., 2006; S. A. Sell et al., 2008; Wnek et al., 2003). Other techniques as extrusion (Raoufi et al., 2016) and self-assembly (G. Chen et al., 2011; Jaseung Koo et al., 2012; Wei, Reichert, & Jandt, 2008) usually deliver comparably lower fiber yield, which can be used for surface coatings, however impeding the formation of 3D-scaffolds. Only recently, (Stapelfeldt, Stamboroski, Mednikova, et al., 2019) and (Hense et al., 2021) demonstrated the feasibility of self-assembly involving high salt concentrations to produce 3D fibrous scaffolds of fibrinogen.

Considering this variety of approaches used to prepare fibrinogen nanofibers under *in vitro* conditions, it is clear that many factors can trigger fiber formation. The literature analyzed and compared in the review paper (Chapter 2) showed how scattered the available data on this topic are. Various conditions were found to induce intermolecular interaction of fibrinogen in an enzyme- and cell-free environment (Stamboroski, Joshi, et al., 2021). Many studies focused on the role of the interaction between fibrinogen molecules and substrates to initiate fiber formation. The majority of substrates claimed to induce fibrinogen fibrillogenesis have a hydrophobic character. Table 1 of Chapter 2, Section 3.1, summarizes the properties of substrate surfaces and associated buffer conditions found to drive fibrinogen assembly and the respective fiber morphology (Stamboroski, Joshi, et al., 2021). Since fiber dimensions and morphology varied a lot among the different studies, the fiber morphology was categorized into protofibrils (small aggregates of fibrinogen molecules), single nanofibers, nanofiber bundles and nanofiber network (fibrin-like structure) as exemplified in Figure 5 of Chapter 2.

In Table 2, Chapter 2 the studies of fibrinogen fiber formation that focus on the role of buffers for fiber formation were gathered and separated between denaturing and non-denaturing buffer conditions. The substrates used for those studies are also mentioned and interestingly many fibers were assembled in the presence of hydrophilic surfaces. Since it is not possible to decipher the role of other parameters as ionic strength, presence of metals, pH and fibrinogen concentration, it is also likely that factors other than surface interaction play a major role, allowing fibrinogen fiber formation also on hydrophilic substrates.

When it comes to buffer conditions that are able to induce fibrinogen fibers self-assembly, most of the literature available uses denaturing buffers conditions as organic solvents, low pH and/or

heating to induce protein aggregation. The use of organic solvents is often used for preparation of fibers *via* electrospinning. However, the use of ethanol has also been used to produce insoluble fibrinogen fibers only by mixing fibrinogen solution with different percentage of ethanol (J. Wang et al., 2014; Wei, Reichert, & Jandt, 2008). Similarly, self-assembly of fibrinogen could also be triggered by decreasing the pH of fibrinogen solutions (Rieu et al., 2020; Wei, Reichert, Bossert, et al., 2008) or elevating the temperature (Barinov et al., 2016). This strategy of using harsher conditions to prepare fibrinogen nanofibers relies on partial denaturation and changes on the conformation of the protein to initiate self-assembly. This is also used, for example, with many proteins to prepare amyloid fibers (Lendel & Solin, 2021) and in general does not promote a high yield of fibrinogen fiber formation (see example of fibers formed from acidic conditions in Figure 7 A-B, Chapter 2).

A good fiber yield with a fibrin-like structure is though possible to be achieved using non-denaturing buffer conditions (e.g. Figure 7 C-D, Chapter 2). 3D-fibrous fibrinogen layers were obtained when fibrinogen was mixed with highly concentrated PBS or sodium phosphate solutions at physiological pH (not exclusively) and room temperature (Stapelfeldt, Stamboroski, Mednikova, et al., 2019) or at lower concentrations of sodium phosphate buffer, but lower temperature (5°C) (Hense et al., 2021). Those fibers are formed independently from the underlying substrate, which shows that buffer conditions may be more relevant than surface interaction during fibrillogenesis of fibrinogen. Therefore, non-denaturing buffers offer a highly promising and cost-effective way to prepare fibrin or fibrin-like fibers *in vitro*, without the need for thrombin. In this way, the evaluation presented in the review paper confirms the first hypothesis showed in Section 1.8, that the presence of salt is one of the main factors for fibrinogen fibrillogenesis *in vitro* under non-denaturing conditions.

Overall, the results of the literature review in Chapter 2 showed that when the different studies used aqueous solution during fiber assembly, metal ions (mostly monovalent) were present. However, only the studies from Jandt and co-workers and Brüggemann and co-workers discussed a possible influence of the presence of those metal ions on fibrinogen self-assembly. Based on the evaluation of the Tables 1 and 2 presented in Chapter 2, most studies used pH values between 7 and 9, which are above the isoelectric point of fibrinogen, resulting in a more negatively charged character of the molecule.

Moreover, an increase in fibrinogen concentration was reported to increase fiber density in many of the works (Jaseung Koo et al., 2012; Reichert et al., 2009; Stapelfeldt, Stamboroski, Mednikova, et al., 2019; Wei, Reichert, Bossert, et al., 2008), showing to be also a parameter

that is key to fiber formation and growth. All those aforementioned parameters shall be considered and analyzed together in order to understand fibrinogen self-assembly. For this reason, Chapters 3, 4 and 5 focused on understanding the impact and interaction of different salts (and respective ions) with fibrinogen under *in vitro* conditions.

7.1.2. Fibrinogen precipitates prepared from highly saline solutions

After elucidating the main trigger factors for fibrinogen fiber formation under *in vitro* conditions, this thesis continued and expanded the work started by Stapelfeldt et al. on the self-assembly of fibrinogen *in vitro* induced by addition of highly saline solutions. The synthesis of fibrinogen nanofibers was based on salt-induced fibrinogen precipitation published earlier (Stapelfeldt, Stamboroski, Mednikova, et al., 2019; Stapelfeldt, Stamboroski, Walter, et al., 2019).

The fibrinogen layers presented in this thesis focused on a simple and straightforward technique of fibrinogen self-assembly triggered by non-denaturing buffer conditions, combining exactly the three factors showed in the upper left of Figure 8, Chapter 2: high ionic strength, drying and high fibrinogen concentration.

For Chapters 3, 4, 5 and 6, fibrinogen layers were prepared by mixing a fibrinogen solution with salt solutions. Figure 7-2 presents a sketch showing how the samples were prepared. First, fibrinogen stock solutions of 10 mg/ml were prepared by dissolving human fibrinogen powder in 10 mM Tris buffer (pH 7.4) and dialyzed overnight with 14 kDa cutoff cellulose membrane dialysis tubing. This step was performed to remove low molecular weight compounds as, for example, traces of sodium citrate that can influence fibrinogen fiber formation (see results of Figure 4C in Chapter 4 and (Hense et al., 2021)).

Different salt solutions (with varying concentrations) were prepared by dissolving salts in 10 mM Tris buffer (pH 7) or in ultrapure water. The details of each salt used and its concentration for each study are detailed in the experimental section of the respective Chapters. After mixing the salt solutions with the fibrinogen solution, the mixtures were left to dry in a home-built humidity chamber. Humidity and temperature were controlled and set according to the salt used to prepare the precipitates. For instance, fibrinogen layers prepared from mixtures containing more hygroscopic salts like MgCl₂ and CaCl₂ had to be dried at lower humidity (5%), while for non-hygroscopic salts like NaCl, the samples were dried at 30% relative humidity.

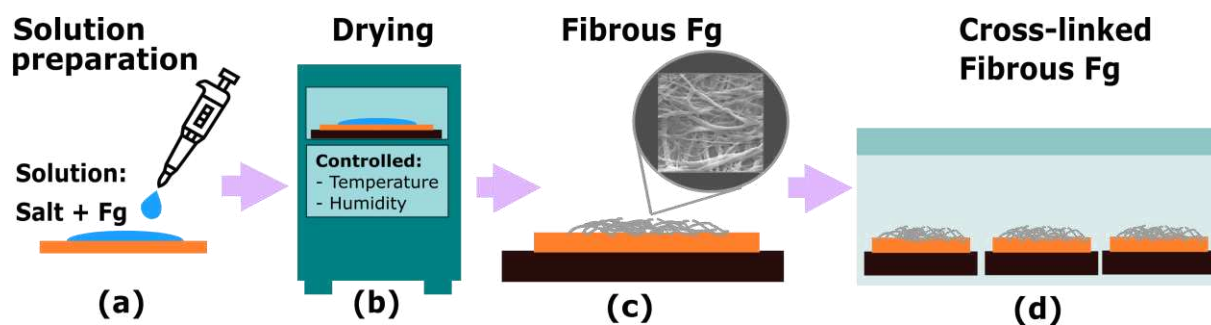


Figure 7-2: Sketch of the standard operating procedure for fibrinogen nanofiber assembly and scaffold post-treatment used in this thesis. Fibrinogen solutions were prepared in Tris buffer. Reference planar samples were prepared by drying fibrinogen solution in Tris. Fibrous samples were prepared by mixing the fibrinogen solution with different salts. After mixing both solutions, the samples were placed in a chamber where temperature and humidity were controlled and left overnight for drying. The precipitated fibrinogen layers were then cross-linked with formaldehyde vapor and subsequently washed.

For Chapter 5, after the drying step the samples were already characterized. In Chapters 3, 4 and 6, however, for fixation the fibrinogen layers were submitted to a cross-linking step using formaldehyde vapor, followed by rinsing off of the salts in ultrapure water.

The drying step was in most cases accompanied by a light scattering technique (on Chapters 3 and 4) and the samples were subsequently characterized with regard to their macroscopic morphology using light optical microscopy. Their nano-morphology was characterized using Scanning Electron Microscopy (SEM). The secondary structure of fibrinogen precipitates was determined using Fourier-Transform Infrared spectroscopy (FTIR) and the surface composition of the fibrinogen layers was studied using X-ray Photoelectron spectroscopy (XPS) and Energy Dispersive X-ray spectroscopy (EDX).

The results presented in the different chapters showed how the morphology, the secondary structure and the composition of the fibrinogen precipitates varied tremendously depending on the salt composition used to assemble them. All combined, those studies presented in Chapters 3-5, start to unravel how important the triad of high ionic strength, fibrinogen concentration and drying is to reproducibly produce fibrinogen nanofibers with tailored topography *in vitro*. Moreover, they highlight the importance of the already known, yet complex interaction between proteins and salts.

The next sections will therefore focus on discussing this interaction of fibrinogen with salts to propose a mechanism of fiber formation initiated by salt addition and drying.

7.2. THE COMPLEX MUTUAL INTERACTIONS BETWEEN FIBRINOGEN AND VARIOUS SALTS

7.2.1. *Fibrinogen precipitates formed from divalent and monovalent salts*

The ability of fibrinogen to self-assemble into nanofibrous structures *in vitro* by salt addition has been reported previously (Stapelfeldt, Stamboroski, Mednikova, et al., 2019; Stapelfeldt, Stamboroski, Walter, et al., 2019) and was described in the procedure to prepare fibrinogen fibers in Section 7.1.2. To some extent, fibers were also observed when fibrinogen was dried in the presence of NaCl and KCl. Moreover, this process of fiber formation was dependent on the fibrinogen concentration and solution pH. Fibers could only be formed with a minimum starting concentration of 2 mg/ml of fibrinogen and at $\text{pH} \geq 7$. The coverage of the samples with fibers increased with increasing salt concentration (Stapelfeldt, Stamboroski, Mednikova, et al., 2019). In a subsequent work, investigation on the secondary structure of fibrinogen using circular dichroism (CD) and FTIR showed an increase in the β -strand content of fibrous fibrinogen prepared from PBS when compared to smooth films prepared with NH_4HCO_3 (Stapelfeldt, Stamboroski, Walter, et al., 2019).

Since salts were found to be the key to fibrinogen fiber formation, in this thesis, a direct comparison between monovalent (Chapter 3 and 4) and divalent salts (Chapter 3) and their influence on fibrinogen layer roughness, morphology and capacity to trigger fiber formation was done. This comparison revealed that depending on the salt and their characteristics on salting in or salting out proteins, different fibrinogen morphologies and roughness could be obtained. Figure 7-3 summarizes the salts tested in this thesis and the resulted fibrinogen morphologies obtained from precipitating fibrinogen in the presence of different salts. In general, divalent salts hamper fibrinogen fiber formation and form mostly very smooth fibrinogen layers, while monovalent salts can form a variety of rough morphologies, network-like structures, and well defined and distinct fibrinogen fibers.

It was expected that divalent cations such as Ca^{2+} would trigger fibrinogen fibrillogenesis, since it is directly involved in the coagulation cascade (Weisel & Litvinov, 2017). For comparison, other divalent cations (all in combination with chloride as anion) involved in other biological process were also tested: Mg^{2+} , Zn^{2+} and Cu^{2+} . This was the second hypothesis formulated (see Section 1.8), which was refuted by the study presented in Chapter 3. Neither the presence of low concentration (10 mM) nor higher concentrations (187 mM and 375 mM) of divalent chlorides could trigger fibrinogen fibrillogenesis with the drying method used to prepare fibers. On the contrary, roughness maps obtained from light scattering, top morphology and cross sections obtained from SEM imaging, revealed compact and smooth fibrinogen layer precipitates (Stamboroski, Boateng, et al., 2021). Fibrinogen precipitates obtained from the

drying of fibrinogen with PBS, NaCl, Na-PO₄ and K-PO₄, however, presented a high roughness in the roughness maps that could be directly correlated with fibrous morphology (Chapter 4). Together with the results presented in Chapter 3 and the outcome depicted in Figure 7-3, this already shows that monovalent ions are a main driving force of fibrinogen fibrillogenesis in an enzyme-free environment, confirming the third hypothesis formulated in Section 1.8 of this thesis.

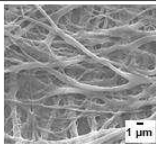
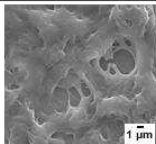
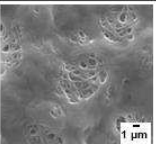
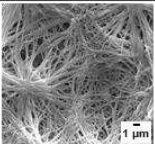
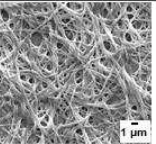
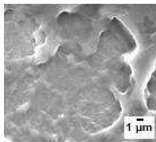
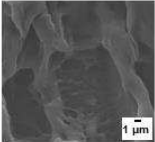
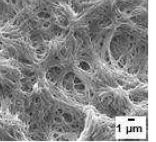
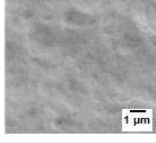
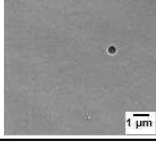
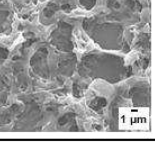
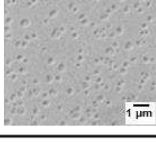
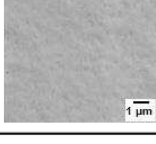
| anion cation | Cl ⁻ | oxalate | citrate | SO ₄ ²⁻ HSO ₄ ⁻ | HPO ₄ ²⁻ H ₂ PO ₄ ⁻ |
|------------------|---|---|---|---|---|
| Na ⁺ |  |  |  |  |  |
| K ⁺ |  | - | - |  |  |
| Ca ²⁺ |  | - | - | - | - |
| Mg ²⁺ |  | - | - |  | - |
| Cu ²⁺ |  | - | - | - | - |
| Zn ²⁺ |  | - | - | - | - |

Figure 7-3: Comparison of monovalent and divalent salts in terms of fibrillogenesis and roughness obtained after drying fibrinogen solutions with different salts and varying ion combinations. Images of fibrinogen dried in presence of divalent salts were modified and reproduced with permission from (Stamboroski, Boateng, et al., 2021). Copyright © 2021, American Chemical Society.

Important to highlight is that for NaCl, fibers were formed only below the areas where bigger sodium chloride crystals precipitated and not completely spread along the whole sample as for the other cited salts. For samples prepared with KCl, a rougher morphology than the ones obtained for divalent chlorides was observed; however, no fibrous structures were found. This last observation contradicts the observations by Stapelfeldt et al. and therefore the different

buffers used to prepare the fibrinogen solutions (Tris in this work versus NH_4HCO_3 for Stapelfeldt) could explain the different observed morphologies for fibrinogen precipitates prepared from KCl. Kurniawan et al, for instance, have already shown that buffers strongly affect fibrin self-assembly (Kurniawan et al., 2017). It was found that Tris can suppress the lateral association of fibrin protofibrils in a concentration-dependent manner. In this regard, future studies comparing the use of different background buffers on the behaviour of the fibrinogen precipitation are recommended.

The FTIR investigations on the secondary structure of the fibrinogen layers formed from divalent chlorides showed strong variations on the amide I band shape and intensity suggesting a conformational diversity within each sample. Moreover, the deconvolution of the averaged amide I band revealed a similar trend than the one obtained by Stapelfeldt et al: there was an increase in β -strand structures accompanied by a decrease in the α -helical content, when the reference planar sample prepared in Tris is compared to fibrinogen layers prepared with PBS, divalent chlorides or even denaturing agents as urea and guanidine hydrochloride. For monovalent salts the FTIR results showed a more coherent spectra and again an increase in β -strand structures when compared to the planar layers prepared with only Tris and no additional salt. Therefore, only by comparing the secondary structure of fibrinogen layers prepared with mono- or divalent salts it was not possible to directly correlate changes in secondary structure with changes in the roughness and morphology of the fibrinogen precipitates, since many smooth as well as rough and fibrous fibrinogen layers both showed an increase in the β -strand content.

Since ions can have direct contact with proteins it was analyzed with XPS and EDX whether the surface composition of fibrinogen layers could also be an indication of the presence or absence of fibers. The analysis of the surface composition of rinsed fibrinogen layers prepared with divalent chlorides showed that even after 5 min rinsing, the salts can be completely washed out and there was no ion uptake of any of the divalent cations within the fibrinogen layers. On the other hand, for fibrous fibrinogen layers prepared with sodium phosphate or PBS, the salts could also be washed away, however there was uptake of the cation (Na^+), which was detected even after rinsing the samples for 30 min. Interestingly, there was no cation uptake for fibrous samples prepared with potassium phosphate. Moreover, for monovalent chlorides as NaCl and KCl, the salts could also be easily washed, and no cation uptake was found. Those results indicate a preference of sodium over potassium to fibrinogen, but only when phosphate was the counterion and rough, clearly fibrous layers were formed.

Although sodium and potassium own the same charge and differ slightly in size, many biological processes depend on discrimination between these two ions, such as sodium-potassium membrane pump (Jagoda-Cwiklik et al., 2007). Vrbka et al have shown that sodium binds at least twice as strongly to protein surfaces than potassium (Vrbka et al., 2006). This preference comes primarily from local cation-specific interactions with the anionic carboxylate group in glutamate and aspartate side chains (Vrbka et al., 2006). Ion pairing could also help to explain this preference of sodium over potassium and why sodium is detected only when sodium phosphate was used and not sodium chloride. At higher salt concentrations, the pairing of cations and anions can become notably prevalent (Bruce et al., 2020). For instance, Jagoda-Cwiklik et al performed calculations using a combination of molecular dynamics simulations and *ab initio* methods showing that smaller anions as HCOO^- (which mimic the negatively charged amino acid side chains of glutamate and aspartate) prefer sodium over potassium. Moreover, they showed that for sodium, ion pairing is stronger with chloride anions than with phosphate, which could explain why sodium was more “free” to interact with fibrinogen nanofibers and bind to its carboxylate groups when the anion used was phosphate instead of chloride (Jagoda-Cwiklik et al., 2007). Another possible explanation for not detecting sodium when fibers were formed from NaCl is that due to the lower amount of fiber formation, consequently there are less points for sodium adsorption, and consequently the sodium concentration on those samples would be below the detection limit of XPS.

Based on the aforementioned discussions and considering that sodium was detected only on clearly fibrous fibrinogen layers, it is likely that the uptake of Na^+ on fibrous fibrinogen layers takes place after the fiber formation and in particular at high salt concentrations. To test this hypothesis, in future works, fibrous fibrinogen layers prepared from potassium phosphate or other salts, shall be exposed to sodium phosphate and sodium chloride solutions.

When comparing the results obtained in Chapter 3 and Chapter 4, the Hofmeister effect seems to be key to understand fibrinogen self-assembly *in vitro*. Moreover, the presence of phosphate anions was crucial for the formation of denser and more distinct fibers. Therefore, in Chapter 4, other polyvalent anions with kosmotropic characteristics as phosphate and sulfate were tested. The results revealed that denser and distinct fibers were formed with the right combination of a kosmotropic anion and a kosmotropic cation (Figure 7-3), showing that although Hofmeister effects are stronger for anions, cations play an important role when it comes to fibrinogen self-assembly *in vitro*. Figure 5 in Chapter 4 illustrates a two-dimensional Hofmeister series for fibrinogen fiber formation considering both anions and cations.

As mentioned before, divalent cations in combination with chloride anions only formed smooth fibrinogen layers. However, when fibrinogen was precipitated with MgSO_4 a rather rough structure was observed. Interestingly, Hense and Strube could form fibrinogen fibers by adding MgSO_4 to their procedure of fiber preparation, yet using a salt concentration lower than what was used in Chapter 4 and temperatures below room temperature (Hense & Strube, 2023b). In this thesis, for potassium, clearly dense and distinct fibers were only observed with K-PO_4 , while sodium in combination with phosphate and sulfate was able to trigger fibrinogen self-assembly and to form distinct and dense fibrinogen fibers.

To summarize the results relating Hofmeister salts with fibrinogen self-assembly, the Hofmeister series depicted in Figure 7-4 is proposed. This series differs from the one depicted in Figure 1-5 because it is specifically for fibrinogen, while Figure 1-5 summarizes salt interactions with various proteins in general.

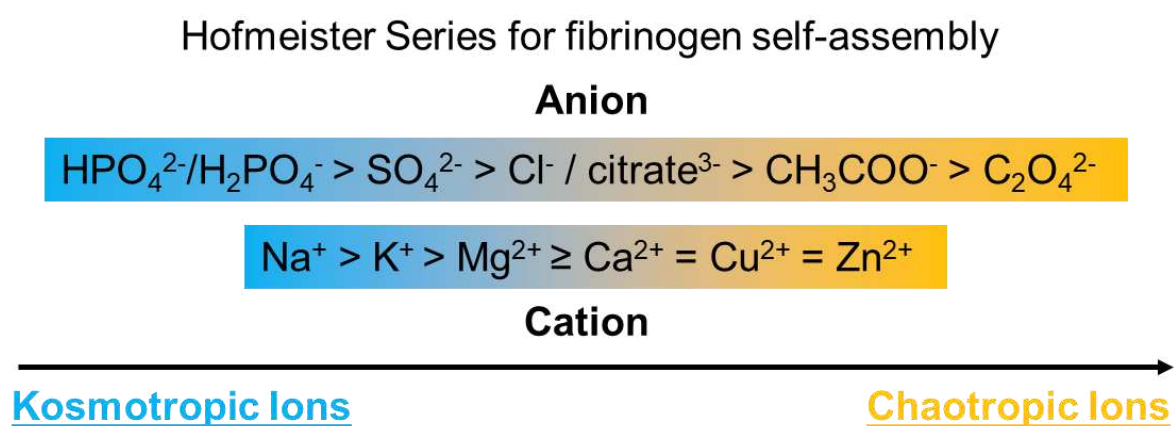


Figure 7-4: Hofmeister Series obtained for the formation of fibrinogen nanofibers based on the studies presented in Chapters 3 and 4. Left side (blue) of the image shows kosmotropic anions and cations, which have a higher tendency to salting out and form fibrinogen nanofibers. Right side (yellow) shows the more chaotropic cations and anions with the tendency of salting in and form smooth layers.

The > signal in the image implies a stronger ability to precipitate the protein (salting-out) and form fibrinogen nanofibers. This order can be considered a direct Hofmeister series for both cations and anions (Gregory et al., 2022; Hyde et al., 2017; Okur et al., 2017). Chloride anions seem to have a greater kosmotropic effect than citrate for fibrinogen fiber formation when considering this ion in combination with Na^+ as counterion. However, further experiments with potassium citrate or different concentrations with NaCl and Na-citrate , are necessary to properly rank these two anions. Therefore, they appear side by side in the proposed Hofmeister series. Additionally, to better distinguish between the divalent cations other divalent salts with other counter ions than Cl^- shall be studied in future as well to understand their effect on fibrinogen fibrillogenesis. Another contribution of this PhD thesis is related to the importance of

considering both kosmotropic cations and kosmotropic anions for the formation of fibrinogen nanofibers *in vitro*, which was highlighted by a two-dimensional Hofmeister series (Figure 5, Chapter 2).

The Hofmeister effect has been used for many years to explain why some salts have a greater tendency for salting in (increasing the solubility of proteins) and others for salting out (promoting protein aggregation and precipitation) of proteins (Baldwin, 1996; Iscen & Schatz, 2019; Okur et al., 2017). In a simplistic way, the ionic species generated by the salts in water with a tendency to salt out the solute are called kosmotropes because of their capacity in bringing “order” to the solution by organizing several layers of water molecules around themselves and in this way “stealing” water from the solute (Okur et al., 2017). On the other hand, the ionic species with a salting in characteristic are called chaotropes because they rather disrupt the water layers and bring “chaos” to the system (Gibb, 2011; Okur et al., 2017). Although this rationalization can be made for anions, it fails for cations, and there are still strong debates in literature regarding the ability of salts to influence the bulk properties of water (Gibb, 2011; Okur et al., 2017). Certain studies have, for instance, shown that ions do not influence hydrogen bonding of water beyond their first solvation shell (Salis & Ninham, 2014).

Therefore, to understand why some salts support fibrinogen fiber formation and others do not, it is important to consider all important interactions in aqueous supramolecular systems, as depicted in Figure 7-5. Not only the interactions between the ions of a salt, interactions between these and water, and interactions between these and the solute are important, but also solute-solute, water-water and solute-water interactions need to be considered for a holistic understanding of fibrinogen fibrillogenesis *in vitro*.

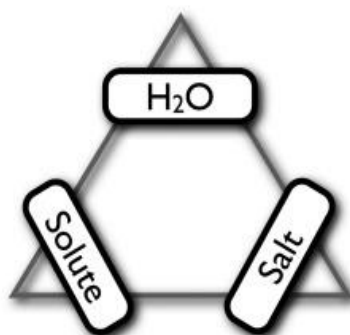


Figure 7-5: The important entities and their interactions in aqueous supramolecular chemistry. Grey lines indicate non-covalent interactions between the three components water, salt, and solute, as well as the interactions between solutes, between ions, and between waters. Reproduced with permission ((Gibb, 2011) Copyright 2011 Wiley-VCH Verlag GmbH&Co. KGaA, Weinheim).

All these interactions and effects show how complex interactions of proteins and salts in aqueous solutions are in general. Depending on protein structure and amino acid sequence, the overall charge of proteins in water varies strongly and this will directly dictate the interactions with surrounding salts. Moreover, it is not possible to completely separate the effects of cations and anions because they are both present in solution, and thus the interaction of a cation with its counter ion must be considered.

For the different parameters/factors presented in Chapter 2 that can trigger fibrinogen nanofiber assembly *in vitro*, some authors have already suggested mechanisms based on fibrinogen aggregation and fiber formation/elongation. The next section will therefore focus on presenting the suggested mechanisms so far. Additionally, considering all the effects and interactions depicted in Figure 7-5, a possible mechanism based on the Hofmeister series for the salt-induced self-assembly of fibrinogen into nanofibers is provided.

7.2.2. New insights into the mechanism of fibrinogen self-assembly *in vitro*

The dynamics of the self-assembly process is not completely understood. For fiber formation, experimental reports suggest that self-assembly follows a multi-stage process characterized by distinct intermediate structures (S. Zhang et al., 2002). In general, it is accepted that protein nanofibers are formed through an aggregation process, where initial fibrillar aggregates elongate by addition of other units at the protofilament ends (Lendel & Solin, 2021). This occurs naturally with fibrin when fibrinogen is cleaved by thrombin (more details on this process is described in Chapter 2 and depicted in Figure 4 of same). For fibrinogen self-assembly *in vitro*, however, different mechanisms of fiber nucleation and elongation have been proposed, depending on the environmental conditions involved in the process.

For fibrinogen fiber formation on hydrophobic substrates, many authors have hypothesized that the direct interaction of fibrinogen molecules with hydrophobic surfaces occurs *via* the D and E domains of fibrinogen, which have a more hydrophobic character. This direct interaction between the D and E domains with hydrophobic surfaces distorts the fibrinogen molecule liberating the α C regions that can then interact and bind other fibrinogen molecules in solution, initiating fibrillogenesis *in vitro* (Hu et al., 2016; Jaseung Koo et al., 2012; Marchin & Berrie, 2003; Ta et al., 1998; L. Zhang et al., 2017). Figure 7-6 shows this mechanism proposed by Koo et al. of fibrinogen fiber self-assembly by interaction with hydrophobic surfaces (Jaseung Koo et al., 2012).

The conformation that fibrinogen assumes when adsorbed to a hydrophobic surface is sketched in Figure 6A of Chapter 2. When the α C domains are not present in the fibrinogen molecule, as it is the case for des- α C fibrinogen, fiber formation upon interaction with hydrophobic surfaces is suppressed (Jaseung Koo et al., 2012). Interestingly, the fiber assembly of fibrin *in vivo* (Figure 4, Chapter 2), also releases the α C regions when thrombin cuts off the fibrinopeptides. The α C regions are then available for intermolecular interactions and contribute to the enhancement of lateral aggregation during fibrin polymerization (McPherson et al., 2021; Weisel & Medved, 2001). These findings show that an involvement of the α C domains during fibrillogenesis of fibrinogen seems key to fiber formation.

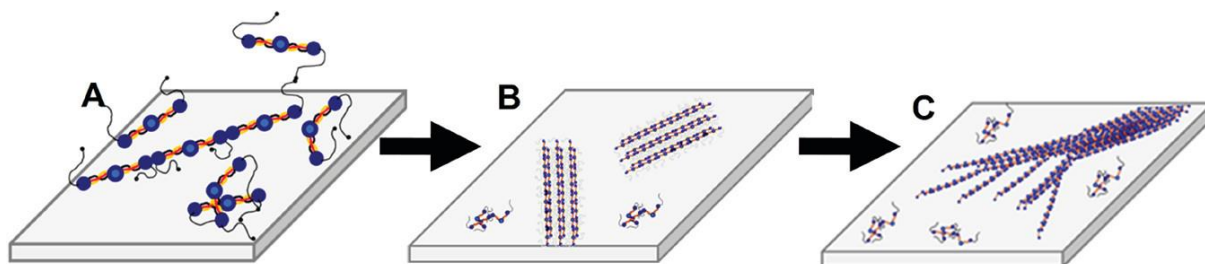


Figure 7-6: Sketch of the proposed mechanism by Koo et al. of surface-induced fibrinogen self-assembly. (A) Adsorption of the initial layer directly onto the surface where the hydrophobic D and E regions are preferentially adsorbed, and the hydrophilic α C regions remain free to interact with other molecules. (B) Once the surface is coated with individual fibrinogen molecules (represented by the image of a trinodular structure), subsequent molecules can migrate and self-assemble into protofibrils. (C) Attractive forces between the α C domains on the exterior of the protofibrils induce further coalescence of the fibers into increasingly larger ones, which remain anchored onto the surface. Reproduced with permission (Jaseung Koo et al., 2012). Copyright © 2012 American Chemical Society.

On hydrophilic surfaces, on the other hand, the adsorption of fibrinogen takes place through the α C regions, which have a more hydrophilic characteristic (refer to Fig. 6B, Chapter 2). In this case the α C regions are not available for interaction with other fibrinogen molecules, since they are in direct contact with the surface, which would in principle impede fiber formation. Despite that, fibrinogen fiber formation was also observed on hydrophilic surfaces (Table 1, Chapter 2). In these circumstances, the mechanism for fiber formation must be analyzed case by case, considering not only the surface energy of the surface, i.e. its hydrophilicity, but also other aspects of the nature of the surface or of the surface-fibrinogen interaction. For instance, fiber formation through the interaction and extrusion of fibrinogen molecules through hydrophilic alumina nanopores, can be explained by the occurrence of shear forces in the confined pores (Raoufi et al., 2016). On gold substrates, an additional factor leading to fiber assembly of fibrinogen could be the interaction of the sulfur containing regions, i.e. the cysteines of the fibrinogen molecule, with gold, forming a stable Au-S bond that breaks the disulfide bonds in the E domain of fibrinogen and releases the α C regions for interaction with other fibrinogen molecules to propagate fiber formation (G. Chen et al., 2011).

Fibrinogen self-assembly can also take place using denaturing buffer conditions, such as low pH and organic solvents (Stamboroski, Joshi, et al., 2021). In this case, the mechanism of fibrinogen self-assembly proposed by Wei and co-workers starts with a change in fibrinogen conformation to an extended shape with the α C domains opened and consequently denaturation caused by the harsh conditions. Due to these changes in the fibrinogen molecule, the aggregation starts *via* its α C domains, and fibrinogen grows to protofibrils and subsequently to nanofibers (Reichert et al., 2009; Wei, Reichert, & Jandt, 2008). Rieu et al. also proposed a similar mechanism for protofibril formation triggered by denaturation of fibrinogen after acidifying fibrinogen solutions to pH = 3.6 (Rieu et al., 2020). Differential Scanning Calorimetry (DSC) and Dynamic Light Scattering (DLS) studies revealed that during acidification fibrinogen undergoes a reversible change in structure that corresponds to a destabilization of its thermolabile D domain and α Cs interaction. Therefore, they proposed that the fibrinogen aggregation started with the interaction *via* the D-domains of two adjacent fibrinogen molecules (Rieu et al., 2020).

As presented in Chapter 2, when using non-denaturing buffers to produce fibrinogen nanofibers, different parameters were proven to unleash fibrinogen self-assembly (Stamboroski, Joshi, et al., 2021). Here, again, there is no single/common mechanism to explain fibrinogen fibrillogenesis. The studies from Hense et al, for instance, showed that different parameters led to the formation of fibrinogen nanofibers. In a first study, nanofibers were produced by adding oxygen-containing, preferably multivalent acid anions like phosphate or citrate (5 to 20 mM) to a fibrinogen solution at slightly acidic pH and low temperatures around 5°C (Hense et al., 2021). For that, no mechanism was proposed. Interestingly, Galanakis et al reported the formation of fibrinogen nanofibers also at low temperature (4°C), slightly acidic pH and 50 mM sodium phosphate (Galanakis et al., 2021, 2022). According to Galanakis et al, nanofibers prepared under these conditions can be generated because soluble fibrin is a substantial component of isolated fibrinogen, which spontaneously self-assembles into protofibrils progressing to fibers at sub-physiologic temperatures (Galanakis et al., 2022).

In a second study, Hense and Strube produced fibrinogen nanofibers by adding up to 50 mM CaCl₂ to fibrinogen solution at 5°C at neutral to basic pH. Moreover, fibers could be produced with higher fibrinogen concentrations of 40 mg/mL at physiological temperature by adding 100 mM of NaCl to increase fibrinogen solubility (Hense & Strube, 2023a). With other divalent salts like MgCl₂, SrCl₂ and BaCl₂ rough morphologies or limited fiber quantities were obtained. They proposed that those nanofibers were produced based on the occupancy of the binding sites for divalent cations. Additionally, they suggested that fibrinogen undergoes changes in its

secondary structure upon Ca^{2+} addition into a conformation which potentially favors a more orientated aggregation and consequently assembly into fibers (Hense & Strube, 2023a).

Finally, in a third study, Hense and Strube presented fibrinogen fiber formation by addition of MgSO_4 (Hense & Strube, 2023b). Fibers were formed again at low temperature. When the temperature was increased to 37°C , the formed fibrous gel dissolved. They hypothesized that Mg^{2+} electrostatically binds to fibrinogen and acts as “bridge” between the molecules. Suited kosmotropic anions, such as sulfate and (hydrogen)phosphate, on the other hand are then responsible for the actual fiber formation. However, how exactly kosmotropic anions could align the fibrinogen molecules it is yet to be understood (Hense & Strube, 2023b).

For the fibrinogen nanofibers prepared by Stapelfeldt et al. and in this PhD thesis, highly saline solutions were used at room temperature. There is evidence that a change in the secondary structure of fibrinogen towards increased amounts of β -strand content could be a trigger to fiber formation (Stapelfeldt, Stamboroski, Walter, et al., 2019). However, this change in secondary structure of fibrinogen was also observed for divalent salts and for monovalent salts (see Chapter 3 and 4) that did not completely convert soluble fibrinogen into fibers (Stamboroski, Boateng, et al., 2021). Therefore, the observed change in secondary structure is not sufficient to explain the fibrinogen self-assembly at room temperature triggered by salt and increase in concentration *via* evaporation of water. Another hypothesis to explain fiber formation under these *in vitro* conditions could be the observed differences in cation uptake after washing out residual salts from crosslinked fibrinogen nanofibers (Stamboroski, Boateng, et al., 2021).

In Chapter 3 it was discussed that divalent ions were not detected in any of the fibrinogen precipitates after rinsing because they have weaker interactions with the molecule than monovalent ions due to a greater interaction of the divalent cations with the water, making it more difficult to break their hydration shell and to get closer to facilitate direct binding to fibrinogen (Stamboroski, Boateng, et al., 2021). This explanation can be expanded together with the more recent results obtained in Chapter 4 and the last publications from Hense and Strube that showed fibrinogen fiber formation with CaCl_2 (Hense & Strube, 2023a) and MgSO_4 (Hense & Strube, 2023b). Although Hense et al. used different parameters to induce fibrillogenesis with salt solutions, the following similarities can be identified.

Hense and Strube observed fiber formation when the fibrinogen solution was getting turbid (Hense et al., 2021; Hense & Strube, 2023a). Similarly, in the current work, turbidity has been seen in solution when monitoring the drying process with light scattering for PBS, NaCl, Na- PO_4 and K- PO_4 . Moreover, when the divalent salts CuCl_2 and ZnCl_2 were added to the

fibrinogen solution and during the drying with CaCl_2 , turbidity as manifested by higher A_q values was observed at the beginning, which disappeared over time (Stamboroski, Boateng, et al., 2021). The initial turbidity observed when adding divalent salts (Chapter 3) could be the same phenomenon observed by Hense and Strube.

Therefore, for divalent salts the following rationale could be made: when the concentration of divalent salts in a fibrinogen solution is not so high, the affinity of the divalent ions for water is greater than the affinity for the protein and there is a salting out effect. This effect is stronger at 5°C because fibrinogen seems to be less soluble at this temperature since turbidity caused by fibrinogen aggregation is then observed. However, when the salt concentration increased even further during the drying, fibrinogen was dissolved again by its interaction with the divalent salts *via* a salting in effect, so that the initial turbidity disappeared again.

In this thesis, when preparing fibrinogen precipitates with monovalent salts, turbidity was detected at the end of the drying process after at least 80% of water had evaporated, and simultaneously the A_q value of the light scattering measurements started to increase (Chapter 4). Therefore, during drying of fibrinogen at room temperature with monovalent salts it was assumed to see a salting out effect. When adding monovalent salts to the fibrinogen solution, the solution stayed transparent showing that fibrinogen was well dissolved. Over time when water evaporated, there was an increase of both fibrinogen and salt concentration in solution, and a salting out effects take place.

For anions, the most accepted mechanism for salting out is that strongly hydrated anions (SO_4^{2-} , $\text{HPO}_4^{2-}/\text{H}_2\text{PO}_4^-$, Cl^-) precipitate proteins due to a combination of electrostatic repulsion and enhancement of the hydrophobic effect (Hyde et al., 2017). For instance, there is evidence that Hofmeister ions alter protein solvation (A Metrick II & Macdonald, 2015). With experiments measuring deuterium ($^1\text{H}/^2\text{H}$) exchange, A Metrick II & Macdonald showed that the presence of strongly hydrated, kosmotropic anions decreases deuterium exchange, suggesting less free water and decreased protein solvation correlated with increased protein stability. On the other hand, increased deuterium exchange was found in the presence of weakly hydrated, chaotropic anions like Cl^- and ClO_4^- , correlating with increased protein solvation and decreased protein thermal stability (A Metrick II & Macdonald, 2015).

Moreover, at higher salt concentrations, specific ion effects can be observed (Hyde et al., 2017; Okur et al., 2017) and local interactions between the protein surface and ions have to be considered. Important regions of the protein surface interacting with ions are its backbone and charged side chains (Okur et al., 2017). Depending on the local charge distribution, anions and

cations from solution will interact differently at different regions of the protein. In general, the protein backbone attracts more of weakly hydrated anions (e.g. I^- , NO_3^- , ClO_4^-) and strongly hydrated cations (e.g. Mg^{2+} , Ca^{2+} , Li^{1+}) (Okur et al., 2017). At negatively charged chains of glutamates and aspartates, cations follow a direct Hofmeister series and, again, strongly hydrated cations interact more than weakly hydrated cations (e.g. K^+ , NH_4^+), and these interactions are stronger than the ones with the backbone (Okur et al., 2017; Vrbka et al., 2006). However, at positively charged chains of arginine, lysine, and histidine, anions follow an indirect Hofmeister order, with strongly hydrated anions (F^- , SO_4^{2-} , HPO_4^{2-}) interacting more than weakly hydrated anions (Okur et al., 2017). In this way, cations adhere to the direct Hofmeister series concerning protein salting-out behavior. In contrast, this pattern holds true for anions only in proteins where the influence of the backbone surpasses that of positively charged side chains. This is likely what happens to fibrinogen for pH values above 5.8, which is the isoelectric point of fibrinogen, the molecule has an overall negative charge (Stamboroski, Joshi, et al., 2021).

Another important effect that needs to be taken into account is that phosphates are classified as both polyvalent and amphoteric anions, which can form several hydrogen bonds and salt bridges in proteins either intra- or intermolecularly (Hunter, 2012). Protein phosphates can act either sterically or ionically to regulate the function or interaction of other proteins or small molecules, or more commonly to elicit a conformational change within a protein molecule. The distinct size and charge properties of covalently attached phosphates also enable specific protein-protein interactions (Hunter, 2012). It is known since long that fibrinogen can be phosphorylated and that phosphorylation of fibrinogen *in vitro* can change its conformation and affect its behavior (De Vries et al., 2020; Martin et al., 1992; Martin & Björk, 1990). The phosphorylation in fibrinogen mainly occurs on serine and threonine located in the A α chain (αC region) (De Vries et al., 2020). Martin and Björk, therefore, proposed that by phosphorylation leads to an increase in the ordered structure of fibrinogen in this region (Martin & Björk, 1990).

The temperature seems to play a role here too, because Hense and Strube observed dissolution of fibers when gels formed at 5°C were heated to 37°C (Hense & Strube, 2023b). For the process used in this PhD thesis, after drying at room temperature, if the samples were not fixated with vapor formaldehyde, the fibers dissolved again when in contact with water. As for other proteins, the solubility of fibrinogen varies with temperature and composition of the salt/fibrinogen mixture. Based on the results obtained in this thesis and the ones reported by Hense et al, fibrinogen seems to be more soluble at room temperature and less soluble at 5°C.

Interestingly, the fibers produced by Hense et al. were spontaneously formed with time, without any other change in the system like the evaporation of water (i.e. drying), which increases both the fibrinogen and salt concentration. Since in this PhD thesis fibrinogen fibers were only obtained after drying, it is likely that for Hense et al., the increase in fibrinogen concentration happened by lowering the temperature. Moreover, Hense et al. associated the formation of a gel in solution with nanofiber formation, but for performing SEM to verify whether fibers were actually formed, they always had to dry their fibrinogen samples (Hense et al., 2021).

Taking into account all the above discussed mechanisms for the Hofmeister effect, the results presented from Chapter 2 to Chapter 4 of this thesis and the discussion in Section 7.2.1, a sketch proposing different mechanisms for salt-induced fibrinogen aggregation *in vitro* is presented in Figure 7-7. The take-home-message of this graphical summary is that fibrinogen precipitation in the presence of salts can follow different scenarios and that only a fine equilibrium between cation/anion/fibrinogen allows the formation of fibrinogen nanofibers.

The first scenario in Figure 7-7 proposes a mechanism for the precipitation of fibrinogen with salts composed of two chaotropic ions, which are in this case the divalent salts presented in Chapter 3: divalent cations with chlorides. As mentioned above, the chaotropic anion Cl^- increases the protein water solvation and therefore decreases its stability. Moreover, during drying at room temperature and consequently evaporation of water, the solution gets more concentrated and hard polyvalent cations like the divalent ions can get closer to the fibrinogen molecule, interacting with Lewis basic sites in the protein (Hyde et al., 2017; Okur et al., 2017). This promotes a salting in effect by increasing the protein solubility as indicated by a decrease in turbidity and consequently leads to more denaturation of the protein, as the FTIR results in Chapter 3 indicate. This sequence of events leads to disorganized fibrinogen aggregation and precipitation, without alignment of the fibrinogen molecules and therefore generating only smooth fibrinogen layers. After fixation of the fibrinogen layers and when water was removed during rinsing of the fibrinogen layers, the divalent salts could be easily washed away due to their high affinity with water (Kiyohara & Kawai, 2019) in comparison to monovalent salts.

The second scenario in Figure 7-7 proposes a mechanism for the precipitation of fibrinogen with salts composed of a combination of a chaotropic ion with a kosmotropic ion, which are in this case salts presented in Chapter 4: monovalent cations with chloride, acetate, oxalate or citrate and divalent cations with sulfate. In this case a competition between salting in and salting out effects occurs that dominates the precipitation of fibrinogen. For instance, there is increased water solvation with chlorides, leading to salting in, but less specific binding with monovalent

cations favoring salting out effects. Another scenario with sulfate is characterized by a decreased water solvation around the protein favoring salting out, while still enough specific binding sites are present that enable salting in. Therefore, the fibrinogen molecules are presented partially unfolded or with a change in the tertiary structure where the α -C domains are released. This molecular arrangement can favor some degree of organized aggregation, resulting in limited fiber formation or rough fibrinogen layers upon drying.

Finally, the third scenario in Figure 7-7 proposes a mechanism for the assembly of fibrinogen nanofibers in the presence of highly saline solutions with kosmotropic ions. When salts with a combination of two kosmotropic ions are mixed with fibrinogen solutions for drying, distinct and dense nanofibers can be formed. The salts capable of inducing fibrinogen nanofibers are presented in Chapter 4: monovalent cations with small anions with high charge density as the oxygen containing polyvalent phosphates and sulfate. Here, once again a combination of effects must be considered during nanofiber formation. Taking into account the Hofmeister series and the ion-specific interactions for cations, sodium and potassium ions are indeed expected to have a more salting out characteristic than divalent salts as magnesium and calcium (Gregory et al., 2022; Okur et al., 2017). For the anions the salting out effect can be explained by a combination of electrostatic repulsion and enhancement of the hydrophobic effect (Gibb, 2011; Hyde et al., 2017). Strongly hydrated anions (SO_4^{2-} , HPO_4^{2-} and H_2PO_4^-) decrease water solvation, which increases the protein stability (A Metrick II & Macdonald, 2015). Adding the fact that phosphate can act as a bridge between two protein molecules and even change fibrinogen tertiary structure at its α C domains (De Vries et al., 2020; Hunter, 2012), an ordered precipitation of fibrinogen can be expected in this scenario. During drying, the increase in salt and protein concentration amplifies all the above-mentioned effects, that can act synergistically to trigger fibrinogen aggregation and the formation of protofibrils that subsequently assemble into nanofibers.

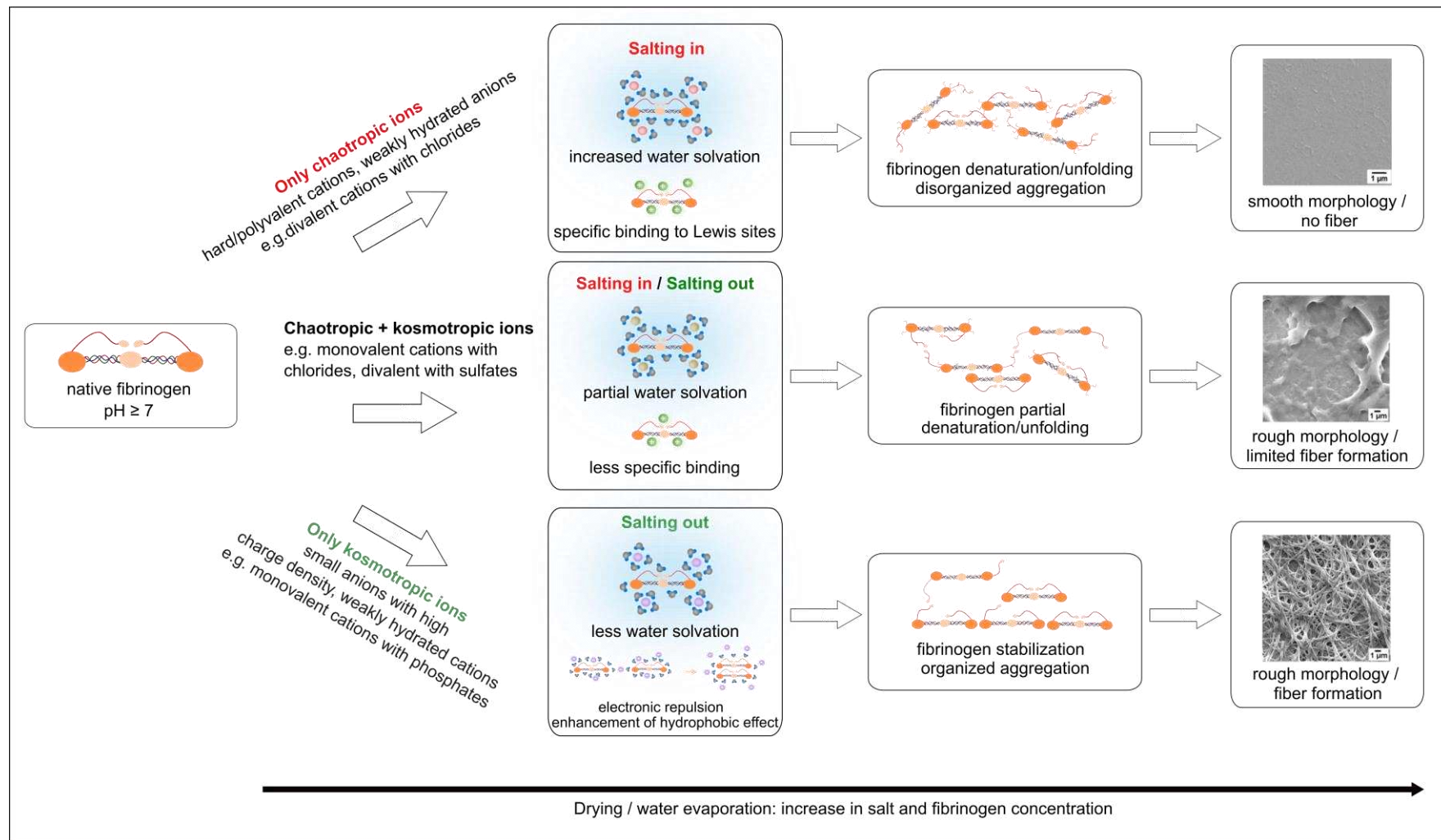


Figure 7-7: Summarizing sketch of the proposed mechanisms for fibrinogen precipitation by drying fibrinogen with highly saline solutions of different salts. The first scenario presents what happens during precipitation of fibrinogen in the presence of salts that contain a combination of chaotropic ions, e.g. the divalent salts studied in Chapter 3 (CaCl_2 , MgCl_2 and others) that resulted in smooth fibrinogen layers upon drying. The second scenario illustrates fibrinogen aggregation in the presence of salts that contain chaotropic and kosmotropic ions, e.g. monovalent cations with chlorides or divalent cations with sulfates as presented in Chapter 4, that resulted in rough fibrinogen layers or partial nanofiber formation. The third scenario proposes a mechanism for fibrinogen nanofiber formation when fibrinogen is dried with salts composed of kosmotropic ions, such as monovalent cations with phosphate or sulfate anions, that were also presented in Chapter 4.

7.2.3. *The co-influence of proteins and salt precipitation*

Another key finding of the current PhD research work is that not only salt can influence the self-assembly of fibrinogen, but also fibrinogen (and other proteins, such as BSA and collagen) can influence the crystallization of salts, which was the focus of the study in Chapter 5. During the investigations of fibrinogen precipitation with NaCl, KCl and PBS (Chapters 3 and 4), it was observed that NaCl and KCl crystals obtained after drying the fibrinogen-salt-mixtures had a different shape than when those salts were dried without the presence of fibrinogen, for instance with only Tris or water (see Figure S3 in the Supporting Information of Chapter 4 and Figure 2 of same).

When dried in the presence of a Tris-HCl buffer solution without any protein, as shown in Chapter 5 – Figure 2A by light microscopy, NaCl crystals were formed in nearly squared shape as halite crystals with a gap between each “tabular” salt crystal. NaCl salt dried in the absence of proteins showed no dendritic-like shape. In the presence of BSA (Chapter 5 – Figure 6A by light microscopy), NaCl crystals still presented a nearly squared shape characteristic for halite crystals. However, dendritic NaCl crystallites were observed further away from the halite crystals, suggesting an influence of BSA on the crystallization of the salt.

The salt crystallization in the presence of fibrinogen (Chapter 5 – Figure 10A) or collagen (Chapter 5 – Figure 13A), on the other hand, yielded polycrystalline large cross-shaped dendritic salts with no large squared crystals. It was hypothesized that proteins can act as nucleation sites, as crystal growth promoters, thus influencing crystallization kinetics (Dutta Choudhury et al., 2015). In Chapter 4, such dendritic cross-shaped salt crystals in the presence of fibrinogen are visible for other monovalent salt like KCl as well (see Chapter 4 – Figure 2D).

Moreover, when KCl was dried without fibrinogen, cubic salt crystals instead of dendritic ones were obtained (Figure S3C-D of Chapter 4). With regard to the distinction between BSA and fibrinogen/collagen, the first is a globular protein, while the later are fibrillar proteins. This can lead to differences in the respective salt-protein interactions. BSA has affected less significantly the crystallization of NaCl when compared to fibrinogen and collagen. In this way, in Chapter 5, it was suggested that the specific protein–salt interactions are guided by the behavior of the respective protein at the salt/liquid interphase, with the topology and relative abundance of apolar and polar side chains in the amino acids, that make up the proteins, influencing the drying behavior of the salts.

The influence of fibrinogen on the crystallization of salts is perceivable not only with morphological analysis by light microscopy, but also by the Aq profiles from light scattering and Aq mappings. As shown in Chapter 3, when divalent salts were dried without fibrinogen much higher Aq values were obtained during drying. In Chapter 3 – Figure 2, this “smoothing effect” of fibrinogen on salt precipitation is clearly visible (Stamboroski, Boateng, et al., 2021) as demonstrated also by Dutta et al. (Dutta Choudhury et al., 2015). Besides smoothing, fibrinogen also had a “delaying effect” on the salt precipitation, as demonstrated by the light scattering measurements presented in Figure 2F in Chapter 3 and Figure 1 in Chapter 4. This interaction was, however, not present for every salt investigated in Chapter 3. In the presence of Tris, the Aq roughness was kept low with or without fibrinogen (Chapter 3 – Figure 2E). On the other hand, for salts which induced fiber formation, in this case PBS and NaCl, the effect of fibrinogen on salt precipitation was clearly observable by an increase in Aq roughness during drying (Chapter 3 – Figure 2F and Chapter 4- Figure 1A-C) and in the dried precipitates (see Aq mappings in Chapter 4, Figures 2B, S3A and S6). The same trend was obtained for KCl, which yielded an increase in the Aq roughness when fibrinogen was present during drying (Chapter 4, Figures 1D-F) and in the dried precipitates (Aq mappings Chapter 4, Figures 2E, S3C and S9).

In summary, the fourth hypothesis formulated in Section 1.8 was confirmed: proteins can influence the morphology of crystallized salts ranging from nearly cubic halites (with a globular protein, such as BSA) to polycrystalline dendrites (with fibrillar proteins, such as fibrinogen and collagen). In the specific case of fibrinogen, this protein can also influence salt precipitation acting as smoothing and delaying factor on the precipitation. This shows that the material transportation within the liquid and the exchange of materials between the solid and liquid phases could be governed by the formed interphase between the advancing salt phase and the densely viscous saline aqueous jelly phase, encompassing proteins.

7.3. BIOFUNCTIONALITY OF FIBRINOGEN SCAFFOLDS

In tissue engineering, the aim of designing protein-based scaffolds with tailored topographies that are similar to the ECM is to control and stimulate the growth and proliferation of cells in a physiological environment. In this regard, Suter et al. created a collagen scaffold structure combining smooth/planar and nanofibrous topographies in a single substrate (Suter et al., 2020). The investigation using collagen scaffolds revealed that 3T3 fibroblasts exhibited different

morphologies according to the topography of the substrate. Small, elongated fibroblasts with few, long filopodia were found on collagen nanofibers. On the other hand, large, flat fibroblasts with many short filopodia were observed on smooth scaffolds (Suter et al., 2020). In another study, Suter et al. explored the biocompatibility of smooth and nanofibrous fibrinogen layers prepared from highly saline mixtures as the ones studied in this thesis, but in separate substrates using 3T3 fibroblasts as model cells for wound healing (Suter et al., 2021). The 3T3 fibroblasts adhered and proliferated well on both fibrinogen topographies. As for collagen topographies, fibroblasts on nanofibers were smaller than on planar films, however many short filopodia were present on nanofibers while few long filopodia were found on planar fibrinogen (Suter et al., 2021). Joshi et al. further studied the co-cultivation of human dermal fibroblasts (HDFs) and HaCaT keratinocytes on the same type of self-assembled fibrinogen scaffolds with nanofibrous and flat/planar topographies. Both nanofibrous and flat fibrinogen topographies were able to support cell adhesion and long-term viability with the expression of cell-specific marker proteins (Joshi et al., 2023).

This capacity of fibrinogen scaffolds prepared by salt-induced self-assembly to promote cell growth on both flat and fibrous topographies opens up a large potential for future applications of this biomaterial in regenerative medicine. It is well known that variations in the topography can tune the interaction with cells, for instance promoting adhesion, migration, differentiation, and morphology, therefore, improving the biocompatibility and bioactivity of a biomaterial (Nitti et al., 2023). For this reason, the possibility to precisely control the fibrinogen topography during salt-induced self-assembly, as it was studied in this thesis in Chapters 3 to 5, is very important for tissue engineering applications (Nitti et al., 2023). To further explore the potential of self-assembled fibrinogen nanofibers as a novel scaffold material for the treatment of both acute and chronic wounds, Chapter 6 presents an evaluation of the interaction between different fibrinogen topographies and human blood platelets. This study was conducted under *in vitro* conditions both with and without the presence of plasma proteins.

The interaction of blood platelets with physisorbed, planar and nanofibers of fibrinogen was investigated in Chapter 6. Compared to planar and physisorbed fibrinogen, fibrinogen nanofibers improved platelet adhesion and spreading when plasma proteins were present (see Chapter 6, Section 2.1). The surface area covered by platelets was significantly larger on nanofibers compared to both flat fibrinogen topographies. Moreover, the adhesion morphology of the platelets varied among the three substrates: most of the platelets appeared partially or fully spread on nanofibers, whereas on both flat surfaces they remained round or were round

with filopodia (see Figure 1 in Chapter 6). Since no differences were found between both flat topographies it was concluded that the crosslinking did not have an effect on the interaction with blood platelets. When incubating washed platelets instead of plasma rich platelets (PRP) on the fibrinogen scaffolds though, the platelets behaved similar on all three fibrinogen topographies, adhering and spreading normally.

In order to investigate if the differences in platelet adhesion between the fibrinogen scaffolds could be caused by the different surface topographies, as it was reported previously by Kämmerer et al. (Kämmerer et al., 2012) and Kikuchi et al. (Kikuchi et al., 2005), images from confocal microscopy analysis of fibrous fibrinogen with and without adhered platelets were analyzed. Due to three-dimensional undulated microarchitecture that overlaid the nanofibrous topography, fibrinogen nanofibers were found to considerably increase the available surface area by a factor of 15 in comparison to planar scaffolds (Kenny et al., 2022; Suter et al., 2021). This 3D-morphology could consequently offer more fibrinogen molecules to be bound by platelet integrins. Blood platelets were even found forming a bridge between two peaks on the nanofibers (Figure 4a in Chapter 6). This finding confirms the fifth and last hypothesis addressed in Section 1.8, showing that self-assembled fibrinogen nanofibers truly influence blood platelet adhesion due to their special topography.

Since there was a difference between the platelet adhesion when using PRP or washed platelets, the influence of the plasma proteins on platelet adhesion was also considered and investigated. For that, the planar and fibrous fibrinogen scaffolds were pre-exposed to platelet poor plasma before seeding of washed platelets. This pre-exposure to plasma reduced platelet adhesion and spreading especially for the planar scaffolds. This shows again the importance of the nanotopography offered by fibrinogen nanofibers, which provided a stronger stimulus to platelet adhesion.

Furthermore, resembling a more physiological environment, planar and nanofibrous fibrinogen topographies were investigated under shear flow conditions ranging from low to elevated venous shear rate as it is present in the blood stream (Chapter 6, Section 2.6). As a result, platelet interactions with planar scaffolds were usually sparse, whereas platelets adhered on nanofiber scaffolds with microaggregate formation, with the latter presenting a tendency for extended platelet-surface interaction. These findings were in alignment with a previous study from Chen et al., which showed increased platelet adhesion from whole blood on patterned poly(dimethylsiloxane) surfaces in comparison to flat ones (Hong Chen et al., 2009).

Therefore, the results presented in Chapter 6 reinforce the importance of fibrinogen scaffolds in platelet adhesion. Here, the particular potential lies on the biofunctionalization of substrates with fibrinogen nanofibers prepared by salt-induced self-assembly and in the control of the morphology/topography of the fibrinogen layers. It has been shown also by other authors that the conformation (Chiumiento et al., 2007) and surface topography (Hong Chen et al., 2009) of fibrinogen can affect platelet activation and adhesion. In this way, by choosing the suitable parameters for salt-induced self-assembly, such as the salt type and, salt and fibrinogen concentration, nanofibrous scaffolds with tailored fiber diameter, density and scaffold porosity can be achieved. In this way, scaffolds with topographical properties can be developed to specifically improve or suppress platelet adhesion.

In the current PhD thesis, it was demonstrated that the proper selection of the salt-fibrinogen pairing could lead to different morphologies and consequently topographies ranging from smooth/flat surface (with divalent salts, see Chapter 3, Figure 1) to rough fibrinogen precipitates (with chaotropic monovalent salts, see Chapter 4, Figure 2F) and nanofibrous scaffolds (with kosmotropic monovalent salts, see Chapter 4, Figure 2I). This provides the opportunity to use the technique of salt-induced fibrinogen self-assembly to tailor the surface topography, i.e. to create customized fibrinogen scaffolds that support the growth of different cell types involved in wound healing. Moreover, it was demonstrated that the surface/crystallization of salts can also be controlled by the selection of the protein present during the salt-protein interaction (Chapter 5). In Chapter 6, it was shown that the topography of nanofibrous fibrinogen obtained by salt-induced self-assembly has a direct influence on the interaction with blood platelets, with the nanofibrous topography enhancing platelet adhesion. These finding opens up a large field for future studies and applications, as outlined in the next section.

7.4. FUTURE PERSPECTIVES

As demonstrated in Sections 7.1 to 7.3, this PhD work dealt with the fibrinogen-salt interactions and how these interactions influence the precipitation and self-assembly of fibrinogen during drying. By tailoring synthesis parameters such as the type of salt, the salt and protein concentration, it was possible to obtain diverse fibrinogen morphologies and surface topographies, which can potentially be employed in a broad spectrum of tissue engineering applications.

To deepen the fundamental understanding of how salts and fibrinogen interact, further investigations need to focus on these interactions at a molecular level by computational chemistry (e.g., molecular dynamics). These simulations could provide important insights into the kinetics, thermodynamics and pathways of salt-induced fibrinogen self-assembly. Addressing individual parts of the protein in a highly saline environment can provide a fundamental understanding of how the salts affect the fibrinogen conformation and complexation. Part of these consecutive investigations, which will help to elucidate the underlying mechanism behind salt-induced self-assembly process is already underway (Sai Malisetty et al., 2023). Moreover, investigating the protein as a whole, as it was done with molecular dynamics by Zuev et al. (Zuev et al., 2017), could reveal the molecular flexibility and conformation to shed light on fibrinogen self-association from individual molecules to nanofibers under highly saline and high fibrinogen concentrations.

As explained in Section 7.2, salt-water-protein interactions are very complex relying on cross-effects from ion-hydration (salt-water), surface-related phenomena (salt-protein), ion pairing (salt-salt), protein hydration (protein-water), intra- and inter-molecular forces (protein-protein), and hydrogen bonding (water-water) interactions (Gibb, 2011). Therefore, since there is so far not a single explanation of the Hofmeister effect for the fibrinogen self-assembly in highly saline environment without the presence of thrombin and many aspects on the interaction of fibrinogen-water-salt must be considered, future experimental and simulation studies assessing the interaction of sodium phosphate and sulfate with water and with fibrinogen are necessary. Dynamic light scattering, circular dichroism spectroscopy and *in situ* atomic force microscopy (AFM) analysis will be well suited to understand at which point and at which salt concentration fibrinogen actually starts to self-assemble into fibers in solution during drying. Further FTIR investigations associated with $^1\text{H}/^2\text{H}$ exchange could also support the understanding of fibrinogen solvation in the presence of different salts. Further investigations using salt mixtures with both a fiber-forming salt (e.g. sodium phosphate) and a smooth forming (e.g. calcium chloride), during the drying of fibrinogen, could contribute to a better understanding of how ion specific interactions and ion pairing can influence the self-assembly of fibrinogen and how they compete with each other. Based on the self-assembly mechanism proposed in Figure 7-7 and described in literature (Galanakis et al., 2022; J. Koo et al., 2010; Rieu et al., 2020), recombinant constructs lacking specific regions of the fibrinogen molecule (e.g. the αC domain) could be used to study their particular involvement in fibrillogenesis. Moreover, the exposure of self-assembled fibrinogen nanofibers to other ions than sodium followed by XPS and EDX surface analysis could be used to better understand the retention of cations by fibrinogen nanofibers.

Since buffer solutions also have an influence on the fibrous structure of fibrin (Kurniawan et al., 2017), it would also be interesting to study whether salt-induced fibrinogen nanofibers are also affected by the background buffer. Considering the recent results obtained by Hense et al. (Hense & Strube, 2023a), other important parameters whose influence on the self-organization process needs to be studied are the temperature during the drying procedure, the pH and the speed of drying, for instance, by varying the relative humidity.

In terms of expanding applications, using self-assembled fibrinogen scaffolds as biofunctionalization for biomaterials and implant surfaces could provide a great path for future investigations. The integration of further bioactive molecules and components, such as proteins, peptides, growth factors, nanoparticles, or drugs, into self-assembled fibrinogen scaffolds could potentially enhance the capability of these scaffolds to improve cell adhesion and differentiation even further or could provide new properties, such as anti-bacterial properties and the reduction of immune reactions. The latter aspect is essential to prevent the host immune system from rejecting a scaffold.

Considering the results on the interaction of fibrinogen nanofibers with blood platelets and how plasma and plasma molecules affect platelet adhesion, further investigations with other plasma components are necessary to clarify the ability of fibrinogen nanofibers to modulate interactions with platelets and other blood components. Additionally, another important step will be to understand how fibrinogen nanofibers interact with different molecules involved in blood clotting and wound healing, for which, AFM and quartz crystal microbalance analysis will be very valuable tools.

In the framework of the current PhD thesis, cell-fibrinogen scaffold interactions were exemplarily studied with blood platelets. Due to the complexity and diversity of human cells and their physiology, future research works focusing on different cell types will certainly broaden the range of biomedical applications of fibrinogen scaffolds prepared by salt-induced self-assembly. Given the variety of structures obtained in the current work (from smooth *via* rough to nanofibrous), future investigations need to involve these various topographies to allow a systematic analysis of the resulting cell interactions.

After achieving a basic understanding of the underlying principles of salt-induced self-assembly of fibrinogen nanofibers and cell-scaffold interactions, another important step will be to scale up the self-assembly process to provide nanofibrous fibrinogen scaffolds that offer the potential for later *in-vivo* applications. In this regard, the mechanical characterization of self-assembled fibrinogen scaffolds is also very important. As they should mimic the native ECM, fibrinogen

scaffolds should closely match the mechanical characteristics of the native tissue they are intended to replace or regenerate. Research works on mechanical characterization could thus ensure that fibrinogen scaffolds mimic the required stiffness, elasticity, and strength, allowing it to effectively support cell growth in the target tissue.

The understanding of the long-term behavior of self-assembled scaffolds *in vivo* is another important focus for future studies. This category for instance requires degradation studies, which could be used to evaluate the chemical and physical stability of fibrinogen scaffolds when exposed to various types of environmental conditions that resemble the physiological conditions. Moreover, it will be important to understand whether self-assembled fibrinogen scaffolds prepared with varying self-assembly parameters degrade at rates consistent with tissue formation. On the other hand, long-term studies could investigate how well fibrinogen scaffolds integrate into the host tissue by specific binding to various molecules involved in tissue regeneration. These studies could also focus on factors such as cell infiltration, vascularization, and the formation of functional tissue structures over time. Lately, the inflammatory response of the host tissue is of vital importance to ensure the long-term biocompatibility of fibrinogen scaffolds obtained through salt-induced self-assembly.

In summary, the current work already addressed several important aspects of salt-induced fibrillogenesis of fibrinogen, which allowed the optimization of the self-assembly synthesis by the selection of suitable salts and their parameters. With its focus on *in vitro* self-assembly of fibrinogen into nanofibers, this PhD thesis brought nanofibrous fibrinogen scaffolds an important step closer to *in vivo* applications, whilst laying the foundation for future investigation on the topic.

REFERENCES

- A Metrick II, M., & Macdonald, G. (2015). Colloids and Surfaces A : Physicochemical and Engineering Aspects Hofmeister ion effects on the solvation and thermal stability of model proteins lysozyme and myoglobin. *Colloids and Surfaces A: Physicochemical and Engineering Aspects*, 469, 242–251. <https://doi.org/10.1016/j.colsurfa.2015.01.038>
- Andreev, M., Chremos, A., De Pablo, J., & Douglas, J. F. (2017). Coarse-Grained Model of the Dynamics of Electrolyte Solutions. *Journal of Physical Chemistry B*, 121(34), 8195–8202. <https://doi.org/10.1021/acs.jpcc.7b04297>
- Asselta, R., Duga, S., & Tenchini, M. L. (2006). The molecular basis of quantitative fibrinogen disorders. *Journal of Thrombosis and Haemostasis*, 4(10), 2115–2129. <https://doi.org/10.1111/j.1538-7836.2006.02094.x>
- Babitha, S., Rachita, L., Karthikeyan, K., Shoba, E., Janani, I., Poornima, B., & Purna Sai, K. (2017). Electrospun protein nanofibers in healthcare: A review. *International Journal of Pharmaceutics*, 523(1), 52–90. <https://doi.org/10.1016/j.ijpharm.2017.03.013>
- Badylak, S. F. (2002). The extracellular matrix as a scaffold for tissue reconstruction. *CELL & DEVELOPMENTAL BIOLOGY*, 13, 377–383. [https://doi.org/10.1016/S1084-9521\(02\)00094-0](https://doi.org/10.1016/S1084-9521(02)00094-0)
- Baldwin, R. L. (1996). How Hofmeister ion interactions affect protein stability. *Biophysical Journal*, 71(4), 2056–2063. [https://doi.org/10.1016/S0006-3495\(96\)79404-3](https://doi.org/10.1016/S0006-3495(96)79404-3)
- Barinov, N. A., Prokhorov, V. V., Dubrovin, E. V., & Klinov, D. V. (2016). AFM visualization at a single-molecule level of denaturated states of proteins on graphite. *Colloids and Surfaces B: Biointerfaces*. <https://doi.org/10.1016/j.colsurfb.2016.07.014>
- Barker, T. H., & Engler, A. J. (2017). The provisional matrix: setting the stage for tissue repair outcomes. *Matrix Biology*, 60–61, 1–4. <https://doi.org/10.1016/j.matbio.2017.04.003>
- Barnes, C. P., Sell, S. A., Boland, E. D., Simpson, D. G., & Bowlin, G. L. (2007). Nanofiber technology: Designing the next generation of tissue engineering scaffolds. *Advanced Drug Delivery Reviews*, 59(14), 1413–1433. <https://doi.org/10.1016/j.addr.2007.04.022>
- BENNETT, J. S. (2006). Platelet-Fibrinogen Interactions. *Annals of the New York Academy of Sciences*, 936(1), 340–354. <https://doi.org/10.1111/j.1749-6632.2001.tb03521.x>
- Bosman, F. T., & Stamenkovic, I. (2003). Functional structure and composition of the extracellular matrix. *Journal of Pathology*, 200(4), 423–428. <https://doi.org/10.1002/path.1437>
- Broughton, G., Janis, J., & Attinger, C. (2006). *Wound Healing: An Overview*. 1–32. <https://doi.org/10.1097/01.prs.0000222562.60260.f9>

- Bruce, E. E., Okur, H. I., Stegmaier, S., Drexler, C. I., Rogers, B. A., Van Der Vegt, N. F. A., Roke, S., & Cremer, P. S. (2020). Molecular mechanism for the interactions of Hofmeister cations with macromolecules in aqueous solution. *Journal of the American Chemical Society*, *142*(45), 19094–19100. <https://doi.org/10.1021/jacs.0c07214>
- Carlisle, C. R., Coulais, C., Namboothiry, M., Carroll, D. L., Hantgan, R. R., Guthold, M., & Lyon, C. B. (2009). Biomaterials The mechanical properties of individual, electrospun fibrinogen fibers. *Biomaterials*, *30*(6), 1205–1213. <https://doi.org/10.1016/j.biomaterials.2008.11.006>
- Chapman, J., & Dogan, A. (2019). Fibrinogen alpha amyloidosis: insights from proteomics. *Expert Review of Proteomics*, *16*(9), 783–793. <https://doi.org/10.1080/14789450.2019.1659137>
- Chen, G., Ni, N., Wang, B., Xu, B., & Chen, G., Ni, N., Wang, B., & Xu, B. (2011). Direct Observation of Self-Assembled Fibrinogen Fiber Formation on Au (1, 1, 1) in the Absence of Thrombin. *Chemphyschem: A European Journal of Chemical Physics and Physical Chemistry*, *11*(3), 565–568. <https://doi.org/10.1002/cphc.200900916>
- Chen, Hong, Song, W., Zhou, F., Wu, Z., Huang, H., Zhang, J., Lin, Q., & Yang, B. (2009). The effect of surface microtopography of poly(dimethylsiloxane) on protein adsorption, platelet and cell adhesion. *Colloids and Surfaces B: Biointerfaces*, *71*(2), 275–281. <https://doi.org/10.1016/j.colsurfb.2009.02.018>
- Chen, Houyang, & Ruckenstein, E. (2015). Hydrated Ions: From Individual Ions to Ion Pairs to Ion Clusters. *Journal of Physical Chemistry B*, *119*(39), 12671–12676. <https://doi.org/10.1021/acs.jpcb.5b06837>
- Chiumiento, A., Lamponi, S., & Barbucci, R. (2007). Role of fibrinogen conformation in platelet activation. *Biomacromolecules*, *8*(2), 523–531. <https://doi.org/10.1021/bm060664m>
- Cieśla, M., Adamczyk, Z., Barbasz, J., & Wasilewska, M. (2013). Mechanisms of Fibrinogen Adsorption at Solid Substrates at Lower pH. *Langmuir*, *29*(23), 7005–7016. <https://doi.org/10.1021/la4012789>
- Collins, K. D. (1997). Charge density-dependent strength of hydration and biological structure. *Biophysical Journal*, *72*(1), 65–76. [https://doi.org/10.1016/S0006-3495\(97\)78647-8](https://doi.org/10.1016/S0006-3495(97)78647-8)
- Cortes-Canteli, M., Paul, J., Norris, E. H., Bronstein, R., Ahn, H. J., Zamolodchikov, D., Bhuvanendran, S., Fenz, K. M., & Strickland, S. (2010). Fibrinogen and β -Amyloid Association Alters Thrombosis and Fibrinolysis: A Possible Contributing Factor to Alzheimer's Disease. *Neuron*, *66*(5), 695–709.

- <https://doi.org/10.1016/j.neuron.2010.05.014>
- Covington, A. K., & Robinson, R. A. (1975). References standards for the electrometric determination, with ion-selective electrodes, of potassium and calcium in blood serum. *Analytica Chimica Acta*, 78(1), 219–223. [https://doi.org/10.1016/S0003-2670\(01\)84768-1](https://doi.org/10.1016/S0003-2670(01)84768-1)
- Cowin, S. C. (2000). How Is a Tissue Built? *Journal of Biomechanical Engineering*, 122(6), 553–569. <https://doi.org/10.1115/1.1324665>
- de Melo, B. A. G., Jodat, Y. A., Cruz, E. M., Benincasa, J. C., Shin, S. R., & Porcionatto, M. A. (2020). Strategies to use fibrinogen as bioink for 3D bioprinting fibrin-based soft and hard tissues. *Acta Biomaterialia*, 117, 60–76. <https://doi.org/10.1016/j.actbio.2020.09.024>
- De Vries, J. J., Snoek, C. J. M., Rijken, D. C., & De Maat, M. P. M. (2020). Effects of Post-Translational Modifications of Fibrinogen on Clot Formation, Clot Structure, and Fibrinolysis: A Systematic Review. *Arteriosclerosis, Thrombosis, and Vascular Biology*, 40(3), 554–569. <https://doi.org/10.1161/ATVBAHA.119.313626>
- Draf, W. (1986). Fibrinogen Glue in Reconstructive Surgery of the Skull Base. In *Fibrin Sealant in Operative Medicine* (pp. 147–161). Springer Berlin Heidelberg. https://doi.org/10.1007/978-3-642-71359-0_21
- Dutta Choudhury, M., Dutta, T., & Tarafdar, S. (2015). Growth kinetics of NaCl crystals in a drying drop of gelatin: Transition from faceted to dendritic growth. *Soft Matter*, 11(35), 6938–6947. <https://doi.org/10.1039/c5sm00742a>
- Feng, Y., Guo, W., Hu, L., Yi, X., & Tang, F. (2022). Application of Hydrogels as Sustained-Release Drug Carriers in Bone Defect Repair. *Polymers*, 14(22). <https://doi.org/10.3390/polym14224906>
- Forget, J., Awaja, F., Gugutkov, D., Gustavsson, J., Ferrer, G. G., Coelho-sampaio, T., Hochman-mendez, C., Salmeron-sánchez, M., & Altankov, G. (2016). Differentiation of Human Mesenchymal Stem Cells Toward Quality Cartilage Using Fibrinogen-Based Nanofibers. *Macromolecular Bioscience*, 16, 1348–1359. <https://doi.org/https://doi.org/10.1002/mabi.201600080>
- Frantz, C., Stewart, K. M., & Weaver, V. M. (2010). The extracellular matrix at a glance. In *Journal of Cell Science* (Vol. 123, Issue 24, pp. 4195–4200). <https://doi.org/10.1242/jcs.023820>
- Galanakis, D. K., Protopopova, A., Li, K., Yu, Y., Ahmed, T., Senzel, L., Heslin, R., Gouda, M., Koo, J., Weisel, J., Manco-Johnson, M., & Rafailovich, M. (2022). Novel characteristics of soluble fibrin: hypercoagulability and acceleration of blood

- sedimentation rate mediated by its generation of erythrocyte-linked fibers. *Cell and Tissue Research*, 387(3), 479–491. <https://doi.org/10.1007/s00441-022-03599-9>
- Galanakis, D. K., Protopopova, A., Zhang, L., Li, K., Marmorat, C., Scheiner, T., Koo, J., Savitt, A. G., Rafailovich, M., & Weisel, J. (2021). Fibers Generated by Plasma Des-AA Fibrin Monomers and Protofibril/Fibrinogen Clusters Bind Platelets: Clinical and Nonclinical Implications. *TH Open*, 05(03), e273–e285. <https://doi.org/10.1055/s-0041-1725976>
- Giavarina, D. (2017). Blood Biochemistry: Measuring Major Plasma Electrolytes. In *Critical Care Nephrology: Third Edition* (Third Edit). <https://doi.org/10.1016/B978-0-323-44942-7.00054-6>
- Gibb, B. C. (2011). Supramolecular assembly and binding in aqueous solution: Useful tips regarding the Hofmeister and hydrophobic effects. *Israel Journal of Chemistry*, 51(7), 798–806. <https://doi.org/10.1002/ijch.201100058>
- Goto, M., Oaki, Y., & Imai, H. (2016). Dendritic growth of NaCl crystals in a gel matrix: Variation of branching and control of bending. *Crystal Growth and Design*, 16(8), 4278–4284. <https://doi.org/10.1021/acs.cgd.6b00323>
- Gregory, K. P., Elliott, G. R., Robertson, H., Kumar, A., Wanless, E. J., Webber, G. B., Craig, V. S. J., Andersson, G. G., & Page, A. J. (2022). Understanding specific ion effects and the Hofmeister series. *Physical Chemistry Chemical Physics*, 24(21), 12682–12718. <https://doi.org/10.1039/d2cp00847e>
- Gugutkov, D., Gustavsson, J., Ginebra, M. P., & Altankov, G. (2013). Fibrinogen nanofibers for guiding endothelial cell behavior. *Biomaterials Science*, 1(10), 1065. <https://doi.org/10.1039/c3bm60124b>
- Guo, P., Huang, J., Zhao, Y., Martin, C. R., Zare, R. N., & Moses, M. A. (2018). Nanomaterial Preparation by Extrusion through Nanoporous Membranes. *Small*, 14(18), 1703493. <https://doi.org/10.1002/sml.201703493>
- Guo, S., & Dipietro, L. A. (2010). *Factors Affecting Wound Healing*. *Mc* 859, 219–229. <https://doi.org/10.1177/0022034509359125>
- Gupta, K. C., Haider, A., Choi, Y. R., & Kang, I. K. (2014). Nanofibrous scaffolds in biomedical applications. *Biomaterials Research*, 18(1), 1–11. <https://doi.org/10.1186/2055-7124-18-5>
- Hämisch, B., Büngeler, A., Kielar, C., Keller, A., Strube, O., & Huber, K. (2019). Self-Assembly of Fibrinogen in Aqueous, Thrombin-Free Solutions of Variable Ionic Strengths. *Langmuir*, 35(37), 12113–12122.

- <https://doi.org/10.1021/acs.langmuir.9b01515>
- Hense, D., Büngeler, A., Kollmann, F., Hanke, M., Orive, A., Keller, A., Grundmeier, G., Huber, K., & Strube, O. I. (2021). Self-Assembled Fibrinogen Hydro- And Aerogels with Fibrin-like 3D Structures. *Biomacromolecules*, 22(10), 4084–4094. <https://doi.org/10.1021/acs.biomac.1c00489>
- Hense, D., & Strube, O. I. (2023a). Fibrillogenesis and Hydrogel Formation from Fibrinogen Induced by Calcium Salts. *Gels*, 9(3). <https://doi.org/10.3390/gels9030175>
- Hense, D., & Strube, O. I. (2023b). Thrombin-Free Fibrillogenesis and Gelation of Fibrinogen Triggered by Magnesium Sulfate. *Gels*, 9(11), 892. <https://doi.org/10.3390/gels9110892>
- Hofmeister, F. (1888). Zur Lehre von der Wirkung der Salze. *Archiv Für Experimentelle Pathologie Und Pharmakologie*, 24(4–5), 247–260. <https://doi.org/10.1007/BF01918191>
- Holzwarth, J. M., & Ma, P. X. (2011). 3D nanofibrous scaffolds for tissue engineering. *Journal of Materials Chemistry*, 21(28), 10243. <https://doi.org/10.1039/c1jm10522a>
- Hu, Y., Jin, J., Liang, H., Ji, X., Yin, J., & Jiang, W. (2016). PH Dependence of Adsorbed Fibrinogen Conformation and Its Effect on Platelet Adhesion. *Langmuir*, 32(16), 4086–4094. <https://doi.org/10.1021/acs.langmuir.5b04238>
- Huang, Z. M., Zhang, Y. Z., Kotaki, M., & Ramakrishna, S. (2003). A review on polymer nanofibers by electrospinning and their applications in nanocomposites. *Composites Science and Technology*, 63(15), 2223–2253. [https://doi.org/10.1016/S0266-3538\(03\)00178-7](https://doi.org/10.1016/S0266-3538(03)00178-7)
- Hunter, T. (2012). Why nature chose phosphate to modify proteins. *Philosophical Transactions of the Royal Society B: Biological Sciences*, 367(1602), 2513–2516. <https://doi.org/10.1098/rstb.2012.0013>
- Hyde, A. M., Zultanski, S. L., Waldman, J. H., Zhong, Y. L., Shevlin, M., & Peng, F. (2017). General Principles and Strategies for Salting-Out Informed by the Hofmeister Series. *Organic Process Research and Development*, 21(1355–1370). <https://doi.org/10.1021/acs.oprd.7b00197>
- Irvine, G. B., El-Agnaf, O. M., Shankar, G. M., & Walsh, D. M. (2008). Protein aggregation in the brain: The molecular basis for Alzheimer’s and Parkinson’s diseases. *Molecular Medicine*, 14(7–8), 451–464. <https://doi.org/10.2119/2007-00100.Irvine>
- Iscen, A., & Schatz, G. C. (2019). Hofmeister Effects on Peptide Amphiphile Nanofiber Self-Assembly. *Journal of Physical Chemistry B*, 123(32), 7006–7013. <https://doi.org/10.1021/acs.jpcc.9b05532>
- Jagoda-Cwiklik, B., Vácha, R., Lund, M., Srebro, M., & Jungwirth, P. (2007). Ion pairing as a

- possible clue for discriminating between sodium and potassium in biological and other complex environments. *Journal of Physical Chemistry B*, *111*(51), 14077–14079. <https://doi.org/10.1021/jp709634t>
- Jin, S., Shen, Z., Li, J., Lin, P., Xu, X., Ding, X., & Liu, H. (2021). Fibrinogen A Alpha-Chain Amyloidosis Associated With a Novel Variant in a Chinese Family. *Kidney International Reports*, *6*(10), 2726–2730. <https://doi.org/10.1016/j.ekir.2021.07.014>
- Joo, J. Y., Amin, M. L., Rajangam, T., & An, S. S. A. (2015). Fibrinogen as a promising material for various biomedical applications. *Molecular and Cellular Toxicology*, *11*(1), 1–9. <https://doi.org/10.1007/s13273-015-0001-y>
- Joshi, A., Nuntapramote, T., & Brüggemann, D. (2023). Self-Assembled Fibrinogen Scaffolds Support Cocultivation of Human Dermal Fibroblasts and HaCaT Keratinocytes. *ACS Omega*, *8*(9), 8650–8663. <https://doi.org/10.1021/acsomega.2c07896>
- Kämmerer, P. W., Gabriel, M., Al-Nawas, B., Scholz, T., Kirchmaier, C. M., & Klein, M. O. (2012). Early implant healing: Promotion of platelet activation and cytokine release by topographical, chemical and biomimetical titanium surface modifications in vitro. *Clinical Oral Implants Research*, *23*(4), 504–510. <https://doi.org/10.1111/j.1600-0501.2011.02153.x>
- Kang, B., Tang, H., Zhao, Z., & Song, S. (2020). Hofmeister Series: Insights of Ion Specificity from Amphiphilic Assembly and Interface Property. *ACS Omega*, *5*(12), 6229–6239. <https://doi.org/10.1021/acsomega.0c00237>
- Kastelic, M., Kalyuzhnyi, Y. V., Hribar-Lee, B., Dil, K. A., & Vlachy, V. (2015). Protein aggregation in salt solutions. *Proceedings of the National Academy of Sciences of the United States of America*, *112*(21), 6766–6770. <https://doi.org/10.1073/pnas.1507303112>
- Kattula S, JR, B., & Wolberg AS. (2017). Fibrinogen and fibrin in hemostasis and thrombosis. *Arteriosclerosis, Thrombosis, and Vascular Biology*, *37*(3), e13–e21. <https://doi.org/10.1161/ATVBAHA.117.308564>.Fibrinogen
- Kenny, M., Stamboroski, S., Taher, R., Brüggemann, D., & Schoen, I. (2022). Nanofiber Topographies Enhance Platelet-Fibrinogen Scaffold Interactions. *Advanced Healthcare Materials*, *2200249*, 2200249. <https://doi.org/10.1002/adhm.202200249>
- Kepchia, D., Huang, L., Dargusch, R., Rissman, R. A., Shokhirev, M. N., Fischer, W., & Schubert, D. (2020). Diverse proteins aggregate in mild cognitive impairment and Alzheimer's disease brain. *Alzheimer's Research and Therapy*, *12*(1), 1–20. <https://doi.org/10.1186/s13195-020-00641-2>
- Kikuchi, L., Park, J. Y., Victor, C., & Davies, J. E. (2005). Platelet interactions with calcium-

- phosphate-coated surfaces. *Biomaterials*, 26(26), 5285–5295. <https://doi.org/10.1016/j.biomaterials.2005.01.009>
- Kiyohara, K., & Kawai, Y. (2019). Hydration of monovalent and divalent cations near a cathode surface. *Journal of Chemical Physics*, 151(10), 104704. <https://doi.org/10.1063/1.5113738>
- Köhler, S., Schmid, F., & Settanni, G. (2015). The Internal Dynamics of Fibrinogen and Its Implications for Coagulation and Adsorption. *PLOS Computational Biology*, 11(9), e1004346. <https://doi.org/10.1371/journal.pcbi.1004346>
- Koo, J., Rafailovich, M. H., Medved, L., Tsurupa, G., Kudryk, B. J., Liu, Y., & Galanakis, D. K. (2010). Evaluation of fibrinogen self-assembly: role of its α C region. *Journal of Thrombosis and Haemostasis*, 8(12), 2727–2735. <https://doi.org/10.1111/j.1538-7836.2010.04072.x>
- Koo, Jaseung, Galanakis, D., Liu, Y., Ramek, A., Fields, A., Ba, X., Simon, M., & Rafailovich, M. H. (2012). Control of Anti-Thrombogenic Properties : Surface-Induced Self- Assembly of Fibrinogen Fibers. *Biomacromolecules*, 13(5), 1259–1268. <https://doi.org/10.1021/bm2015976>
- Kular, J. K., Basu, S., & Sharma, R. I. (2014). The extracellular matrix: Structure, composition, age-related differences, tools for analysis and applications for tissue engineering. In *Journal of Tissue Engineering* (Vol. 5). SAGE Publications Ltd. <https://doi.org/10.1177/2041731414557112>
- Kumbar, S. G., James, R., Nukavarapu, S. P., & Laurencin, C. T. (2008). Electrospun nanofiber scaffolds: Engineering soft tissues. *Biomedical Materials*, 3(3). <https://doi.org/10.1088/1748-6041/3/3/034002>
- Kurniawan, N. A., Van Kempen, T. H. S., Sonneveld, S., Rosalina, T. T., Vos, B. E., Jansen, K. A., Peters, G. W. M., Van De Vosse, F. N., & Koenderink, G. H. (2017). Buffers Strongly Modulate Fibrin Self-Assembly into Fibrous Networks. *Langmuir*, 33(25), 6342–6352. <https://doi.org/10.1021/acs.langmuir.7b00527>
- Laage, D., Elsaesser, T., & Hynes, J. T. (2017). Water Dynamics in the Hydration Shells of Biomolecules. *Chemical Reviews*, 117(16), 10694–10725. <https://doi.org/10.1021/acs.chemrev.6b00765>
- Laurens, N., & deMaat, M. P. M. (2006). Fibrin structure and wound healing. *Journal of Thrombosis and Haemostasis*, 4(5), 932–939. <https://doi.org/10.1111/j.1538-7836.2006.01861.x>
- Lendel, C., & Solin, N. (2021). Protein nanofibrils and their use as building blocks of

- sustainable materials. *RSC Advances*, *11*(62), 39188–39215. <https://doi.org/10.1039/d1ra06878d>
- Liao, H.-S., Lin, J., Liu, Y., Huang, P., Jin, A., & Chen, X. (2016). Self-assembly mechanisms of nanofibers from peptide amphiphiles in solution and on substrate surfaces. *Nanoscale*, *8*(31), 14814–14820. <https://doi.org/10.1039/C6NR04672J>
- Makogonenko, E., Tsurupa, G., Ingham, K., & Medved, L. (2002). Interaction of fibrin(ogen) with fibronectin: Further characterization and localization of the fibronectin-binding site. *Biochemistry*, *41*(25), 7907–7913. <https://doi.org/10.1021/bi025770x>
- Mao, H., Yang, L., Zhu, H., Wu, L., Ji, P., Yang, J., & Gu, Z. (2020). Recent advances and challenges in materials for 3D bioprinting. *Progress in Natural Science: Materials International*, *30*(5), 618–634. <https://doi.org/10.1016/j.pnsc.2020.09.015>
- Marchin, K. L., & Berrie, C. L. (2003). Conformational changes in the plasma protein fibrinogen upon adsorption to graphite and mica investigated by atomic force microscopy. *Langmuir*, *19*(23), 9883–9888. <https://doi.org/10.1021/la035127r>
- Martin, S. C., & Björk, I. (1990). Conformational changes in human fibrinogen after in vitro phosphorylation and their relation to fibrinogen behaviour. *FEBS Letters*, *272*(1–2), 103–105. [https://doi.org/10.1016/0014-5793\(90\)80458-U](https://doi.org/10.1016/0014-5793(90)80458-U)
- Martin, S. C., Ekman, P., Forsberg, P. O., & Ersmark, H. (1992). Increased phosphate content of fibrinogen in vivo correlates with alteration in fibrinogen behaviour. *Thrombosis Research*, *68*(6), 467–473. [https://doi.org/10.1016/0049-3848\(92\)90059-J](https://doi.org/10.1016/0049-3848(92)90059-J)
- Mcmanus, M., Boland, E., Sell, S., Bowen, W., Koo, H., Simpson, D., & Bowlin, G. (2007). Electrospun nanofibre fibrinogen for urinary tract tissue reconstruction. *Biomedical Materials*, *2*, 257–262. <https://doi.org/10.1088/1748-6041/2/4/008>
- McManus, M. C., Boland, E. D., Koo, H. P., Barnes, C. P., Pawlowski, K. J., Wnek, G. E., Simpson, D. G., & Bowlin, G. L. (2006). Mechanical properties of electrospun fibrinogen structures. *Acta Biomaterialia*, *2*(1), 19–28. <https://doi.org/10.1016/j.actbio.2005.09.008>
- McManus, M. C., Boland, E. D., Simpson, D. G., Barnes, C. P., & Bowlin, G. L. (2007). Electrospun fibrinogen: Feasibility as a tissue engineering scaffold in a rat cell culture model. *Journal of Biomedical Materials Research Part A*, *81A*(2), 299–309. <https://doi.org/10.1002/jbm.a.30989>
- McPherson, H. R., Duval, C., Baker, S. R., Hindle, M. S., Cheah, L. T., Asquith, N. L., Domingues, M. M., Ridger, V. C., Connell, S. D. A., Naseem, K. M., Philippou, H., Ajjan, R. A., & Ariëns, R. A. S. (2021). Fibrinogen α c-subregions critically contribute blood clot fibre growth, mechanical stability, and resistance to fibrinolysis. *ELife*, *10*, 1–20.

- <https://doi.org/10.7554/eLife.68761>
- Medved, L., & Weisel, J. W. (2009). Recommendations for nomenclature on fibrinogen and fibrin. *Journal of Thrombosis and Haemostasis*, 7(2), 355–359. <https://doi.org/10.1111/j.1538-7836.2008.03242.x>
- Midwood, K. S., Williams, L. V., & Schwarzbauer, J. E. (2004). *Tissue repair and the dynamics of the extracellular matrix*. 36, 1031–1037. <https://doi.org/10.1016/j.biocel.2003.12.003>
- Mirzaei-Parsa, M. J., Ghanizadeh, A., Ebadi, M. T. K., & Faridi-Majidi, R. (2018). An alternative solvent for electrospinning of fibrinogen nanofibers. *Bio-Medical Materials and Engineering*, 29(3), 279–287. <https://doi.org/10.3233/BME-181736>
- Monroe, D. M., Hoffman, M., & Roberts, H. R. (2002). Platelets and thrombin generation. *Arteriosclerosis, Thrombosis, and Vascular Biology*, 22(9), 1381–1389. <https://doi.org/10.1161/01.ATV.0000031340.68494.34>
- Mosesson, M. W. (2005). Fibrinogen and fibrin structure and functions. *Journal of Thrombosis and Haemostasis*, 3(8), 1894–1904. <https://doi.org/10.1111/j.1538-7836.2005.01365.x>
- Mottaghalab, F., Farokhi, M., Zaminy, A., Kokabi, M., Soleimani, M., Mirahmadi, F., Shokrgozar, M. A., & Sadeghizadeh, M. (2013). A Biosynthetic Nerve Guide Conduit Based on Silk/SWNT/Fibronectin Nanocomposite for Peripheral Nerve Regeneration. *PLoS ONE*, 8(9), 6–17. <https://doi.org/10.1371/journal.pone.0074417>
- Murdoch, T. J., Humphreys, B. A., Willott, J. D., Gregory, K. P., Prescott, S. W., Nelson, A., Wanless, E. J., & Webber, G. B. (2016). Specific Anion Effects on the Internal Structure of a Poly(N-isopropylacrylamide) Brush. *Macromolecules*, 49(16), 6050–6060. <https://doi.org/10.1021/acs.macromol.6b01001>
- Nezafati, N., Moztarzadeh, F., & Hesarakhi, S. (2012). Surface reactivity and in vitro biological evaluation of sol gel derived silver/calcium silicophosphate bioactive glass. *Biotechnology and Bioprocess Engineering*, 17(4), 746–754. <https://doi.org/10.1007/s12257-012-0046-x>
- Nihonyanagi, S., Yamaguchi, S., & Tahara, T. (2014). Counterion effect on interfacial water at charged interfaces and its relevance to the hofmeister series. *Journal of the American Chemical Society*, 136(17), 6155–6158. <https://doi.org/10.1021/ja412952y>
- Nikolova, M. P., & Chavali, M. S. (2019). Recent advances in biomaterials for 3D scaffolds: A review. *Bioactive Materials*, 4(October 2019), 271–292. <https://doi.org/10.1016/j.bioactmat.2019.10.005>
- Nitti, P., Narayanan, A., Pellegrino, R., Villani, S., Madaghiele, M., & Demitri, C. (2023). Cell-Tissue Interaction: The Biomimetic Approach to Design Tissue Engineered Biomaterials. *Bioengineering*, 10(10). <https://doi.org/10.3390/bioengineering10101122>

- Okur, H. I., Hladílková, J., Rembert, K. B., Cho, Y., Heyda, J., Dzubiella, J., Cremer, P. S., & Jungwirth, P. (2017). Beyond the Hofmeister Series: Ion-Specific Effects on Proteins and Their Biological Functions. *The Journal of Physical Chemistry B*, *121*(9), 1997–2014. <https://doi.org/10.1021/acs.jpcc.6b10797>
- Page, M. J., Thomson, G. J. A., Nunes, J. M., Engelbrecht, A. M., Nell, T. A., de Villiers, W. J. S., de Beer, M. C., Engelbrecht, L., Kell, D. B., & Pretorius, E. (2019). Serum amyloid A binds to fibrin(ogen), promoting fibrin amyloid formation. *Scientific Reports*, *9*(1), 1–14. <https://doi.org/10.1038/s41598-019-39056-x>
- Palchesko, R. N., Sun, Y., Zhang, L., Szymanski, J. M., Jallerat, Q., & Feinberg, A. W. (2013). Nanofiber Biomaterials. In *Springer Handbook of Nanomaterials* (pp. 977–1010). Springer Berlin Heidelberg. https://doi.org/10.1007/978-3-642-20595-8_27
- Palta, S., Saroa, R., & Palta, A. (2014). Overview of the coagulation system. *Indian Journal of Anaesthesia*, *58*(5), 515–523. <https://doi.org/10.4103/0019-5049.144643>
- Pankov, R., & Yamada, K. M. (2002). Fibronectin at a glance. *Journal of Cell Science*, *115*(20), 3861–3863. <https://doi.org/10.1242/jcs.00059>
- Patel, P. R., & Gundloori, R. V. N. (2023). A review on electrospun nanofibers for multiple biomedical applications. *Polymers for Advanced Technologies*, *34*(1), 44–63. <https://doi.org/10.1002/pat.5896>
- Pereira, M., Rybarczyk, B. J., Odrliin, T. M., Hocking, D. C., Sottile, J., & Simpson-Haidaris, P. J. (2002). The incorporation of fibrinogen into extracellular matrix is dependent on active assembly of a fibronectin matrix. *Journal of Cell Science*, *115*(3), 609–617. <https://doi.org/10.1242/jcs.115.3.609>
- Rajangam, T., & An, S. S. A. (2013). Fibrinogen and fibrin based micro and nano scaffolds incorporated with drugs , proteins , cells and genes for therapeutic biomedical applications. *International Journal of Nanomedicine*, *8*, 3641–3662. <https://doi.org/10.2147/IJN.S43945>
- Raoufi, M., Aslankoochi, N., Mollenhauer, C., Boehm, H., Spatz, J. P., & Brüggemann, D. (2016). Template-assisted extrusion of biopolymer nanofibers under physiological conditions. *Integrative Biology (United Kingdom)*, *8*(10), 1059–1066. <https://doi.org/10.1039/c6ib00045b>
- Raoufi, M., Das, T., Schoen, I., Vogel, V., Brüggemann, D., & Spatz, J. P. (2015). Nanopore Diameters Tune Strain in Extruded Fibronectin Fibers. *Nano Letters*, *15*(10), 6357–6364. <https://doi.org/10.1021/acs.nanolett.5b01356>
- Reichert, J., Wei, G., & Jandt, K. D. (2009). Formation and Topotactical Orientation of

- Fibrinogen Nanofibrils on Graphite Nanostructures. *Advanced Engineering Materials*, 11(11), B177–B181. <https://doi.org/10.1002/adem.200900084>
- Rieu, C., Mosser, G., Haye, B., Sanson, N., Coradin, T., & Trichet, L. (2020). Thrombin-free polymerization leads to pure fibrin(ogen) materials with extended processing capacity. *BioRxiv*, 1–38. <https://doi.org/10.1101/2020.05.12.091793>
- Sai Malisetty, A., Stamboroski, S., Lierath, J., Noeske, M., Brueggemann, D., & Köppen, S. (2023). Salt-induced precipitation of fibrinogen: New insights from experiments and simulations. *Biophysical Journal*, 122(3), 40a. <https://doi.org/10.1016/j.bpj.2022.11.428>
- Salgado, E. N., Radford, R. J., & Tezcan, F. A. (2010). Metal-Directed Protein Self-Assembly. *Accounts of Chemical Research*, 43(5), 661–672. <https://doi.org/10.1021/ar900273t>
- Salis, A., & Ninham, B. W. (2014). Models and mechanisms of Hofmeister effects in electrolyte solutions, and colloid and protein systems revisited. *Chem. Soc. Rev*, 43(21), 7358. <https://doi.org/10.1039/c4cs00144c>
- Samitsu, S., Zhang, R., Peng, X., Krishnan, M. R., Fujii, Y., & Ichinose, I. (2013). Flash freezing route to mesoporous polymer nanofibre networks. *Nature Communications*, 4, 1–7. <https://doi.org/10.1038/ncomms3653>
- Schwartz, C. P., Uejio, J. S., Duffin, A. M., England, A. H., Kelly, D. N., Prendergast, D., & Saykally, R. J. (2010). Investigation of protein conformation and interactions with salts via X-ray absorption spectroscopy. *Proceedings of the National Academy of Sciences of the United States of America*, 107(32), 14008–14013. <https://doi.org/10.1073/pnas.1006435107>
- Scott, L. E., Mair, D. B., Narang, J. D., Feleke, K., & Lemmon, C. A. (2015). Fibronectin fibrillogenesis facilitates mechano-dependent cell spreading, force generation, and nuclear size in human embryonic fibroblasts. *Integrative Biology*, 7(11), 1454–1465. <https://doi.org/10.1039/c5ib00217f>
- Sell, S. A., Francis, M. P., Garg, K., McClure, M. J., Simpson, D. G., & Bowlin, G. L. (2008). Cross-linking methods of electrospun fibrinogen scaffolds for tissue engineering applications. *Biomedical Materials*, 3(4). <https://doi.org/10.1088/1748-6041/3/4/045001>
- Sell, S. A., Wolfe, P. S., Garg, K., McCool, J. M., Rodriguez, I. A., & Bowlin, G. L. (2010). The use of natural polymers in tissue engineering: A focus on electrospun extracellular matrix analogues. *Polymers*, 2(4), 522–553. <https://doi.org/10.3390/polym2040522>
- Sell, S., Barnes, C., Simpson, D., & Bowlin, G. (2008). Scaffold permeability as a means to determine fiber diameter and pore size of electrospun fibrinogen. *Journal of Biomedical Materials Research - Part A*, 85(1), 115–126. <https://doi.org/10.1002/jbm.a.31556>

- Silberstein, L., Williams, L., Hughlett, M., Magee, D., & Weisman, R. (1988). An autologous fibrinogen-based adhesive for use in otologic surgery. *Transfusion*, 28(4), 319–321. <https://doi.org/10.1046/j.1537-2995.1988.28488265257.x>
- Soleimanpour, M., Mirhaji, S. S., Jafari, S., Derakhshankhah, H., Mamashli, F., Nedaei, H., Karimi, M. R., Motasadizadeh, H., Fatahi, Y., Ghasemi, A., Nezamtaheri, M. S., Khajezade, M., Teimouri, M., Goliaei, B., Delattre, C., & Saboury, A. A. (2022). Designing a new alginate-fibrinogen biomaterial composite hydrogel for wound healing. *Scientific Reports*, 12(1), 1–17. <https://doi.org/10.1038/s41598-022-11282-w>
- Solovieva, E. V., Fedotov, A. Y., Mamonov, V. E., Komlev, V. S., & Panteleyev, A. A. (2018). Fibrinogen-modified sodium alginate as a scaffold material for skin tissue engineering. *Biomedical Materials*, 13(2), 025007. <https://doi.org/10.1088/1748-605X/aa9089>
- Spicer, P. P., & Mikos, A. G. (2010). Fibrin glue as a drug delivery system. *Journal of Controlled Release*, 148(1), 49–55. <https://doi.org/10.1016/j.jconrel.2010.06.025>
- Sreerenganathan, M., Mony, U., & Rangasamy, J. (2014). Thermo-responsive fibrinogen nanogels: A viable thermo-responsive drug delivery agent for breast cancer therapy? *Nanomedicine*, 9(18), 2721–2723. <https://doi.org/10.2217/nnm.14.181>
- Stamboroski, S., Boateng, K., Lierath, J., Kowalik, T., Thiel, K., Köppen, S., Noeske, P.-L. M., & Brüggemann, D. (2021). Influence of divalent metal ions on the precipitation of the plasma protein fibrinogen. *Biomacromolecules*, In press. <https://doi.org/10.1021/acs.biomac.1c00930>
- Stamboroski, S., Joshi, A., Noeske, P.-L. M., Köppen, S., & Brüggemann, D. (2021). Principles of fibrinogen fiber assembly in vitro. *Macromolecular Bioscience*, 21(5), 2000412. <https://doi.org/10.1002/mabi.202000412>
- Stapelfeldt, K., Stamboroski, S., Mednikova, P., & Brüggemann, D. (2019). Fabrication of 3D-nanofibrous fibrinogen scaffolds using salt-induced self assembly. *Biofabrication*, 11(2), 025010. <https://doi.org/10.1088/1758-5090/ab0681>
- Stapelfeldt, K., Stamboroski, S., Walter, I., Suter, N., Kowalik, T., Michaelis, M., & Br, D. (2019). Controlling the multiscale structure of nanofibrous fibrinogen scaffolds for wound healing. *Nano Letters*, 49(0), 1–15. <https://doi.org/https://doi.org/10.1021/acs.nanolett.9b02798>
- Stavrou, E., & Schmaier, A. H. (2010). Factor XII: What does it contribute to our understanding of the physiology and pathophysiology of hemostasis & thrombosis. *Thrombosis Research*, 125(3), 210–215. <https://doi.org/10.1016/j.thromres.2009.11.028>
- Strukova, S. (2006). Blood coagulation-dependent inflammation. Coagulation-dependent

- inflammation and inflammation-dependent thrombosis. *Frontiers in Bioscience*, 11(1), 59. <https://doi.org/10.2741/1780>
- Suter, N., Joshi, A., Wunsch, T., Graupner, N., Stapelfeldt, K., Radmacher, M., Müssig, J., & Brüggemann, D. (2021). Self-assembled fibrinogen nanofibers support fibroblast adhesion and prevent E. Coli infiltration. *Materials Science and Engineering C*, 126, 112156. <https://doi.org/https://doi.org/10.1016/j.msec.2021.112156>
- Suter, N., Stebel, S., Rianna, C., Radmacher, M., & Brüggemann, D. (2020). Spatial patterning of nanofibrous collagen scaffolds modulates fibroblast morphology. *Biofabrication*, 13(1). <https://doi.org/10.1088/1758-5090/abb744>
- Ta, T. C., Sykes, M. T., & McDermott, M. T. (1998). Real-time observation of plasma protein film formation on well-defined surfaces with scanning force microscopy. *Langmuir*, 14(9), 2435–2443. <https://doi.org/10.1021/la9712348>
- Theocharis, A. D., Skandalis, S. S., Gialeli, C., & Karamanos, N. K. (2016). Extracellular matrix structure. In *Advanced Drug Delivery Reviews* (Vol. 97, pp. 4–27). Elsevier B.V. <https://doi.org/10.1016/j.addr.2015.11.001>
- Tracy, P. B., & Mann, K. G. (1983). Prothrombinase complex assembly on the platelet surface is mediated through the 74,000-dalton component of factor V(a). *Proceedings of the National Academy of Sciences of the United States of America*, 80(8 I), 2380–2384. <https://doi.org/10.1073/pnas.80.8.2380>
- Tsapikouni, T. S., & Missirlis, Y. F. (2007). pH and ionic strength effect on single fibrinogen molecule adsorption on mica studied with AFM. *Colloids and Surfaces B: Biointerfaces*, 57(1), 89–96. <https://doi.org/10.1016/j.colsurfb.2007.01.011>
- Varki, A., Cummings, R., Esko, J., Stanley, P., Hart, G., Aebi, M., Darvill, A., Kinoshita, T., Packer, N., Prestegard, J., Schnaar, R., & Seeberger, P. (1999). Essentials of Glycobiology. In *Cold Spring Harbor (NY)*. Cold Spring Harbor (NY): Cold Spring Harbor Laboratory Press. <https://www.ncbi.nlm.nih.gov/books/NBK20693/?report=classic>
- Vasconcelos, D. M., Gonçalves, R. M., Almeida, C. R., Pereira, I. O., Oliveira, M. I., Neves, N., Silva, A. M., Ribeiro, A. C., Cunha, C., Almeida, A. R., Ribeiro, C. C., Gil, A. M., Seebach, E., Kynast, K. L., Richter, W., Lamghari, M., Santos, S. G., & Barbosa, M. A. (2016). Fibrinogen scaffolds with immunomodulatory properties promote in vivo bone regeneration. *Biomaterials*, 111, 163–178. <https://doi.org/10.1016/j.biomaterials.2016.10.004>
- Vasita, R., & Katti, D. S. (2006). Nanofibers and their applications in tissue engineering. *International Journal of Nanomedicine*, 1(1), 15–30.

- <https://doi.org/10.2147/nano.2006.1.1.15>
- Verma, A., Verma, M., & Singh, A. (2020). Animal tissue culture principles and applications. In *Animal Biotechnology* (pp. 269–293). Elsevier. <https://doi.org/10.1016/B978-0-12-811710-1.00012-4>
- Vogel, V. (2018). Unraveling the Mechanobiology of Extracellular Matrix. *Annual Review of Physiology*, 80(1), 353–387. <https://doi.org/10.1146/annurev-physiol-021317-121312>
- Vrbka, L., Vondrasek, J., Jagoda-cwiklik, B., Vacha, R., & Jungwirth, P. (2006). *Quantification and rationalization of the higher affinity of sodium over potassium to protein surfaces*. <https://doi.org/10.1073/pnas.0606959103>
- Wang, J., Wang, H., Wang, Y., Li, J., Su, Z., & Wei, G. (2014). Alternate layer-by-layer assembly of graphene oxide nanosheets and fibrinogen nanofibers on a silicon substrate for a biomimetic three-dimensional hydroxyapatite scaffold. *J. Mater. Chem. B*, 2(42), 7360–7368. <https://doi.org/10.1039/C4TB01324G>
- Wang, K., Meng, X., & Guo, Z. (2021). Elastin Structure, Synthesis, Regulatory Mechanism and Relationship With Cardiovascular Diseases. *Frontiers in Cell and Developmental Biology*, 9(November), 1–10. <https://doi.org/10.3389/fcell.2021.596702>
- Wasilewska, M., & Adamczyk, Z. (2011). Fibrinogen adsorption on mica studied by AFM and in situ streaming potential measurements. *Langmuir*, 27(2), 686–696. <https://doi.org/10.1021/la102931a>
- Wei, G., Reichert, J., Bossert, J., & Jandt, K. D. (2008). Novel biopolymeric template for the nucleation and growth of hydroxyapatite crystals based on self-assembled fibrinogen fibrils. *Biomacromolecules*, 9(11), 3258–3267. <https://doi.org/10.1021/bm800824r>
- Wei, G., Reichert, J., & Jandt, K. D. (2008). Controlled self-assembly and templated metallization of fibrinogen nanofibrils. *Chemical Communications*, 33, 3903–3905. <https://doi.org/10.1039/b806316h>
- Weisel, J. W. (2005). Fibrinogen and fibrin. In *Advances in Protein Chemistry* (Vol. 70, pp. 247–299). [https://doi.org/10.1016/S0065-3233\(05\)70008-5](https://doi.org/10.1016/S0065-3233(05)70008-5)
- Weisel, J. W., & Litvinov, R. I. (2017). Fibrin formation, structure and properties. In *Subcellular Biochemistry* (Vol. 82, pp. 405–456). Springer. https://doi.org/10.1007/978-3-319-49674-0_13
- Weisel, J. W., & Medved, L. (2001). The structure and function of the alpha C domains of fibrinogen. *Annals of the New York Academy of Sciences*, 936, 312–327. <https://doi.org/10.1111/j.1749-6632.2001.tb03517.x>
- Wnek, G. E., Carr, M. E., Simpson, D. G., & Bowlin, G. L. (2003). Electrospinning of nanofiber

- fibrinogen structures. *Nano Letters*, 3(2), 213–216. <https://doi.org/10.1021/nl025866c>
- Zhang, J. (2012). Protein-Protein Interactions in Salt Solutions. In *Protein-Protein Interactions - Computational and Experimental Tools*. IntechOpen. <https://doi.org/10.5772/38056>
- Zhang, L., Casey, B., Galanakis, D. K., Marmorat, C., Skoog, S., Vorvolakos, K., Simon, M., & Rafailovich, M. H. (2017). The influence of surface chemistry on adsorbed fibrinogen conformation, orientation, fiber formation and platelet adhesion. *Acta Biomaterialia*, 54, 164–174. <https://doi.org/10.1016/j.actbio.2017.03.002>
- Zhang, S., Marini, D. M., Hwang, W., & Santoso, S. (2002). Design of nanostructured biological materials through self-assembly of peptides and proteins. *Current Opinion in Chemical Biology*, 6(6), 865–871. [https://doi.org/10.1016/S1367-5931\(02\)00391-5](https://doi.org/10.1016/S1367-5931(02)00391-5)
- Zhang, Y., & Cremer, P. S. (2006). Interactions between macromolecules and ions: the Hofmeister series. In *Current Opinion in Chemical Biology* (Vol. 10, Issue 6, pp. 658–663). Elsevier Current Trends. <https://doi.org/10.1016/j.cbpa.2006.09.020>
- Zhang, Y., Furyk, S., Bergbreiter, D. E., & Cremer, P. S. (2005). Specific ion effects on the water solubility of macromolecules: PNIPAM and the Hofmeister series. *Journal of the American Chemical Society*, 127(41), 14505–14510. <https://doi.org/10.1021/ja0546424>
- Zhao, L., Qiao, S., & Liu, J. (2016). Protein self-assembly: technology and strategy. *Science China Chemistry*, 59(12), 1531–1540. <https://doi.org/10.1007/s11426-016-0231-3>
- Zuev, Y. F., Litvinov, R. I., Sitnitsky, A. E., Idiyatullin, B. Z., Bakirova, D. R., Galanakis, D. K., Zhmurov, A., Barsegov, V., & Weisel, J. W. (2017). Conformational Flexibility and Self-Association of Fibrinogen in Concentrated Solutions. *The Journal of Physical Chemistry B*, 121(33), 7833–7843. <https://doi.org/10.1021/acs.jpcc.7b05654>